TRINITY COLLEGE DUBLIN
SCHOOL OF PHYSICS

Interrogation and refinement of DFT+U+J energetics in magnetic systems

Author:
Lórien MacEnulty
Advisor:
David D. O'Regan

May 6, 2025

Declaration

I declare that this thesis has not been submitted as an exercise for a degree at this or any other university and it is entirely my own work.

I agree to deposit this thesis in the University's open access institutional repository or allow the Library to do so on my behalf, subject to Irish Copyright Legislation and Trinity College Library conditions of use and acknowledgement.

I consent to the examiner retaining a copy of the thesis beyond the examining period, should they so wish (EU GDPR May 2018).

Name: Lórien MacEnulty

Signature: 

Date: 06/05/2025

Summary

With quantum computing just beyond the horizon, more emphasis than ever in history is placed on adaptable, efficient, yet accurate algorithms for routinely modeling properties of large-scale material systems. Among those electronic structure theories receiving the most scientific attention is density functional theory (DFT), which, despite its failures in the available computationally tractable local or semi-local approximative functionals, has undoubtedly accelerated the collective understanding of quantum many-body interactions and their precipitation of macroscopic phenomena.

Meanwhile, a surge in interest in technologically viable classes of materials with environmentally friendly applications—among them transition metal oxides, Prussian Blue analogues, and spin-crossover molecules—has impelled DFT practitioners and theorists to develop minimally invasive methods to manage DFT's characteristic errors while preserving its first-principles status. Noticeably pronounced for the aforementioned strongly correlated systems are the self-interaction error (SIE, or more generally, the delocalization error) implicated in band-gap underestimation and energy-density non-linearity and quantified by the Hubbard U—and the static correlation error (SCE), associated with energy-magnetization curvature in degenerate and multi-valence systems.

The Hubbard family of corrective functionals (DFT+U+J) featuring *in situ*-calculated Hubbard U and Hund's J parameters are called to rise to the challenge, spurring a return to first principles in search of innovative, efficient, and minimally parametrized ways to address SIE and SCE. The following dissertation describes a series of meticulously composed studies designed within the DFT+U+J framework to interrogate and rectify some of its remaining weaknesses and ambiguities.

We focus on obtaining state-of-the-art spin-based total energy differences in magnetic systems, metrics that DFT+U+J-type functionals have hitherto struggled to achieve. In one project, we calculate Heisenberg interatomic exchange-coupling parameters in terms of strict density-functional accessible total energy differences between magnetic configurations in nickel oxide and directly compare these parameters against other available theoretical values, such as those from costly hybrid functionals, and available experimental parameters (i.e., derived from magnon frequencies). Another project centers on spin-crossover adiabatic energy differences in a series of octahedrally coordinated iron

II molecules. Generally, these studies resoundingly indicate that common Hubbard functionals with bespoke parametrization informed by the magnetic environment do not result in comparable total energies. Moreover, our results point toward misconstruction of the Hubbard functionals in incorporating magnetic considerations and a breakdown in either the two main linear response formalisms for determining the Hund's J or how the functionals incorporate this parameter.

Throughout these investigations are suggestions towards best practices in calculating the Hubbard U and Hund's J for non-ground-state magnetic orderings via linear response. Further projects takes this refinement to the next level by (i) automating linear response for the ABINIT open-source electronic structure suite and (ii) identifying its dominant components, error analysis protocol, and logistics for practical implementation. Specifically, we lend a critical eye to the projector functions—the mechanisms that isolate the atomic subspaces destined for corrective treatment from the charge bath in which they are immersed. Our final project asserts that the projectors influence the magnitude of the Hubbard parameters in extremizable ways.

Without an accurate microscopic description of spin-based energetics and electronic structure properties, we are unlikely to design and/or discover new materials that optimize and tailor functionality while simultaneously minimizing, if not eliminating, impracticalities. Ultimately, this dissertation strives to contribute to the establishment of resilient techniques that go on to inform and facilitate automation of first-principles methods for high-throughput informatics. It represents a specialized but important cog in the machine we collectively build to accelerate materials discovery.

Acknowledgement

Unequivocal thanks is extended to the Trinity Provost PhD Project Award by which this research was subsidized.

The work in Part II would not have come to fruition without the support of the ABINIT team, in particular the enthusiasm and initiative of Gian-Marco Rignanese, whom I thank warmly. I also thank Matteo Giantomassi for patience and technical guidance.

The work in Part III was refined through helpful discussions with Daniel Lambert, Andrew Burgess, Stefano Sanvito, and Alessandro Lunghi.

The work in Part IV was further made possible by the French Research Residency program of 2023 from l'Ambassade de France en Irlande. Much of my gratitude is owed to Roberta Poloni for bringing keen expertise and perspective to the collaboration. Many thanks, mutually, to João Paulo Almeida de Mendonça for wisdom and optimism.

Calculations were principally performed on the Boyle and Lonsdale clusters, the facilities of which were funded through grants from the European Research Council and Taighde Éireann—Research Ireland (formerly Science Foundation Ireland) and are maintained by Research IT (formerly TCHPC) at Trinity College Dublin. Additional computational resources, facilities, and support were provided by the Irish Centre for High-End Computing (ICHEC). Extension funding was received from the Higher Education Authority.

Many thanks to my cats—Whomst, then Pangur Bán—for inspiration. To Jeremy Joiner and Karen Hirsch, who believed in me. To my mother, Kristen MacEnulty, and my sister, Israel MacEnulty, whose love, spectatorship, and counsel have armed me in this fight against—and ultimate triumph over—self-doubt. A hearty thanks is extended to David D. O'Regan for guidance, advice, advocacy, and allyship. But my most heartfelt gratitude is reserved for my partner Justin Bec-Canet, whose unyielding loyalty and accumulated sacrifice have made the existential tumult of the past four years so much easier to bear.

Toebeanz McGee

Kathleen J. Upton
Feb. 1, 1943 – May 18, 2023

James A. Richardson
May 24, 1944 – May 26, 2023

Whomst MacBec
Oct. 2021 – July 2023

List of Publications

Listed here are the author's publications that contribute, in part or in entirety, to the investigations comprising this dissertation.

L. MacEnulty, J.P.A. de Mendonça, R. Poloni, & D. D. O'Regan, "[Working Title] Breakdown and potential remedies for DFT+U+J total energy differences and linear response parameter calculations in spin-crossover complexes" | *manuscript under preparation*

•

L. MacEnulty, M. Giantomassi, B. Amadon, G.-M. Rignanese, & D. D. O'Regan, "Facilities and practices for linear response Hubbard parameters U and J in Abinit," *Electronic Structure* **6** 037003 (2024) | DOI: 10.1088/2516-1075/ad610f

•

L. MacEnulty & D. D. O'Regan, "Optimization strategies developed on NiO for Heisenberg exchange-coupling calculations using projector-augmented wave based first-principles DFT+U+J," *Physical Review B* **108**, 245137 (2023)
DOI: 10.1103/PhysRevB.108.245137

Listed below are other relevant publications that did not directly contribute to this dissertation but were nonetheless undertaken during the author's postgraduate program or the years leading up to it.

A. Burgess, E. D'Arcy, L. MacEnulty, D. Gavin, & D. D. O'Regan "[Working Title] Hubbard parameters and resulting PBE+U±J band gaps for select quarternary kesterite chalcogenide photovoltaic materials" | *manuscript under preparation*

•

L. MacEnulty & D. D. O'Regan, "Calculation of the Magnetostatic Energy in Spin Density Functional Theory," *Journal of Undergraduate Reports in Physics* **30** (1) 22-25 100005 (2020) | DOI: 10.1063/10.0002045

Presentations & Outreach

Keeping with the ethos of a more accessible and inclusive science culture, the author engaged in a variety of presentations and outreach activities during their postgraduate program (Sept. 2020- Jan. 2025). These activities and other relevant pursuits are categorized and listed below.

talk | poster | invited | link to abstract | link to material | volunteer

Presentations

ICTP Total Energy & Force Methods Workshop
Jan. 9, 2025 | Trieste, IT
poster | link to abstract
Limitations of DFT+U+J & linear response highlighted in spin-state energetics of Fe(II) SCO molecules
L. MacEnulty, J.P.A. de Mendonça, R. Poloni & D. D. O'Regan

•

Abinit Developer's Meeting 2024
Jul. 3, 2024 | Trois-Rivières, QC
invited talk | link to material
The `lrUJ` utility for linear response in Abinit
L. MacEnulty

•

Université Grenoble Alpes, SimAP
Nov. 22, 2023 | Grenoble, FR
invited talk
Assessing total energy differences from first-principles DFT+U+J using magnetic orderings in NiO
L. MacEnulty & D. D. O'Regan

ACS Fall Meeting 2024
Aug. 21, 2024 | Denver, USA
talk | poster | link to abstract | link to material
Breakdown & potential remedies for DFT+U total energy differences & linear-response parameter calculations in SCO complexes
L. MacEnulty, J.P.A. de Mendonça, R. Poloni & D. D. O'Regan

•

Trinity College Dublin, SoP Postgraduate Seminar
May 31, 2024 | Dublin, IE
invited talk
The Abinit `lrUJ` utility for linear response
L. MacEnulty

•

University of Cambridge, Dept. Materials Science & Metallurgy
July 5, 2023 | Cambridge, UK
invited talk
Navigating the interference of Hubbard corrections and magnetic model mappings in DFT
L. MacEnulty & D. D. O'Regan

ACS Fall Meeting 2024
Aug. 20, 2024 | Denver, USA
poster | link to abstract | link to material
Assessing total energy differences from first-principles DFT+U+J using Heisenberg model mappings of NiO
L. MacEnulty & D. D. O'Regan

•

Trinity College Dublin, Physics 300 Thesis-in-3
Apr. 17, 2024 | Dublin, IE
talk | link to material
1st place winner
How to Save Tony Stark with Computational Quantum Materials Physics
L. MacEnulty

•

Trinity College Dublin, SoP
Apr. 25, 2023 | Dublin, IE
invited talk
Science Communication for the General Public
L. MacEnulty

Université Catholique de Louvain, IMCN
Nov. 9, 2022 | Louvain-La-Neuve, BE

Projectors and Hubbard Parameters and Abinit
L. MacEnulty & D. D. O'Regan

•

Paris International School on Advanced Computational Materials Science
Aug. 30, 2022 | Paris, FR

First-principles PAW+U(+J) mapping of NiO onto the magnetic Heisenberg model: towards accurate exchange-coupling parameters
L. MacEnulty & D. D. O'Regan

•

33rd IUPAP Conference on Computational Physics
Aug. 3, 2022 | Online

Linear Response Hubbard U and Hund's J, PAW population analysis, Heisenberg exchange-coupling parameters: A three-fold investigation featuring NiO
L. MacEnulty & D. D. O'Regan

•

QUOROM-V
Nov. 18, 2021 | Online

Hubbard U and Hund's coupling J parameters from first principles: Towards accurate Heisenberg exchange-coupling parameters for NiO
L. MacEnulty & D. D. O'Regan

Ma Thèse en 180 Secondes, Finale Internationale
Oct. 6, 2022 | Montréal, QC

Paramètres d'Hubbard via principes-premiers et informés des projecteurs, et protocole correctif pour le traitement des interactions fortes dans la théorie de la fonctionnelle de la densité
L. MacEnulty

•

Ma Thèse en 180 Secondes, Finale Nationale d'Irlande
May 31, 2022 | Dublin, IE

1st place winner
Sauver Tony Stark avec des Simulations Numériques de Matériaux Quantiques
L. MacEnulty

•

EUROMAT 2021
Sept. 13, 2021 | Online

On using an auxiliary magnetic charge density to calculate the magnetostatic dipole-dipole correction to spin density functional theory (DFT)
L. MacEnulty & D. D. O'Regan

ETSF Young Researchers Meeting
Sept. 7, 2022 | Marseille, FR

PAW+U+J mapping of NiO onto the magnetic Heisenberg model: best practices, population analysis, and spin-symmetry investigations
L. MacEnulty & D. D. O'Regan

•

Psi-k Conference 2022
Aug. 25, 2022 | Lausanne, CH

NCCR Marvel Fellow
Assessment of first-principles DFT+U+J for NiO: PAW projector dependence and Heisenberg model mappings
L. MacEnulty & D. D. O'Regan

•

Trinity College Dublin, 3-Minute Thesis
March 2022 | Dublin, IE

2nd place winner & People's Choice Award
Saving Tony Stark with Quantum Materials Simulation
L. MacEnulty

•

MRS Spring Meeting and Exhibit
Apr. 23, 2021 | Online

Calculation of the Magnetostatic Dipole-Dipole Correction to Periodic Spin Density Functional Theory Using an Auxiliary Magnetic Charge Density
L. MacEnulty & D. D. O'Regan

Memberships

American Chemical Society (*2024*)
Royal Society of Chemistry (*2022-23*)
Materials Research Society (*2021-22*)
American Physical Society (*2018-20*)

Outreach

Athena Swan Silver Award

Application Graphic Designer & Copy Editor

Awarded to the School of Physics in 2024 for demonstrable and well-documented commitment to gender diversity.

June - July 2024

•

Trinity Students' Union Tourism Proposal

Writer & Model Developer

Proposal commissioned by the TCD Students' Union for submission to administration; developed models to propose tourism-based alternatives to raising master's degree program fees for Trinity students.

May 2024

•

qToM Website

Developer and Curator

Developed and curated the official website and "brand" for our research group, the Quantum Theory of Materials group at Trinity College Dublin.

September 2021 - February 2022

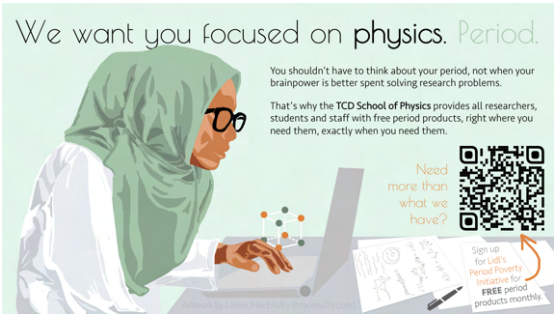

School of Physics Executive Committee

Postgraduate Representative |

Formally elected representative to school governance; devised and ensured implementation of period product initiative, where SoP furnishes its washroom facilities with free period products for all students and staff; lobbied administrative and funding bodies locally and nationally to increase postgraduate stipends in Ireland.

April - November 2022

•

Four years of doctoral research? Try presenting it in three minutes!

Article Coauthor |

Article written for Trinity online research news site on collective 3-Minute-Thesis experience.

July 21, 2022

•

School of Physics Equity, Diversity, & Inclusion Committee

Member |

Devise, advise on, and carry out EDI-related school policy and activities.

March 2022 - present

Secondments

ABINIT, Université Catholique de Louvain

Louvain-la-Neuve, BE

Two secondments supported by Gian-Marco Rignanese to renovate linear response in ABINIT, including development of the `lrUJ` utility and AbiPy plotting facilities.

November 2022 & November 2023

SimAP, Université Grenoble Alpes

Grenoble, FR

Secondment to study with Roberta Poloni; supported by a **French Research Residency Award** obtained in 2023 from l'Ambassade de France en Irlande.

May - June 2023 & October 2023

Other

Postgraduate Teaching Award

School of Physics, Trinity College Dublin

For excellence in graduate assistantship for those courses of the following list taught in 2022.

Introduction to Physics Laboratory | *Michaelmas 2020*
Multivariable Calculus for Science | *Michaelmas 2020*
Mathematics for Scientists/Engineering | *Hilary 2021*
Introduction to Python, Physics | *Michaelmas 2022*
Introduction to Physics Laboratory | *Hilary 2023*

2022

Contents

Glossary of Abbreviations, Symbols & Nomenclature

Common abbreviations, symbols, and nomenclature used throughout this thesis are tabulated here. Other nomenclature is defined locally as needed. For ease of reference, characters are sorted among the following categories:

- **Abbreviations**
- **Constants, Functions & Parameters**
- **Iconography & Symbols**
- **Units**

Abbreviations

AE	All-electron
AF_I	Type I Antiferromagnetic in the {001} direction
AF_{II}	Type II Antiferromagnetic in the {111} direction
AP	QUANTUM ESPRESSO Atomic Projector
AS	Augmentation Sphere
BOA	Born-Oppenheimer Approximation
BLOR	Burgess-Linscott-O'Regan functional
BZ	Brillouin Zone
C	Carbon
CASPT2	Complete Active Space + 2^{nd}-order Perturbation Theory
CC	Coupled Cluster
cDFT	Constrained Density Functional Theory
cRPA	Constrained Random Phase Approximation
CI	Configuration Interaction
dc	double-counting
DFA	Density Functional Approximation
DFT	Density Functional Theory
DFPT	Density Functional Perturbation Theory
DFT+U	Any DFT functional w/ Hubbard U Ch. 5, 7, & 9: Dudarev functional
DFT+U–J	Dudarev functional with $U = U_{eff} = U - J$
DFT+U+J	Any DFT+U functional w/ Hund's J Ch. 5 & 7: Liechtenstein functional Ch. 9: Himmetoglu functional
DMC	Diffusion quantum Monte Carlo
DMPT	Density Matrix Perturbation Theory
DMFT	Dynamical Mean-Field Theory
`dmatpuopt`	Density MATrix for PAW+U OPTion in ABINIT
DOS	Density of States
EBT	Electronic Band Theory
EDI	Equity, Diversity, and Inclusion

EPR	Electron Paramagnetic Resonance
Eq(s).	Equation(s)
Fe	Iron
(F)FT	(Fast) Fourier Transform
Fig(s).	Figure(s)
FM	Ferromagnetic
GGA	Generalized Gradient Approximation
H	Hydrogen
HDvV	Heisenberg-Dirac-van Vleck
HEG	Homogeneous Electron Gas
HF	Hartree-Fock
HK	Hohenberg-Kohn
HOMO	Highest Occupied Molecular Orbital
HP(s)	Hubbard Parameter(s) (U and/or J)
hs,HS	High-Spin state
Hub	Hubbard
hxc,HXC	Hartree and eXchange-Correlation
I	Insulating character
ICHEC	Irish Centre for High-End Computing
INS	Inelastic Neutron Scattering
JTH	Jollet-Torrent-Holzwarth PAW dataset
KS	Kohn-Sham
LP	Lattice Parameter
LR	Linear Response
`lrUJ`	ABINIT Linear Response U(J) utility
L(S)DA	Local (Spin-)Density Approximation
ls,LS	Low-Spin state
LUMO	Lowest Unoccupied Molecular Orbital
M	Metallic character
MAE	Mean Average Error
MIC	Minimum Image Convention
MO	Magnetic Ordering
MOT	Molecular Orbital Theory
MT	Minimum-Tracking or Martyna-Tuckerman
NCPP	Norm-Conserving Pseudopotential
N	Nitrogen
NGWF	Non-orthogonalized Generalized Wannier Function
Ni	Nickel
nl	non-local
NN	Nearest-Neighbor
NNN	Next Nearest-Neighbor
O	Oxygen
OAP	Orthogonalized Atomic Projector in QUANTUM ESPRESSO
ONETEP	Order-N Electronic Total Energy Package
PAO	Pseudoatomic Orbitals in ONETEP
PAW	Projector-Augmented Wave method
PB(A)	Prussian Blue (Analogue)
PBE	Perdew-Burke-Ernzerhof exchange-correlation functional
PDOS	Projected Density of States
PEP	Pauli Exclusion Principle
PP	Pseudopotential
PS	Pseudo
PT	Perturbation Theory
PV	Photovoltaic
QMC	Quantum Monte Carlo
qToM	Quantum Theory of Materials group
Ref(s).	Reference(s)
RMS(E)	Root Mean Squared (Error)
SCE	Static-Correlation Error
SCF	Self-Consistent Field
SCO	Spin Crossover
SD	Spin Density
SIC	Self-Interaction Correction
SIE	Self-Interaction Error
SoP	(TCD) School of Physics
TCD	Trinity College Dublin
TCHPC	Trinity Centre for High Performance Computing (now Research IT)
TD	Time-Dependent
TM	Transition Metal
TMO	Transition Metal Oxide
`UJdet`	ABINIT U(J) determination utility
USPP	Ultrasoft Pseudopotential
VBT	Valence Bond Theory
wrt	with respect to
XC	eXchange-Correlation

Constants, Functions, & Parameters

a, b	atomic site indices
α,β	types of perturbations
c	speed of light
δ_{ij}	Kronecker delta $= \begin{cases} 0 & \text{if } i \neq j \\ 1 & \text{if } i = j \end{cases}$
e_g	the d_{z^2} and $d_{x^2-y^2}$ orbitals from crystal-field splitting
E	energy
F	universal variational functional
$\mathcal{F}$	Fourier transform
g_e	g-factor for a free electron
G	Gibb's free energy
$\hbar$	Planck's constant
H	enthalpy
$\hat{H}$	Hamiltonian
$\mathbb{i}$, $\mathbb{j}$, $\mathbb{k}$	atomic subspace indices $= \{a, n, \ell\}$ pertaining to orbital $n\ell$ on atom a
j_ℓ	spherical Bessel function of order ℓ
J, J_H	Hund's coupling J parameter
J_1	nearest-neighbor interatomic exchange-interaction parameter
J_2	next nearest-neighbor interatomic exchange-interaction parameter
k	k-point
$\mathbf{k}$	wave vector, or crystal momentum vector
ℓ	angular quantum number
L	total orbital angular momentum
m_a	nuclear mass
m_e	mass of electron
m_ℓ	magnetic quantum number
m_s	spin magnetic quantum number
M	subspace magnetization
M_s	total spin magnetic quantum number
$\mathcal{M}$	spin density
μ_s	electron magnetic moment
μ_z	z-axis projection of μ_s
n,N	number of particles (electrons, typically)
n_0	unscreened subspace occupancy
$\hat{P}$	projection operator
$\hat{\mathbb{I}}$	permutation operator
Π	spin-product term
ψ	many-body electronic wavefunction
Ψ	many-body atomic wavefunction
R	ideal gas constant
$\mathbf{r}$,$\mathbf{R}$	spatial coordinates
ρ	density
s	spin quantum number
s_z	z-axis component of spin quantum number
$\mathbf{s}$	electron spin vector
$\hat{\mathbf{s}}$	electron spin operator
S	magnitude of total spin angular momentum Ch. 8: entropy
S_z	z-axis component of total spin vector
$\mathbf{S}$	total electronic spin vector
$\hat{\mathbf{S}}$	total spin vector operator
σ	error or spin index
$\boldsymbol{\sigma}$	vector of Pauli matrices $= \begin{bmatrix}\sigma_x & \sigma_y & \sigma_z\end{bmatrix}^\top$
σ_x	$= \left[\begin{smallmatrix} 0 & 1 \\ 1 & 0 \end{smallmatrix}\right]$
σ_y	$= \left[\begin{smallmatrix} 0 & -i \\ i & 0 \end{smallmatrix}\right]$
σ_z	$= \left[\begin{smallmatrix} 1 & 0 \\ 0 & -1 \end{smallmatrix}\right]$
t	time
t_{2g}	The d_{xy}, d_{xz}, and d_{yz} orbitals from crystal-field splitting
T	Ch. 1: kinetic energy Ch. 8: temperature
$\hat{\tau}$	PAW transformation operator
U	Hubbard U parameter
U_{eff}	effective Hubbard U parameter $=$ U $-$ J
V	potential (or potential energy)
x_a, $\boldsymbol{x}_i$	combined electronic degrees of freedom, including spatiotemporal and spin coordinates (defined *in situ*)
χ	screened response function
χ_0	unscreened response function
χ_M	screened magnetic response function
χ_{0_M}	unscreened magnetic response function
$Y_{\ell m}$	Spherical Harmonics
Z_a	nuclear charge
Z_{eff}	effective nuclear charge
ζ-axis	The continuum $\perp$ derivative of LR at zero perturbation

Iconography & Symbols

↑	spin-up/majority-spin channel
↓	spin-down/minority-spin channel
□	QED; end of proof
§, ‖, ‡ ...	footnote indicators
$\bigcirc$	some variable mathematical object
$\mathbf{\bigcirc}$	vector or matrix (bolded variable)
$\widetilde{\bigcirc}$	pseudized form of $\bigcirc$
$\widehat{\bigcirc}$	operator
$\bigcirc^*$	excited state or complex conjugate of $\bigcirc$
$\overline{\bigcirc}$	average of $\bigcirc$
$\bigcirc_0$	ground-state value of $\bigcirc$ (except in the case of χ_0 and n_0—see separate definitions)
$\langle\widehat{\bigcirc}\rangle$	expectation value of operator $\bigcirc$
Tr[$\mathbf{\bigcirc}$]	trace of a matrix-like object $\mathbf{\bigcirc}$
$\mathbf{\bigcirc}^\mathsf{T}$	transpose of a matrix-like object $\mathbf{\bigcirc}$
e^-	electron

Units

a.u.	atomic units
a_0	Bohr radius
Å	Angstrom
e	elementary charge
eV	electron Volt
Ha	Hartree (units of energy)
i	imaginary unit = $\sqrt{-1}$
K	degrees Kelvin
μ_B	Bohr magneton (= $1/2$ in a.u.)

List of Figures

List of Tables

Introduction and Outline

Braving the most formidable obstacles of our age—climate change, food and energy insecurities, human and animal health pandemics, etc.—the modern scientist is increasingly compelled to innovate around or harness the unique capabilities of quantum materials. In particular, devices that make use of induced changes in spin state, among them magnetic materials alongside materials with small or transient moments, are vital to many state-of-the-art technologies, from high-performance battery cathodes,[1–5] water-splitting catalysts,[6,7] spintronics,[8] to efficient photovoltaic devices for sustainable energy storage.[9–11] To understand the mechanisms that render the technological viability of materials currently known and synthesized in laboratories, materials scientists and engineers defer to some combination of experiment and simulation.[12–16] Meanwhile, frustration with and scarcity of current resources continues to propel concerted interest in the properties of undiscovered, as-of-yet unsynthesized materials.[17,18]

Both endeavors spur active development and routine use of density functional theory (DFT), an electronic structure theory for calculating quantum material properties *ab initio*. DFT has undoubtedly accelerated the collective understanding of quantum many-body interactions and their precipitation of macroscopic phenomena. But the systems we now look to model are bigger, disorderly, and more complex. They have strongly-correlated, open-shell electronic subspaces. Obtaining solutions within realistic time-frames, subject to contemporary hardware constraints, comes at the expense of physical accuracy. Compromises are made, approximations sanctioned.

As a result, approximative DFT finds its realms of applicability and achievable accuracy hindered by tenacious errors.[19–21] Among these are the self-interaction error (SIE)—more broadly, the delocalization error—and the static correlation error (SCE), both of which arise from the poor description of interactions between correlated electrons.[22–25] Unchecked, these errors often amount to results that fall short of, if not entirely contradict, experimental observations. While some theorists work to reduce the computation time associated with other theories, techniques, and methods, a sizable part of the electronic structure literature is dedicated to the alternative: making DFT more accurate.

This dissertation is an exercise in the latter pursuit. Wielding approximative DFT's well-established implementations and robust theoretical versatility, the research herein addresses its intrinsic errors through the DFT+U+J method,[26–28] a family of corrective functionals that restores a subspace's physicality via penalizing energy terms. The severity of such penalties is managed through the judicious prescription of the corrective parameters, embodied by the magnitude of the Hubbard U and Hund's coupling J.[29–33] We devise experiments to monitor and automate the determination, via linear re-

sponse,[29] of these parameters in an effort to understand, and then predict, how they change both inside and across open-shell quantum systems. Our efforts here produced a thematic overtone related to the projector functions—the widely variable mechanisms that isolate the Hubbard manifold from the rest of the system. In linear response and cinemas, it seems, an image is only as good as its projectors.

Parameters in hand, we probe how functionals incorporating the U—and, more critically, the Hund's J, which occupies further untested territory—impact metrics of magnetism, such as Heisenberg exchange-coupling parameters[34–39] or spin-crossover thermodynamic properties.[40–42] The current work asserts that these spin-based metrics are expedient indicators of the quality and reliability of DFT+U+J total energies, and in so doing, it explores the boundaries of the regime of accuracy of first-principles Hubbard functional energetics, delineating its remaining weaknesses and ambiguities.

Ultimately, we seek to contribute to the establishment of resilient techniques that go on to inform and facilitate automation of first-principles methods for high-throughput informatics. As a result, this work represents a specialized but important cog in the machine that scientists collectively build to accelerate materials discovery.

1 Thesis Outline

This dissertation, a visual depiction of which is provided in Fig. 1, is composed of four distinct but related projects, each of which receives its own delineated "part." The literature review by which these projects were fashioned was found to be best expressed by delocalizing and embedding it there where its information is most useful in the context of each project. In other words, there is no delimited "Literature Review" section; we prefer to more organically cite the global context for our projects as we construct the projects themselves. Following the same line of reasoning, each part (in addition to the introductory and concluding sections) is immediately followed by its bibliography.

All projects draw on the theoretical background provided in Part I, in and of itself comprising three chapters. Chapter 1 discusses the fundamental physics of fermionic particle interactions in many-body quantum systems. Chapter 2, leading first with a brief discussion on electronic structure theory methods, goes on to probe the specifics of collinear-spin DFT, including its foundational theorems, its components, its errors, and the DFT+U+J method to remedy those errors. Chapter 3 goes into common features of and facilities for computational implementations of spin-unrestricted Kohn-Sham DFT, matters that feature in the more technical aspects of the investigations in Parts II through IV. Other topic "keywords" addressed in Part I are shown non-comprehensively in Fig. 1.

All projects also rely on the theory and resolutions of Chapter 4, but due to the nature of the ABINIT `lrUJ` utility discussed in Chapter 5, it made more sense to group these two topics together under one umbrella and call it Part II, a compartment dedicated entirely to the minutiae of the linear response determination of the Hubbard U and Hund's J parameters. Chapter 5 describes the output of the first—and heavily programmatic—project.

The second project, featuring an investigation into the energetic properties of the magnetically ordered prototypical Mott-Hubbard insulator nickel oxide (NiO), is relegated to Part III. The two chapters therein—Chapter 6 relaying the relevant theoretical details for the work in Chapter 7—recounts the investigation into NiO, calculating its electronic structure in its antiferromagnetic I/II and

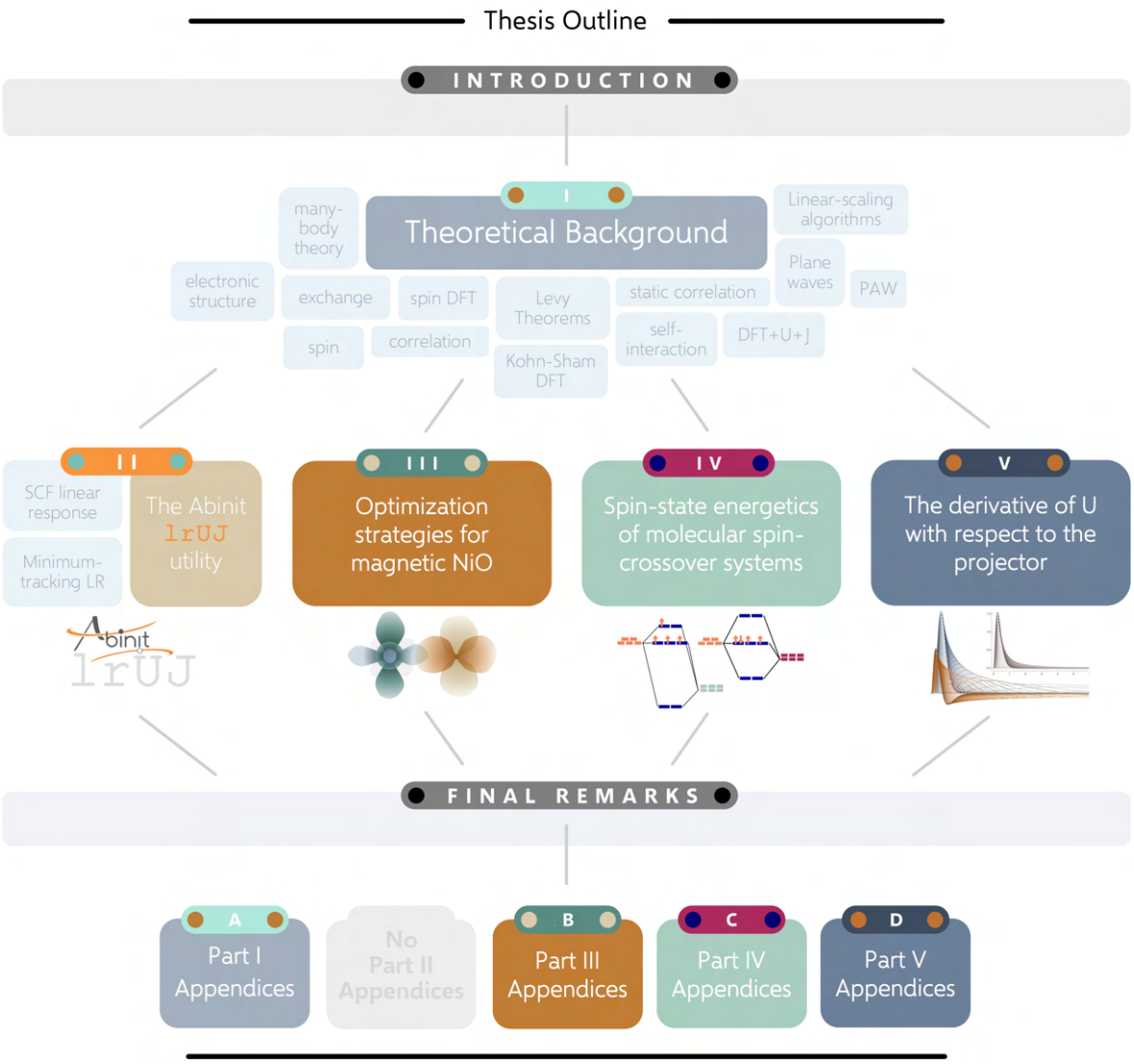

Figure 1: Outline of this dissertation

ferromagnetic states, aiming to establish accurate Heisenberg exchange-coupling parameters in terms of strict density-functional accessible total energy differences weighted according to various spin-parametrization methods. The work also includes a rigorous assessment of projector-augmented wave (PAW)-based corrective functionals involving *in situ*-calculated U and J parameters.

Part IV, otherwise known as the third project, devises (Chapter 8) and executes (Chapter 9) a detailed study designed to determine whether fully first-principles Hubbard-like corrective functionals, specifically those incorporating the Hund's J, in spin DFT can achieve accurate adiabatic energy differences for spin-crossover materials. Briefly, the study probes the overlap between common Hubbard parametrization schema and basis-set projector functions in search of the simplest combination to yield reliable spin-state energetics with respect to those obtained by state-of-the-art wavefunction methods.

Chapter 10, or synonymously Part V, constitutes the fourth and final project broaching the—highly theoretical—subject of the Hubbard manifold as sequestered by the projector functions. The Hubbard

projectors, as a topic, amount to a topical undercurrent addressed in each project. This feasibility study seeks to gain more direct insight into their influence on the Hubbard U parameter.

The dissertation concludes with an assembly of final remarks, including conclusions reached here and possible extensions for future work. The appendices are organized according to which part their subject matter pertains. Note that Part II does not have any appendices, so the order is as follows: Appendix A corresponds to Part I, Appendix B to Part III, Appendix C to Part IV, and Appendix D to Part V. The appendices will typically include representative input files for calculations undertaken in each project in addition to other relevant figures not necessary for comprehension of the main body.

Note on design elements

All figures, schematics, illustrations, and graphics were designed by the author, often through a combination of design utilities. Color is deployed strategically and selectively, principally to emphasize concepts, information, or coherence across that information and secondarily to promote accessibility; for example, the use of blue and orange hues is optimal for most colorblindness variants. Where possible, concepts are doubly conveyed with a second property to that of color (e.g., font family, boldness, dashing, position, labeling). Skeuomorphs, illustrations, and icons are designed to facilitate efficient absorption of information and not necessarily to accurately depict physical concepts or bodies (e.g., atoms represented by spheres).

Unless otherwise specified, Hartree units are assumed throughout the entirety of this dissertation (i.e., $\hbar = c = m_e = 1$).

Bibliography

[1] A. Chakraborty, M. Dixit, and D. T. Major, npj Computational Materials **4**, 60 (2018).

[2] K. Saritas, E. R. Fadel, B. Kozinsky, and J. C. Grossman, The Journal of Physical Chemistry C **124**, 5893 (2020).

[3] J. Shu, T.-F. Yi, M. Shui, Y. Wang, R.-S. Zhu, X.-F. Chu, F. Huang, D. Xu, and L. Hou, Computational Materials Science **50**, 776 (2010).

[4] Y. S. Meng and M. E. Arroyo-de Dompablo, Energy & Environmental Science **2**, 589 (2009).

[5] M. Shishkin and H. Sato, The Journal of Physical Chemistry C **125**, 1531 (2021).

[6] F. S. Hegner, J. R. Galán-Mascarós, and N. López, Inorganic Chemistry **55**, 12851 (2016).

[7] A. Aziz, *Electronic structure simulations of energy materials: chalcogenides for thermoelectrics and metal-organic frameworks for photocatalysis*, Chemistry, University of Reading, United Kingdom (2017).

[8] D. Lupo, M. Schneider, C. Busse, G. Kresse, C. Schneider, S. Thiel, D. Eder, M. Stengel, G. P. Diego, *et al.*, Nature Materials **20**, 559 (2021).

[9] S. Siebentritt and S. Schorr, Progress in Photovoltaics: Research and Applications **20**, 512 (2012).

[10] A. Polman, M. Knight, E. C. Garnett, B. Ehrler, and W. C. Sinke, Science **352**, aad4424 (2016).

[11] C. Yan, K. Sun, J. Huang, S. Johnston, F. Liu, B. P. Veettil, K. Sun, A. Pu, F. Zhou, J. A. Stride, M. A. Green, and X. Hao, ACS Energy Letters **2**, 930 (2017).

[12] H. Shin, Y. Luo, P. Ganesh, J. Balachandran, J. T. Krogel, P. R. C. Kent, A. Benali, and O. Heinonen, Physical Review Materials **1**, 073603 (2017).

[13] J.-W. Lee, L. Mitas, and L. K. Wagner, preprint (2004).

[14] H. Kino, L. K. Wagner, and L. Mitas, Journal of Computational and Theoretical Nanoscience **6**, 2583 (2009).

[15] L. K. Wagner, Journal of Physics: Condensed Matter **19**, 343201 (2007).

[16] Z. Deng, Y. Mo, and S. P. Ong, NPG Asia Materials **8**, e254 (2016).

[17] Z. Lu, Materials Reports: Energy **1**, 100047 (2021).

[18] C. Duan, F. Liu, A. Nandy, and H. J. Kulik, The Journal of Physical Chemistry Letters **12**, 4628 (2021).

[19] A. Schrön, C. Rödl, and F. Bechstedt, Physical Review B **82**, 165109 (2010).

[20] M. Cococcioni and N. Marzari, Physical Review Materials **3**, 033801 (2019).

[21] W. Zhang, D. G. Truhlar, and M. Tang, Journal of Chemical Theory and Computation **10**, 2399 (2014).

[22] A. J. Cohen, P. Mori-Sánchez, and W. Yang, Science **321**, 792 (2008).

[23] P. Mori-Sánchez, A. J. Cohen, and W. Yang, The Journal of Chemical Physics **125**, 201102 (2006).

[24] E. B. Isaacs, S. Patel, and C. Wolverton, Physical Review Materials **4**, 065405 (2020).

[25] A. Georges, L. d. Medici, and J. Mravlje, Annual Review of Condensed Matter Physics **4**, 137 (2013).

[26] V. I. Anisimov, J. Zaanen, and O. K. Andersen, Physical Review B **44**, 943 (1991).

[27] V. I. Anisimov and O. Gunnarsson, Phys. Rev. B **43**, 7570 (1991).

[28] V. I. Anisimov, I. V. Solovyev, M. A. Korotin, M. T. Czyżyk, and G. A. Sawatzky, Phys. Rev. B **48**, 16929 (1993).

[29] M. Cococcioni and S. de Gironcoli, Physical Review B **71**, 035105 (2005).

[30] J. W. Bennett, B. G. Hudson, I. K. Metz, D. Liang, S. Spurgeon, Q. Cui, and S. E. Mason, Computational Materials Science **170**, 109137 (2019).

[31] B. Kim, K. Kim, and S. Kim, Physical Review Materials **5**, 035404 (2021).

[32] K. Yu and E. A. Carter, The Journal of Chemical Physics **140**, 121105 (2014).

[33] O. K. Orhan and D. D. O'Regan, Physical Review B **101**, 245137 (2020).

[34] O. Le Bacq, A. Pasturel, C. Lacroix, and M. D. Nunez-Regueiro, Phys. Rev. B **71**, 014432 (2005).

[35] B. Dorado, B. Amadon, M. Freyss, and M. Bertolus, Phys. Rev. B **79**, 235125 (2009).

[36] B. Dorado, G. Jomard, M. Freyss, and M. Bertolus, Phys. Rev. B **82**, 035114 (2010).

[37] D. A. Tompsett, D. S. Middlemiss, and M. S. Islam, Phys. Rev. B **86**, 205126 (2012).

[38] C. E. Patrick and K. S. Thygesen, Phys. Rev. B **93**, 035133 (2016).

[39] P. Gopal, R. D. Gennaro, M. S. dos Santos Gusmao, R. A. R. A. Orabi, H. Wang, S. Curtarolo, M. Fornari, and M. B. Nardelli, Journal of Physics: Condensed Matter **29**, 444003 (2017).

[40] A. Droghetti, D. Alfè, and S. Sanvito, The Journal of Chemical Physics **137**, 124303 (2012).

[41] L. A. Mariano, B. Vlaisavljevich, and R. Poloni, Journal of Chemical Theory and Computation **16**, 6755 (2020).

[42] D. Vidal, J. Cirera, and J. Ribas-Arino, Dalton Trans. **50**, 17635 (2021).

Part I

Theoretical Background

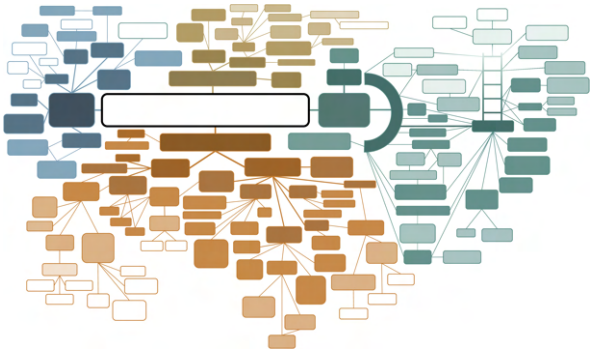

Chapter 1

Particle interactions in many-body quantum systems

The greatest achievement of any quantum practitioner lies in the absolute decryption of the complex-valued n-body wavefunction $\Psi(\{\mathbf{r_i}\}, t)$—the mathematical unicum encoding all spatiotemporally related information of a quantum state—and its corresponding energy profile E. Both entities are, for any given quantum mechanical system, encrypted in the many-body time-independent eigenvalue equation

$$\hat{H}\ \Psi(\{\mathbf{r_i}\}, t) = E\ \Psi(\{\mathbf{r_i}\}, t)\,, \tag{1.1}$$

where $\hat{H}$ is the Hamiltonian establishing the nature of the energy landscape that molds and interacts with $\Psi(\{\mathbf{r_i}\}, t)$, a function of spatial coordinates $\mathbf{r_i}$ and propagated in time t.

The energy landscape under immediate consideration is that of a crystal lattice or molecular configuration of N atoms, comprising n electrons at positions $\{\mathbf{r_i}\}$ swarming nuclei located at $\{\mathbf{R_a}\}$. The non-relativistic time-independent Hamiltonian for this system is

$$\hat{H} = \underbrace{-\frac{1}{2}\left[\sum_{i=1}^{n}\nabla_i^2 + \sum_{a=1}^{N}\frac{\nabla_a^2}{m_a}\right]}_{\text{kinetic energy}} \underbrace{-\sum_{a=1}^{N}\sum_{i=1}^{n}\frac{Z_a}{|\mathbf{r_i}-\mathbf{R_a}|}}_{\text{external potential}} + \underbrace{\frac{1}{2}\sum_{i=1}^{n}\sum_{j\neq i}^{n}\frac{1}{|\mathbf{r_i}-\mathbf{r_j}|}}_{e^-\text{–}e^- \text{ interactions}} + \underbrace{\frac{1}{2}\sum_{a=1}^{N}\sum_{b\neq a}^{N}\frac{Z_a Z_b}{|\mathbf{R_a}-\mathbf{R_b}|}}_{\text{internuclear interactions}}, \tag{1.2}$$

where m_a and Z_a denote, respectively, the nuclear masses and charges of each constituent atom.

The computational wherewithal required to successfully confront such a complex mathematical system renders exact solution inaccessible to modern day computers. Even if a particular machine could compute exact wavefunctions for something more than the simplest systems, the memory required to store it exceeds the world's cumulative storage capacities. To make the theory more tractable, we need sophisticated simplification techniques such as the Born Oppenheimer Approximation (BOA),[1] described below.

1.0.1 The Born-Oppenheimer approximation

The nucleus of an atom moves slowly in relation to its electrons, which are some three orders of magnitude less massive and adjust effectively instantaneously to system dynamics. It is reasonable to assume, then, that we may measure their coordinates with respect to the comparatively fixed nuclear coordinates of the system. This is the Born-Oppenheimer Approximation (BOA),[1] and in taking it we accept two lemmata: (i) The many-body wavefunction $\Psi(\{\mathbf{r_i}\}, \{\mathbf{R_a}\}, t)$ for this system,

$$\Psi(\{\mathbf{r_i}\}, \{\mathbf{R_a}\}, t) = \phi(\{\mathbf{R_a}\}, t)\, \psi(\{\mathbf{r_i}\}, \{\mathbf{R_a}\}, t), \tag{1.3}$$

can be separated into the product of a nuclear wavefunction ϕ reliant solely on nuclear positions and an electronic wavefunction ψ reliant on both electronic and nuclear coordinates; and (ii) Hamiltonian 1.2 can be reorganized into terms relying only on $\{\mathbf{R_a}\}$, on $\{\mathbf{r_i}\}$, or both $\{\mathbf{R_a}\}$ and $\{\mathbf{r_i}\}$.

$$\hat{H} = \underbrace{-\frac{1}{2}\left[\sum_{a=1}^{N}\frac{\nabla_a^2}{m_a} - \sum_{a=1}^{N}\sum_{b\neq a}^{N}\frac{Z_a Z_b}{|\mathbf{R_a}-\mathbf{R_b}|}\right]}_{\hat{H}_{\text{nuc}}(\{\mathbf{R_a}\})} \underbrace{-\frac{1}{2}\left[\sum_{i=1}^{n}\nabla_i^2 - \sum_{i=1}^{n}\sum_{j\neq i}^{n}\frac{1}{|\mathbf{r_i}-\mathbf{r_j}|}\right]}_{\hat{H}_e(\{\mathbf{r_i}\})} \underbrace{-\sum_{a=1}^{N}\sum_{i=1}^{n}\frac{Z_a}{|\mathbf{r_i}-\mathbf{R_a}|}}_{V(\{\mathbf{R_a}\},\{\mathbf{r_i}\})} \tag{1.4}$$

Applying Eq. (1.4) to the now separable wavefunction in Eq. (1.3), the many-body time-independent eigenvalue equation of Eq. (1.2) transforms into a nested electronic eigenvalue problem subject to an external potential (energy) V,[§]

$$\left[\hat{H}_e(\{\mathbf{r_i}\}) + V(\{\mathbf{R_a}\}, \{\mathbf{r_i}\})\right] \psi(\{\mathbf{r_i}\}, \{\mathbf{R_a}\}, t) = E_e(\{\mathbf{R_a}\})\, \psi(\{\mathbf{r_i}\}, \{\mathbf{R_a}\}, t), \tag{1.5}$$

the solution $E_e(\{\mathbf{R_a}\})$ of which feeds into a nuclear eigenvalue problem,

$$\left[\hat{H}_{\text{nuc}}(\{\mathbf{R_a}\}) + E_e(\{\mathbf{R_a}\})\right] \phi(\{\mathbf{R_a}\}, t) = E\, \phi(\{\mathbf{R_a}\}, t), \tag{1.6}$$

to yield the many-body energy profile and ϕ, the last component needed to determine Ψ via Eq. (1.3).

Under the BOA, electrons and atomic nuclei can be treated separately. The nuclear part of this algorithm in Eq. (1.6) can often be well-modeled by classical equations of motion provided the electronic energy profile E_e as a function of nuclear coordinates $\{\mathbf{R_a}\}$ is known.

Even within the BOA, however, finding an analytical solution to the many-body problem is still exceedingly intractable. Using the BOA as a starting point, quantum practitioners have developed increasingly creative methods to simulate properties of matter and materials. We will discuss these methods in more detail in Chapter 2. For now, we focus on emergent physical properties of many-body systems that will become relevant later in this dissertation.

[§] We will call this body a potential due to convention, but strictly speaking it is a potential energy.

1.1 Indistinguishability and symmetry[§]

Consider an isolated system with two particles a and b, identical in every property except for their spatiotemporal coordinates (degrees of freedom collectively denoted by x). The wavefunction for this system is $\Psi(x_a, x_b)$. Since the assignment of the degrees of freedom to a particular particle is arbitrary, we should be able to exchange those assignments, yielding a state $\Psi(x_b, x_a)$ whose observables are identical to those of $\Psi(x_a, x_b)$ (i.e., $\|\Psi(x_a, x_b)\|^2 = \|\Psi(x_b, x_a)\|^2$). We perform such a permutation using the operator $\hat{\mathbb{P}} = e^{i\theta}$, resulting in

$$\hat{\mathbb{P}}\Psi(x_a, x_b) = e^{i\theta}\Psi(x_a, x_b) = \Psi(x_b, x_a) \tag{1.7}$$

for some phase θ. Similarly, if we permute the state a second time, we should get the same state back: $\hat{\mathbb{P}}^2 = \mathbb{1}$. Imposition of this requisite yields $e^{2i\theta} = 1$, meaning θ can take on integer multiples of π: $\theta = n\pi$. If n is even, the resulting wavefunction is classified as symmetric, as it does not change its state upon permutation $\hat{\mathbb{P}}$; if n is odd, the wavefunction is a negative image of the initial one, rendering it antisymmetric under permutation. A property of antisymmetric wavefunctions is that as $x_b \to x_a$, $\Psi(x_a, x_b) \to 0$. This is the Pauli Exclusion Principle (PEP): no two otherwise identical particles that permute asymmetrically can carry the same coordinates simultaneously.

The antisymmetric properties of a many-body system are the same as those of the two-body system; observables like the Hamiltonian, which involve any number of indistinguishable particles, cannot change under any permutation of those particles (i.e., $[\hat{\mathbb{P}}, \hat{H}] = 0$). If the wavefunction describing the many-body system is antisymmetric, so it will remain.

1.1.1 Spin

Elementary particles and their composites possess a quantum property called spin, an intrinsic angular momentum of immutable magnitude represented by spin quantum number $s = \frac{i}{2}$, where $i \in \mathbb{Z}_0^+$. Spin is one of two types of electronic angular momenta encountered in quantum theory, the other being orbital angular momentum.

Although it is not derivable under non-relativistic conditions, there exists a relation between the symmetry of an indistinguishable particle's wavefunction and its spin; bosons, or particles with integer values of spin, have symmetric wavefunctions, whereas fermions, the classification inclusive of electrons, have antisymmetric wavefunctions, adopting odd values of i and thus half-integer values of spin. Notationally, we assert the **spin quantum number** s for electrons is equal to $\frac{1}{2}$, meaning an electron can adopt one of two **spin *magnetic* quantum numbers** $m_s = \{\frac{1}{2}, -\frac{1}{2}\}$.[‖] The effects of spin emerge physically upon immersion in electromagnetic fields.

Spin dichotomy is introduced *ad hoc* into the non-relativistic framework leading to Eq. (1.1) via

[§]The explanation in these sections and much of their notation follow the work of Eric Koch in Chapter 2 of Ref. [2].

[‖]These two quantum numbers, s and m_s, are analogs to the angular quantum numbers ℓ and m_ℓ in that m_s can take values ranging from $-s$ to s in integer increments. The non-boldfaced s is not to be confused with boldfaced $\mathbf{s}$ referring to the quantum spin vector, which we introduce shortly.

vector representation of the one-body wavefunction,

$$\psi(\mathbf{r}) = \begin{bmatrix} \psi^{\uparrow}(\mathbf{r}) \\ \psi^{\downarrow}(\mathbf{r}) \end{bmatrix}, \tag{1.8}$$

where $\uparrow$ and $\downarrow$ represent, respectively and arbitrarily, the majority- and minority-spin channels. Spin-independent operators like $\hat{H}_e$ of Eq. (1.5) are made proportional to the 2×2 unit matrix. Spin-dependent operators, by contrast, are composed of Pauli matrices $\{\sigma_x, \sigma_y, \sigma_z\}$,[3] which probe the Cartesian components of this dual wavefunction. For example, electron spin is modeled by the spin operator

$$\hat{\mathbf{s}} = \frac{\hbar}{2}\boldsymbol{\sigma} = \frac{\hbar}{2}\left[\sigma_x, \sigma_y, \sigma_z\right]^{\top}, \tag{1.9}$$

the components of which abide by the same commutation relations as those regulating orbital angular momentum. Spin angular momentum is quantized and takes on a magnitude of $|\hat{\mathbf{s}}| = \hbar\sqrt{s(s+1)}$.

In the non-relativistic formalism, the spin operator is related to an electron's intrinsic magnetic moment, described by

$$\boldsymbol{\mu}_s = -\frac{g_e \mu_B}{\hbar}\hat{\mathbf{s}}, \tag{1.10}$$

where $g_e \approx 2.002319$ is the g-factor for a free electron; $\mu_B = \frac{e\hbar}{2m} = \frac{1}{2}$ [a.u.] is the Bohr magneton.[4,5] The total spin magnetic moment is the sum of spin magnetic moments of all N particles in the system (in our case, N electrons on a particular atom). That is, $\boldsymbol{\mu}_{\mathbf{S}} = -g_e \mu_B \hat{\mathbf{S}}$, where $\hat{\mathbf{S}} = \sum_i^N \hat{\mathbf{s}}_i$.[5,6]

Working with a vector wavefunction becomes cumbersome in a many-electron formalism. A more convenient notation expresses the wavefunction in terms of spin coordinates alongside the spatial coordinates. We introduce the spin functions $\uparrow(m_s)$ and $\downarrow(m_s)$—where m_s is the spin magnetic quantum number that may only adopt values of $\frac{1}{2}$ and $-\frac{1}{2}$—defined such that

$$\begin{aligned} \uparrow(\tfrac{1}{2}) = 1 \quad \textit{and} \quad \uparrow(-\tfrac{1}{2}) = 0, \\ \downarrow(\tfrac{1}{2}) = 0 \quad \textit{and} \quad \downarrow(-\tfrac{1}{2}) = 1. \end{aligned} \tag{1.11}$$

One may thus express the single-electron wavefunction of Eq. (1.8) as

$$\psi(\mathbf{r}, m_s) = \psi^{\uparrow}(\mathbf{r}) \uparrow (m_s) + \psi^{\downarrow}(\mathbf{r}) \downarrow (m_s), \tag{1.12}$$

where $\psi(\mathbf{r}, \frac{1}{2}) = \psi^{\uparrow}(\mathbf{r})$ and $\psi(\mathbf{r}, -\frac{1}{2}) = \psi^{\downarrow}(\mathbf{r})$. The spin-dependent operators described above act exclusively on the spin-related wavefunction components, while the spin-independent operators, notable among them the Hamiltonian, act only on the wavefunction components that are functions of $\mathbf{r}$. The consequence of the latter assertion is that every eigenvalue of the one-electron Hamiltonian is doubly degenerate; i.e., electrons with identical quantum numbers save that of spin may occupy the same orbital without violating the PEP.[7]

Our newfound capacity to represent spin as a coordinate allows us to write the many-electron

wavefunction of Eq. (1.5) as $\psi(\{\mathbf{r}_i\},\{m_{s_i}\}) = \psi(\{\boldsymbol{x}_i\})$. Unlike its one-electron counterpart, however, this wavefunction cannot be separated into spin and spatial coordinate components.

Notable spin-dependent operators in the many-body formalism are the square of the total spin $\hat{\mathbf{S}}^2$ and the z-component of the total spin operator $\hat{S}_z$, defined as

$$\hat{S}_z = \sum_i^N \hat{s}_{z_i} \tag{1.13}$$

where $\hat{s}_z$ is obtained from the projection of the vector in Eq. (1.9) onto the z-axis. Both $\hat{\mathbf{S}}^2$ and $\hat{S}_z$ commute with $\hat{H}_e$, meaning that we may choose its eigenfunctions $\psi(\{\boldsymbol{x}_i\})$ to also be eigenfunctions of $\hat{\mathbf{S}}^2$ and $\hat{S}_z$.

$$\hat{\mathbf{S}}^2\,\psi(\{\boldsymbol{x}_i\}) = S(S+1)\hbar^2\,\psi(\{\boldsymbol{x}_i\}) \tag{1.14}$$

$$\hat{S}_z\,\psi(\{\boldsymbol{x}_i\}) = M_s\hbar\,\psi(\{\boldsymbol{x}_i\}) \quad \text{with} \quad M_s = \{-S,...,S\} \tag{1.15}$$

Importantly, by Eq. (1.15), each energy eigenvalue splits into $2S+1$ degenerate eigenfunctions of different spin states denoted by M_s.

1.1.2 Exchange

The (anti)-symmetry of a system's many-body wavefunction measurably affects its physical observables. To demonstrate, consider another two-particle system with one particle in state ϕ_a and the other in state ϕ_b. The many-body wavefunction of this system for indistinguishable particles is

$$\Psi_\pm(x_a,x_b) = \frac{1}{\sqrt{2}}\left(\Phi_{ab}(x_a,x_b) \pm \Phi_{ba}(x_a,x_b)\right), \tag{1.16}$$

where the (negative) positive of the $\pm$ corresponds to the (anti-)symmetric many-body wavefunction, and Φ_{ab} and Φ_{ba} are the many-body wavefunctions corresponding to the same two-body system of distinguishable particles,

$$\begin{aligned}\Phi_{ab} &= \phi_a(x_a)\phi_b(x_b)\\ \Phi_{ba} &= \phi_b(x_a)\phi_a(x_b).\end{aligned} \tag{1.17}$$

To observe a physical property of this system, say, the square of the distance between two indistinguishable particles, we take its expectation value

$$\left\langle (x_a - x_b)^2 \right\rangle = \left\langle x_a^2 \right\rangle + \left\langle x_b^2 \right\rangle - 2\left\langle x_a x_b \right\rangle \tag{1.18}$$

and operate on $\Psi_\pm$. For purposes of conciseness, we do not delve into the algebra of this derivation, noting only the final result,

$$\left\langle (x_a - x_b)^2 \right\rangle_\pm = \left\langle x^2 \right\rangle_a + \left\langle x^2 \right\rangle_b - 2\left(\langle x\rangle_a \langle x\rangle_b \pm |\langle x\rangle_{ab}|^2\right), \tag{1.19}$$

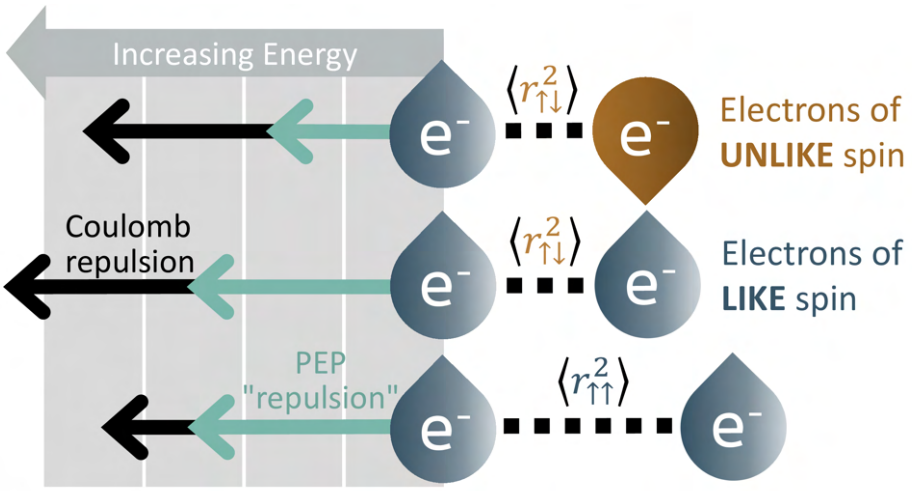

Figure 1.1: Illustration of the expectation value of the distance squared between electrons of like- or unlike-spin.

in which several terms have vanished if assuming ϕ_a is orthogonal to (i.e., does not overlap with) ϕ_b. For a more thorough derivation of Eq. (1.19), see Section 2.1.1 of Ref. [2].

Despite the orthogonality condition, however, the term $2|\langle x \rangle_{ab}|^2$ remains, and it has the effect of decreasing the expectation value of the square of the distance for symmetric wavefunctions while increasing it for antisymmetric wavefunctions. In other words, fermions avoid each other more than bosons do. This phenomenon is called exchange. The non-vanishing exchange terms in a many-body wavefunction force the expectation values for symmetric and antisymmetric wavefunctions to be different. As the exchange term for the expectation value of the square of the distance between two particles increases, the more the indistinguishable particles avoid each other.

In satisfying the PEP, electrons with the same spin (i.e., indistinguishable fermions) tend to avoid each other more. That is, due to what can effectively be called a sort of PEP "repulsion," the expectation value of the distance between aligned electrons is higher than that between anti-aligned electrons. It follows, then, that the electrostatic repulsion, which is inversely related to the distance between electrons, is smaller for electrons with parallel spin and thus more energetically favorable. This spin-based coupling of electrons, illustrated in Fig. 1.1, is called Coulomb exchange. Coulomb exchange is the basis of Hund's first rule, which favors ferromagnetic alignment of spins.

There are other types of exchange, and we will discuss these as they become relevant in Chapter III. We will also discuss exchange in the context of modeling electron-electron interactions, a feature of Sections 2.3.1 and 2.4.

1.1.3 Correlation

Strictly speaking, Coulomb exchange is considered a type of electronic correlation (called Pauli correlation). However, the concept of correlation has evolved to take on different definitions in different domains of many-body theory. In chemistry, for example, correlation describes all the electronic inter-

action effects not described by restricted Hartree-Fock, which includes part of the Coulomb exchange described earlier. In a similarly misnomered convention, we will often refer to strongly correlated subspaces in the chapters that follow, by which we mean principally that these subspaces are poorly described by local and semi-local exchange-correlation functionals among the approximate density functional methods. We will clarify this static correlation and the conventions surrounding its reference as they become relevant in Chapter 2.

Phenomenologically, correlation is a dynamic process. It's a description of how much the movement of an electron depends on the presence of all other electrons. This type of correlation is called dynamical correlation as it relates to the movement of electrons. In another framework, correlation is conceptualized as an effective reduction in probability of having an electron at, say, location r given the existence of an electron with the opposite spin at location r'.[8]

When electrons are uncorrelated, we may assert that the multi-electron density is well-described by the antisymmetrized product of its constituent one-electron densities (as in Hartree-Fock theory). This approximation breaks down, however, when the electrons are correlated; that is, in being subject to interactions beyond the PEP, the position of an electron in the many-body system is informed to some extent by the positions of the other electrons. The manner by which the many-body electron density differs from the product of one-electron densities describes the correlation of the electrons. The function describing that manner is called the pair-correlation function of particles, and it is required to vanish when two particles attempt to occupy the same state. Only Pauli correlation (Coulomb exchange) is related to the PEP; electrons in configurations that obey the PEP experience other forms of correlation related to Coulomb repulsion as well as spin-symmetry.

In many-body field theory, a system is considered strongly correlated if the movement of its electrons is greatly restricted by the application of penalizing energy terms. While many strongly correlated systems have high electron densities (i.e., distance between electrons is small), high electron density is not necessarily a requisite of strongly correlated systems. To determine if a system is strongly or weakly correlated, one must compare the magnitudes of the kinetic E_T and interacting E_{ee} energy terms. When $E_{ee} >> E_T$, the electrons are strongly correlated. When $E_T >> E_{ee}$, the electrons are considered weakly correlated.[9]

Chapter 2

Collinear-spin density functional theory

Quantum mechanics provides a robust formalism with which one may describe the many-body problem for a material system and how the particles of that system interact. In doing so, the intractability of analytical solution, even under the BOA, becomes acutely evident.

Development of crucial technologies for addressing the most urgent obstacles of our age—climate change, food and energy insecurities, human and animal health pandemics, and other biochemical threats—rely noncircumventably on accurate computational descriptions of material systems, from molecules to nanomaterials to protein chains to bulk solids. In particular, magnetic materials alongside materials with small or transient moments are increasingly vital constituents of many technologies, from high-performance battery cathodes,[10–14] and water-splitting catalysts,[15,16] to efficient photovoltaic devices for sustainable energy storage[17–19] and molecular qubits.[20,21] Understanding the macroscopic magnetic properties of materials requires a sophisticated description of the competing spin-related energy terms relevant at microscopic scales.

These demands have prompted the emergence, in the last century, of a vast web of approximative techniques designed to make the modeling of large-scale quantum systems—specifically, their electronic, energetic, and magnetic structures—more feasible and quotidian. The exercises pertaining to this endeavor constitute the field of electronic structure theory.

2.0.1 The field of electronic structure theory

How to classify electronic structure methods is the subject of some debate among practitioners of this field. For pedagogical and demonstrative purposes, a non-comprehensive and non-exact map of electronic structure methods is presented in Fig. 2.1. In printing this schematic, the author does not claim omniscience and recognizes the intrinsic ambiguity in concisely mapping an inherently multi-dimensional field on two-dimensional paper. Fig. 2.1 almost certainly contains personal interpretations and should be referenced/studied skeptically as such. We recommend that readers use this diagram as a contextualizing guide for their own literature reviews.

Viewed as intended through an indeterminate lens, however, the schematic demonstrates the complexity of the field and approximative solution to the many-body problem that inspires it. To train the schematic's focus, we consider the central starting point for these methods to be the electronic

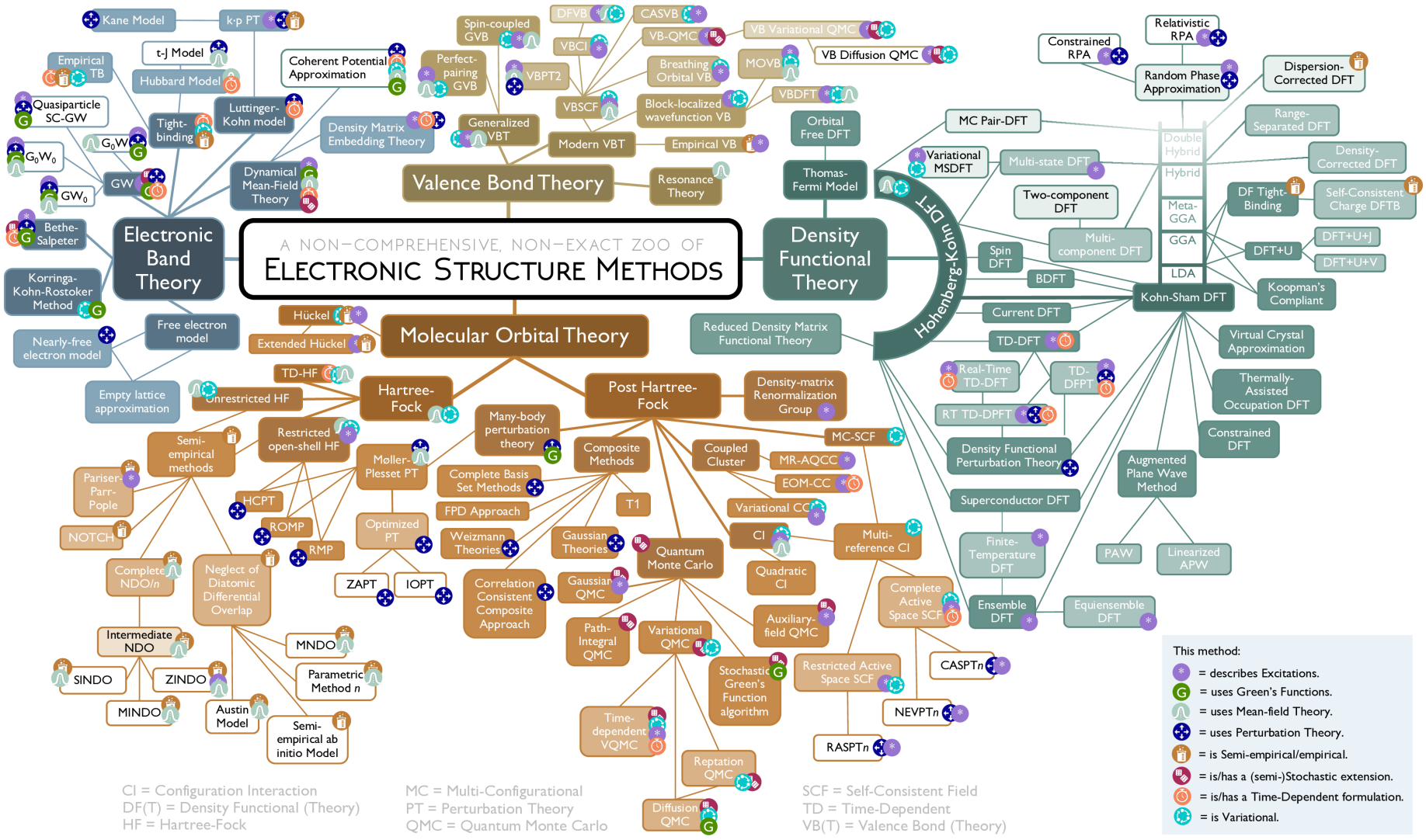
A NON-COMPREHENSIVE, NON-EXACT ZOO OF
ELECTRONIC STRUCTURE METHODS
Electronic Band Theory
Kane Model
k·p PT
t-J Model
Empirical TB
Hubbard Model
Quasiparticle SC-GW
Tight-binding
Luttinger-Kohn model
G_0W
G_0W_0
GW
GW_0
Bethe-Salpeter
Korringa-Kohn-Rostoker Method
Nearly-free electron model
Free electron model
Empty lattice approximation
Coherent Potential Approximation
Density Matrix Embedding Theory
Dynamical Mean-Field Theory
Valence Bond Theory
Spin-coupled GVB
Perfect-pairing GVB
Generalized VBT
DFVB
CASVB
VBCI
VB-QMC
VB Variational QMC
VB Diffusion QMC
VBPT2
Breathing Orbital VB
MOVB
VBSCF
Block-localized wavefunction VB
VBDFT
Modern VBT
Empirical VB
Resonance Theory
Molecular Orbital Theory
Hückel
Extended Hückel
TD-HF
Unrestricted HF
Hartree-Fock
Restricted open-shell HF
Semi-empirical methods
Pariser-Parr-Pople
NOTCH
HCPT
ROMP
RMP
Møller-Plesset PT
Optimized PT
ZAPT
IOPT
Complete NDO/n
Neglect of Diatomic Differential Overlap
Intermediate NDO
SINDO
ZINDO
MINDO
MNDO
Parametric Method n
Austin Model
Semi-empirical ab initio Model
Post Hartree-Fock
Many-body perturbation theory
Complete Basis Set Methods
FPD Approach
Weizmann Theories
Composite Methods
T1
Gaussian Theories
Gaussian QMC
Correlation Consistent Composite Approach
Quantum Monte Carlo
Path-Integral QMC
Variational QMC
Time-dependent VQMC
Stochastic Green's Function algorithm
Reptation QMC
Diffusion QMC
Coupled Cluster
MR-AQCC
EOM-CC
Variational CC
CI
Quadratic CI
Auxiliary-field QMC
Density-matrix Renormalization Group
MC-SCF
Multi-reference CI
Complete Active Space SCF
Restricted Active Space SCF
CASPTn
NEVPTn
RASPTn
Density Functional Theory
Hohenberg-Kohn DFT
Orbital Free DFT
Thomas-Fermi Model
Reduced Density Matrix Functional Theory
MC Pair-DFT
Variational MSDFT
Multi-state DFT
Two-component DFT
Multi-component DFT
Spin DFT
BDFT
Current DFT
TD-DFT
Real-Time TD-DFT
TD-DFPT
RT TD-DPFT
Density Functional Perturbation Theory
Superconductor DFT
Finite-Temperature DFT
Ensemble DFT
Equiensemble DFT
Kohn-Sham DFT
Double Hybrid
Hybrid
Meta-GGA
GGA
LDA
Constrained RPA
Relativistic RPA
Random Phase Approximation
Dispersion-Corrected DFT
Range-Separated DFT
Density-Corrected DFT
DF Tight-Binding
Self-Consistent Charge DFTB
DFT+U
DFT+U+J
DFT+U+V
Koopman's Compliant
Virtual Crystal Approximation
Thermally-Assisted Occupation DFT
Constrained DFT
Augmented Plane Wave Method
PAW
Linearized APW
CI = Configuration Interaction
DF(T) = Density Functional (Theory)
HF = Hartree-Fock
MC = Multi-Configurational
PT = Perturbation Theory
QMC = Quantum Monte Carlo
SCF = Self-Consistent Field
TD = Time-Dependent
VB(T) = Valence Bond (Theory)
This method:
= describes Excitations.
= uses Green's Functions.
= uses Mean-field Theory.
= uses Perturbation Theory.
= is Semi-empirical/empirical.
= is/has a (semi-)Stochastic extension.
= is/has a Time-Dependent formulation.
= is Variational.

Hamiltonian of the BOA. As such, the schematic does not explicitly include molecular mechanics methods, even though some methods do have molecular mechanics extensions. We have also excluded explicitly relativistic methods, noting that many methods implement off-shoots for including relativistic effects, ranging from simple spin-coupling corrections to full-on derivation starting with the relativistic wavefunction equation.

Four dominant categories of electronic structure methods are identified: those deriving from valence bond theory (tan), electronic band theory (blue), molecular orbital theory (orange), and density functional theory (green). Each category has different strengths, weaknesses and realms of applicability, which we will broadly and briefly discuss (*vide infra*) after clarifying the schematic's other visual components, notably the use of qualifying icons, which highlight particular areas of similarity across method classes. The presence of an icon signifies that this method

- can describe excited states, i.e., non-ground-state electronic configurations of the system, including absorption or emission of a photon or collisions with more energetic electrons.
- uses electronic Green's functions, which are, briefly, linear operators defined inside a specified, bounded frequency domain corresponding to a particular differential equation. Many, but not all, methods of the electronic band theory class use Green's functions.
- uses mean-field theory. By this, we mean that at some point in its derivation, the specified method approximates the behavior of a high-dimensional stochastic model by replacing it with a simpler model that averages over degrees of freedom.
- uses perturbation theory, another technique for describing a complicated system in terms of a simpler one. The algorithm starts with a simple system for which an exact mathematical formulation is known, onto which one tacks perturbing Hamiltonians that model slight, non-disruptive changes to the system. In the limit of small perturbations, changes to physical observables of the perturbed system can be considered corrections to those of the unperturbed system in increasingly higher orders.
- is semi-empirical/empirical, i.e., it relies in some fashion on empirical data.
- is stochastic or has a stochastic expansion. By this, we refer to methods that evolve probabilistically by randomly sampling the configuration space pertaining to the physical body of interest (e.g., the wavefunction) in search of the ground state.
- is/has a time-dependent formulation, which considers the time-dependent analog to the wavefunction equation and the BOA.
- is variational. Variational methods are those that iteratively result in an energy that is an upper bound of the exact energy.

The tonal value of each method's box is used loosely to visually differentiate appendages from their nodes, as the trees can get quite complicated spatially.

Valence bond theory (VBT) constituted one of the first quantum mechanical descriptions of elec-

Figure 2.1: A non-comprehensive and non-exact map of electronic structure methods. The meaning of each qualifier (icon in colored circle) is described in the text (vide supra).

tronic structure.[22] A generalization of resonance theory,[23] VBT emerged in the early 20th century among chemists to explain chemical bonds as overlapping linear combinations of atom-centered valence bond structures. Although its popularity as an electronic structure theory largely ceded to the other three categories in the mid-20th century, VBT is still taught in introductory chemistry courses as an intuitive, multi-atomic extension of Lewis structures.[24] Research into VBT has experienced a resurgence in the last few decades as it draws on and contributes to developments in Molecular Orbital Theory (MOT), its historical rival. Modern VBT strives to introduce simulation methods for smaller molecules, competitive (in terms of accuracy and computational thrift) with those of MOT. Modern VBT also increasingly interfaces with density functional theory (DFT). The reviews in Refs. [22], [25], and [26] offer a more detailed and nuanced picture of VBT as a field of study.

MOT, by contrast, generally posits that electrons engaged in bonding of atoms may be approximated as linear combinations of atomic orbitals and, like VBT, centralizes the many-body wavefunction as the primary physical body of interest. Historically and formatively notable among this class of methods is the (restricted) Hartree-Fock (HF) method.[27–29]

Restricted HF assumes that the N-body electronic wavefunction can be approximated by a single Slater determinant,[30–32] a mathematical body that satisfies the requirements of fermionic antisymmetry discussed in the previous chapter. Slater determinants are orthogonal to one another, and their overlap is relatively easy to calculate, even for systems with large numbers of constituents. Equipped with single-Slater determinant formalism, the HF method invokes the variational method, deriving a set of N equations for the N orbitals of the system, the solution of which yields the HF wavefunction and corresponding energy. Due to the variational nature of the HF method, which requires any trial HF wavefunction to be an upper bound to the exact many-body wavefunction, the HF method can make use of self-consistent-field (SCF) algorithms to converge to the approximate ground-state solution.

Within single-Slater determinant formalism, electrons of opposite spin are uncorrelated, so HF does not correctly account for all types of correlation.[33] Correlation is thus redefined in the HF context, where it is used as a measure of the cumulative deficiencies of the HF method as a solution to the nonrelativistic many-body wavefunction equation.

Due to HF's shortcomings in addressing correlation, as well as its laborious and often unfeasible implementation for anything larger than small molecules, MOT bifurcated into HF-like and post-HF methods. Notable post-HF methods considered as benchmarks for the methodology we develop in this dissertation are the Complete Active Space Perturbation Theory with Coupled Cluster (CASPT2/CC)[34] and Diffusion Quantum Monte Carlo.[35] We will explain these choices as they become relevant *in situ*.

Electronic Band Theory (EBT) constitutes a different approach to electronic structure. Often formulated in the language of second quantization, methods pertaining to the EBT class often rely heavily on Green's functions. These methods are useful for descriptions of the band structure of materials and their electronic transport and optical properties. A powerful EBT method worth mentioning is Dynamical Mean-Field Theory (DMFT),[36] which can be interfaced with DFT to yield accurate properties of materials systems.[37]

The foci of this dissertation are offshoots of DFT. We dedicate the remainder of Part I to describing its intricacies.

2.0.2 Why DFT?

A 2014 Nature review found that DFT features in 12 of the top 100 (two of which are in the top 10) most cited scientific papers of all time, a testament to the class's widespread popularity as an electronic structure theory.[38] There are over 50 large-scale quantum chemistry and solid-state physics computer programs, both commercial and open-source, in existence today; over 45 of those have DFT implementations, slightly outnumbering those that implement HF.

By several metrics, DFT is popular. It is used alike by theoretical and computational quantum physicists, quantum chemists, and materials scientists to determine properties of diverse molecular and material systems with quotidian ease. Instead of focusing on the electronic wavefunction, a cumbersome and computationally expensive object, DFT reformulates the observables of a many-body system in terms of the electronic density, a function modeling the charge properties of every point in three-dimensional space. As we will see in the coming sections, this recasting, coupled with various approximations that allow tailorable trade-off between computational expense and accuracy, renders calculation of a system's electronic, energetic, thermodynamic, geometric, magnetic, etc., properties in a more accessible time-frame.

DFT programs are built to quickly handle atomic, molecular, and periodic crystal systems, whereas the wavefunction methods of MOT and VBT, while often reliably accurate, converge far too slowly for systems on the order of 10^2 atoms. One can attribute DFT's widespread success to exactly this type of tractability; its linear-scaling variants have enabled the occasional ambitious calculation at the mesoscale, with cells comprising well over a million atoms.[39,40]

The wavefunction-based methods further lose out in modeling open-shell systems—materials with non-zero magnetic moment—where multi-reference treatment is generally mandatory and thus inaccessibly time- and resource-consuming for even polynuclear complexes and nano-clusters.[7,41] While there are theorists working to reduce the computation time associated with precise wavefunction methods, a sizeable part of electronic structure literature is dedicated to the alternative: making spin DFT more accurate.

Our research here contributes to the latter pursuit, building on spin DFT's broad range of applicability and well-established theoretical versatility while simultaneously addressing its intrinsic errors. In the following sections, we describe the formative basis for collinear-spin DFT, starting with the Levy constrained-search formulation of DFT in Section 2.2 and continuing with a description of the Kohn-Sham auxiliary in Section 2.3, which leads to the emergence of the unknown exchange-correlation energy functional (Section 2.3.1). This chapter ends with a description of the errors that afflict approximate spin DFT, launching a discussion on this dissertation's namesake methodology, DFT+U+J, in Section 2.5. Wherever relevant, we focus the discussion on collinear-spin-based extensions to base DFT theory.

2.1 The spin-resolved electronic density[§]

The total electronic density $\rho(\mathbf{r})$ of a multi-electron system is a mathematical object describing the probability of finding an electron at location $\mathbf{r}$. In a spin-polarized environment with N electrons, we calculate $\rho(\mathbf{r})$ as the normalized, integrated square norm of the spin-resolved electronic wavefunction (following the discussion in Section 1.1.1), or

$$\rho(\mathbf{r}) = N \int |\psi(\mathbf{r}, m_s, \boldsymbol{x}_2, ..., \boldsymbol{x}_N)|^2 \; dm_s d\boldsymbol{x}_2 ... d\boldsymbol{x}_N \; . \tag{2.1}$$

In expanding the above integral explicitly in terms of the spin degree of freedom, where $m_s = \{-\frac{1}{2}, \frac{1}{2}\}$, we obtain $\rho(\mathbf{r}) = \rho^{\uparrow}(\mathbf{r}) + \rho^{\downarrow}(\mathbf{r})$. In other words, the total electronic density is the sum of the majority- and minority-spin densities. Their integrals across spatial coordinates,

$$n^{\square} = \int \rho^{\square}(\mathbf{r}) \; d^3r \; , \tag{2.2}$$

respectively yield the total number of electrons in the majority- and minority-spin states. Here, $\square$ is assigned either $\uparrow$ or $\downarrow$ to refer to the majority- or minority-spin channels.

Another useful type of density, the spin density $\mathcal{M}(\mathbf{r})$, organically emerges here:

$$\begin{aligned} \mathcal{M}(\mathbf{r}) &= N \int \psi^*(\mathbf{r}, m_s, \boldsymbol{x}_2, ..., \boldsymbol{x}_N) \; \sigma_z(m_s) \; \psi(\mathbf{r}, m_s, \boldsymbol{x}_2, ..., \boldsymbol{x}_N) \; \; dm_s d\boldsymbol{x}_2 ... d\boldsymbol{x}_N \\ &= \rho^{\uparrow}(\mathbf{r}) - \rho^{\downarrow}(\mathbf{r}) \; , \end{aligned} \tag{2.3}$$

where the Pauli matrix σ_z operates on m_s to antisymmetrically distinguish the majority- and minority-spin channels and, ultimately, introduce the negative sign to the latter in Eq. (2.3). Crucially, the use of σ_z over $\boldsymbol{\sigma}$ highlights our preference for a collinear-spin model, where we assume all spin vectors in the system may be averaged as projections of the total spin vector onto a singular global quantization axis (arbitrarily chosen as the z-axis over, for example, the x- and y-axes). One may use the spin-density to calculate the expectation value of the spin operator's z-axis projection $\hat{S}_z$ as well as its $2S + 1$ eigenvalues M_s,

$$\langle \hat{S}_z \rangle = \frac{\hbar}{2} \int \mathcal{M}(\mathbf{r}) \; d^3r = \hbar M_s = \frac{\hbar}{2} \left(N^{\uparrow} - N^{\downarrow} \right) \; . \tag{2.4}$$

This can be a sizeable assumption outside of the non-relativistic limit, considering that in many materials, the direction of the spin vector depends strongly on the position in a way that nullifies the simplified aligned-(anti-aligned) dichotomy.[42–44] As we will see in the coming sections, the choice to consider spin collinearly will have consequences, some beneficial—in terms of the mathematical simplicity and computational tractability—and others controversial.

[§]This section's recounting and much of its notation follow that of Ref. [7].

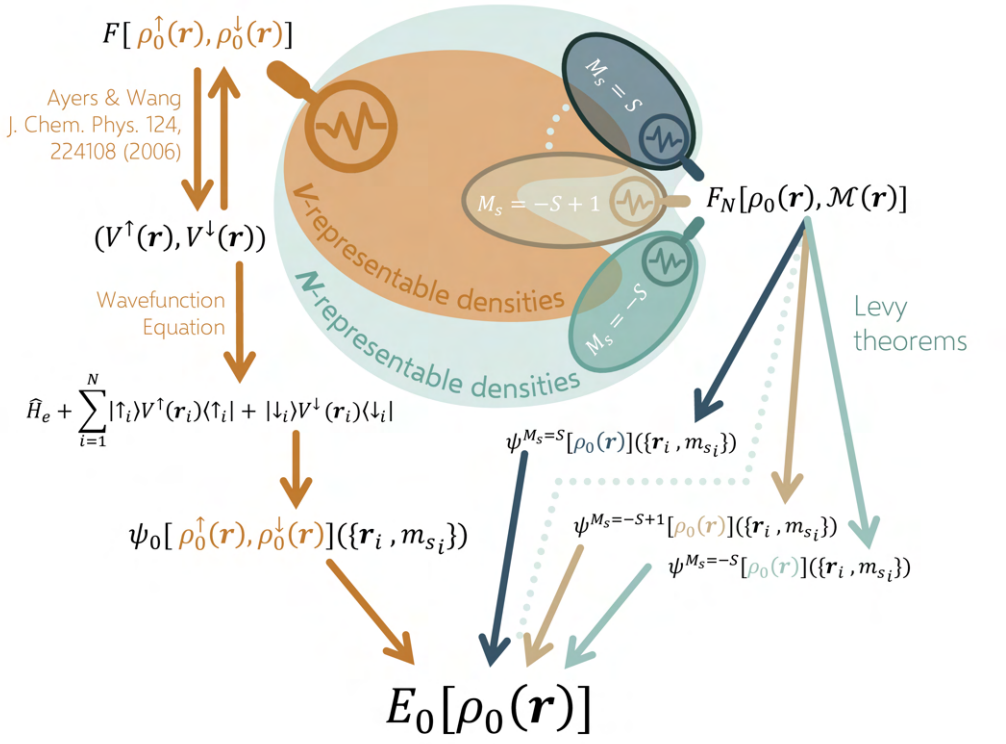

Figure 2.2: Schematic of derivations for spin DFT, starting with constrained searches for densities following certain definitions of the universal functional (F defined in Eq. (A.5), whereas F_N defined in Eq. (2.5)).

2.2 Levy constrained-search formulation of DFT

Density Functional Theory (DFT) emerged in the 1960s as the fruit of two theorems by Hohenberg and Kohn,[45] which proved not only that the total energy of a system of electrons immersed in an external potential is a unique functional of the electronic density $\rho(\mathbf{r})$, but that the same total energy functional $E_{\text{DFT}}[\rho]$ is minimized when $\rho = \rho_0(\mathbf{r})$, the ground-state electronic density. We transcribe these derivations and discuss the consequences of these two theorems in Appendix A1.

Eigenstate degeneracies were originally explicitly excluded from the derivation of the Hohenberg-Kohn (HK) theorems. The universal functional $F[\rho(\mathbf{r})]$ that emerges therefrom is defined for trial densities $\rho(\mathbf{r})$ that are V-representable, meaning they can be associated with an antisymmetric ground-state wavefunction (by virtue of solution to the wavefunction equation pertaining to a particular external potential V). Open-shell systems, however, require a pairwise resolution of the variables involved, transforming the V-representability property into a more complex assertion; that only one pair of trial densities $\{\rho^{\uparrow}(\mathbf{r}),\rho^{\uparrow}(\mathbf{r})\}$ can be associated with the ground-state wavefunction of a system under the influence of two external potentials $\{V^{\uparrow},V^{\downarrow}\}$. The resolution of two potentials, one of which acts only on spin-up electrons and the other only on spin-down electrons, comes from the understanding the spin-up and spin-down electrons are identical in the absence of a magnetic field, requiring an expansion of the Hamiltonian central to the derivations (see orange path in Fig. 2.2). This V-representability problem

was somewhat controversially overcome in 1972[46–52] but proved on arguably more firm theoretical foundations in 2006 by following Ref. [53] in redefining $F[\rho(\mathbf{r})]$ as a supremum over one-electron potentials.[54,55]

One may altogether circumvent the V-representability issue by expanding the space of trial densities to those that are N-representable, a subset of which are the V-representable densities.[56] N-representable densities are those associated with any antisymmetric wavefunction, not just those pertaining to a ground state. The $(2S+1)$-fold degenerate wavefunctions ψ^{M_s}, all of which are obtained from the same ground-state density and all of which simultaneously minimize the universal variational functional, will still give rise to a single ground-state density that fulfills the N-representability criterion. Should the need arise for a unique minimizing wavefunction—as it does if interested in the spin-resolved densities $\rho^{\uparrow}(\mathbf{r})$ and $\rho^{\downarrow}(\mathbf{r})$ as well as the spin density $\mathcal{M}(\mathbf{r})$—one need simply specify a value for M_s and constrain the search to such spin states alone.[7] This concept is demonstrated on the right side of the schematic in Fig. 2.2.

To expand the space of trial densities, we rely on a different definition of the universal variational functional than that of the HK theorems (Eq. (A.5)). Following the description of Ref. [56], let

$$F_N[\rho(\mathbf{r})] = \min \langle \psi'_\rho \mid \hat{H}_e \mid \psi'_\rho \rangle \tag{2.5}$$

be such a functional that searches through all antisymmetric wavefunctions $\{\psi'_\rho\}$ that yield a (N-representable) trial density $\rho(\mathbf{r})$, which is not necessarily V-representable. $F_N[\rho(\mathbf{r})]$ is designed to select the wavefunction $\psi_\rho \in \{\psi'_\rho\}$ that minimizes the expectation value of $\hat{H}_e$. It follows, then, that for the ground-state density $\rho_0(\mathbf{r})$,

$$F_N[\rho_0(\mathbf{r})] = \langle \psi_{\rho_0} \mid \hat{H}_e \mid \psi_{\rho_0} \rangle. \tag{2.6}$$

To show that $F_N[\rho_0(\mathbf{r})]$ is a universal variational functional, the following two theorems—which we call here the Levy theorems—must be proven.[56]

2.2.1 The first Levy theorem[§]

Theorem: The ground-state energy E_0 of any system with N electrons is bounded above by the total energy corresponding to any trial N-representable density $\rho(\mathbf{r})$; i.e.,

$$E_0 \;\leq\; F_N[\rho(\mathbf{r})] \;+ \int V(\mathbf{r})\,\rho(\mathbf{r})\,d\mathbf{r}.$$

Proof: Consider a system of N electrons moving under the influence of an external potential $V(\mathbf{r})$ and represented by N-representable density $\rho(\mathbf{r})$. This system has total energy

$$E[\rho(\mathbf{r})] \;=\; \langle \psi'_\rho \mid \hat{H}_e + V(\mathbf{r}) \mid \psi'_\rho \rangle \;=\; F_N[\rho(\mathbf{r})] \;+ \int V(\mathbf{r})\,\rho(\mathbf{r})\,d\mathbf{r}, \tag{2.7}$$

which, by our notation introduced at the end of Section 2.2, is minimized when the wavefunction

[§]This proof was originally published in Ref. [56].

$\psi_\rho \in \{\psi'_\rho\}$ is selected to minimize $F_N[\rho(\mathbf{r})]$. Then, the second and third clauses of Eq. (2.7) become

$$\langle \psi_\rho \mid \hat{H}_e + V(\mathbf{r}) \mid \psi_\rho \rangle \;=\; F_N[\rho(\mathbf{r})] \;+ \int V(\mathbf{r})\, \rho(\mathbf{r})\, d\mathbf{r}, \tag{2.8}$$

the left-hand side of which is, by the variational principle, greater than or equal to the ground-state energy E_0 of the system. Therefore,

$$E_0 \;\leq\; F_N[\rho(\mathbf{r})] \;+ \int V(\mathbf{r})\, \rho(\mathbf{r})\, d\mathbf{r}, \tag{2.9}$$

which concludes the proof. □

2.2.2 The second Levy theorem[§]

Theorem: The N-representable density functional that yields the ground-state energy of the system delivers the lowest energy if and only if the input density is the ground-state density $\rho_0(\mathbf{r})$. That is,

$$E_0[\rho_0(\mathbf{r})] \;=\; F_N[\rho_0(\mathbf{r})] \;+ \int V(\mathbf{r})\, \rho_0(\mathbf{r})\, d\mathbf{r}.$$

Proof: Applying the variational principle to the same system described above,

$$E_0 \;=\; \langle \psi_0 \mid \hat{H}_e + V(\mathbf{r}) \mid \psi_0 \rangle \;\leq\; \langle \psi_{\rho_0} \mid \hat{H}_e + V(\mathbf{r}) \mid \psi_{\rho_0} \rangle, \tag{2.10}$$

or more explicitly,

$$\begin{aligned} \langle \psi_0 \mid \hat{H}_e \mid \psi_0 \rangle \;+ \int V(\mathbf{r})\, \rho_0(\mathbf{r})\, d\mathbf{r} \;&\leq\; \langle \psi_{\rho_0} \mid \hat{H}_e \mid \psi_{\rho_0} \rangle \;+ \int V(\mathbf{r})\, \rho_0(\mathbf{r})\, d\mathbf{r} \\ \langle \psi_0 \mid \hat{H}_e \mid \psi_0 \rangle \;&\leq\; \langle \psi_{\rho_0} \mid \hat{H}_e \mid \psi_{\rho_0} \rangle\,. \end{aligned} \tag{2.11}$$

However, the definition of ψ_{ρ_0} mandates that the reverse inequality hold; that is,

$$\langle \psi_0 \mid \hat{H}_e \mid \psi_0 \rangle \;\geq\; \langle \psi_{\rho_0} \mid \hat{H}_e \mid \psi_{\rho_0} \rangle. \tag{2.12}$$

Both Eqs. (2.11) and (2.12) hold only in the case of equality. Substituting Eq. (2.6) in for the right-hand side and tacking on the integral over potential, we find

$$\int V(\mathbf{r})\, \rho_0(\mathbf{r})\, d\mathbf{r} \;+ \langle \psi_0 \mid \hat{H}_e \mid \psi_0 \rangle \;=\; F_N[\rho_0(\mathbf{r})] \;+ \int V(\mathbf{r})\, \rho_0(\mathbf{r})\, d\mathbf{r}, \tag{2.13}$$

where the left-hand side of Eq. (2.13) is simply the ground-state energy $E_0[\rho_0(\mathbf{r})]$ as a functional of the ground-state density. Therefore,

$$E_0[\rho_0(\mathbf{r})] \;=\; F_N[\rho_0(\mathbf{r})] \;+ \int V(\mathbf{r})\, \rho_0(\mathbf{r})\, d\mathbf{r}, \tag{2.14}$$

[§]This proof was originally published in Ref. [56].

thereby completing the proof. □

These proofs remain true even if we select a particular value of M_s by which to constrain the search for the wavefunction ψ_{ρ_0}. In doing so, we effectively use one spin density $\mathcal{M}(\mathbf{r})$ in the definition of the universal functional such that $F_N[\rho_0(\mathbf{r})] \to F_N[\rho_0(\mathbf{r}), \mathcal{M}(\mathbf{r})] = \min \langle \psi_\rho^{M_s} \mid \hat{H}_e \mid \psi_\rho^{M_s} \rangle$.

The second Levy theorem establishes the variational principle for a density-centered formulation of the many-body problem. Coupled with the first, one is in a position to make some very powerful and workable conclusions. For example, the degenerate ground-state electronic wavefunction as it is reformulated in Eq. (1.12) and used in Eq. (1.5) is a unique functional of the ground-state density. That is,

$$\psi_0(\{\boldsymbol{x}_i\}) \;=\; \psi[\rho_0(\mathbf{r})]. \tag{2.15}$$

The ground-state expectation value of any observable $\hat{O}$ is thus a functional of $\rho_0(\mathbf{r})$:

$$O_0 \;=\; O[\rho_0(\mathbf{r})] \;=\; \langle \rho_0(\mathbf{r}) \,|\, \hat{O} |\, \psi[\rho_0(\mathbf{r})] \rangle \,. \tag{2.16}$$

By reformulating a multi-atomic system's observables—chief among them the energy, shown in Eq. (2.17)—in terms of the electronic density, one may find the ground state and its properties through variational minimization of

$$E_{\mathrm{DFT}}[\rho(\mathbf{r})] \;=\; T[\rho(\mathbf{r})] \;+\; E_{ee}[\rho(\mathbf{r})] \;+\; \int V(\mathbf{r})\, \rho(\mathbf{r})\, d\mathbf{r}, \tag{2.17}$$

where T is the electron kinetic energy of the system, E_{ee} is the electron-electron interaction energy, and $V(\mathbf{r})$ is the external potential term as a function of real-space coordinates, which includes the nucleus-electron interactions in addition to any other local potential (e.g., electric field) in which the system is immersed.

Crucially, the Hohenberg-Kohn theorems, and the analogous Levy constrained-search formulation of DFT, imply that we no longer have to keep track of the locations of individual electrons. A continuous density makes electrons easier to work with mathematically and simplifies significantly the computations required in solving the many-body problem. The only obstacle is that the precise kinetic and electron-electron interaction energy functionals remain unknown.

2.3 The spin-unrestricted Kohn-Sham auxiliary

To truly harness the power of DFT as a theory and approximatively circumvent the issue of the unknown universal functional, one must consider an auxiliary system identical in every way to that resulting from the BOA but with non-interacting electrons. In 1965, Kohn and Sham showed that the ground-state density of both the exact and auxiliary systems are identical.[57]

Within a spin-DFT formalism, we can impose the requirement that (i) only the electronic densities of the interacting and non-interacting systems agree, or (ii) both the electronic densities *and* the spin densities of the interacting and non-interacting systems agree. Option (i) results in the so-called spin-

restricted KS-DFT formalism and option (ii) in spin-unrestricted KS DFT.[7]

The derivation of the Kohn-Sham (KS) equations in the spin-restricted case follows the same logic as that of the spin-independent case, which we transcribe in Appendix A2. We focus here on the spin-unrestricted formalism.[§] For simplicity in transcription, we repurpose the variable σ to refer to the spin variable, which may take on the values $\uparrow$ or $\downarrow$ to refer to bodies pertaining to the majority- and minority-spin states respectively.[‖]

In the KS approach, we map a system of $N = n^{\uparrow} + n^{\downarrow}$ interacting electrons onto a system of $N = n^{\uparrow} + n^{\downarrow}$ non-interacting electrons with the same spin-resolved electronic density, expressed as

$$\rho(\mathbf{r}) = \sum_{\sigma}^{\uparrow\downarrow} \sum_{i}^{n^{\sigma}} |\psi_i^{\sigma}(\mathbf{r})|^2 \,, \tag{2.18}$$

where $\{\psi_i^{\sigma}(\mathbf{r})\}$ are called the KS orbitals or KS wavefunctions. By selecting values for $n^{\uparrow}$ and $n^{\downarrow}$, we impose a spin state M_s. To ensure the same number of electrons in this auxiliary system, we further impose the normalization constraint in Eq. (2.2). Using the KS orbitals, we can express the kinetic energy functional of the interacting system in Eq. (2.17) as

$$T[\rho^{\uparrow}(\mathbf{r}), \rho^{\downarrow}(\mathbf{r})] = \underbrace{\left(-\frac{1}{2} \sum_{\sigma}^{\uparrow\downarrow} \sum_{i}^{n^{\sigma}} \int \psi_i^{\sigma}(\mathbf{r}) \nabla^2 \psi_i^{\sigma}(\mathbf{r}) \, d\mathbf{r} \right)}_{T_s[\rho^{\uparrow}(\mathbf{r}), \rho^{\downarrow}(\mathbf{r})]} + \Delta T[\rho^{\uparrow}(\mathbf{r}), \rho^{\downarrow}(\mathbf{r})] \,, \tag{2.19}$$

featuring the single-particle kinetic energy functional $T_s[\rho^{\uparrow}(\mathbf{r}), \rho^{\downarrow}(\mathbf{r})]$ and a corrective term ΔT. In other words, we approximate the total kinetic energy of the system of interacting electrons as the sum of kinetic energy terms pertaining to N non-interacting electrons, capturing non-descriptively in a separate term the exchange and correlation contributions to the kinetic energy.

Analogously, we may expand the electron-electron interaction energy E_{ee} as the sum of the Hartree energy E_{Ha}—the Coulombic repulsion of constituent one-electron densities—and a corrective term representing all other exchange and correlation effects not made explicit.

$$E_{ee}[\rho^{\uparrow}(\mathbf{r}), \rho^{\downarrow}(\mathbf{r})] = \underbrace{\frac{1}{2} \iint \frac{\rho(\mathbf{r}) \, \rho(\mathbf{r}')}{|\mathbf{r} - \mathbf{r}'|} d\mathbf{r} \, d\mathbf{r}'}_{E_{\text{Ha}}[\rho(\mathbf{r})]} + \Delta E_{ee}[\rho^{\uparrow}(\mathbf{r}), \rho^{\downarrow}(\mathbf{r})] \tag{2.20}$$

Inserting Eqs. (2.19) and (2.20) in Eq. (2.17) yields the KS energy

$$E_{\text{KS}}[\rho^{\uparrow}(\mathbf{r}), \rho^{\downarrow}(\mathbf{r})] = T_s[\rho^{\uparrow}(\mathbf{r}), \rho^{\downarrow}(\mathbf{r})] + E_{\text{Ha}}[\rho(\mathbf{r})] + E_{\text{xc}}[\rho^{\uparrow}(\mathbf{r}), \rho^{\downarrow}(\mathbf{r})] + \int V(\mathbf{r}) \rho(\mathbf{r}) \, d\mathbf{r}, \tag{2.21}$$

where $E_{\text{xc}}[\rho^{\uparrow}(\mathbf{r}), \rho^{\downarrow}(\mathbf{r})] = \Delta T[\rho^{\uparrow}(\mathbf{r}), \rho^{\downarrow}(\mathbf{r})] + \Delta E_{ee}[\rho^{\uparrow}(\mathbf{r}), \rho^{\downarrow}(\mathbf{r})]$ is the infamously elusive exchange-correlation (XC) energy functional to be discussed in Section 2.3.1. One may variationally minimize Eq. (2.21) to find the ground-state densities $\rho^{\uparrow}(\mathbf{r})$ and $\rho^{\downarrow}(\mathbf{r})$.

Section 2.2.2 establishes the existence of a minimal energy functional achieved with the spin-

[§] We follow the format presented in Ref. [58].

[‖] We also adopt the notation $\bar{\sigma}$, which refers to the opposite spin state (i.e., when $\sigma = \uparrow$, then $\bar{\sigma} = \downarrow$ and vice versa).

resolved ground-state density $\rho^\sigma(\mathbf{r})$. In the calculus of variations, we may therefore identify this energy functional as a stationary point subject to the constraint that the integrated density is equal to the total number of electrons n^σ. Minimization of Eq. (2.21) with respect to $\rho^\sigma(\mathbf{r})$ yields Euler-Grange equations of the form[§]

$$\frac{\delta E_{\mathrm{KS}}[\rho(\mathbf{r})]}{\delta\rho^\sigma(\mathbf{r})} - \mu^\sigma = \frac{\delta T_s[\rho^\uparrow(\mathbf{r}),\rho^\downarrow(\mathbf{r})]}{\delta\rho^\sigma(\mathbf{r})} + V_{\mathrm{KS}}[\rho^\uparrow(\mathbf{r}),\rho^\downarrow(\mathbf{r})] - \mu^\sigma = 0, \tag{2.22}$$

where μ^σ is the chemical potential for electrons of spin σ. Eq. (2.22) is precisely that obtained in applying DFT to a system of non-interacting electrons subject to a potential modeled by

$$V^\sigma_{\mathrm{KS}}[\rho^\uparrow(\mathbf{r}),\rho^\downarrow(\mathbf{r})](\mathbf{r}) = V(\mathbf{r}) + \frac{\delta E_{\mathrm{xc}}[\rho^\uparrow(\mathbf{r}),\rho^\downarrow(\mathbf{r})]}{\delta\rho^\sigma(\mathbf{r})} + \int \frac{\rho(\mathbf{r}')}{|\mathbf{r}-\mathbf{r}'|}\,d\mathbf{r}'\,, \tag{2.23}$$

the last term of which is called the Hartree potential. Ground-state solutions may thus be sought variationally in the more restrained KS energy eigenspace,

$$\left[-\frac{1}{2}\nabla^2 + V^\sigma_{\mathrm{KS}}[\rho^\uparrow(\mathbf{r}),\rho^\downarrow(\mathbf{r})](\mathbf{r})\right]\psi^\sigma_i(\mathbf{r}) = \epsilon^\sigma_i\psi^\sigma_i(\mathbf{r}), \tag{2.24}$$

wherein the set of wavefunctions $\{\psi^\sigma_i(\mathbf{r})\}$ are the KS orbitals introduced earlier, and ϵ^σ_i is the corresponding spin-resolved energy profile of the system. Under the KS scheme, therefore, solution to the electronic eigenvalue problem of N bodies is reduced to solution of two (one for each spin state) $\times\, N$ single-body wavefunction equations, one for each KS orbital $\psi^\sigma_i(\mathbf{r})$. The biggest obstacle for practical implementation of the KS scheme remains the definition of E_{xc}.

2.3.1 The exchange-correlation energy functional

The only unknown in Eq. (2.21) is E_{xc}. The term's indefiniteness absorbs all other non-relativistic many-body effects not explicitly considered in Eq. (2.17), although the primary function of the XC energy is to quantify all exchange and correlation effects between electrons.[33] In practice, DFT would not manifest as an approximation at all if the XC potential were known exactly; thus, accuracy in DFT calculations relies almost exclusively on state-of-the-art approximations to this term and/or any post-initialization corrections applied to it.

The Local Density Approximation (LDA), proposed by Kohn and Sham in their eponymous paper, attempts a basic evaluation of $E_{\mathrm{xc}} = E_{\mathrm{x}} + E_{\mathrm{c}}$ by assuming that all electron-electron interactions resemble those interactions in an homogeneous electron gas (HEG).[57] LDA's slightly more sophisticated offspring, the Local Spin-Density Approximation (LSDA), introduces spin polarization to the XC functional. Expressions for exchange and correlation are sought separately, the former of which can be approximated for a non-homogenous density by assuming a HEG:[57,59]

$$E^{\mathrm{LSDA}}_{\mathrm{x}}[\rho^\uparrow(\mathbf{r}),\rho^\downarrow(\mathbf{r})] = \int \rho(\mathbf{r})\,\epsilon^{\mathrm{LSDA}}_{\mathrm{x}}(\rho^\uparrow(\mathbf{r}),\rho^\downarrow(\mathbf{r}))\,d\mathbf{r} \quad \text{and} \tag{2.25}$$

[§]Physicists and mathematicians each adhere to different conventions regarding the mathematical representation of the partial derivative (i.e., the use of δ over d and vice versa). Appendix A3 clarifies these conventions.

$$\epsilon_{\mathrm{x}}^{\mathrm{LSDA}}(\rho^{\uparrow}(\mathbf{r}),\rho^{\downarrow}(\mathbf{r})) = -\frac{3^{4/3}}{8\pi^{1/3}}\rho(\mathbf{r})^{1/3}\left[(1+\gamma)^{4/3}+(1-\gamma)^{4/3}\right]. \tag{2.26}$$

Here, $\epsilon_{\mathrm{x}}^{\mathrm{LSDA}}$ is the exchange energy density (i.e., the energy per particle of a HEG), and $\gamma = \frac{\rho^{\uparrow}(\mathbf{r})-\rho^{\downarrow}(\mathbf{r})}{\rho(\mathbf{r})}$ is the spin polarization.[60] The analogous correlation energy density $\epsilon_{\mathrm{c}}^{\mathrm{LSDA}}$, by contrast, is only determinable analytically in the high- and low-density limits. Quantum Monte Carlo simulations of increasing quality are often used to determine E_{xc} for any HEG with any given density.[61–63] In many cases, particularly those with relatively homogeneous or slowly-varying charge densities, these approximations are satisfactory.[64] The most common LDA used in practical applications today is the Perdew-Zunger functional.[65]

A rung above the LDA on the metaphorical "Jacob's Ladder" of XC functionals[66] is the set of Generalized Gradient Approximation (GGA) functionals, which take the form

$$E_{\mathrm{xc}}^{\mathrm{GGA}}[\rho(\mathbf{r})] = \int d\mathbf{r}\ \mathcal{F}(\rho^{\uparrow}(\mathbf{r}),\rho^{\downarrow}(\mathbf{r}),\nabla\rho^{\uparrow}(\mathbf{r}),\nabla\rho^{\downarrow}(\mathbf{r}))\,, \tag{2.27}$$

where $\mathcal{F}$ is a widely tailorable function of the density and its gradient, accommodating, with variable specificity and computational complexity, sharper changes in density than those of an homogeneous electron gas.[67–69]

Other XC functionals that address the fallibilities of LDA and GGAs by venturing into non-local descriptions of the density have been developed and proven effective in a variety of DFT contexts.[70] The meta-GGA and hybrid functional classes—the former of which depends either on $\nabla^2\rho(\mathbf{r})$ or the kinetic energy density[71–73] and the latter of which introduces a percentage of exact HF exchange[74,75]—are generally more computationally demanding and/or evaluated semi-empirically, rendering them less accessible than their (semi-)local ancestors.

The XC functional featuring most in the following investigations is the time-tested Perdew-Burke-Ernzerhof (PBE) GGA functional.[68] Its spin-resolved XC functional takes the following form, having been designed to (a) focus only on satisfying the most energetically significant constraints and (b) rely on fundamental constants:

$$E_{\mathrm{x}}^{\mathrm{PBE}}[\rho(\mathbf{r})] = \int \rho(\mathbf{r})\,\epsilon_{x}^{\mathrm{LSDA}}(\rho(\mathbf{r}))\left[1+\kappa-\frac{\kappa}{1+\mu\varsigma^2/\kappa}\right]d\mathbf{r} \tag{2.28}$$

$$E_{\mathrm{c}}^{\mathrm{PBE}}[\rho^{\uparrow}(\mathbf{r}),\rho^{\downarrow}(\mathbf{r}),\nabla\rho^{\uparrow}(\mathbf{r}),\nabla\rho^{\downarrow}(\mathbf{r})] = \int \rho(\mathbf{r})\left[\epsilon_{c}^{\mathrm{LSDA}}(\rho(\mathbf{r}))+\Xi^{\mathrm{PBE}}(\rho^{\uparrow},\rho^{\downarrow},\xi)\right]d\mathbf{r}\,. \tag{2.29}$$

Featuring in either equation are the exchange- and correlation-adapted reduced density gradients ς and ξ, respectively, defined as

$$\varsigma = \frac{|\nabla\rho(\mathbf{r})|}{2(3\pi^2)^{1/3}\rho^{4/3}} \qquad \xi = |\nabla\rho(\mathbf{r})|\left[2\left(\frac{3}{\pi}\right)^{1/6}\left[(1+\gamma)^{2/3}+(1-\gamma)^{2/3}\right]\rho(\mathbf{r})^{7/6}\right]^{-1}. \tag{2.30}$$

The constants of note are $\kappa = 0.804$ (a nameless parameter) and $\mu \approx 0.21951$ (the effective gradient coefficient for exchange). We refer the reader to Eq. (3.35) in Ref. [60] for an expansion of the gradient correction Ξ^{PBE} (referred to therein as H^{PBE}).

We depend on PBE due to its simplicity and semi-locality, its widespread implementation in DFT

programs and pseudopotential generators, as well as the wealth of DFT literature and data with which to compare the results of our methodologies.

2.4 Errors in approximate spin DFT

Conceptually speaking, DFT is, at its core, a ground-state theory. Some properties pertaining to excited states, including non-ground-state magnetic orderings, are in principle inaccessible at the level of theory covered hitherto. Additionally, by virtue of their reliance on a fictitious system of non-interacting electrons, all KS wavefunctions (except the highest occupied, by Janak's theorem[76]) are mathematical auxiliaries rather than physical embodiments of actual electronic states within pure DFT. The connection between KS wavefunctions and physical observables, therefore, suffers from a litany of concept-driven errors (examples of which can be found in Refs. [77–81]) arising from the concessions made in Section 2.3.

(Semi-)Local XC functionals like LSDA and PBE, however, give rise to a separate category of errors that emerge when KS DFT is applied to strongly correlated electron systems.[82–88] By strongly correlated, in this context, we refer not necessarily to the quantum mechanical understanding of correlation described in Section 1.1.3, but to the impoverished description of the electronic structure associated with localized subspaces within the local (LSDA) and semi-local (GGA) mean-field approximations to the XC energy functional.[89] Consequences of these errors afflict, for example, the band gaps of Mott insulators like transition metal oxides, which are severely underestimated, often by an order of magnitude if not already qualitatively incorrect in predicting metallic behavior.

In the sections that follow, we outline the challenges of describing XC effects with only a local or semi-local functional dependence and based on a single-determinant reference system.

2.4.1 Fractional charge

Chief among the characteristic errors in the available computationally tractable local or semi-local approximate functionals[82–84] is the self-interaction error (SIE), the spurious exposure of an electron to its own Coulombic potential. Recall from Eq. (2.20) that the electron-electron interaction energy in the KS auxiliary is approximated by the single-particle density-density interaction of the Hartree term, which effectively allows an electron to interact with its own density in the understanding that this unphysicality will be corrected by the XC functional. At best, LDA and GGA functionals only partially cancel this self-interaction, leaving a non-rectified quadratic contribution to the energy.

The relation between SIE and fractional charge is most visible when considering the dissociation of the H_2^+ molecule, comprising one electron and two nuclei.[85,90] As the H nuclei are pulled apart, to the dissociation limit, the exact electron density predicts $1/2$ an electron on each H atom. The PBE density replicates this behavior, but the total energy it predicts for this configuration is far too low.[91] DFT effectively delocalizes the electron, giving the energy as a function of fractional charge erroneous curvature.[70,85,86,90,92]

Delocalization error—the manifestation of SIE in many-body systems and defined, at present, only for open quantum systems—similarly impedes DFT in describing properties of multi-electron

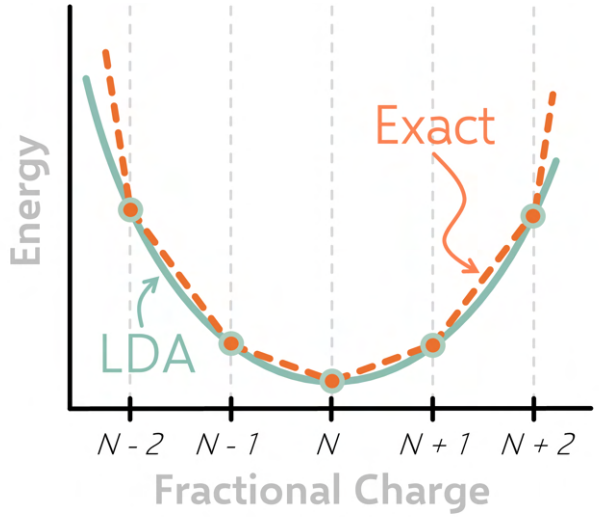

Figure 2.3: Schematic of global curvature of DFT total energy with respect to fractional charge. Adapted from Fig. 3.1 of Ref. [93].

systems.[86–88,90,94] In an ensemble formulation of DFT, the exact energy functional E as a function of fractional charge $N + \delta N$ is

$$E(N + \delta N) = (1 - \delta N)E(N) + \delta E(N + 1)\,, \tag{2.31}$$

with $0 < \delta N < 1$, a relation expressing piecewise linearity with derivative discontinuity at integer values of charge and demonstrated by the orange dashed line in Fig. 2.3.[95] What approximate DFT calculations yield, however, is a convex parabola-like structure, represented by the blue solid line in Fig. 2.3, indicating that the lowest energy of any system will most likely be acquired with fractional charge.[70,85,86,90,92,96] The curvature of the energy as a function of total charge is referred to as the global curvature, and as it becomes more significant for increasingly localized electronic densities, it is often used as a measure of the delocalization error.[85,97]

The localized curvature, by contrast, is the second derivative of the energy with respect to the occupancy of a single orbital, region, or subspace within a system kept at constant charge. DFT+U, the corrective protocol to be introduced in Section 2.5, operates exclusively via localized curvature in aiming to reconstruct the piecewise linearity of systems by adding or removing charge from a localized subshell, keeping the global curvature constant. There is no evidence to suggest that the two are equal, although there seems to be a negative correlation between them.[97] Through their investigations for various molecules, Ref. [97] showed that the global curvature tends to be more pronounced than the localized curvature.

Despite its extensive documentation, delocalization error is tenacious. It renders density functional approximations (DFAs), like those described in Section 2.3.1, especially and cumulatively errant in highly localized subspaces such as the d and f orbitals of atoms. The misrepresentation of these subspaces is implicated in band-gap underestimation and energy-density non-linearity, causing inaccuracies in a multitude of system properties, from deviations in energy to full-on qualitative mischaracterizations of Mott insulators.[98–100]

2.4.2 Fractional spin

Less discussed than SIE, but no less pervasive, is the static-correlation error (SCE) that particularly arises in degenerate and multi-valence systems and, more generally, in systems of significant multi-reference character.[101] SCE is related to systems with large static correlation, described in Section 1.1.3 in the chemists' sense as all the electronic interaction effects not described by restricted Hartree-Fock, which includes part of Coulomb exchange.

Analogous to the piecewise linearity condition of Eq. (2.31), SCE manifests largely as an energetic deviation from constancy with respect to fractional spin.[102] Recall that states with $S > 0$, represented by degenerate wavefunctions ψ^{M_s}, share the same electron density and exact total energy $E[\rho(\mathbf{r}), \mathcal{M}(\mathbf{r})]$ but differ in spin density $\mathcal{M}(\mathbf{r})$. For any linear combination of such spin densities, in fact, given the S corresponding to the lowest energy for a given electron count N, it can be shown that the exact spin-dependent HK functional of Eq. (2.5) satisfies

$$F_N[\rho(\mathbf{r}), \delta\mathcal{M}(\mathbf{r})] = \text{constant}, \tag{2.32}$$

where $-1 \leq \delta \leq 1$, corresponding to non-integer numbers of majority- and minority-spin electrons.[7] Violation of Eq. (2.32) results in SCE.[101,102] The combination of the piecewise linearity and constancy conditions of Eqs. (2.31) and (2.32) amount to the flat-plane condition.[103–105] An important distinction to make is that even though, in closed shell systems for example, the total spin vanishes, the error in the energy functional concerned with the spin degree of freedom does not.

Some articles have found tentative associations between SCE and the Hund's coupling parameter J.[106–108] Based on recent investigations into the suitability of Hubbard model-based functionals in correcting SIE and SCE, when applied to s-orbitals including terms proportional to a positive-valued first-principles Hund's J, do not succeed in correcting for SCE and may even increase the magnitude of SCE.[103] We discuss this further in Section 2.5.

Another spin-related phenomenon arises from the spin-unrestricted KS formalism, where the non-interacting Hamiltonian does not commute with $\hat{\mathbf{S}}^2$. The expectation value of $\hat{\mathbf{S}}^2$ is approximated by[7,109,110]

$$\langle \hat{\mathbf{S}}^2 \rangle = M_s \left(M_s + 1 \right) \hbar^2 + \hbar^2 \left[n^{\downarrow} - \sum_i^{n_\uparrow} \sum_j^{n_\downarrow} \left| \int \psi_i^{\uparrow}(\mathbf{r}) \psi_j^{\downarrow}(\mathbf{r}) \, d\mathbf{r} \right|^2 \right], \tag{2.33}$$

the last term of which finds the number of doubly occupied orbitals. In a spin-unrestricted formalism, where the majority- and minority-spin orbitals do not necessarily overlap, the bracketed term of Eq. (2.33) only partially cancels, resulting in a larger-than-expected expectation value. This deviation is called spin contamination, a phenomenon often cited as a reason to avoid spin-unrestricted electronic structure calculations.[7,110,111]

The current dissertative works do not seek to address spin contamination, focusing instead on rectification of SIE and SCE. We discuss protocol to achieve these aims in Section 2.5.

2.5 The DFT+U+J method

The pursuit of accuracy in DFT-based modeling of materials—particularly those whose technological capacities are characterized by the strongly correlated physics happening on a microscopic scale, like high-performance batteries,[10–14,112–118] heterogeneous catalysts,[15,16,119] and next-generation photovoltaics,[17–19,120–129] to name a few—has recently motivated the systematic consideration of SIE and SCE as described in described in Section 2.4, and with it possible corrective protocols.[82–84]

Many methods may be interpreted as addressing SIE and/or SCE, among them Self-Interaction-Corrected (SIC) DFT,[65] the use of exact exchange or hybrid functionals,[130] dynamical mean-field theory (DMFT),[131,132] and reduced density matrix functional theory.[133]

Among the more computationally inexpensive techniques often interpreted as addressing SIE and SCE, however, are the Hubbard-like corrective functionals, which fall under the DFT+U umbrella.[98–100,134–136] Inspired by (but nowadays bearing little resemblance to) the Hubbard model,[137] DFT+U[§] and related corrective methodologies (e.g., DFT+U, DFT+(U−J), DFT+U+V) offer efficient treatment of SIE and delocalization error in well-localized electronic states while minimizing additional computational expense.[106,138–142] The central concept of these methods is to exactly counter the net-overestimated Coulombic interactions by penalizing orbitals occupied by non-integer numbers of electrons, specifically in highly localized subspaces where the spurious curvature of energy is particularly pronounced. These penalties are enforced self-consistently with the application of a corrective term, added to the total energy to reinstate piecewise linearity of Eq. (2.31). The total energy in DFT+U is defined as

$$E_{\mathrm{DFT+U}}[\rho(\mathbf{r})] = E_{\mathrm{DFA}}[\rho(\mathbf{r})] + \sum_{\mathbb{i}} \underbrace{E_{\mathrm{Hub}}[\{n^{\mathbb{i}\sigma}_{mm'}\}] - E_{\mathrm{dc}}[\{n^{\mathbb{i}\sigma}\}]}_{E_{\mathrm{U}}[\{n^{\mathbb{i}\sigma}_{mm'}\}]} \tag{2.34}$$

where $\rho(\mathbf{r})$ is the density, $E_{\mathrm{DFT}}[\rho(\mathbf{r})]$ is the total energy of the DFA (LDA, LSDA, GGA, etc.) to which is added the E_{U} corrective terms for all subspaces $\mathbb{i} = \{a, n, \ell\}$ (pertaining to orbital $n\ell$ on atom a) to undergo treatment. The original derivations of DFT+U considered the energy E_{Hub}, itself a functional of the projected KS occupancy matrices $\{n^{\mathbb{i}\sigma}_{mm'}\}$ (discussed further in Chapter 4.3) for the localized subspaces we want to treat for SIE, associated with the Hubbard model and a single-determinant assumption for the wavefunction, together with a double-counting term E_{dc} subtracting those energetic components that may be already included in the underlying Hartree and XC energy. The double-counting correction is usually considered to be dependent solely on the total electron

[§]The consensed terminology of this method is misleading in that it implies a correction is being made to DFT—in and of itself a comprehensive theory—not the underlying XC approximations to DFT. Some in the literature prefer to name these methods according to the DFA being corrected, e.g., LSDA+U, GGA+U. Here, we use DFT+U to refer generally to any Hubbard-like corrective protocol including the Hubbard U. We use DFT+U+J to refer to the subset of DFT+U methods that incorporate the Hund's J, although, this definition changes in our scientific investigations to account for other literature conventions; notably, DFT+U+J has been used to refer, on separate occasions, to two specific common Hubbard functionals—the Liechtenstein and the Himmetoglu (*vide infra*). Where possible, we distinguish between the two by name (i.e., the Liechtenstein DFT+U+J) and, failing that for purposes of brevity, make it clear now that in Parts II and III, DFT+U+J will refer to the Liechtenstein functional, and in Part IV, DFT+U+J refers to the Himmetoglu DFT+U+J functional. Another way to distinguish them is through the electronic structure codes that implement these functionals. ABINIT implements the Liechtenstein DFT+U+J functional. ONETEP implements the Himmetoglu DFT+U+J functional.

occupancy of each subspace and spin component. The exact form of E_{dc} is not precisely known. Primarily two formulations of E_{dc} remain relevant today: (i) the Full Localized Limit formulation proposed by Anisimov *et al.*,[98,143] which, in simulating a reference system that assumes the diagonal elements of the diagonalized occupancy matrix are integers, takes on the form

$$E_{\text{dc}} = \frac{U}{2} N\left(N-1\right) - \frac{J}{2} \sum_{\sigma} n^{\sigma}\left(n^{\sigma}-1\right) ; \tag{2.35}$$

and (ii) the Around Mean-Field double-counting expression, found in Eq. (7) of Ref. [144]. In modernity, it is conventional to operate using option (i), also called sometimes the atomic limit.[134]

The efficacy of Hubbard corrective techniques depends on the underlying XC functional as well as the appropriate prescription of the accompanying constants, the Hubbard U and the intra-atomic exchange-coupling J[§] (simply denoted J in the literature, but sometimes referred to as J_{H} here to avoid confusion with the Heisenberg exchange constants $\boldsymbol{J}_{ij}$).[106,138,140–142] We have periodically referred to the Hubbard U and Hund's J as the Hubbard parameters, a practice we will continue, particularly in Part II where we explore and discuss how to determine the U and J *ab initio*. As they often manifest analogously, in practice and in theory, we speak mainly of the Hubbard U and expect the reader to extend assertions made thereof to the Hund's J. Distinguishing properties will be mentioned explicitly.

Although all electronic subspaces are afflicted by SIE and SCE to some extent, not all are conventionally treated with Hubbard corrections; partitioning by subspace implies that pragmatic choices are being made. Only those with some occupancy matrix eigenvalues significantly deviating from integer values and/or spectral weight adjacent to the band-gap edges (i.e., *d* and *f* orbitals of TMs) have been hitherto prioritized for such treatment. However, the proliferation of DFT+U+J implementations across a variety of accessible platforms—and the increasing sophistication of software that facilitate Hubbard parameter calculation—have enabled widespread use of DFT+U+J protocol for any subspace in most systems. Topical questions arising from this context, and indeed questions this thesis hopes to answer in part, weigh the value of Hubbard corrections to non-conventional subspaces like *s* or *p* valence orbitals.

As the literature has progressively probed the limitations of DFT+U, a variety of Hubbard functionals have been proposed, including those that incorporate exchange considerations via the Hund's coupling J. Which Hubbard functional is also a topical inquiry in the literature, one addressed from a pragmatic rather than theoretical point of view by the investigations in Parts III and IV of this dissertation. To this end, we introduce in Sections 2.5.1-2.5.3 a series of common Hubbard-like functionals that are easily, if not already completely, implemented across a variety of open-sourced electronic structure platforms. A fourth, state-of-the-art Hubbard functional, BLOR,[103] does not feature directly in our investigations but is nonetheless topical to mention; BLOR is described in Appendix A4.

[§]It is worth noting that the J parameter computed and employed here pertains, as defined, only to the spin population present in collinear-spin DFT. It is elsewhere sometimes termed the Hund's coupling strength because it is affiliated with Hund's coupling-related exchange splitting that manifests in collinear-spin DFT. Strictly speaking, however, to measure that mechanism's strength, one would look instead at the energy pre-factor of the effective interaction of the form $\mathbf{S}\cdot\mathbf{S}$; this for vector spin $\mathbf{S}$, either on a per-spatial-orbital or per-atomic-subspace basis, depending on the preferred definition as opposed to its *z*-axis projection S_z.

2.5.1 The Liechtenstein DFT+U+J functional

As originally proposed by Ref. [98], DFT+U was not rotationally invariant (dependent on the basis used). A rotationally invariant alternative, which we reference here as the Liechtenstein DFT+U+J, was proposed Liechtenstein *et al.*[143] We write this Hubbard functional in the following manner,

$$E_{\text{Hub}}[\{n^{\mathbb{i}\sigma}_{mm'}\}] = \frac{1}{2}\sum_{\sigma,m}[\langle m,m''|V_{ee}|m',m'''\rangle n^{\mathbb{i}\sigma}_{mm'}n^{\mathbb{i}\bar{\sigma}}_{m''m'''} + \left(\langle m,m''|V_{ee}|m',m'''\rangle - \langle m,m''|V_{ee}|m''',m'\rangle\right) n^{\mathbb{i}\sigma}_{mm'}n^{\mathbb{i}\sigma}_{m''m'''}], \tag{2.36}$$

where V_{ee} is the screened Coulomb interaction between $n\ell$ electrons, and the electron–electron interactions are expressed as integrals of the Coulomb operator operating on the basis-set wavefunctions for each m, i.e.,

$$\langle m,m''|V_{ee}|m',m'''\rangle = \iint \psi^*_{\ell m}(\mathbf{r})\psi_{\ell m'}(\mathbf{r})\,\frac{1}{|\mathbf{r}-\mathbf{r}'|}\,\psi^*_{\ell m''}(\mathbf{r}')\psi_{\ell m'''}(\mathbf{r}')\;d\mathbf{r}d\mathbf{r}'\,. \tag{2.37}$$

If the basis consists of localized atomic orbitals, one may expand the Coulomb kernel in terms of the spherical harmonics, rendering these integrals the product of radial contributions and angular functions.[145] The latter may then be written in terms of products of Clebsch-Gordan coefficients and the former in terms of Slater integrals of the radially symmetric hydrogen-like atomic orbitals $R_{nl}(r)$, written explicitly in Eq. (10.1) of Part V. Taking these simplifications alongside the double-counting term in Eq. (5.2), we can calculate the U and J as subspace-averaged Coulomb integrals, which we may find embedded in Eq. (2.36) through its algebraic reorganization. For more information, see Eqs. (8)-(12) of Ref. [136].

The Liechtenstein functional—the Hubbard term of which is described by Eq. (2.36) and from which a double-counting expression (either the Around Mean-Field or Full Localized Limit formulations available as options) is subtracted—is implemented in ABINIT. We test its capacity to correct spin-based energetics of NiO in Chapter 7. It is worth noting that for atomic s-orbitals, the Liechtenstein functional reduces to the Dudarev functional of Eq. (2.38) with $\mathrm{U}^{\mathbb{i}} = \mathrm{U}^{\mathbb{i}}_{\text{eff}}$.

2.5.2 The Dudarev DFT+U_{eff} functional

A time-tested rotationally invariant formulation of DFT+U is known as the Dudarev functional,[135,146]

$$E_{\mathrm{U}}[\{n^{\mathbb{i}\sigma}_{mm'}\}] = \sum_{\mathbb{i}\sigma}\frac{\mathrm{U}^{\mathbb{i}}_{\text{eff}}}{2}\mathrm{Tr}[\mathbf{n}^{\mathbb{i}\sigma}(1-\mathbf{n}^{\mathbb{i}\sigma})]. \tag{2.38}$$

This formulation of DFT+U demonstrates that the corrective term is a mathematical mechanism designed to penalize fractional occupancies of subspaces $\mathbb{i}$ for positive $\mathrm{U}^{\mathbb{i}}_{\text{eff}}$ values. When an eigenvalue of $\mathbf{n}^{\mathbb{i}\sigma}$ assumes an integer value, the corresponding contribution to E_{U} is zero. By contrast, when that eigenvalue is maximally fractionalized at $1/2$, the contribution to E_{U} is also maximized.

The effective parameter is $\mathrm{U}_{\text{eff}} = \mathrm{U} - \mathrm{J}$, where U is the spherically averaged on-site Coulomb repulsion (in other words, the Coulombic energy cost to place two electrons at the same site) and J

is the (also spherically averaged) intra-atomic Hund's coupling exchange parameter. The Hund's J is included in DFT+U implementations (DFT+U−J) as a mitigating coefficient weakening the strength of intra-site Coulombic repulsion to account for the effect of Hund's rules on spin and orbital polarization.[108,134] The degree of corrective power of the functional is determined by the magnitudes of U and J. It is argued that the neglect of the Hund's J can result in excessive correction. In the literature, U_{eff} and U are often referenced interchangeably depending on the consideration given to J.[147]

2.5.3 The Himmetoglu DFT+U+J functional

An extension of the DFT+U formalism proposed by Himmetoglu *et al.*[148] includes the Hund's J as a distinct correction to more accurately represent the interplay between electron localization and magnetic valence orbital character arising in strongly-correlated materials. In this form of DFT+U+J, which we call the Himmetoglu functional, the Hubbard correction is found to be

$$E_{\mathrm{U}}[\{n^{i\sigma}_{mm'}\}] = \sum_{i\sigma} \frac{\mathrm{U}^{i} - \mathrm{J}^{i}}{2} \mathrm{Tr}\left[\mathbf{n}^{i\sigma}\left(1 - \mathbf{n}^{i\sigma}\right)\right] + \sum_{i\sigma} \frac{\mathrm{J}^{i}}{2}\left(\mathrm{Tr}\left[\mathbf{n}^{i\sigma}\mathbf{n}^{i\bar{\sigma}}\right] - 2\delta^{\sigma\sigma_m} n^{i\sigma}\right), \tag{2.39}$$

where σ_m is the minority-spin index. Here, we see that the Hund's J terms function in two ways; (i) they mitigate the effect of U on the interactions between electrons with parallel spin, and (ii) they penalize the occupancy of anti-aligned spins on the same site. The final minority-spin term is often excluded from DFT+U+J implementations in practice.[148,149] Extensions of the Himmetoglu functional that addresses the flat-plane condition (discussed in Appendix A4) are called the judiciously-modified (jmDFT) and BLOR functionals, introduced, respectively, by Bajaj *et al.*,[150,151] and Burgess *et al.*[103]

Chapter 3

Practical implementations of KS DFT

J.A.R.V.I.S, the fictional Artificial Intelligence (AI) assistant to Tony Stark in the Marvel Cinematic Universe, romanticizes the West's vision for the future of materials discovery and design through simulation in this[§] Iron Man II scene.[152,153] Interactive holographic elements aside, J.A.R.V.I.S's calculations are at least two orders of magnitude faster than the real-world state-of-the-art, and they yield non-problematic, trustworthy results that translate seamlessly and promptly into world-saving gadgets.

The vision is not entirely a fiction. Even in the Marvel Universe, engineers have concluded that experimenting with material properties in a lab via trial and error (sometimes described as the Edisonian method) is both too expensive and too slow; we need materials simulations to guide our development of new technologies. And Tony and J.A.R.V.I.S have reached a realistic bottleneck, having simulated well over 400 of these materials with little to no success.

But the CGI understandably glosses over the nuts and bolts of the everyday electronic structure calculation. The last 30 years have witnessed the evolution of increasingly sophisticated KS DFT algorithms designed to facilitate the material demands of increasingly sophisticated human activity. Under the hood of these algorithms are theory, simplifications, patches, and accessories that go into making such materials simulations feasible in industry-relevant time-frames and suitable for modern computing capacities. We devote the following chapter to describing the most quintessential elements of these algorithms. In Section 3.1.1, we introduce the description of solids as infinitely repeating tessellations of unit cells, followed by a description of two methodologies for the

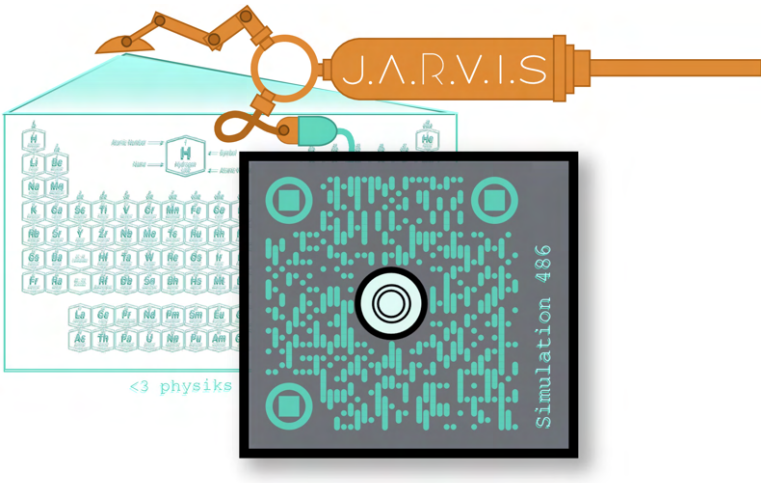

[§]To watch the scene, scan the QR code in the graphic, or look up "Extended scene: Tony and the periodic table, Iron Man 2" on YouTube. Or watch the movie.[152]

treatment of the ionic potentials—pseudopotentials in Section 3.1.3 and the projector-augmented wave (PAW) method in Section 3.1.4. These basics facilitate both the plane-wave and linear-scaling algorithmic implementations of KS DFT that we discuss in Sections 3.1.2 and 3.2, respectively.

3.1 Techniques to facilitate the simulation of material systems

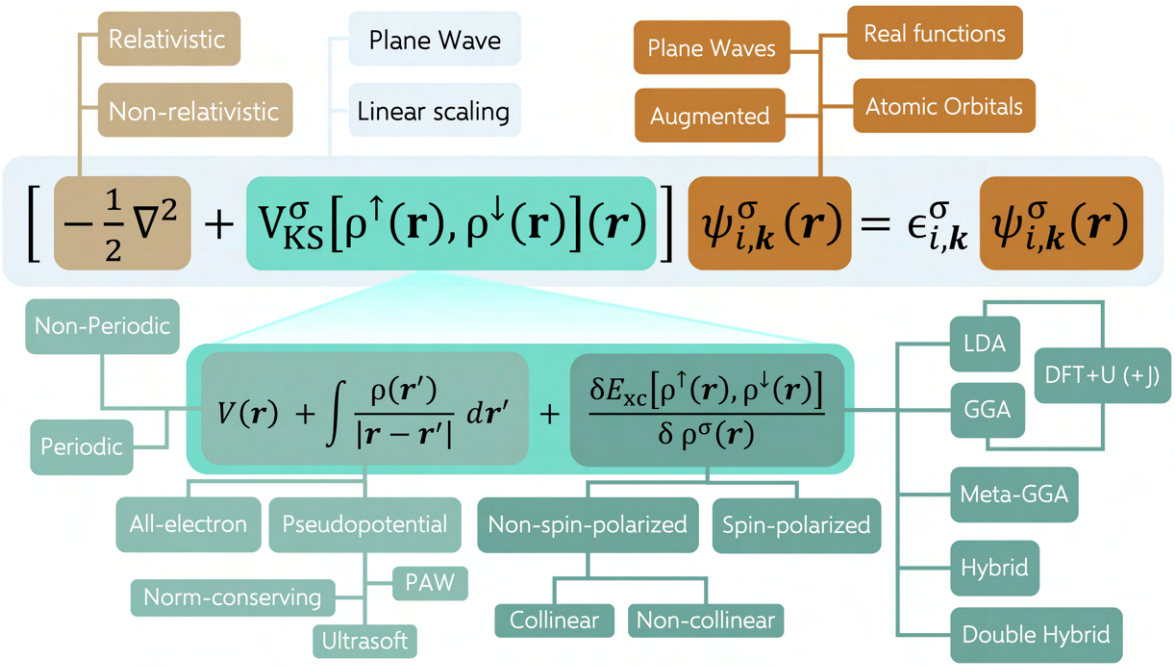

Figure 3.1: Some typical options available in standard DFT codes to both simplify and expand the reach of KS calculations. Adapted from a similar diagram by Deutsch et al. [154]

3.1.1 Cell-periodic descriptions of solids

There are many ways to organize atoms into materials. Molecules, for example, have finite lists of atomic coordinates. Solid materials, however, are atomic systems mapped onto lattices (called Bravais lattices [155]), with dimensions that approach infinity in one or more Cartesian directions. Pure solids without any defects (also called crystals), comprise an infinitely repeating isolatable configuration of atoms called a unit cell, a region of space delineated by the three lattice vectors $\{\mathbf{a}_1, \mathbf{a}_2, \mathbf{a}_3\}$.

Crystals have conventional unit cells, for example, boxes with lattice vectors parallel to the Cartesian axes that hold one or more complete atoms. A minimalist description of a crystal, however, requires a lattice constant—the distance between two adjacent lattice points along the lattice vectors—and the primitive unit cell, the smallest possible cell that still describes the coordination chemistry of the solid. Its three primitive unit vectors describe the slant of the rhombohedron relative to the standard Cartesian coordinate system.

Infinities, like those approached (from a microscopic point of view) by the dimensions of a solid, are difficult to deal with directly. The abstraction of reciprocal space—where distance is measured in

inverted spatial units—provides an avenue for representing the macroscopic properties of a solid in terms of more finite objects. In reciprocal space, a unit cell is delineated by inverted spatial vectors $\mathbf{b} = \left[\mathbf{b}_1, \mathbf{b}_2, \mathbf{b}_3\right]^\top = \left[2\pi/\mathbf{a}_1, 2\pi/\mathbf{a}_2, 2\pi/\mathbf{a}_3\right]^\top$, where $\mathbf{a}_j \cdot \mathbf{b}_l = 2\pi\delta_{jl}$ with $j, l \in \{1, 2, 3\}$.

We can flip between real and reciprocal space using a Fourier Transform (FT), a useful tool built to convert functions in real space into continuous, infinite superpositions of sinusoidal functions with varying frequency distributions. Mathematically, the FT is defined in three dimensions for a continuous, piecewise, smooth, and integrable function $f\colon \mathbb{R} \to \mathbb{C}$ as

$$\mathcal{F}(\mathbf{k}) = (2\pi)^{\frac{-3}{2}} \int_{-\infty}^{\infty} f(\mathbf{r}) e^{-i\mathbf{k}\cdot\mathbf{r}} d\mathbf{r}, \tag{3.1}$$

which maps the function onto the frequency domain with coordinates $\mathbf{k}$ with units of inverse distance (here, $i = \sqrt{-1}$ is the imaginary unit). The function $\mathcal{F}(\mathbf{k})$ has many advantageous properties.[§] Notably, there is a relationship between the periodicity of a function, like the electronic wavefunction or its observables, and the wave vector $\mathbf{k}$, also known as the crystal momentum vector.

Consider, for example a periodic solid described by primitive lattice vectors $\{\mathbf{a}_1, \mathbf{a}_2, \mathbf{a}_3\}$, the unit cell of which is repeated $X = X_1X_2X_3$ (X_j times in the $\mathbf{a}_j$ direction). In the early 20th century, the Bloch theorem[157] showed that location $\mathbf{r}$ in the unit cell will be subject to the same potential and have the same wavefunction properties as location $\mathbf{r} + \mathbf{R}$, where $\mathbf{R} = \sum_j^3 x_j \mathbf{a}_j$ is a translation incurred $x_j \in \mathbb{Z}$ times in the $\mathbf{a}_j$ direction. In other words, a Bloch state of the form $\psi_\mathbf{k}(\mathbf{r}) = u(\mathbf{r})\, e^{i\mathbf{k}\cdot\mathbf{r}}$ will require that any periodic function defined on the primitive unit cell must satisfy $u(\mathbf{r}) = u(\mathbf{r} + \mathbf{R})$. By consequence, the following can be proved.

$$\psi_\mathbf{k}(\mathbf{r} + \mathbf{R}) = e^{i\mathbf{k}\cdot\mathbf{R}} \psi_\mathbf{k}(\mathbf{r}). \tag{3.2}$$

Relatedly, Ref. [158] showed that the same solid is subject to the following boundary conditions.

$$\psi_\mathbf{k}(\mathbf{r}) = \psi_\mathbf{k}(\mathbf{r} + X_1\mathbf{a}_1 + X_2\mathbf{a}_2 + X_3\mathbf{a}_3) \tag{3.3}$$

Reconciling Eqs. (3.2) and (3.3) requires $e^{i\mathbf{k}\cdot(X_1\mathbf{a}_1 + X_2\mathbf{a}_2 + X_3\mathbf{a}_3)} = 1$. Thus, for an integer $q \in \mathbb{Z}$,

$$\sum_j^3 X_j\, \mathbf{k}\cdot\mathbf{a}_j = 2\pi q \quad \Longrightarrow \quad \mathbf{k} = \sum_j^3 \frac{q}{X_j} \mathbf{b}_j\,. \tag{3.4}$$

Remarkably, by extension of Eq. (3.2), we can show that wavefunctions translated by integer multiples of reciprocal lattice vectors—as we define to be the case for a wave vector $\mathbf{G}$, for which $\frac{q}{X_j} \in \mathbb{Z}$ in Eq. (3.4)—are equal modulo $\mathbf{G}$. This means that all eigenstates parametrized by wave vectors $\mathbf{k}$ corresponding to $\frac{q}{X_j} > 1$ are redundant, mirror images of those with $\frac{q}{X_j} \geq 1$, which lie inside what is called the first Brillouin zone (BZ).[159] All properties of the infinite solid are therefore confined to finite $\mathbf{k}$ space, where we may accordingly train our focus.

[§]Chief among them, for example, the capacity to elegantly convert inhomogeneous partial differential equations in the real domain into algebraic relations in reciprocal space. The 2020 study in Ref. [156] takes advantage of this property to approximate a fictitious magnetic charge density.

The number of **k** vectors in the first BZ, however, scales with the number of unit cells, which approaches infinitely in the bulk limit, rendering a tightly packed **k** space impossible to resolve analytically. But since the functions there are typically well-behaved and smoothly varying, it is acceptable to approximate them by sampling the first BZ with degrees of finesse tailorable to hardware constraints (noting that finer k-point resolutions will reduce interpolation errors).[160–162] The BZ sampling scheme we use for these dissertative investigations is that of Monkhorst and Pack,[162] consisting of an evenly spaced sampling lattice generated by spreading $\mathbf{x_j} \in \mathbb{Z}$ points along the $\mathbf{a}_j$ lattice vector. Encouragingly, however, the larger the supercell simulated explicitly, the less sampling needed; for large enough supercells, only one k-point is needed: the Γ-point where $\mathbf{k} = 0$.

Most, if not all, DFT programs are built to facilitate Bloch states, which do not represent well aperiodic materials like molecules or defective crystals. These systems are simulatable all-the-same by maximally separating the initialized atoms from their periodic images, either with vacuum or pure crystal and sampling only the Γ-point. Additionally, DFT programs often have in-built fast Fourier transform (FFT) algorithms, of which there are many variations,[163–169] to calculate the discretized version of Eq. (3.1).

3.1.2 Plane-wave basis set

The choice of basis with which the electronic wavefunction is constructed is a practical way to classify quantum chemistry programs. Many programs, like PySCF,[170,171] ORCA,[172] or Gaussian 16[173] deconstruct the wavefunction into a series of Gaussian orbitals. In Section 3.2, we will introduce ONETEP,[174] a linear-scaling algorithm that uses non-generalized Wannier functions (NGWFs).

Alternatively, we can use plane waves to express the KS wavefunctions as a natural extension of the Bloch theorem. Popular codes that use plane-wave basis functions include QUANTUM ESPRESSO,[175,176] ABINIT,[177–179] VASP,[180] and WIEN2k.[181]

Scalar plane waves are characterized by wave fronts parallel to flat planes that are azimuthally symmetric about the direction of propagation. They take the same form as the Bloch states, i.e., they

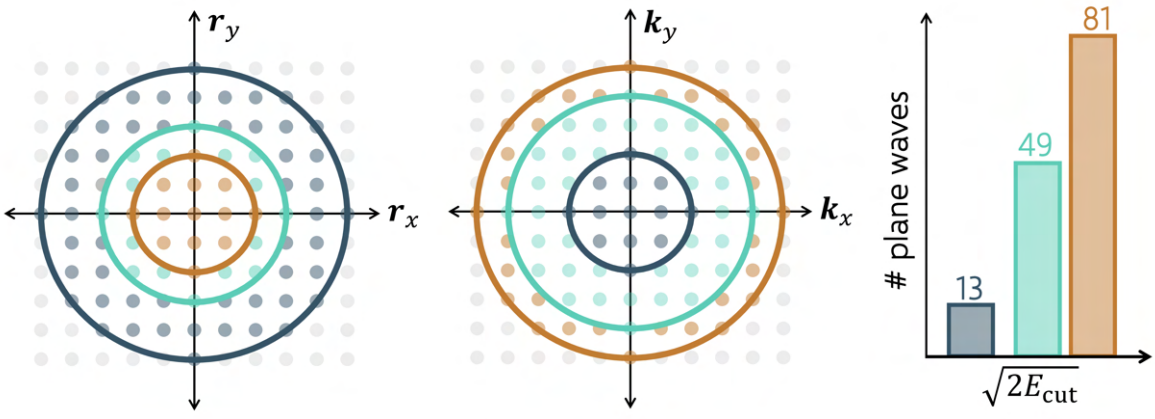

Figure 3.2: Schematic demonstrating how the number of plane waves relates to the atomic lattice [left], the corresponding reciprocal lattice [center], and the value of E_{cut} [right].

are proportional to $e^{i\mathbf{k}\cdot\mathbf{r}}$ and extend infinitely spatially. Expressing the KS wavefunction with wavevector $\mathbf{k}$ in terms of a plane-wave basis yields

$$\psi_{\mathbf{k}}(\mathbf{r}) = \frac{1}{\sqrt{\Omega}} \sum_{\mathbf{G}} u_{\mathbf{k}}(\mathbf{G}) e^{i(\mathbf{k}+\mathbf{G})\cdot\mathbf{r}}, \tag{3.5}$$

where $\Omega = |\mathbf{a}_1 \cdot \mathbf{a}_2 \times \mathbf{a}_3|$ is the volume of the cell and $\mathbf{G}$ are the reciprocal lattice vectors satisfying $\mathbf{G} \cdot \mathbf{R} = 2\pi q$ with $q \in \mathbb{Z}$. All periodic functions in the primitive unit cell can thus be described as a linear combination of the basis vectors $\{\mathbf{G}\}$ through the FT in Eq. (3.1). For example, it can be derived that the kinetic energy of a plane wave is inversely proportional to the square of the lattice constant and thus proportional to $(\mathbf{k}+\mathbf{G})^2$; the closer it is to the nucleus, the higher the kinetic energy. Relatedly, the periodic coefficients $u_{\mathbf{k}}(\mathbf{G})$ of Eq. (3.5) are found to be

$$u_{\mathbf{k}}(\mathbf{G}) = \frac{1}{\sqrt{\Omega}} \int_{\Omega} u_{\mathbf{k}}(\mathbf{r})\, e^{-i\mathbf{G}\cdot\mathbf{r}}\, d\mathbf{r}. \tag{3.6}$$

The coefficients $u_{\mathbf{k}}(\mathbf{G})$ for the lowest eigenvectors of the valence state attenuate as the kinetic energy decreases. It is often more computationally feasible to truncate the infinite sum over basis vectors $\{\mathbf{G}\}$ such that those we use satisfy

$$\frac{1}{2}(\mathbf{k}+\mathbf{G})^2 < E_{\text{cut}}, \tag{3.7}$$

where E_{cut} is a cutoff energy predefined by the user, made smaller for less accuracy (less plane waves to represent the KS wavefunction) or larger for more accuracy. The number of plane waves as a function of E_{cut} is not continuous, but rather a discontinuous function of lattice parameter at fixed energy, as demonstrated in Fig. 3.2.

In order to accommodate large numbers of plane waves, DFT programs will usually realize both real space functions and their reciprocals, switching between the two frequently with FFT algorithms. FFT algorithms scale by $\omega\log(\omega)$, where ω is the number of plane waves. This scaling remains prohibitively expensive for simulating most relevant periodic solids. DFT practitioners thus use further approximations to limit the number of KS orbitals and plane waves, namely, pseudopotentials.

3.1.3 Pseudopotentials for simplified ionic potentials

The core KS wavefunctions of atoms are localized in the vicinity of the nucleus to which they are bound. In order to maintain orthogonality to those core orbitals, the valence KS wavefunctions are encumbered by tight, wrinkly oscillations near the nucleus.[59,182,183] Precisely simulating this regime, within DFT or other wavefunction-based methods, requires very high resolution and sometimes inaccessibly high computational power. Materials scientists, however, are less interested in an atom's core electrons, which, as a result of their proximity to the positively charged nucleus, do not shift dramatically with changes in the atom's chemical environment. The valence electrons, by contrast, are the major contributors to bonding, atomic magnetization, ionizations, hybridizations, conductivity, and other electronic structure phenomena that cumulatively award molecules and materials their properties. Accurate simulation of valence electrons and their wavefunctions beyond the core region

is usually less computationally demanding than inside the core region.

The pseudopotential technique emerged as early as the 1930s to address these observations and simplify the numerical treatment of the atomic core.[184–186] The method bypasses explicit treatment of the core states by considering them as screens to and thus indistinct from the nuclear potential. Indeed, Refs. [184] and [187] show that a pseudo-valence wavefunction will—upon subjection to the electronic wavefunction equation of a non-local (nl) potential modeled by

$$V_{\text{nl}} = \sum_{i}^{\#\text{ core states}} (E - E_i)|\psi_i\rangle\langle\psi_i|, \tag{3.8}$$

where ψ_i are the core states and E_i their corresponding eigenenergies—yield the same eigenvalues E as the original wavefunction. V_{nl} is hence more weakly repulsive than the standard nuclear potential.

To generate a pseudopotential, the energies and core states of Eq. (3.8), considered by-and-large chemically inert, are typically calculated for an isolated atom. "In the wild," though, the core states do respond to changes in chemical environment,[188] and so the use of an isolated atom as a reference contributes to performance failures. The art of making pseudopotentials is largely tied to minimization of these transferability errors.

A popular type of pseudopotential is the Norm-Conserving Pseudopotential (NCPP), which not only requires that the original and pseudo-wavefunctions be identical beyond a pre-defined core radius, but that the norm of these functions is the same. These requirements were added to reproduce the scattering properties of the potential.[189,190] Ultrasoft pseudopotentials[191] relax these constraints in a manner similar to the operations of the PAW method, to which we dedicate the coming sections.

3.1.4 The projector-augmented wave method

Most relevant to the investigations comprising this dissertation (Parts II-IV) is the projector-augmented wave (PAW) method, introduced by Peter Blöchl in 1994 and built on previous work in the augmented-wave methods and ultrasoft pseudopotentials.[191] The relevant details of the PAW formalism, the construction of PAW datasets, PAW pseudopotentials are summarized in the following subsections. A minute but relevant correction to the PAW formalism, the compensation charge density, is discussed in Appendix A5. We refer readers to Ref. [192] for a more comprehensive dive into the theory.

PAW Formalism

The PAW formalism starts by positing that there exists a true, full all-electron (AE) wavefunction Ψ—a Slater determinant of one-electron KS orbitals tightly oscillating in magnitude about each atomic nucleus—that can be linked to a well-behaved pseudized (PS) wavefunction $\tilde{\Psi}$ with few or no oscillations by a linear transformation $\hat{\tau}$,

$$\Psi = \hat{\tau}\tilde{\Psi}. \tag{3.9}$$

With this postulate in hand, we can derive physical quantities using the expectation value of an operator A[§] by sandwiching it between the transformation operator $\hat{\tau}$ and its Hermitian conjugate $\hat{\tau}^\dagger$

[§]We typically represent operators using $\hat{\bigcirc}$; however, in the PAW context, the $\hat{\bigcirc}$ interferes with the conventional use of

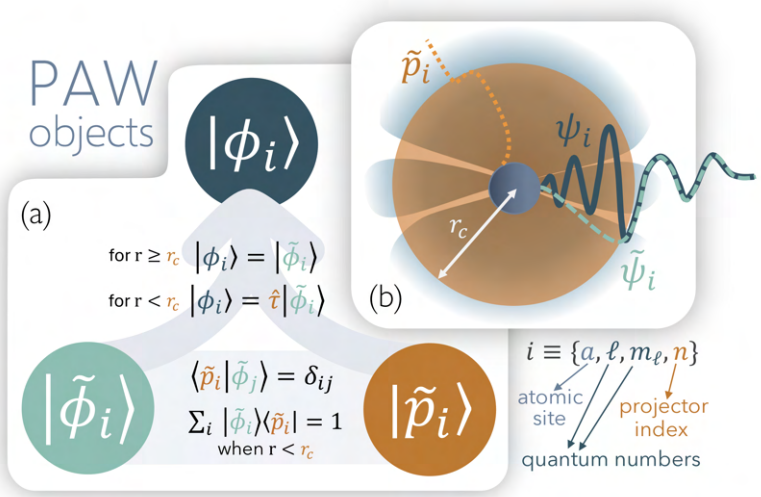

Figure 3.3: (a) Schematic outlining the mathematical relationship between the three canonical bodies used to construct PAW datasets. (b) The atom-centered augmentation sphere, defined by projector $\tilde{p}_i$, where i refers to the set of four indices $\{a, \ell, m_\ell, n\}$ inside cutoff radius r_c. When $r > r_c$, the AE wavefunction ψ_i and the pseudo-wavefunction $\tilde{\psi}_i$ are equivalent.

to yield the operator's pseudized counterpart $\tilde{A}$. Accordingly, the variational principle for the total energy is found to be

$$\frac{\partial E\left[\hat{\tau}|\widetilde{\Psi}\rangle\right]}{\partial\langle\widetilde{\Psi}|} = \varepsilon\hat{\tau}^\dagger\hat{\tau}|\widetilde{\Psi}\rangle, \tag{3.10}$$

such that one may derive the pseudized equivalent of the KS equations. Now, instead of looking for the ground state in real space, one may seek the ground-state energy in an equivalent pseudospace.

A better-defined transformation operator $\hat{\tau}$ is necessary to pursue this method any further. As a prerequisite, $\hat{\tau}$ must modify the smooth, pseudo-valence wavefunction within a defined atomic region in order to yield the correct nodal structure for the AE wavefunction. This modification is only necessary in the regions closest to the atomic nuclei. We then tailor our treatment specifically to this atom-centered region, spherically symmetric about the nucleus, by defining a cutoff radius, inside which we consider only the smooth, pseudized representation of the AE wavefunction, and outside of which the AE and pseudo-wavefunctions are equivalent. Fig. 3.3(b) illustrates this concept.

In this way, we define the augmentation sphere: a spherically symmetric region of radius r_c centered around each atomic site of the system. Consider constructing a pseudized wavefunction for a particular orbital ψ with quantum numbers ℓ and m_ℓ on atom a. When $r < r_c$, we impose the constraint that $\tilde{\psi}$ is a well-behaved projection of the AE wavefunction ψ. Moreover, when $r > r_c$, $\tilde{\psi} = \psi$. To satisfy these requirements, the transformation operator $\hat{\tau}$ may be defined as an identity operator plus the sum of atomic orbital-based modifications,

$$\hat{\tau} = \mathbb{1} + \sum_i \left(|\phi_i\rangle - |\tilde{\phi}_i\rangle\right)\langle\tilde{p}_i|, \tag{3.11}$$

$\widetilde{\ }$ to represent pseudization. We have thus omitted the operator symbol in this context.

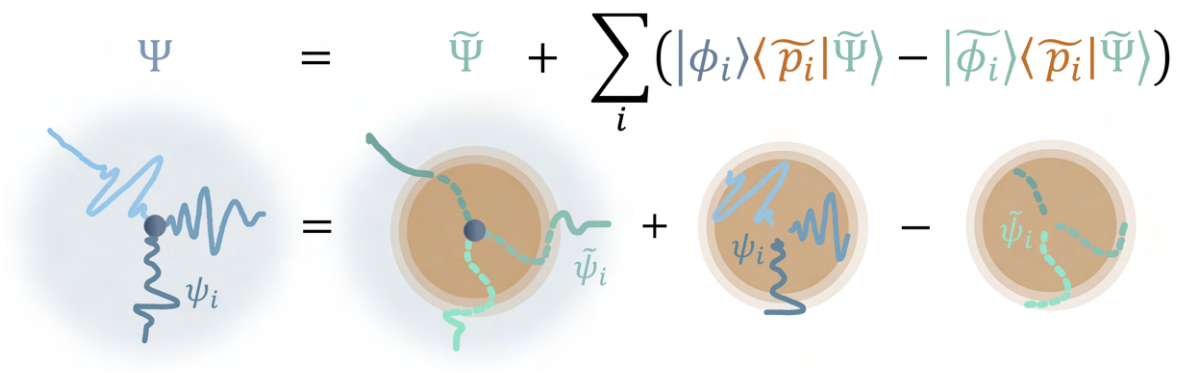

Figure 3.4: Schematic of the structure of the AE wavefunction in the PAW formalism. In this way, we can restrict our treatment of the cumbersome AE wavefunction (blue) to the interior of the augmentation sphere (orange).

where $\{\phi_i\}$ ($\{\widetilde{\phi}_i\}$) is the set of AE (pseudo-) partial-wave basis functions with which we define the AE (pseudo-) wavefunctions $\{\psi_i\}$ ($\{\tilde{\psi}_i\}$). Here, i refers to the set of four indices $\{a, \ell, m_\ell, n\}$, respectively representing the atomic site, angular quantum number, magnetic quantum number, and projector index. An AE partial wave ϕ_i may be defined in any way, although an organic choice would be a linear combination of the bound and scattering state solutions to the exact many-body wavefunction equation for an isolated atom. In a manner analogous to the wavefunctions they construct, the pseudo-partial waves $\{\widetilde{\phi}_i\}$ corresponding to a $\tilde{\psi}_i$ are well-behaved projections of $\{\phi_i\}$ when $r < r_c$ and identical to $\{\phi_i\}$ when $r \geq r_c$. The objects that allow us to restrict these projections to the pertinent regions of space are the projector functions $\{\tilde{p}_i\}$.

These are the three objects intrinsic to the PAW formalism (and those of any ultrasoft pseudopotential method, for that matter). Fig. 3.3(a) makes explicit the nature of the mathematical duality between these functions. Note the relation between the pseudo-partial waves and the projectors; they are dual to one another, and their projections are normalized inside the augmentation region.

We can represent the KS wavefunctions—which may, as described in Section 3.1.2, be approximated using plane waves (i.e., waves with wave fronts parallel to flat planes that are azimuthally symmetric about the direction of propagation)—by an infinite sum of spherically symmetric constituents called partial waves (i.e., waves with spherical wave fronts that propagate along a radius emanating from a central point). Such partial waves, also known as spherical waves, are the products of spherical Bessel functions and the spherical harmonics, which are, in turn, functions of angular momentum ℓ and azimuthal quantum number m_ℓ. In the PAW context, therefore, a partial wave refers to a wave that is spherically symmetric about an atom and a function of a given angular momentum ℓ.

Per Eq. (3.11), the atomic orbital based modifications that transform properties into their pseudo-space counterparts comprise the cumulative differences between (i) the projection of the AE partial wave on the augmentation region, and (ii) the pseudo-partial waves on the augmentation region. The transformation operator, when applied to the wavefunction, is illustrated in Fig. 3.4. Due to the structure of $\hat{\tau}$, objects such as the density and the energy are formulated analogously.

Construction of PAW datasets

The three PAW basis sets $\{\psi_i\}$, $\{\tilde{\psi}_i\}$, and $\{\tilde{p}_i\}$, are typically read into one's chosen electronic structure program from a file, called a PAW dataset, not so unlike a pseudopotential. Such datasets will typically include the following data for a specified atom.

1. r — Radial grid on which all ensuing functions are defined
2. $\{\psi_i\}$, $\{\tilde{\psi}_i\}$, and $\{\tilde{p}_i\}$ for all valence orbitals
3. n_c — AE core charge density
4. $\tilde{n}_c$ — PS core charge density
5. $\tilde{n}^1$ — PS valence charge density
6. $\tilde{v}_{\text{loc}}$ — A local ionic pseudopotential (see Section 3.1.4)
7. Information for the construction of $\hat{n}$, the compensation charge density (i.e., a shape function)

A variety of publicly available programs exist to generate these datasets, e.g., *atompaw*[193–195] or the Vanderbilt USPP code.[191] Generally, these algorithms begin by defining the AE partial waves as descriptors of all orbitals of the element under scrutiny. As mentioned earlier, the eigenfunctions of the solution to the KS wavefunction equation for the isolated atom are a good starting point; they are partial waves and thus comprise a sum of products—radial functions (typically of polynomial form, although other options are often implemented) multiplied by spherical harmonics. DFT calculations are performed using the XC potential V_{xc} of choice to obtain the AE basis functions defined on a radial grid of variable mesh density. For this reason, PAW datasets are categorized in terms of the associated XC functional (e.g., PAW-LDA, PAW-PBE). The *atompaw* algorithm, specifically, mandates that the partial waves be defined as the atomic eigenfunctions resulting from these calculations.

We assume here that the electronic states resulting from this calculation can be separated into core orbitals—to be "frozen" only in the sense that they are grouped with the nucleus and neither represented individually by PAW basis sets nor updated in the environment of the atom at each SCF iteration—and valence orbitals, which will be represented individually in the PAW basis.[195] In principle, the frozen core approximation that inspired this treatment would necessitate the core electron density remain unchanged from that of the relaxed isolated atom despite immersion in different environmental potentials and configurations. By drawing more or less orbitals out of the core and into the valence, the accuracy of this frozen core approximation may be tailored to the system at hand. The number of PAW basis functions used to describe these valence orbitals follows from this decision.

In practice, however, DFT programs adopt a soft-core scheme to restore the core electrons' involvement in and response to the physics of the system. A pseudo-density representing the nucleus and core electrons, called $\tilde{n}_{\text{Zc}}$, is used to generate its namesake share of the Hartree potential, and a soft-core density $\tilde{n}_c$ contributes to calculations of any non-linear core corrections.[196] Additionally, a compensation charge density $\hat{n}$, described further in Appendix A5, is introduced to restore the correct

multipole moments of the AE charge density $n^1 + n_{Zc}$, evaluated on a radial grid exclusively inside the augmentation region.[197]

Often, only one or two partial waves are necessary to accurately describe a valence orbital's radial component for a given angular momentum as the partial-wave expansion of orbitals rapidly converges. At least one partial wave constructing a PS plane wave represents a bound electronic state of the atom.

The pseudo-partial waves and the associated projectors are then constructed from one of many pseudization schema designed to ensure that these bodies fulfill the requisites established earlier in this section. The PS partial waves are solutions to the PAW Hamiltonian, which features a screened, pseudized local potential that is equal to the AE atomic potential outside of a specified radius r_{pp}. One option for the pseudization scheme is that of Blöchl, in which the pseudized basis functions are solutions to the non-relativistic many-body eigenvalue equation of an isolated atom immersed in a pseudopotential defined for each AE partial wave. In other words, the projector functions are chosen first, and then the PS basis functions are derived.[194] This procedure is described more in Section VI B of Ref. [192]. Yet another option involves the RRKJ optimization scheme,[198] which represents the PS wavefunction as a sum of two Bessel functions.

The pseudization scheme with which we are most concerned, for reasons that will be made known in Chapter 7, is the so-called Vanderbilt[191] scheme implemented in *atompaw*. Via this scheme, the pseudo-wavefunctions are eighth-degree polynomials inside the augmentation region,

$$\tilde{\psi}_i(r) = r^{\ell+1} \sum_{k=0}^{4} c_k r^{2k}, \tag{3.12}$$

from which the basis and projector functions are deduced by fitting the five coefficients c_k such that $\tilde{\phi}_i = \phi_i$ in the vicinity of r_c. The Vanderbilt scheme thus ensures that (a) $\tilde{\psi}_i(r)$ is an eigenfunction of the atomic PAW Hamiltonian; and (b) the $\tilde{\psi}_i(r)$ satisfies the generalized norm-conserving condition $Q_{ij} = 0$, where

$$Q_{ij} = \int_{r<r_{\text{c},i}} \left[\phi_i^*(\mathbf{r})\,\phi_j(\mathbf{r}) - \widetilde{\phi}_i^*(\mathbf{r})\,\widetilde{\phi}_j(\mathbf{r})\right] d\mathbf{r}, \tag{3.13}$$

and j represents a set of quantum numbers $\{a, \ell, m_\ell, n\}$ distinct from that of i. The integrand of Eq. (3.13) is known as the pseudized augmentation function between two partial waves i and j. For more details on this scheme, we refer the reader to Refs. [191] and [194].

Following the pseudization process, the pseudo-basis functions and their accompanying projectors are orthogonalized according to a chosen orthogonalization scheme, such as the Gram-Schmidt scheme or that proposed by Vanderbilt (also published in Ref. [191]).

With the AE basis functions, pseudo-basis functions, and projector functions defined, PAW dataset generators output their values on a radial grid in the form of a pseudopotential in an increasing number of formats compatible with popular electronic structure theory programs. Predefined, open-source, and tested PAW datasets for many elements can be acquired from, for example, the *atompaw* or PseudoDojo[195,199] websites, among others.

The PAW pseudopotential

PAW dataset generators construct a local ionic pseudopotential using the chosen PAW basis functions via a method that is closely analogous to Vanderbilt's ultrasoft pseudopotential generation, described in Ref. [191]. Here, we briefly describe the construction of a PAW pseudopotential from pre-established basis functions.[196,197]

The first step is to construct a screened local atomic pseudopotential $\tilde{V}_{\text{loc}}$ for an atom in some reference configuration (usually the isolated atom), which is to be equivalent to the AE atomic potential V_{loc} beyond some radius r_{pp}. (The cutoff radius r_{c} is not necessarily the same as r_{pp}.) As an example of such a construction, Vanderbilt proposed the use of a zero-order spherical Bessel function (Eq. (58) in Ref. [191]).

The pseudopotential $\tilde{V}_{\text{loc}}$ comprises contributions from both the core and valence densities. To expand the contribution of the latter, we take the pseudo-partial waves—which have been defined such that outside of the cutoff radius r_{c} they are equivalent to the AE basis functions—and use them to generate a different set of functions χ_i via

$$|\chi_i\rangle = (\epsilon_i - \hat{T} - \tilde{V}_{\text{loc}}(r))|\tilde{\phi}_i\rangle \,, \tag{3.14}$$

where ϵ_i are the orbital energy eigenvalues associated with the AE basis functions, and $\hat{T}$ is the kinetic energy operator. The projectors $\tilde{p}_i$ are then represented in terms of χ_i,

$$|\tilde{p}_i\rangle = \sum_j |\chi_i\rangle P^{-1}_{ij} \,, \tag{3.15}$$

whereupon, owing to the orthogonality condition $\langle\tilde{p}_i|\tilde{\phi}_i\rangle = \delta_{ij}$,

$$P_{ij} = \langle\tilde{\phi}_i|\chi_i\rangle. \tag{3.16}$$

We take the operator P_{ij} and employ it in the definition of a non-local potential $D_{ij} = P_{ij} + \epsilon_j Q_{ij}$, where Q_{ij} is as defined in Eq. (3.13). In a final step, we effectively unscreen the potentials D_{ij} and $\tilde{V}_{\text{loc}}$ to deduce a valence potential

$$D^0_{ij} = P_{ij} + \epsilon_j Q_{ij} - \int \tilde{V}_{\text{loc}}(r)\left(\phi^*_i(\mathbf{r})\,\phi_j(\mathbf{r}) - \tilde{\phi}^*_i(\mathbf{r})\,\tilde{\phi}_j(\mathbf{r})\right) d\mathbf{r} \tag{3.17}$$

and a local ionic pseudopotential

$$\tilde{V}_{\text{H}}[\tilde{n}_{Zc}] = \tilde{V}_{\text{loc}} - V_{\text{H}}[\tilde{n}^1 + \hat{n}] - V_{\text{xc}}[\tilde{n}^1 + \hat{n} + \tilde{n}_c], \tag{3.18}$$

where V_{H} and V_{xc} are the Hartree and XC potentials, respectively. Finally, the PAW pseudopotential representing the atom in its entirety is

$$V_{\text{PP}} = \tilde{V}_{\text{H}}[\tilde{n}_{Zc}] + \sum_{ij} D^0_{ij}|\widetilde{p}_i\rangle\langle\widetilde{p}_j|. \tag{3.19}$$

3.1.5 Diagonalization schema and SCF convergence

Even wielding physical considerations to limit the size of the plane-wave basis as much as theoretically possible, diagonalizing the matrix for various system properties (like the density, the wavefunction, or the Hamiltonian) across that basis, an endeavor undertaken at least once per SCF iteration, remains a bottleneck in DFT algorithms.

Propitiously, efficient diagonalization schema are ever-topical subjects of linear algebra research. An elementary method, for example, is that of steepest descents.[200] The time-tested Davidson algorithm,[201] developed in 1975 specifically for the sparse, diagonally dominant Hamiltonians of the Configuration Interaction method, remains a favorite among DFT practitioners due to its parallelizability and speed. This algorithm iteratively diagonalizes a projection of the matrix onto the most relevant subspace, yielding the extremum eigenvalues. Briefly, it does this by searching the space of and accumulating increasingly successful orthogonal trial vectors.

Another option for diagonalization is the conjugate gradient (CG) algorithm, which has the advantageous feature of rendering unnecessary the storage of old trial vectors in order to ensure the orthogonality of new trial vectors. The demand on RAM and computation time are thus significantly reduced. We refer the reader to Refs. [202] and [203] for more details.

All these methods rely on a convergence threshold—necessarily predefined by the user in all DFT programs—for the function being diagonalized. Diagonalization schemes—implemented as an inner loop within each SCF iteration—are often coupled with preconditioning or mixing schemes designed to converge the outer SCF loop faster. The latter becomes relevant in Chapter 5, and so we refer the interested reader to Section 5.1.2 for more information.

3.2 Linear-scaling DFT algorithms[§]

Despite the facility introduced by approximations and simplifications of the formalism, KS DFT based on plane waves remains a computationally expensive method to execute on modern hardware, with the CPU hour and RAM demands scaling as $\mathcal{O}(N^3)$ and $\mathcal{O}(N^2)$, respectively, where N is the number of electrons. Even as high performance computing centers become bigger and more sophisticated, FFT algorithms remain a bottleneck in the parallelalizability of these programs because they require instantaneous communication throughout all processors to maintain the orthogonality of the KS states. In practice, these constraints limit simulation to moderately sized systems: molecules, small nanoclusters, or ideal periodic solids with few atoms in the periodic cell.

An alternative approach, employed heavily in the following investigations, is the linear-scaling DFT algorithm. As the name suggests, CPU time approaches linear scaling with large numbers of electrons, facilitating calculation of thousands, sometimes millions of atoms without sacrificing accuracy.[39,40] These implementations exploit the near-sightedness of quantum systems by constructing a spatially localized basis set. Examples of packages with linear-scaling DFT implementations include SIESTA,[204,205] CP2K,[206,207] ONETEP,[174] CONQUEST,[208,209] BigDFT,[210] and OpenMX.[211]

[§]The explanations in the ensuing (sub)sections follow the dissertative work of O.K. Orhan, Ref. [58].

The sections that follow briefly describe, without loss of generality, the components and functionalities of the Order N Electronic Total Energy Package (ONETEP),[89,139,174,196,212–217] in particular the use of density matrices (Section 3.2.1), supporting and basis functions (Sections 3.2.2 and 3.26), and direct minimization protocol (Section 3.2.4).

3.2.1 Density matrices

A practical way to bypass the orthogonality constraint of the KS wavefunctions emerges when reformulating the problem in terms of density matrices, defined as

$$\rho(\mathbf{r},\mathbf{r}') = \sum_{i=1}^{N} f_i\, \psi_i(\mathbf{r})\psi_i^*(\mathbf{r}'), \tag{3.20}$$

for particular subspaces. Eq. (3.20) is powerful as its diagonal elements recover the electronic density (i.e., $n(\mathbf{r}) = \rho(\mathbf{r},\mathbf{r})$) if two conditions concerning its occupancies are met: (a) the number of particles is conserved, and (b) the wavefunctions obey the Pauli exclusion principle. Condition (a) requires $\mathrm{Tr}[\hat{\rho}] = N$. Condition (b), also called the idempotency condition, is expressed as $\hat{\rho}^2 = \hat{\rho}$, which necessarily means that

$$\rho(\mathbf{r},\mathbf{r}') = \int \rho(\mathbf{r},\mathbf{r}'')\,\rho(\mathbf{r}'',\mathbf{r}')\,d\mathbf{r}''. \tag{3.21}$$

The SCF nature of DFT can be reframed in terms of the density-matrix, and within this framework, one may avoid constructing the KS wavefunctions explicitly in each iteration. However, idempotency and particle conservation remain challenging constraints to satisfy efficiently. ONETEP employs a variety of techniques to make these constraints more feasible and to maintain the integrity of the density matrix as the energy is minimized self-consistently. Readers interested in the theory and implementation of these techniques may consult Ref. [213]. For more information on density matrix theory, see Refs. [218–221].

The density matrix for an insulating system can also be written as

$$\rho(\mathbf{r},\mathbf{r}') = \sum_{i=1}^{N}\sum_{\mathbf{R}} f_i\, w_{i,\mathbf{R}}(\mathbf{r})w_{i,\mathbf{R}}^*(\mathbf{r}'), \tag{3.22}$$

where $w_{i,\mathbf{R}}$ are Wannier functions,[222] spatially localized functions defined on simulation cells represented by vector $\mathbf{R}$ (the same as in Section 3.1.1). More mathematically, Wannier functions are Fourier transforms of the Bloch states in Eq. (3.2), defined over the first BZ as

$$w_{i,\mathbf{R}}(\mathbf{r}) = \frac{1}{\sqrt{V_{\mathrm{BZ}}}}\int e^{-i\mathbf{k}\cdot\mathbf{R}}\psi_{i,\mathbf{k}}(\mathbf{r})\,d\mathbf{k}. \tag{3.23}$$

For insulating systems, Wannier functions, and thus the density matrix elements of Eq. (3.22), fulfill spatial locality by decaying exponentially with distance from the origin.[223–225] All the same, for practical implementation, the Wannier functions may be truncated at a certain cutoff radius r_{cut}. Appropriate selection of r_{cut} permits the sparse construction of the density matrix and its corresponding Hamiltonian, which are then easily and efficiently diagonalized by linear-scaling algorithms.

It should be noted that non-insulating systems have **k**-dependent occupancies for KS wavefunctions near the Fermi level, and so Fourier transforms of the Bloch states are poorly defined.

3.2.2 The density kernel and basis functions

Recall from Section 3.1.2 that KS wavefunctions can be expressed in terms of a finite sum of basis functions subject to certain truncation conditions. Plane waves, while orthogonal, are not spatially localized enough to maintain linear-scaling diagonalization of the density matrix. Instead, a well-localized basis set can be constructed such that the density matrix is expressed as

$$\rho(\mathbf{r},\mathbf{r}') = \sum_{\alpha,\beta} \phi_\alpha(\mathbf{r}) K^{\alpha\beta} \phi^*_\beta(\mathbf{r}') \tag{3.24}$$

where $K^{\alpha\beta}$ is called the density kernel and $\{\phi_\alpha\}$ the support functions. The former is thus

$$K^{\alpha\beta} = \sum_i \langle \phi^\alpha \mid \psi_i \rangle f_i \langle \psi_i \mid \phi^\beta \rangle, \tag{3.25}$$

with $|\phi^\beta\rangle = |\phi^\alpha\rangle\langle\phi^\alpha \mid \phi^\beta\rangle$ and $\langle \psi_\alpha \mid \phi^\beta \rangle = \delta^\beta_\alpha$.[226–228] One may rewrite the total energy of the independent particle system and the particle number conservation requisite in terms of this basis set. We refer the reader to Ref. [227] for more information.

ONETEP uses non-orthogonalized generalized Wannier functions (NGWFs), real-valued functions that are spatially localized on atomic centers, as the support functions. The NGWFs are then expanded using an orthonormalized variational function set of what are called periodic cardinal sine (psinc) functions, discussed in the next section. This expansion enables smooth application of the density matrix formalism to periodic systems, equivalent to plane-wave implementations.

3.2.3 The periodic cardinal sine (psinc) basis

ONETEP uses periodic cardinal sine (psinc) functions—defined for a particular grid point x as

$$D_x(\mathbf{r}) = D(\mathbf{r}-\mathbf{r}_x) = \prod_i^3 \frac{1}{N_i} \sum_{p_i=-J_i}^{J_i} e^{ip_i \mathbf{b}_i \cdot (\mathbf{r}-\mathbf{r}_x)} \tag{3.26}$$

where

$$\mathbf{r}_x = \sum_i^3 \frac{n_i}{N_i} \mathbf{a}_i \,, \tag{3.27}$$

$\{\mathbf{b}_i\}$ are the reciprocal unit vectors, J_i are integers that enforce maximization at $\mathbf{r}_x$ and nil amplitude at the borders of the simulation cell, and $N_i = 2J_i + 1$ is the total number of grid points in the i-direction—for the variational basis through which the NGWFs are expanded. These functions hold a variety of useful properties and are particularly advantageous in expediting FFT algorithms, employed sparingly in ONETEP for the evaluation of the kinetic energy operator in reciprocal space. Linear scaling is maintained by limiting the FT to local regions centered about the NGWFs.[229] Furthermore, there is a direct relationship between the grid spacing of the psinc functions and the number of plane

waves (subject to the same kinetic energy cutoff) used in PW KS-DFT implementations, enabling direct translation of such runtime conditions across platforms. Refs. [230] and [231] go into further detail about the advantages of psinc functions in this context.

NGWFs may therefore be expressed in a psinc basis about a given localized center as

$$\phi_\alpha^D(\mathbf{r}) = \sum_i^3 \sum_{n_i}^{N_i-1} C_{x,\alpha} D_x(\mathbf{r}). \tag{3.28}$$

Here, $C_{x,\alpha}$ are coefficients corresponding to the overlap of the NGWFs and psinc functions, i.e.,

$$C_{x,\alpha} = \int D_x(\mathbf{r})\phi_\alpha(\mathbf{r}) = \frac{V_{\text{cell}}}{\prod_i^3 N_i}\phi_\alpha^D(\mathbf{r}_x)d\mathbf{r}. \tag{3.29}$$

3.2.4 Direct minimization protocol

What remains is to formulate the energy functional in terms of the above-defined bodies. Through the density matrix in Eq. (3.24), we can write

$$E[\rho] = E[K^{\alpha\beta}, \{\phi_\alpha\}] = E[K^{\alpha\beta}, C_{x,\alpha}]. \tag{3.30}$$

One may obtain the ground-state energy of any system through self-consistent minimization of this energy functional, each iteration of which requires, by Eq. (3.30), updating both the density kernel and the NGWF expansion coefficients. The algorithm starts with an initial guess for $K^{\alpha\beta}$, whereby the energy functional of the expansion coefficients is optimized via an inner iterative cycle. Once obtained, a new outer iteration with updated $K^{\alpha\beta}$ begins, and so on until $K^{\alpha\beta}$ is optimized. In other words, the inner loop

$$\mathcal{L}[C_{x,\alpha}] = \min_{K^{\alpha\beta}} E[K^{\alpha\beta}, C_{x,\alpha}] \tag{3.31}$$

minimizes the functional $\mathcal{L}$ with respect to $K^{\alpha,\beta}$, while the outer loop

$$E_0 = \min_{C_{x,\alpha}} \mathcal{L}[C_{x,\alpha}] \tag{3.32}$$

minimizes E with respect to $C_{x,\alpha}$.[231] As with any SCF algorithm, convergence thresholds for the total energy are set to achieve desired precision of results.

3.2.5 ONETEP's pseudoatomic solver[§]

ONETEP generates NGWF basis sets using in-built machinery called the (pseudo)atomic solver. This mechanism will become particularly important for testing the theories in Chapter 10. When summoned for a particular atom, the atomic solver performs a KS-DFT calculation for its isolated ion, using its given pseudopotential as the external potential, to obtain self-consistently its single-electron KS states. These states comprise a basis of "ideal" atomic orbitals on which the initial set of NGWFs are built.

[§]This section follows the description and notation of ONETEP's atomic solver as described by the ONETEP documentation on the subject and Appendix 1 of Ref. [216].

More explicitly, the atomic solver constructs pseudoatomic orbitals (PAOs) $\psi_{n\ell m}$ for quantum numbers n, ℓ, m that satisfy the KS equation

$$\hat{H}_{\mathrm{KS}}\psi_{n\ell m}(\mathbf{r}) = \epsilon_{n\ell}\psi_{n\ell m}(\mathbf{r}) \tag{3.33}$$

for an isolated atom in spherical confinement subject to Hamiltonian

$$\hat{H}_{\mathrm{KS}} = \frac{-\nabla^2}{2} + V_{\mathrm{loc}}(\mathbf{r}) + V_{\mathrm{nl}}(\mathbf{r}), \tag{3.34}$$

where, for a given fixed charge distribution $\rho(\mathbf{r}) = \sum_{n\ell} f_{n\ell}|\psi_{n\ell m}(\mathbf{r})|^2$ facilitated by occupancies $f_{n\ell}$—which include spin degeneracy, satisfy the Aufbau principle, and sum to the total number of electrons N—$V_{\mathrm{nl}}(\mathbf{r})$ comprises all non-local potentials defined in the pseudopotential, and

$$V_{\mathrm{loc}}(\mathbf{r}) = V_{\mathrm{ps,loc}}(\mathbf{r}) + V_{\mathrm{hxc}}[\rho](\mathbf{r}) + V_{\mathrm{conf.}}(\mathbf{r}). \tag{3.35}$$

Here, $V_{\mathrm{hxc}}[\rho](\mathbf{r})$ is the standard Hartree and XC potential as defined in Eq. (2.23), and $V_{\mathrm{conf.}}(\mathbf{r})$ is a confining potential that can be further tailored in ONETEP (using functionalities that are not relevant to the current work but on which Ref. [232] elaborates). By virtue of its spherical symmetry (i.e., Eq. (3.33) is solved inside a cutoff radius R_c), the problem may be reduced in two ways: (i) m_ℓ-degenerate orbitals are equal, meaning we need only consider radial dependencies and solve for one given $n\ell$ state using the summation over occupancies of the $2\ell + 1$ degenerate states; and (ii) one may write the pseudoatomic orbitals as the product of two factors: an angular part, represented by the real spherical harmonics $Z_{\ell m}(\theta, \varphi)$,[§] and a radial part, constructed explicitly in ONETEP in terms of a basis (indexed by ν) of normalized spherical Bessel functions of given angular momentum ℓ,[‖]

$$B_{\ell\nu}(\mathbf{r}) = j_{\ell\nu}(q_{\ell\nu}r)\left[\int_0^{R_c} r^2|j_{\ell\nu}(q_{\ell\nu}r)|^2 dr\right]^{-1/2} \tag{3.37}$$

Strategically, $q_{\ell\nu}$ are chosen such that $q_{\ell\nu}R_c$ are the Bessel function nodes to the end that $B_{\ell\nu}(R_c) = 0$ and $\int_0^{R_c} r^2|B_{\ell\nu}(r)|^2 dr = 1$ for all ν satisfying $\frac{1}{2}q_{\ell\nu}^2 < E_{\mathrm{cut}}$. Finally, we may take the basis in Eq. (3.37) and use it to define the Hamiltonian and overlap matrices (see Eqs. (A4)-(A6) in Ref. [216]) necessary to relax self-consistently the coefficients $c_{n\ell\nu}$ that, in turn, describe the PAOs,

$$\psi_{n\ell m} = \sum_\nu c_{n\ell\nu}B_{\ell\nu}(\mathbf{r})Z_{\ell m}(\theta, \varphi). \tag{3.38}$$

In effect, this implementation allows us to subtly alter the shape of the projector functions by changing the fixed occupancy distribution $\rho(\mathbf{r})$, changes that ONETEP permits for any atomic sub-

[§]The real spherical harmonics are defined in terms of associated Legendre polynomials P_ℓ^m (derivatives of ordinary Legendre polynomials). That is, $Z_{\ell m}(\theta, \varphi) = \mathcal{N}e^{im\varphi}P_\ell^m(\cos\theta)$, where $\mathcal{N}$ is a normalization constant, and θ and ϕ are the colatitudinal and longitudinal angles in a polar coordinate system.

[‖]The spherical Bessel functions in this situation are defined as

$$j_{\ell\nu}(q_{\ell\nu}r) = \sqrt{\frac{\pi}{2q_{\ell\nu}r}}\sum_{m=0}^{\infty}\frac{(-1)^m}{m!\Gamma(m+\ell\nu+3/2)}\left(\frac{q_{\ell\nu}r}{2}\right)^{2m+\ell\nu+1/2}. \tag{3.36}$$

space and any pseudopotential. This functionality is exploited in Chapter 10, where we elaborate more on its utility.

Another convenient implementation, manipulated through ONETEP's pseudoatomic solver, is the so-called "splitnorm" basis. At its default, ONETEP creates a minimal *in situ*-optimized basis representing all KS orbitals in an atom with the same number of NGWFs. Through the split-valence approach, one may split all the PAOs in that basis into two (or more) functions. The resulting expanded basis is unoptimized but improves the radial flexibility of the valence orbitals. For more information on this functionality, please see Refs. [216] and [233].

Bibliography

[1] M. Born and R. Oppenheimer, Annalen der Physik **389**, 457 (1927).

[2] E. Pavarini, E. Koch, and U. Schollwöck, eds., *Emergent Phenomena in Correlated Matter*, Schriften des Forschungszentrums Jülich. Reihe modeling and simulation, Vol. 3 (Forschungszentrum Jülich GmbH Zentralbibliothek, Verlag, Jülich, 2013) p. 520 S.

[3] W. Pauli, Zeitschrift für Physik **43**, 601 (1927).

[4] V. R. Eisberg and R. R. J. Wiley, *Quantum Physics of Atoms, Molecules, Solids, Nuclei and Particles* (John Wiley & Sons, 1976) pp. 127–128.

[5] J. Coey and J. Coey, *Magnetism and Magnetic Materials*, Magnetism and Magnetic Materials (Cambridge University Press, 2010).

[6] X. Li, H. Yu, L. Feng, F. J.S., M.-H. Whangbo, and H. Xiang, Molecules **26**, 803 (2021).

[7] C. R. Jacob and M. Reiher, International Journal of Quantum Chemistry **112**, 3661 (2012).

[8] K. Capelle, "A bird's-eye view of density-functional theory," (2006), arXiv:cond-mat/0211443 [cond-mat.mtrl-sci].

[9] V. Shenoy, "Review of many body field theory I," (2014).

[10] A. Chakraborty, M. Dixit, and D. T. Major, npj Computational Materials **4**, 60 (2018).

[11] K. Saritas, E. R. Fadel, B. Kozinsky, and J. C. Grossman, The Journal of Physical Chemistry C **124**, 5893 (2020).

[12] J. Shu, T.-F. Yi, M. Shui, Y. Wang, R.-S. Zhu, X.-F. Chu, F. Huang, D. Xu, and L. Hou, Computational Materials Science **50**, 776 (2010).

[13] Y. S. Meng and M. E. Arroyo-de Dompablo, Energy & Environmental Science **2**, 589 (2009).

[14] M. Shishkin and H. Sato, The Journal of Physical Chemistry C **125**, 1531 (2021), publisher: American Chemical Society.

[15] F. S. Hegner, J. R. Galán-Mascarós, and N. López, Inorganic Chemistry **55**, 12851 (2016).

[16] A. Aziz, *Electronic structure simulations of energy materials: chalcogenides for thermoelectrics and metal-organic frameworks for photocatalysis*, Chemistry, University of Reading, United Kingdom (2017).

[17] S. Siebentritt and S. Schorr, Progress in Photovoltaics: Research and Applications **20**, 512 (2012).

[18] A. Polman, M. Knight, E. C. Garnett, B. Ehrler, and W. C. Sinke, Science **352** (2016).

[19] C. Yan, K. Sun, J. Huang, S. Johnston, F. Liu, B. P. Veettil, K. Sun, A. Pu, F. Zhou, J. A. Stride, M. A. Green, and X. Hao, ACS Energy Letters **2**, 930 (2017).

[20] R. H. Lavroff, D. L. Pennington, A. S. Hua, B. Y. Li, J. A. Williams, and A. N. Alexandrova, The Journal of Physical Chemistry Letters **12**, 10742 (2021).

[21] G. Timco, S. Carretta, F. Troiani, F. Tuna, R. Pritchard, C. Muryn, E. McInnes, A. Ghirri, A. Candini, P. Santini, G. Amoretti, M. Affronte, and R. Winpenny, Nature Nanotechnology **4**, 173 (2009).

[22] S. Shaik, D. Danovich, and P. C. Hiberty, Molecules **26** (2021).

[23] J. Thiele, Justus Liebigs Annalen der Chemie **306**, 87 (1899).

[24] G. N. Lewis, Journal of the American Chemical Society **38**, 762 (1916).

[25] Z. Chen and W. Wu, The Journal of Chemical Physics **153**, 090902 (2020).

[26] W. Wu, P. Su, S. Shaik, and P. C. Hiberty, Chemical Reviews **111**, 7557 (2011).

[27] V. Fock, Zeitschrift für Physik **62**, 795 (1930).

[28] D. R. Hartree and W. Hartree, Proceedings of the Royal Society of London. Series A, Mathematical and Physical Sciences **150**, 9 (1935).

[29] J. C. Slater, Phys. Rev. **35**, 210 (1930).

[30] J. C. Slater, Physical Review **34**, 1293 (1929).

[31] P. A. M. Dirac, Proceedings of the Royal Society A **112**, 661 (1926).

[32] W. Heisenberg, Zeitschrift für Physik **38**, 411 (1926).

[33] E. Koch, in *Emergent Phenomena in Correlated Matter Modelling and Simulation*, Vol. 3, edited by E. Pavarini, E. Koch, and U. Schollwock (Forschungsentrum Julich, 2013) Chap. 2, pp. 2.2–2.26.

[34] Q. M. Phung, M. Feldt, J. N. Harvey, and K. Pierloot, Journal of Chemical Theory and Computation **14**, 2446 (2018).

[35] P. J. Reynolds, J. Tobochnik, and H. Gould, Computer in Physics **4**, 662 (1990).

[36] A. Georges, G. Kotliar, W. Krauth, and M. J. Rozenberg, Rev. Mod. Phys. **68**, 13 (1996).

[37] X. Qu, P. Xu, R. Li, G. Li, L. He, and X. Ren, Journal of Chemical Theory and Computation **18**, 5589 (2022).

[38] R. Van Noorden, B. Maher, and R. Nuzzo, Nature **514**, 550–553 (2014).

[39] D. R. Bowler and T. Miyazaki, Journal of Physics: Condensed Matter **22**, 074207 (2010).

[40] L. Hung and E. A. Carter, Chemical Physics Letters **475**, 163 (2009).

[41] U. Rastetter, A. Jacobi von Wangelin, and C. Herrmann, Journal of Computational Chemistry **44**, 468 (2023).

[42] G. Venkat, D. A. Allwood, and T. J. Hayward, Journal of Physics D: Applied Physics **57**, 063001 (2023).

[43] M. Hervé, B. Dupé, R. Lopes, M. Böttcher, M. D. Martins, T. Balashov, L. Gerhard, J. Sinova, and W. Wulfhekel, Nature Communications **9**, 1015 (2018).

[44] F. Jonietz, S. Mühlbauer, C. Pfleiderer, A. Neubauer, W. Münzer, A. Bauer, T. Adams, R. Georgii, P. Böni, R. A. Duine, K. Everschor, M. Garst, and A. Rosch, Science **330**, 1648 (2010).

[45] P. Hohenberg and W. Kohn, Phys. Rev. **136**, B864 (1964).

[46] U. von Barth and L. Hedin, Journal of Physics C: Solid State Physics **5**, 1629 (1972).

[47] K. Capelle and G. Vignale, Phys. Rev. Lett. **86**, 5546 (2001).

[48] H. Eschrig and W. Pickett, Solid State Communications **118**, 123 (2001).

[49] K. Capelle and G. Vignale, Phys. Rev. B **65**, 113106 (2002).

[50] W. Kohn, A. Savin, and C. A. Ullrich, International Journal of Quantum Chemistry **100**, 20 (2004).

[51] C. A. Ullrich, Phys. Rev. B **72**, 073102 (2005).

[52] K. Capelle and V. L. Líbero, International Journal of Quantum Chemistry **105**, 679 (2005).

[53] E. H. Lieb, International Journal of Quantum Chemistry **24**, 243 (1983).

[54] P. W. Ayers and W. Yang, The Journal of Chemical Physics **124**, 224108 (2006).

[55] A. Holas and R. Balawender, The Journal of Chemical Physics **125**, 247101 (2006).

[56] M. Levy, Proceedings of the National Academy of Sciences of the United States of America **76**, 6062 (1979).

[57] W. Kohn and L. J. Sham, Phys. Rev. **140**, A1133 (1965).

[58] O. K. Orhan, *Corrective First-Principles Approaches for the Theoretical Spectroscopy of Transition-Metal Systems*, Physics, School of Physics, Trinity College Dublin, The University of Dublin, College Green, Dublin 2, Ireland (2018).

[59] P. A. M. Dirac, Mathematical Proceedings of the Cambridge Philosophical Society **26**, 376–385 (1930).

[60] J. Toulouse, "Review of approximations for the exchange-correlation energy in density-functional theory," in *Density Functional Theory: Modeling, Mathematical Analysis, Computational Methods, and Applications*, edited by E. Cancès and G. Friesecke (Springer International Publishing, Cham, 2023) pp. 1–90.

[61] D. M. Ceperley and B. J. Alder, Phys. Rev. Lett. **45**, 566 (1980).

[62] S. Moroni, D. M. Ceperley, and G. Senatore, Phys. Rev. Lett. **75**, 689 (1995).

[63] G. Ortiz, M. Harris, and P. Ballone, Phys. Rev. Lett. **82**, 5317 (1999).

[64] J. P. Perdew and S. Kurth, in *Strongly Coupled Coulomb Systems*, edited by G. J. Kalman, J. M. Rommel, and K. Blagoev (Springer US, Boston, MA, 1998) pp. 281–285.

[65] J. P. Perdew and A. Zunger, Phys. Rev. B **23**, 5048 (1981).

[66] J. P. Perdew, A. Ruzsinszky, J. Tao, V. N. Staroverov, G. E. Scuseria, and G. I. Csonka, The Journal of Chemical Physics **123**, 062201 (2005).

[67] J. P. Perdew, J. A. Chevary, S. H. Vosko, K. A. Jackson, M. R. Pederson, D. J. Singh, and C. Fiolhais, Phys. Rev. B **46**, 6671 (1992).

[68] J. P. Perdew, K. Burke, and M. Ernzerhof, Phys. Rev. Lett. **77**, 3865 (1996).

[69] J. P. Perdew, A. Ruzsinszky, G. I. Csonka, O. A. Vydrov, G. E. Scuseria, L. A. Constantin, X. Zhou, and K. Burke, Phys. Rev. Lett. **100**, 136406 (2008).

[70] A. J. Cohen, P. Mori-Sánchez, and W. Yang, The Journal of Chemical Physics **126**, 191109 (2007).

[71] C. Adamo, M. Ernzerhof, and G. E. Scuseria, The Journal of Chemical Physics **112**, 2643 (2000).

[72] F. Zahariev, S. S. Leang, and M. S. Gordon, The Journal of Chemical Physics **138**, 244108 (2013).

[73] J. Sun, A. Ruzsinszky, and J. P. Perdew, Phys. Rev. Lett. **115**, 036402 (2015).

[74] W. Kohn, A. D. Becke, and R. G. Parr, The Journal of Physical Chemistry **100**, 12974 (1996).

[75] R. H. Hertwig and W. Koch, Chemical Physics Letters **268**, 345 (1997).

[76] J. F. Janak, Phys. Rev. B **18**, 7165 (1978).

[77] S. J. A. van Gisbergen, P. R. T. Schipper, O. V. Gritsenko, E. J. Baerends, J. G. Snijders, B. Champagne, and B. Kirtman, Phys. Rev. Lett. **83**, 694 (1999).

[78] A. J. Cohen and Y. Tantirungrotechai, Chemical Physics Letters **299**, 465 (1999).

[79] M. Grüning, O. V. Gritsenko, and E. J. Baerends, The Journal of Chemical Physics **116**, 6435 (2002).

[80] A. J. Cohen, P. Mori-Sánchez, and W. Yang, Chemical Reviews **112**, 289 (2012).

[81] B. Champagne, E. A. Perpète, D. Jacquemin, S. J. A. van Gisbergen, E.-J. Baerends, C. Soubra-Ghaoui, K. A. Robins, and B. Kirtman, The Journal of Physical Chemistry A **104**, 4755 (2000).

[82] A. Schrön, C. Rödl, and F. Bechstedt, Physical Review B **82**, 165109 (2010).

[83] M. Cococcioni and N. Marzari, Physical Review Materials **3**, 033801 (2019).

[84] W. Zhang, D. G. Truhlar, and M. Tang, Journal of Chemical Theory and Computation **10**, 2399 (2014).

[85] A. J. Cohen, P. Mori-Sánchez, and W. Yang, Science **321**, 792 (2008).

[86] P. Mori-Sánchez, A. J. Cohen, and W. Yang, The Journal of Chemical Physics **125**, 201102 (2006).

[87] E. B. Isaacs, S. Patel, and C. Wolverton, Physical Review Materials **4**, 065405 (2020).

[88] A. Georges, L. d. Medici, and J. Mravlje, Annual Review of Condensed Matter Physics **4**, 137 (2013).

[89] D. D. O'Regan, M. C. Payne, and A. A. Mostofi, Phys. Rev. B **83**, 245124 (2011).

[90] A. Ruzsinszky, J. P. Perdew, G. I. Csonka, O. A. Vydrov, and G. E. Scuseria, The Journal of Chemical Physics **126**, 104102 (2007).

[91] Y. Zhang and W. Yang, The Journal of Chemical Physics **109**, 2604 (1998).

[92] P. Mori-Sánchez, A. J. Cohen, and W. Yang, Phys. Rev. Lett. **100**, 146401 (2008).

[93] M. Cococcioni, *A LDA+U study of selected iron compounds*, Physics, Scuola Internazionale Superiore di Studi Avanzati, Scuola Internazionale Superiore di Studi Avanzati (2002).

[94] J. P. Perdew and A. Zunger, Phys. Rev. B **23**, 5048 (1981).

[95] J. P. Perdew, R. G. Parr, M. Levy, and J. L. Balduz, Phys. Rev. Lett. **49**, 1691 (1982).

[96] P. W. Ayers, Journal of Mathematical Chemistry **43**, 285 (2008).

[97] Q. Zhao, E. I. Ioannidis, and H. J. Kulik, The Journal of Chemical Physics **145**, 054109 (2016).

[98] V. I. Anisimov, J. Zaanen, and O. K. Andersen, Physical Review B **44**, 943 (1991).

[99] V. I. Anisimov and O. Gunnarsson, Phys. Rev. B **43**, 7570 (1991).

[100] V. I. Anisimov, I. V. Solovyev, M. A. Korotin, M. T. Czyżyk, and G. A. Sawatzky, Phys. Rev. B **48**, 16929 (1993).

[101] A. J. Cohen, P. Mori-Sánchez, and W. Yang, The Journal of Chemical Physics **129**, 121104 (2008).

[102] W. Yang, Y. Zhang, and P. W. Ayers, Phys. Rev. Lett. **84**, 5172 (2000).

[103] A. C. Burgess, E. Linscott, and D. D. O'Regan, Phys. Rev. B **107**, L121115 (2023).

[104] A. C. Burgess, E. Linscott, and D. D. O'Regan, The Journal of Chemical Physics **159**, 211102 (2023).

[105] A. C. Burgess, E. Linscott, and D. D. O'Regan, Phys. Rev. Lett. **133**, 026404 (2024).

[106] O. K. Orhan and D. D. O'Regan, Physical Review B **101**, 245137 (2020).

[107] D. S. Lambert and D. D. O'Regan, Phys. Rev. Res. **5**, 013160 (2023).

[108] A. Georges, L. d. Medici, and J. Mravlje, Annual Review of Condensed Matter Physics **4**, 137 (2013).

[109] J. Wang, A. Becke, and J. Smith, The Journal of Chemical Physics **102**, 3477 (1995).

[110] A. J. Cohen, D. J. Tozer, and N. C. Handy, The Journal of Chemical Physics **126**, 214104 (2007).

[111] J. M. Wittbrodt and H. B. Schlegel, The Journal of Chemical Physics **105**, 6574 (1996).

[112] P. Nie, L. Shen, H. Luo, B. Ding, G. Xu, J. Wang, and X. Zhang, J. Mater. Chem. A **2**, 5852 (2014).

[113] M. Pasta, R. Y. Wang, R. Ruffo, R. Qiao, H.-W. Lee, B. Shyam, M. Guo, Y. Wang, L. A. Wray, W. Yang, M. F. Toney, and Y. Cui, Journal of Materials Chemistry A **4**, 4211 (2016).

[114] X. Guo, Z. Wang, Z. Deng, X. Li, B. Wang, X. Chen, and S. P. Ong, Chemistry of Materials **31**, 5933 (2019).

[115] B. Wang, Y. Han, X. Wang, N. Bahlawane, H. Pan, M. Yan, and Y. Jiang, iScience **3**, 110 (2018).

[116] K. Hurlbutt, F. Giustino, M. Pasta, and G. Volonakis, Chemistry of Materials **33**, 7067 (2021).

[117] Q. Wang, J. Li, H. Jin, S. Xin, and H. Gao, InfoMat **4**, e12311 (2022).

[118] G. Oh, J. Kim, S. Kansara, H. Kang, H.-G. Jung, Y.-K. Sun, and J.-Y. Hwang, Journal of Energy Chemistry **93**, 627 (2024).

[119] F. S. Hegner, J. R. Galán-Mascarós, and N. López, The Journal of Physical Chemistry Letters **13**, 4104 (2022).

[120] C. Wadia, A. P. Alivisatos, and D. M. Kammen, Environmental Science & Technology **43**, 2072 (2009).

[121] D. B. Khadka and J. Kim, J. Phys. Chem. **119**, 1706 (2015).

[122] Y. S. Lee, T. Gershon, O. Gunawan, T. K. Todorov, T. Gokmen, Y. Virgus, and S. Guha, Advanced Energy Materials **5**, 1401372 (2015).

[123] S. Kim, K. M. Kim, H. Tampo, H. Shibata, and S. Niki, Applied Physics Express **9**, 102301 (2016).

[124] Y.-F. Qi, D.-X. Kou, W.-H. Zhou, Z.-J. Zhou, Q.-W. Tian, Y.-N. Meng, X.-S. Liu, Z.-L. Du, and S.-X. Wu, Energy Environ. Sci. **10**, 2401 (2017).

[125] M. Mesbahi, F. Serdouk, and M. Benkhedir, Acta Physica Polonica A **134**, 358 (2018).

[126] Q. Liu, Z. Cai, D. Han, and S. Chen, Scientific Reports **8**, 1604 (2018).

[127] L. H. Wong, A. Zakutayev, J. D. Major, X. Hao, A. Walsh, T. K. Todorov, and E. Saucedo, Journal of Physics: Energy **1**, 032001 (2019).

[128] S. Giraldo, Z. Jehl, M. Placidi, V. Izquierdo-Roca, A. Pérez-Rodríguez, and E. Saucedo, Advanced Materials **31**, 1806692 (2019).

[129] P. Mangelis, A. Aziz, I. da Silva, R. Grau-Crespo, P. Vaqueiro, and A. V. Powell, Phys. Chem. Chem. Phys. **21**, 19311 (2019).

[130] J. Heyd and G. E. Scuseria, The Journal of Chemical Physics **120**, 7274 (2004).

[131] A. Georges and G. Kotliar, Phys. Rev. B **45**, 6479 (1992).

[132] A. Georges, G. Kotliar, W. Krauth, and M. J. Rozenberg, Rev. Mod. Phys. **68**, 13 (1996).

[133] S. Sharma, J. K. Dewhurst, N. N. Lathiotakis, and E. K. U. Gross, Phys. Rev. B **78**, 201103 (2008).

[134] I. V. Solovyev, P. H. Dederichs, and V. I. Anisimov, Phys. Rev. B **50**, 16861 (1994).

[135] S. L. Dudarev, G. A. Botton, S. Y. Savrasov, C. J. Humphreys, and A. P. Sutton, Phys. Rev. B **57**, 1505 (1998).

[136] B. Himmetoglu, A. Floris, S. de Gironcoli, and M. Cococcioni, International Journal of Quantum Chemistry **114**, 14 (2014).

[137] J. Hubbard and B. H. Flowers, Proceedings of the Royal Society of London. Series A. Mathematical and Physical Sciences **276**, 238 (1963).

[138] M. Cococcioni and S. de Gironcoli, Physical Review B **71**, 035105 (2005).

[139] D. D. O'Regan, N. D. M. Hine, M. C. Payne, and A. A. Mostofi, Phys. Rev. B **85**, 085107 (2012).

[140] J. W. Bennett, B. G. Hudson, I. K. Metz, D. Liang, S. Spurgeon, Q. Cui, and S. E. Mason, Computational Materials Science **170**, 109137 (2019).

[141] B. Kim, K. Kim, and S. Kim, Physical Review Materials **5**, 035404 (2021).

[142] K. Yu and E. A. Carter, The Journal of Chemical Physics **140**, 121105 (2014).

[143] A. I. Liechtenstein, V. I. Anisimov, and J. Zaanen, Phys. Rev. B **52**, R5467 (1995).

[144] M. T. Czyżyk and G. A. Sawatzky, Phys. Rev. B **49**, 14211 (1994).

[145] B. R. Judd, *Operator Techniques in Atomic Spectroscopy* (Princeton University Press, 1998).

[146] V. I. Anisimov, F. Aryasetiawan, and A. I. Lichtenstein, Journal of Physics: Condensed Matter **9**, 767 (1997).

[147] H. J. Kulik, The Journal of Chemical Physics **142**, 240901 (2015).

[148] B. Himmetoglu, R. M. Wentzcovitch, and M. Cococcioni, Physical Review B **84**, 115108 (2011).

[149] O. K. Orhan and D. D. O'Regan, Physical Review B **101**, 245137 (2020).

[150] A. Bajaj, J. P. Janet, and H. J. Kulik, The Journal of Chemical Physics **147**, 191101 (2017).

[151] A. Bajaj, F. Liu, and H. J. Kulik, The Journal of Chemical Physics **150**, 154115 (2019).

[152] "Iron Man 2," (2010), Marvel Studios, directed by Jon Favreau.

[153] K. Persson, "The Materials Project—A Google of Materials," (2016), supercomputing Conference Series, Salt Lake City, Utah.

[154] T. Deutsch and L. Genovese, École thématique de la Société Française de la Neutronique **12**, 33 (2011).

[155] A. Bravais, *Mémoire sur les systèmes formés par des points distribués régulièrement sur un plan ou dans l'espace* (Bachelier, 1850).

[156] L. MacEnulty and D. D. O'Regan, Journal of Undergraduate Reports in Physics **30**, 100005 (2020).

[157] F. Bloch, Zeitschrift für Physik **52**, 555 (1929).

[158] M. Born and T. von Karman, Physikalische Zeitschrift **13**, 297 (1912).

[159] L. Brillouin, Comptes Rendus Hebdomadaires des Séances de l'Académie des Sciences **191**, 292 (1930).

[160] L. P. Bouckaert, R. Smoluchowski, and E. Wigner, Phys. Rev. **50**, 58 (1936).

[161] D. J. Chadi and M. L. Cohen, Phys. Rev. B **8**, 5747 (1973).

[162] H. J. Monkhorst and J. D. Pack, Phys. Rev. B **13**, 5188 (1976).

[163] C. F. Gauss, *Werke*, Vol. 3 (Königliche Gesellschaft der Wissenschaften, Göttingen, Germany, 1866) pp. 265–327, [1805].

[164] J. W. Cooley and J. W. Tukey, Mathematics of Computation **19**, 297 (1965).

[165] S. Winograd, Proceedings of the National Academy of Sciences of the United States of America **73**, 1005 (1976).

[166] L. H. Thomas, in *Applications of Digital Computers* (Ginn, Boston, 1963).

[167] G. Bruun, IEEE Transactions on Acoustics, Speech, and Signal Processing **26**, 56 (1978).

[168] C. M. Rader, Proceedings of the IEEE **56**, 1107 (1968).

[169] J. B. Birdsong and N. I. Rummelt, in *2016 IEEE International Conference on Image Processing (ICIP)* (2016) pp. 1809–1812.

[170] Q. Sun, X. Zhang, S. Banerjee, P. Bao, M. Barbry, N. S. Blunt, N. A. Bogdanov, G. H. Booth, J. Chen, Z.-H. Cui, J. J. Eriksen, Y. Gao, S. Guo, J. Hermann, M. R. Hermes, K. Koh, P. Koval, S. Lehtola, Z. Li, J. Liu, N. Mardirossian, J. D. McClain, M. Motta, B. Mussard, H. Q. Pham, A. Pulkin, W. Purwanto, P. J. Robinson, E. Ronca, E. R. Sayfutyarova, M. Scheurer, H. F. Schurkus, J. E. T. Smith, C. Sun, S.-N. Sun, S. Upadhyay, L. K. Wagner, X. Wang, A. White, J. D. Whitfield, M. J. Williamson, S. Wouters, J. Yang, J. M. Yu, T. Zhu, T. C. Berkelbach, S. Sharma, A. Y. Sokolov, and G. K.-L. Chan, The Journal of Chemical Physics **153**, 024109 (2020).

[171] Q. Sun, T. C. Berkelbach, N. S. Blunt, G. H. Booth, S. Guo, Z. Li, J. Liu, J. D. McClain, E. R. Sayfutyarova, S. Sharma, S. Wouters, and G. K.-L. Chan, WIREs Computational Molecular Science **8**, e1340 (2018).

[172] F. Neese, F. Wennmohs, U. Becker, and C. Riplinger, Journal of Chemical Physics **152**, L224108 (2020).

[173] M. J. Frisch, G. W. Trucks, H. B. Schlegel, G. E. Scuseria, M. A. Robb, J. R. Cheeseman, G. Scalmani, V. Barone, G. A. Petersson, H. Nakatsuji, X. Li, M. Caricato, A. V. Marenich, J. Bloino, B. G. Janesko, R. Gomperts, B. Mennucci, H. P. Hratchian, J. V. Ortiz, A. F. Izmaylov, J. L. Sonnenberg, D. Williams-Young, F. Ding, F. Lipparini, F. Egidi, J. Goings, B. Peng, A. Petrone, T. Henderson, D. Ranasinghe, V. G. Zakrzewski, J. Gao, N. Rega, G. Zheng, W. Liang, M. Hada, M. Ehara, K. Toyota, R. Fukuda, J. Hasegawa, M. Ishida, T. Nakajima, Y. Honda, O. Kitao, H. Nakai, T. Vreven, K. Throssell, J. A. Montgomery, Jr., J. E. Peralta, F. Ogliaro, M. J. Bearpark, J. J. Heyd, E. N. Brothers, K. N. Kudin, V. N. Staroverov, T. A. Keith, R. Kobayashi, J. Normand, K. Raghavachari, A. P. Rendell, J. C. Burant, S. S. Iyengar, J. Tomasi, M. Cossi, J. M. Millam, M. Klene, C. Adamo, R. Cammi, J. W. Ochterski, R. L. Martin, K. Morokuma, O. Farkas, J. B. Foresman, and D. J. Fox, "Gaussian~16 Revision C.01," (2016), gaussian Inc. Wallingford CT.

[174] C.-K. Skylaris, P. D. Haynes, A. A. Mostofi, and M. C. Payne, The Journal of Chemical Physics **122**, 084119 (2005).

[175] P. Giannozzi, S. Baroni, N. Bonini, M. Calandra, R. Car, C. Cavazzoni, D. Ceresoli, G. L. Chiarotti, M. Cococcioni, I. Dabo, A. D. Corso, S. de Gironcoli, S. Fabris, G. Fratesi, R. Gebauer, U. Gerstmann, C. Gougoussis, A. Kokalj, M. Lazzeri, L. Martin-Samos, N. Marzari, F. Mauri, R. Mazzarello, S. Paolini, A. Pasquarello, L. Paulatto, C. Sbraccia, S. Scandolo, G. Sclauzero, A. P. Seitsonen, A. Smogunov, P. Umari, and R. M. Wentzcovitch, Journal of Physics: Condensed Matter **21**, 395502 (2009).

[176] P. Giannozzi, O. Andreussi, T. Brumme, O. Bunau, M. B. Nardelli, M. Calandra, R. Car, C. Cavazzoni, D. Ceresoli, M. Cococcioni, N. Colonna, I. Carnimeo, A. D. Corso, S. de Gironcoli, P. Delugas, R. A. DiStasio, A. Ferretti, A. Floris, G. Fratesi, G. Fugallo, R. Gebauer, U. Gerstmann, F. Giustino, T. Gorni, J. Jia, M. Kawamura, H.-Y. Ko, A. Kokalj, E. Küçükbenli, M. Lazzeri, M. Marsili, N. Marzari, F. Mauri, N. L. Nguyen, H.-V. Nguyen, A. O. de-la Roza, L. Paulatto, S. Poncé, D. Rocca, R. Sabatini, B. Santra, M. Schlipf, A. P. Seitsonen, A. Smogunov, I. Timrov, T. Thonhauser, P. Umari, N. Vast, X. Wu, and S. Baroni, Journal of Physics: Condensed Matter **29**, 465901 (2017).

[177] X. Gonze, B. Amadon, P. M. Anglade, J. M. Beuken, F. Bottin, P. Boulanger, F. Bruneval, D. Caliste, R. Caracas, M. Côté, T. Deutsch, L. Genovese, P. Ghosez, M. Giantomassi, S. Goedecker, D. R. Hamann, P. Hermet, F. Jollet, G. Jomard, S. Leroux, M. Mancini, S. Mazevet, M. J. T. Oliveira, G. Onida, Y. Pouillon, T. Rangel, G. M. Rignanese, D. Sangalli, R. Shaltaf, M. Torrent, M. J. Verstraete, G. Zerah, and J. W. Zwanziger, Computer Physics Communications 40 YEARS OF CPC: A celebratory issue focused on quality software for high performance, grid and novel computing architectures, **180**, 2582 (2009).

[178] X. Gonze, B. Amadon, G. Antonius, F. Arnardi, L. Baguet, J.-M. Beuken, J. Bieder, F. Bottin, J. Bouchet, E. Bousquet, N. Brouwer, F. Bruneval, G. Brunin, T. Cavignac, J.-B. Charraud, W. Chen, M. Côté, S. Cottenier, J. Denier, G. Geneste, P. Ghosez, M. Giantomassi, Y. Gillet, O. Gingras, D. R. Hamann, G. Hautier, X. He, N. Helbig, N. Holzwarth, Y. Jia, F. Jollet, W. Lafargue-Dit-Hauret, K. Lejaeghere, M. A. L. Marques, A. Martin, C. Martins, H. P. C. Miranda, F. Naccarato, K. Persson, G. Petretto, V. Planes, Y. Pouillon, S. Prokhorenko, F. Ricci, G.-M. Rignanese, A. H. Romero, M. M. Schmitt, M. Torrent, M. J. van Setten, B. V. Troeye, M. J. Verstraete, G. Zérah, and J. W. Zwanziger, Comput. Phys. Commun. **248**, 107042 (2020).

[179] A. H. Romero, D. C. Allan, B. Amadon, G. Antonius, T. Applencourt, L. Baguet, J. Bieder, F. Bottin, J. Bouchet, E. Bousquet, F. Bruneval, G. Brunin, D. Caliste, M. Côté, J. Denier, C. Dreyer, P. Ghosez, M. Giantomassi, Y. Gillet, O. Gingras, D. R. Hamann, G. Hautier, F. Jollet, G. Jomard, A. Martin, H. P. C. Miranda, F. Naccarato, G. Petretto, N. A. Pike, V. Planes, S. Prokhorenko, T. Rangel, F. Ricci, G.-M. Rignanese, M. Royo, M. Stengel, M. Torrent, M. J. van Setten, B. V. Troeye, M. J. Verstraete, J. Wiktor, J. W. Zwanziger, and X. Gonze, J. Chem. Phys. **152**, 124102 (2020).

[180] G. Kresse and J. Hafner, Physical Review B **47**, 558 (1993).

[181] P. Blaha, K. Schwarz, G. K. H. Madsen, D. Kvasnicka, J. Luitz, R. Laskowski, F. Tran, and L. D. Marks, *WIEN2k, An Augmented Plane Wave + Local Orbitals Program for Calculating Crystal Properties* (Karlheinz Schwarz, Techn. Universität Wien, Austria, 2018).

[182] P. D. Haynes, *Linear-scaling methods in ab initio quantum-mechanical calculations*, Physics, Christ's College, University of Cambridge, United Kingdom (1998).

[183] J. Zeng and J. Yuan, Phys. Rev. E **76**, 026401 (2007).

[184] H. Hellmann, The Journal of Chemical Physics **3**, 61 (1935).

[185] V. Heine (Academic Press, 1970) pp. 1–36.

[186] J. C. Phillips and L. Kleinman, Phys. Rev. **116**, 287 (1959).

[187] C. Herring, Phys. Rev. **57**, 1169 (1940).

[188] V. A. Rassolov, J. A. Pople, P. C. Redfern, and L. A. Curtiss, Chemical Physics Letters **350**, 573 (2001).

[189] D. R. Hamann, M. Schlüter, and C. Chiang, Phys. Rev. Lett. **43**, 1494 (1979).

[190] D. R. Hamann, Phys. Rev. B **40**, 2980 (1989).

[191] D. Vanderbilt, Physical Review B **41**, 7892 (1990).

[192] P. E. Blöchl, Physical Review B **50**, 17953 (1994).

[193] N. Holzwarth, A. Tackett, and G. Matthews, Computer Physics Communications **135**, 329 (2001).

[194] N. A. W. Holzwarth, "Notes for revised form of atompaw code," (2010).

[195] F. Jollet, M. Torrent, and N. Holzwarth, Computer Physics Communications **185**, 1246 (2014).

[196] N. D. M. Hine, Journal of Physics: Condensed Matter **29**, 024001 (2017).

[197] G. Kresse and D. Joubert, Physical Review B **59**, 1758 (1999).

[198] A. M. Rappe, K. M. Rabe, E. Kaxiras, and J. D. Joannopoulos, Phys. Rev. B **41**, 1227 (1990).

[199] M. J. van Setten, M. Giantomassi, E. Bousquet, M. J. Verstraete, D. R. Hamann, X. Gonze, and G. M. Rignanese, Computer Physics Communications **226**, 39 (2018).

[200] P. Debye, Mathematische Annalen **67**, 535 (1909).

[201] E. R. Davidson, Journal of Computational Physics **17**, 87 (1975).

[202] J. R. Shewchuk (1994).

[203] M. C. Payne, M. P. Teter, D. C. Allan, T. A. Arias, and J. D. Joannopoulos, Rev. Mod. Phys. **64**, 1045 (1992).

[204] J. M. Soler, E. Artacho, J. D. Gale, A. García, J. Junquera, P. Ordejón, and D. Sánchez-Portal, Journal of Physics: Condensed Matter **14**, 2745 (2002).

[205] E. Artacho, E. Anglada, O. Diéguez, J. D. Gale, A. García, J. Junquera, R. M. Martin, P. Ordejón, J. M. Pruneda, D. Sánchez-Portal, and J. M. Soler, Journal of Physics: Condensed Matter **20**, 064208 (2008).

[206] V. Weber, J. VandeVondele, J. Hutter, and A. M. N. Niklasson, The Journal of Chemical Physics **128**, 084113 (2008).

[207] T. D. Kühne, M. Iannuzzi, M. Del Ben, V. V. Rybkin, P. Seewald, F. Stein, T. Laino, R. Z. Khaliullin, O. Schütt, F. Schiffmann, D. Golze, J. Wilhelm, S. Chulkov, M. H. Bani-Hashemian, V. Weber, U. Borštnik, M. Taillefumier, A. S. Jakobovits, A. Lazzaro, H. Pabst, T. Müller, R. Schade, M. Guidon, S. Andermatt, N. Holmberg, G. K. Schenter, A. Hehn, A. Bussy, F. Belleflamme, G. Tabacchi, A. Glöß, M. Lass, I. Bethune, C. J. Mundy, C. Plessl, M. Watkins, J. VandeVondele, M. Krack, and J. Hutter, The Journal of Chemical Physics **152**, 194103 (2020).

[208] D. R. Bowler, T. Miyazaki, and M. J. Gillan, Journal of Physics: Condensed Matter **14**, 2781 (2002).

[209] M. Gillan, D. Bowler, A. Torralba, and T. Miyazaki, Computer Physics Communications **177**, 14 (2007), proceedings of the Conference on Computational Physics 2006.

[210] L. Genovese, B. Videau, M. Ospici, T. Deutsch, S. Goedecker, and J.-F. Méhaut, Comptes Rendus. Mécanique **339**, 149 (2011).

[211] T. Ozaki and H. Kino, Phys. Rev. B **72**, 045121 (2005).

[212] N. D. Hine, "Using the Pseudoatomic Solver to Generate NGWFs in ONETEP," (2011).

[213] P. D. Haynes, C.-K. Skylaris, A. A. Mostofi, and M. C. Payne, Journal of Physics: Condensed Matter **20**, 294207 (2008).

[214] D. D. O'Regan, N. D. M. Hine, M. C. Payne, and A. A. Mostofi, Phys. Rev. B **82**, 081102 (2010).

[215] N. D. M. Hine, M. Robinson, P. D. Haynes, C.-K. Skylaris, M. C. Payne, and A. A. Mostofi, Phys. Rev. B **83**, 195102 (2011).

[216] A. Ruiz-Serrano, N. D. M. Hine, and C.-K. Skylaris, The Journal of Chemical Physics **136**, 234101 (2012).

[217] S. J. Fox, C. Pittock, T. Fox, C. S. Tautermann, N. Malcolm, and C.-K. Skylaris, The Journal of Chemical Physics **135**, 224107 (2011).

[218] R. McWeeny, Rev. Mod. Phys. **32**, 335 (1960).

[219] R. W. Nunes and D. Vanderbilt, Phys. Rev. B **50**, 17611 (1994).

[220] M. S. Daw, Phys. Rev. B **47**, 10895 (1993).

[221] X.-P. Li, R. W. Nunes, and D. Vanderbilt, Phys. Rev. B **47**, 10891 (1993).

[222] G. H. Wannier, Phys. Rev. **52**, 191 (1937).

[223] J. D. Cloizeaux, Phys. Rev. **135**, A685 (1964).

[224] L. He and D. Vanderbilt, Phys. Rev. Lett. **86**, 5341 (2001).

[225] C. Brouder, G. Panati, M. Calandra, C. Mourougane, and N. Marzari, Phys. Rev. Lett. **98**, 046402 (2007).

[226] E. Artacho and L. Miláns del Bosch, Phys. Rev. A **43**, 5770 (1991).

[227] E. Hernández and M. J. Gillan, Phys. Rev. B **51**, 10157 (1995).

[228] C. A. White, P. Maslen, M. S. Lee, and M. Head-Gordon, Chemical Physics Letters **276**, 133 (1997).

[229] C.-K. Skylaris, A. A. Mostofi, P. D. Haynes, C. J. Pickard, and M. C. Payne, Computer Physics Communications **140**, 315 (2001).

[230] A. A. Mostofi, C.-K. Skylaris, P. D. Haynes, and M. C. Payne, Computer Physics Communications **147**, 788 (2002).

[231] C.-K. Skylaris, A. A. Mostofi, P. D. Haynes, O. Diéguez, and M. C. Payne, Phys. Rev. B **66**, 035119 (2002).

[232] V. Blum, R. Gehrke, F. Hanke, P. Havu, V. Havu, X. Ren, K. Reuter, and M. Scheffler, Computer Physics Communications **180**, 2175 (2009).

[233] E. Artacho, D. Sánchez-Portal, P. Ordejón, A. García, and J. M. Soler, physica status solidi (b) **215**, 809 (1999).

Part II

The Hubbard U and Hund's J Parameters with Linear Response

Chapter 4

Calculation of the Hubbard parameters via linear response

Original definitions aside, the Hubbard U and Hund's J are intrinsic, measurable ground-state properties of any multi-atomic system treated with a DFA and thus objects that admit first-principles calculation.[1,2] They are related, respectively, to the interaction contribution to spurious curvature of the total energy with respect to subspace occupancy (described in Section 2.4.1) and, to a more recently established extent, subspace magnetization (see Section 2.4.2). When calculated *in situ*, the Hubbard parameters are expected to appropriately set the strength of the corrective functionals and precisely cancel the systematic errors of DFAs.[1–3]

Many methods for the *in situ* calculation of the Hubbard U parameter have been developed over the last three decades, such as those deriving from constrained DFT (cDFT),[4–13] the constrained Random Phase Approximation (cRPA),[14–20] HF-based approaches,[21–25] and, more recently, density functional perturbation theory (DFPT).[26–28] As a rule, these first-principles determination methods eliminate reliance on empirical data and pave the road for more accurate simulations of obscure or yet-to-be discovered materials. While many of these methods are formally equivalent to each other, others simply do not carry the same definition of the Hubbard U; and for those that do, it remains an open question whether or not parameters deriving from such methods are even comparable since each method makes use of different projector functions, pseudopotentials, and technical details upon practical implementation. As such, very few studies have attempted to make such comparisons.[2,17,29]

In this chapter, we expand on two cDFT approaches: first, in Section 4.1, that of Cococcioni and de Gironcoli,[4] who, following from the work of Pickett *et al.*,[3] developed a practical method for calculating U from first principles called the SCF linear response (LR) method. This method is now widely implemented across a variety of plane-wave-based electronic structure platforms. In Section 4.2, we describe the minimum-tracking LR method,[13,30] technically different to SCF LR and initially designed for direct-minimization algorithms. Both methods have the advantage of defining Hubbard parameters congruent to the functionals by which they will be applied—as modified second derivatives of the total energy with respect to subspace occupancy or magnetization. For both methods, we outline practical protocol with which to assess the response linearity using basic regression and

error analysis methods drawn from statistics. The chapter ends with a section on the occupancy matrices—important constructs that determine the efficacy of DFT+U+J as a corrective method—and how they are influenced by various projector functions.

The core tenet of LR, on which both the SCF and minimum-tracking methods are built, is to apply a small, uniform perturbation to the external potential of the subspace for which U is under assessment.[§][‖] The occupancy response as a result of that perturbation is monitored on the perturbed subspace. The response is expected, for small perturbations, to be a linear function of the perturbation's magnitude.

4.1 SCF linear response for plane-wave DFT schemes

Based on this phenomenon, Ref. [4], following work from Refs. [3] and [31], defined a protocol for calculating the Hubbard U from first principles. This process can be described in terms of constraint formalism and Lagrange coefficients. Consistent with U's definition as the second derivative of the total energy with respect to charge occupancy, site occupancies are penalized when they adopt fractional values of charge. The idea is to control the occupancies of localized subspaces by introducing occupancy targets, where the total energy is found to be[‡]

$$E[\{q_I\}] = \min_{n(\mathbf{r}),\alpha_I} \left\{ E[n(\mathbf{r})] + \sum_I \alpha_I (n_I - q_I) \right\}, \tag{4.2}$$

where the α_I are Lagrange multipliers enforcing constraints on site occupancies n_I. The second derivative of Eq. (4.2) is not quite equal to the spurious curvature we seek to correct, however, because it includes both the *interacting* and *non-interacting* response. The change in site occupancies introduces a hybridization of those localized orbitals with other degrees of freedom, thereby allowing the perturbed subspace to interact extraneously with all other extra-atomic subspaces in the system. These interactions are an artifact of the perturbation only and not related to the curvature associated with intra-atomic Coulomb interactions; therefore, we must subtract from the second derivative of Eq. (4.2) the curvature arising from a conjectured system in which electrons don't interact.[2,5,32] This system has

[§] All atoms, including those with the subspace under scrutiny, in the unit cell of a bulk material are bound to each other by symmetry. Altering the subspace potential and/or occupancies of one atom will alter the subspaces potentials of the other symmetry-related atoms of the same species, both inside the explicitly defined cell and among its mirror images. This ripple effect is counterproductive to the perturbation cardinal to linear response. The occupancy of the perturbed subspace must be allowed to evolve separately to both its mirror images and other atoms of the same species, and the perturbed subspace must be isolated from its periodic images. This will be further explained later in the relevant context.

[‖] It is generally not useful to visualize this perturbation in terms of its uniform effect on the potential of the subspace in question. For the sake of completeness, however, we include such a definition of the perturbation. In the basis of the orbitals that define the subspace $\mathbb{i}$, this contribution to the external potential $V^{\mathbb{i}\sigma}_{mm'}$ is defined in terms of the subspace projection operator $P^{\mathbb{i}}_{mm'}$ by

$$V^{\mathbb{i}\sigma}_{mm'} = \alpha P^{\mathbb{i}}_{mm'} \delta_{m'm}. \tag{4.1}$$

[‡] We adopt without modification the nomenclature as it is in Ref. [4], to which we refer readers for more information on the Langrange-multiplier formulation of linear response.

Kohn-Sham energy:

$$E^{\mathrm{KS}}[\{q_I\}] = \min_{n(\mathbf{r}),\alpha_I} \left\{ E^{\mathrm{KS}}[n(\mathbf{r})] + \sum_I \alpha_I^{\mathrm{KS}}(n_I - q_I) \right\}. \tag{4.3}$$

Thus, U is defined as

$$\mathrm{U} = \frac{\partial^2 E[\{\alpha_I\}]}{\partial q_I^2} - \frac{\partial^2 E^{\mathrm{KS}}[\{\alpha_I\}]}{\partial q_I^2}. \tag{4.4}$$

In computation, it is impractical to place constraints on orbital occupancies. It is more convenient to recast Eqs. (4.2) and (4.3) in terms of a more flexible property, the Lagrange multiplier:

$$E[\{\alpha_I\}] = \min_{n(\mathbf{r})} \left\{ E[n(\mathbf{r})] + \sum_I \alpha_I n_I \right\} \tag{4.5}$$

$$E^{\mathrm{KS}}[\{\alpha_I\}] = \min_{n(\mathbf{r})} \left\{ E^{\mathrm{KS}}[n(\mathbf{r})] + \sum_I \alpha_I^{\mathrm{KS}} n_I \right\} \tag{4.6}$$

As before, we take the second derivative of these energies with respect to occupancy and discount the KS energy curvature (the non-interacting response),[2,5,32] obtaining the Dyson-like equation,

$$\mathrm{U} = \underbrace{\frac{\partial^2 E^{\mathrm{KS}}[\{\alpha_I\}]}{\partial n_I^2}}_{\chi_0^{-1}} - \underbrace{\frac{\partial^2 E[\{\alpha_I\}]}{\partial n_I^2}}_{\chi^{-1}}. \tag{4.7}$$

In practical terms, the response functions χ and χ_0 are determined by serially applying several perturbations of strength $\{\alpha\}$ in equal magnitude to the up- and down-spin channels of a subspace's external potential. Once the potential perturbation is applied, but before the density is calculated and the Hamiltonian updated to start the new SCF iteration, the ground-state spin-up and spin-down charge occupancies on the perturbed atom respond to the perturbation, but not to each others' response—in principle, a micro-system in which the electrons of the ground state do not interact. Within this system, we're interested only in the change in total non-interacting occupancy ($n_0^{\uparrow} + n_0^{\downarrow}$) with respect to α, which then goes on to define the non-interacting response

$$\chi_0 = \frac{d(n_0^{\uparrow} + n_0^{\downarrow})}{d\alpha}. \tag{4.8}$$

Following the update of the Hamiltonian in the next SCF iteration, the system self-consistently screens the perturbation, reorganizing its charge once again until it reaches an equilibrium state. The derivative of this equilibrium occupancy with respect to the perturbation magnitude is the finally fully converged interacting response function,

$$\chi = \frac{d(n^{\uparrow} + n^{\downarrow})}{d\alpha}, \tag{4.9}$$

where $n^{\uparrow}$ and $n^{\downarrow}$ are the ground-state occupancies of the subspace harvested after the last self-consistent

iteration. Finally, the response functions are inverted, and their difference composes the Dyson equation for the Hubbard U term,

$$U = \chi_0^{-1} - \chi^{-1}. \tag{4.10}$$

Ideally, U is calculated for a cell of infinite size so that the perturbed subspace is isolated from its periodic images. Since this is computationally unfeasible, U must be converged with respect to an increasing number of atoms, organized into a roughly cubic supercell to isotropically distribute the effect of the perturbation.

The Hund's coupling J parameter can be calculated similarly [13,33]; instead of monitoring the change in total subspace occupancy as a function of the applied perturbation α, however, the Hund's J monitors changes in magnetization, or the difference between the up- and down-spin occupancies, in response to a perturbation β applied in positive magnitude to the spin-up channel and in negative magnitude to the spin-down channel.[§] Positive β perturbations make the spin-down channel more attractive to electrons in the bath while repulsing electrons in the spin-up channel, ultimately encouraging the subspace to adopt a smaller magnetization. Negative β, alternatively, result in larger magnetizations. Noting the minus-sign convention, within SCF linear response J is given by [34]

$$\begin{aligned} \mathrm{J} &= -\left[\frac{d\beta}{d(n_0^{\uparrow} - n_0^{\downarrow})} - \frac{d\beta}{d\left(n^{\uparrow} - n^{\downarrow}\right)}\right] \\ &= -\left[\chi_{0_M}^{-1} - \chi_M^{-1}\right]. \end{aligned} \tag{4.12}$$

In Section 4.1.2, we show that χ_0 and χ_{0_M} are equivalent, a particularly convenient result for verifying linear response implementations like that proposed in Chapter 5. We note here that Eqs. (4.10) and (4.12) have been derived for use within approximate collinear-spin KS DFT, where only the z-projection of spin magnetic moments is considered in the treatment of XC effects. The extension of such error quantities to approximate non-collinear-spin DFT is a subject worthy of investigation in its own right but outside the scope of this thesis.

Defined as they are here, the U and J can be thought of as error descriptors for SIE and SCE, respectively, in the approximate XC functional within the subspace-bath decoupling picture of DFT+U+J rather than as absolute interaction strengths. Furthermore, on the topic of interpretation and terminology, we note that J is an exchange parameter only in the magnetic sense, and it may comprise a significant or even dominant contribution from correlation (as distinct from exchange in the sense of accessibility at the HF level of theory). Indeed, as calculated here it will, by construction, contain a 'spin-flip exchange' contribution, which is considered a contribution to correlation as it does not appear in a HF treatment. [35]

[§]The β perturbation takes on the following form with regards to the effect on the $\mathbb{i}$ subspace potential:

$$V_{mm'}^{\mathbb{i}\uparrow} = \beta P_{mm'}^{\mathbb{i}} \delta_{m'm}, \quad V_{mm'}^{\mathbb{i}\downarrow} = -\beta P_{mm'}^{\mathbb{i}} \delta_{m'm}. \tag{4.11}$$

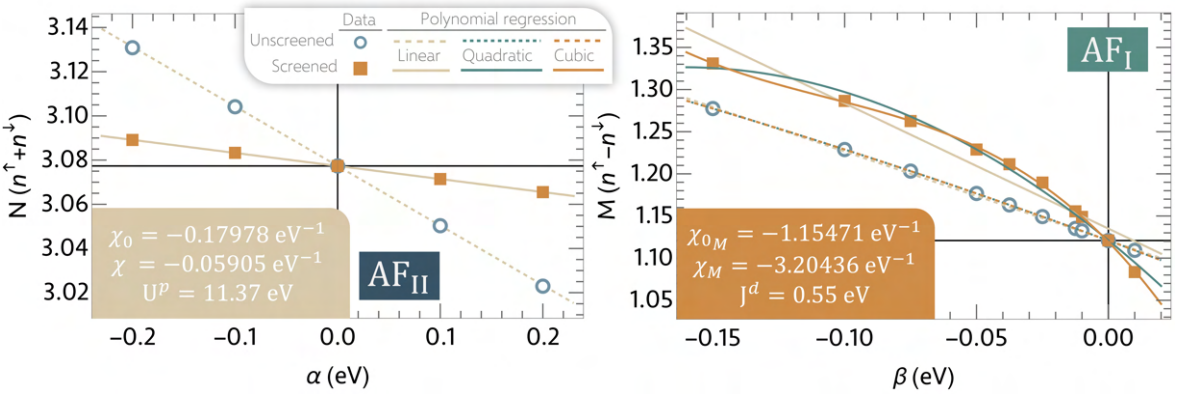

Figure 4.1: [Left] Example of the linear response (LR) procedure with first-order polynomial regression only, conducted to find the Hubbard U *for* O *2p orbitals on* AF_{II} NiO. *[Right]* J *parameter LR for* Ni *3d orbitals on* AF_I NiO. *Line and box color indicate first, second, or third order polynomial fit on the data. Axes are aligned with ground-state (unperturbed) data. Note:* χ_0, χ_{0_M} *data points and fits are transformed to account for technical considerations. (See Section 5.3.4 for elaboration.) See Part III Section 7.1.1 for computational details for these systems.*

4.1.1 Determining the error on linear response Hubbard parameters

The linearity condition manifests in the nature of χ and χ_0 as functions; however, the response behavior is not always linear. Fig. 4.1(b) demonstrates this for an exceptionally ill-behaved system. With some exceptions, linearity is expected in the limit of small perturbations, but this region is not always accessible, particularly when the response is excessively rigid (e.g., close to full filling). If the perturbations are too large, one can generally expect some non-linear behavior. Non-linearity, and sometimes asymmetry across the line perpendicular to the derivative at zero perturbation (an axis I will call ζ), is also encountered. This non-linearity could be caused in part by anharmonicity in the total and band structure energies. Otherwise, we intuit that it has something to do with the system's energy landscape. For example, a particularly shallow energy landscape (i.e., when the response is excessively soft, e.g., close to a phase transition), one could expect some non-linear response as the perturbation pushes the system away from its ground state. More research is needed to determine the source(s) of this behavior.

As a palliative fix for such anomalies, we fit a regression function to the LR data and differentiate at $\alpha = \beta = 0.0$ eV to find the response functions.[34] We use polynomial regressions, typically up to the cubic degree, due to their versatility, simple derivatives, and variable symmetry across the ζ-axis. This is sufficient for most LR we've insofar encountered, however it is suspected that there are more physically justifiable functions better-suited to response.

To demonstrate how this is done in practice, consider one (either the screened or unscreened case) of two datasets consisting of m pairs of (α_i, μ_i) perturbation-total occupancy data points for determination of the Hubbard U. We consider there to be no uncertainty on the perturbation strengths α_i and that the total occupancies ($\mu_i = n_i^{\uparrow} + n_i^{\downarrow}$ in the screened case or $\mu_i = n_{0_i}^{\uparrow} + n_{0_i}^{\downarrow}$ in the unscreened case) adhere to a Gaussian distribution about the least-squares-fitted polynomial function $f^{(p)}(\alpha) = \sum_{q=0}^{p} c_q \alpha^q$, where p is the polynomial degree and c_q are the polynomial coefficients. Since we differentiate $f^{(p)}$

at $\alpha = 0.0$ eV to obtain the scalar response values, it follows that $\mathrm{X} = \{\chi_0, \chi\}$ are embodied by the $q = 1$ coefficient c_1 for polynomials of any degree. The estimated polynomial coefficients are obtained through a least-squares fitting of the data.

There exist several statistical methods for the determination of the uncertainty on the regression coefficients.[36–39] We select an approach that avoids overfitting the polynomials to the data by incorporating the polynomial degree in the evaluation of the sample standard deviation of the μ_i residuals. This type of uncertainty on the $q = 1$ regression coefficient for the unscreened and screened responses, $\sigma_{\chi_0}^{(p)}$ and $\sigma_{\chi}^{(p)}$ respectively, is thus found to be

$$\sigma_{\mathrm{X}}^{(p)} = \sqrt{\frac{\sum_{i=1}^{m}\left[\mu_i - f^{(p)}\left(\alpha_i\right)\right]^2}{m-p-1}\left(\mathbf{A}^{\top}\mathbf{A}\right)_{22}^{-1}}\,, \tag{4.13}$$

where $\mathbf{A}$ is a $m \times (p+1)$ matrix with elements $A_{i,q+1} = \alpha_i^q$. The error on the Hubbard parameter is then calculated as

$$\sigma_{\mathrm{U}}^{(p)} = \sqrt{\left(\frac{\sigma_{\chi_0}^{(p)}}{\chi_0^2}\right)^2 + \left(\frac{\sigma_{\chi}^{(p)}}{\chi^2}\right)^2}\,. \tag{4.14}$$

The same error assessment in Eqs. (4.13)-(4.14) is true for J, where χ_{0_M} (χ_M) substitutes for χ_0 (χ), and the LR dataset is composed of β_i-perturbations and corresponding subspace magnetization ($\mu_i = n_i^{\uparrow} - n_i^{\downarrow}$ in the screened case or $\mu_i = n_{0_i}^{\uparrow} - n_{0_i}^{\downarrow}$ in the unscreened case) data points. It is necessary to emphasize that in accompanying the HPs with an error range $\pm\sigma_{\mathrm{HP}}$, we do not assert to know the global value of the Coulomb- and exchange-interaction strengths to within this degree of precision. Rather, σ_{HP} is considered a measure of how well-behaved was the LR conducted on this particular subspace. To avoid overfitting the data, $m \geq 5$ and $p \leq 3$ for all response conducted in the studies comprising this thesis, and the polynomials selected for χ and χ_0 have the same degree for coherence and simplicity in the resulting parameters. Choosing which polynomial best represents the response is a matter of minimizing the error on the Hubbard parameter and eyeing the response itself. For example, in some cases, the polynomial corresponding to a minimized σ_{HP} is not the same as the polynomial that best fits the raw response data, which exhibit from time-to-time noticeable and well-defined ζ-axis symmetries (as demonstrated in Fig. 4.1).

4.1.2 Proof of equivalence of unscreened response for α and β perturbations

Theorem: The unscreened response matrices $\chi_0 = \frac{d(n_0^{\uparrow}+n_0^{\downarrow})}{d\alpha}$ and $\chi_{0_M} = \frac{d(n_0^{\uparrow}-n_0^{\downarrow})}{d\beta}$ are equivalent.

Proof: Suppose we apply a potential perturbation to separate spin channels $dV_{\mathrm{ext}}^{\uparrow} = \alpha$ and $dV_{\mathrm{ext}}^{\downarrow} = \alpha$ to a subspace on an atom. The unscreened change in occupancy of the spin-up channel (without loss of generality) $n_0^{\uparrow}$ resulting from this perturbation is

$$\frac{dn_0^{\uparrow}}{dV_{\mathrm{ext}}} = \frac{dn_0^{\uparrow}}{dV_{\mathrm{ext}}^{\uparrow}}\frac{dV_{\mathrm{ext}}^{\uparrow}}{dV_{\mathrm{ext}}} + \frac{dn_0^{\uparrow}}{dV_{\mathrm{ext}}^{\downarrow}}\frac{dV_{\mathrm{ext}}^{\downarrow}}{dV_{\mathrm{ext}}}. \tag{4.15}$$

The second term of Eq. (4.15) disappears because the occupancy of a spin channel does not change as a result of a potential perturbation on the opposing spin channel (i.e., $dn_0^{\uparrow}/dV_{\text{ext}}^{\downarrow} = 0$). Then $dV_{\text{ext}}^{\uparrow}/dV_{\text{ext}} = 1$, leaving

$$\frac{dn_0^{\uparrow}}{dV_{\text{ext}}} = \frac{dn_0^{\uparrow}}{dV_{\text{ext}}^{\uparrow}} = \frac{dn_0^{\uparrow}}{d\alpha}. \tag{4.16}$$

Analogously, we find

$$\frac{dn_0^{\downarrow}}{dV_{\text{ext}}} = \frac{dn_0^{\downarrow}}{d\alpha}, \tag{4.17}$$

and thus the unscreened change in total occupancy of the subspace, where $N_0 = n_0^{\uparrow} + n_0^{\downarrow}$, is

$$\chi_0 = \frac{dN_0}{dV_{\text{ext}}} = \frac{d(n_0^{\uparrow} + n_0^{\downarrow})}{d\alpha}. \tag{4.18}$$

Now consider on a completely identical subspace on a completely identical atom, we apply a potential perturbation of $dV_{\text{ext}}^{\uparrow} = \beta$ to the spin-up channel and $dV_{\text{ext}}^{\downarrow} = -\beta$ to the spin-down channel. Monitoring now the unscreened change in magnetization $M_0 = n_0^{\uparrow} - n_0^{\downarrow}$ as a result of this perturbation, we find

$$\begin{aligned} \chi_{0_M} &= \frac{dM_0}{dV_{\text{ext}}} = \frac{d(n_0^{\uparrow} - n_0^{\downarrow})}{d\beta} \\ &= \frac{dn_0^{\uparrow}}{d\beta} - \frac{dn_0^{\downarrow}}{d\beta}. \end{aligned} \tag{4.19}$$

The change in spin-up occupancy with respect to β is found to be identical to Eq. (4.15). But because a negatively valued β perturbation is applied to the spin-down channel potential,

$$\frac{dn_0^{\downarrow}}{dV_{\text{ext}}} = -\frac{dn_0^{\downarrow}}{d\beta}. \tag{4.20}$$

Thus,

$$\begin{aligned} \chi_{0_M} &= \frac{dM_0}{dV_{\text{ext}}} = \frac{dn_0^{\uparrow}}{d\beta} - \left(-\frac{dn_0^{\downarrow}}{d\beta}\right) \\ \therefore \chi_{0_M} &= \frac{d(n_0^{\uparrow} + n_0^{\downarrow})}{d\beta} \end{aligned} \tag{4.21}$$

In the event that $\alpha = \beta$, therefore, $\chi_0 = \chi_{0_M}$ following Eqs. (4.18) and (4.21). □

4.2 Minimum-tracking linear response

The formalism for the *ab initio* calculation of the Hubbard parameters via linear reponse, as described in Section 4.1, was constructed explicitly for implementation in electronic structure theory packages that locate the ground state of a quantum system by relaxing the electronic density by self-consistent cycle. We see this architecture manifest in how the non-interacting response term χ_0 is harvested. However, algorithms like ONETEP employ schemes in which the total-energy is directly minimized to locate the ground state. To make *ab initio* Hubbard parameter calculations accessible to these codes, Moynihan[40] and Linscott *et al.*[13] reformulated Cococcioni and de Gironcoli's[4] linear response formalism in terms of direct-minimization procedure-specific bodies. This procedure is called minimum-tracking linear response, and it may be implemented also in SCF codes.

We start by applying a perturbing potential $d\hat{V}_{\text{ext}} = dV^{\mathbb{j}}_{\text{ext}}\hat{P}^{\mathbb{j}}$ to the Hubbard subspace $\mathbb{j}$. The response recorded by the KS potential of subspace $\mathbb{i}$ is

$$\frac{dV^{\mathbb{i}}_{\text{KS}}}{dV^{\mathbb{j}}_{\text{ext}}} = \frac{dV^{\mathbb{i}}_{\text{ext}}}{dV^{\mathbb{j}}_{\text{ext}}} + \frac{dV^{\mathbb{i}}_{\text{hxc}}}{dV^{\mathbb{j}}_{\text{ext}}} = \frac{dV^{\mathbb{i}}_{\text{ext}}}{dV^{\mathbb{j}}_{\text{ext}}} + \sum_{\mathbb{k}} \frac{dV^{\mathbb{i}}_{\text{hxc}}}{dn^{\mathbb{k}}} \frac{dn^{\mathbb{k}}}{dV^{\mathbb{j}}_{\text{ext}}}\,, \tag{4.22}$$

where we see that V_{KS} decomposes to the sum of the external potential V_{ext} and the Hartree and XC potential V_{hxc}. This formula may be written in a way that makes its self-consistent nature more obvious. Defining $f_{\mathbb{ij}} \equiv dV^{\mathbb{i}}_{\text{hxc}}/dn^{\mathbb{j}}$, $\left(\varepsilon^{-1}\right)_{\mathbb{ij}} \equiv dV^{i}_{\text{KS}}i/dV^{\mathbb{j}}_{\text{ext}}$, and noting that to a reasonable approximation $dV^{\mathbb{i}}_{\text{ext}}/dV^{\mathbb{j}}_{\text{ext}} = \delta_{\mathbb{ij}}$, Eq. (4.22) becomes

$$f = \left(\varepsilon^{-1} - \delta_{\mathbb{ij}}\right)\chi^{-1}, \tag{4.23}$$

where χ^{-1} is the projected response matrix. From here, defining the Hubbard U parameter as precisely the change in the HXC potential of the $\mathbb{i}$ subspace with respect to its own occupancy, we find

$$\mathrm{U}^{\mathbb{i}} = f_{\mathbb{ii}} = \left[\left(\frac{dV_{\text{KS}}}{dV_{\text{ext}}} - 1\right)\left(\frac{dn}{dV_{\text{ext}}}\right)^{-1}\right]_{\mathbb{ii}}. \tag{4.24}$$

Eq. (4.24) is simply a recasting of the SCF linear response definition of U in Eq. (4.10), wherein the effective non-interacting response χ_0 in addition to χ can be clearly identified. Importantly, the two formalisms also differ in the sets of densities employed in the calculation of U. The minimum-tracking algorithm ensures that U is exclusively a ground-state property due to its exclusive employment of the ground-state densities in the perturbed system. Conversely, the SCF procedure calculates U with a non-consistent density. It is not clear whether this distinction generates any meaningful numerical discrepancies.

The Hubbard energy in Eq. (2.38) treats atomic sites and spin channels as though they are interchangeable. To manifest the same in minimum-tracking, we define the response matrices as

$$\chi^{\sigma\sigma'}_{\mathbb{ij}} = \frac{dn^{\mathbb{i}\sigma}}{dV^{\mathbb{j}\sigma'}_{\text{ext}}}. \tag{4.25}$$

These matrices can be visualized as rank-four tensors flattened to rank-two tensors, as in Eq. (14) of Ref. [13]. What becomes important in this definition is how to perform the inversion intrinsic to Eq. (4.24). There are three methods available for such an inversion procedure: (a) point-wise inversion, in which both site and spin are simultaneously decoupled. The system is treated as a one-site Hubbard model connected to a charge bath wherein the opposite spin subspace is embedded. The Hubbard parameters are thus screened by the opposite spin on the same site. The split will lend itself to the calculation of two U parameters: one for spin-up and the other for spin-down. The final Hubbard U, which is spin-independent, is then calculated as the average of the two spin-resolved U; (b) full inversion, where the matrix is fully inverted. All sites and spins remain coupled, and both spin channels on one atomic site are treated as a singular Hubbard site. This implies the necessity for another corrective term to compensate for inter-site interactions; and (c) atom-wise inversion: decouple the sites, but not the spins. In the investigations to follow, we typically employ option (c) and thus expand on its procedure.

In atom-wise inversion, the Hubbard parameters are not screened by the spin channels on the same atomic site. This effectively treats the subspace as a two-site system connected to a charge bath. However, in applying this approach, one must manage the spin-screened interactions in another way (i.e., through the addition of the Hund's J parameter). If we make the assumption that the response matrices of both spin channels on all sites are equivalent, we arrive at the following definitions,

$$\mathrm{U} = \frac{1}{4}(f^{\uparrow\uparrow} + f^{\uparrow\downarrow} + f^{\downarrow\uparrow} + f^{\downarrow\downarrow}) \qquad \mathrm{J} = -\frac{1}{4}(f^{\uparrow\uparrow} - f^{\uparrow\downarrow} - f^{\downarrow\uparrow} + f^{\downarrow\downarrow})\,, \tag{4.26}$$

where $f^{\sigma\sigma'}$ are the site- and spin-specific U values defined as in Eq. (4.24),

$$f^{\sigma\sigma'} = \left[\left(\frac{dV_{\mathrm{KS}}}{dV_{\mathrm{ext}}} - 1\right)\left(\frac{dn}{dV_{\mathrm{ext}}}\right)^{-1}\right]^{\sigma\sigma'}. \tag{4.27}$$

The U and J in Eq. (4.26) are called the 'simple 2x2' parameters. A more sophisticated approach, however, is to assume that the spin channels will react differently to the perturbations applied to them. With this in mind, the 'scaled 2x2' Hubbard parameters are found to be

$$\mathrm{U} = \frac{1}{2}\frac{\lambda_{\mathrm{U}}\left(f^{\uparrow\uparrow} + f^{\downarrow\uparrow}\right) + f^{\uparrow\downarrow} + f^{\downarrow\downarrow}}{\lambda_{\mathrm{U}} + 1} \qquad \mathrm{J} = -\frac{1}{2}\frac{\lambda_{\mathrm{J}}\left(f^{\uparrow\uparrow} - f^{\downarrow\uparrow}\right) + f^{\uparrow\downarrow} - f^{\downarrow\downarrow}}{\lambda_{\mathrm{J}} + 1} \tag{4.28}$$

where $\lambda_{\substack{\mathrm{U}\\\mathrm{J}}} = \left(\chi^{\uparrow\uparrow} \pm \chi^{\uparrow\downarrow}\right) / \left(\chi^{\downarrow\uparrow} \pm \chi^{\downarrow\downarrow}\right)$. In terms of the practical implementation of the scalar U and J parameters, however, the following definitions are found to be entirely equivalent,

$$\mathrm{U} = \frac{1}{2}\frac{d(V^{\uparrow}_{\mathrm{hxc}} + V^{\downarrow}_{\mathrm{hxc}})}{d(n^{\uparrow} + n^{\downarrow})} \qquad J = -\frac{1}{2}\frac{d(V^{\uparrow}_{\mathrm{hxc}} - V^{\downarrow}_{\mathrm{hxc}})}{d(n^{\uparrow} - n^{\downarrow})}\,, \tag{4.29}$$

where $n^{\uparrow} \pm n^{\downarrow} = \mathrm{Tr}[\hat{P}(\hat{\rho}^{\uparrow} \pm \hat{\rho}^{\downarrow})]$ is the total charge occupancy N / magnetization M as a function of the spin density operator $\hat{\rho}^{\sigma}$. This solidifies the necessity of including the Hund's J parameter on the same footing as U in any linear response procedure. In the studies that follow, unless otherwise stated, we use Eq. (4.29) as the minimum-tracking LR definitions of the Hubbard U and Hund's J. We refer

the reader to Ref. [13] for more information on spin considerations in this methodology.

4.2.1 Determining the error on the minimum-tracking Hubbard parameters

In a manner analogous to the uncertainty quantification in SCF LR (see Section 4.1.1), we address non-linearity in the response by fitting degree p polynomial regressions $f^{(p)}\left(N(\alpha)\right) = \sum_{q=0}^{p} c_q N(\alpha)^q$, where c_q are the polynomial coefficients determined via a least-squares fitting to the response data set. In the case of the Hubbard U, the response data comprises m occupancy-HXC potential pairs $\left(N(\alpha_i), V^{+}_{\mathrm{hxc}_i}\right)$, where $N(\alpha_i) = \left[n^{\uparrow} + n^{\downarrow}\right]\Big|_{\alpha_i}$ is the total occupancy arising from the α_i-perturbed subspace, and $V^{+}_{\mathrm{hxc}_i} = V^{\uparrow}_{\mathrm{hxc}_i} + V^{\downarrow}_{\mathrm{hxc}_i}$. The Hubbard U is then calculated following Eq. (4.29) through the evaluation of the derivative of the regression at $\alpha = 0$,

$$\mathrm{U} = \frac{1}{2}\sum_{q=0}^{p} q\, c_q\, N(0)^{q-1}\ . \tag{4.30}$$

The Hubbard U is thus a multivariate function with respect to the fitted coefficients. It is important (and, indeed, numerically imperative) to assert that the fitted polynomial coefficients are covariate, meaning their uncertainties do not vary independently. Therefore, the error on the minimum-tracking LR Hubbard U is found to be

$$\sigma^{(p)}_{\mathrm{U}} = \frac{1}{2}\sqrt{\sum_{q=0}^{p}\sum_{r=0}^{p} q\, r\, C_{q+1,r+1}\, N(0)^{q+r-2}}\quad , \tag{4.31}$$

where, as in Eq. (4.13), we use the unbiased standard deviation and the $m \times (p+1)$ design matrix $\mathbf{A}$ with elements $A_{i,q+1} = N(\alpha_i)^q$ to compute the covariance matrix $\mathbf{C}$, featuring matrix elements

$$C_{q+1,r+1} = \frac{\sum_{i=1}^{m}\left[V^{+}_{\mathrm{hxc}_i} - f^{(p)}\left(N(\alpha_i)\right)\right]^2}{m-p-1}\left(\mathbf{A}^{\top}\mathbf{A}\right)^{-1}_{q+1,r+1}\ . \tag{4.32}$$

Uncertainty on the Hund's J may be calculated by replacing all instances of α with β, total occupancy $N(\alpha)$ with subspace magnetization $M(\beta) = \left[n^{\uparrow} - n^{\downarrow}\right]\Big|_{\beta}$, and $V^{+}_{\mathrm{hxc}_i}$ with $V^{-}_{\mathrm{hxc}_i} = V^{\uparrow}_{\mathrm{hxc}_i} - V^{\downarrow}_{\mathrm{hxc}_i}$. Furthermore, the $\frac{1}{2}$ prefactor in Eq. (4.30) should be replaced by $-\frac{1}{2}$. Encouragingly, for all subspaces on which we conduct MT linear response in this dissertation, we found that the uncertainty incorporating the covariance between polynomial coefficients, described by Eqs. (4.31) and (4.32) is, in practice, reasonably identical to the regression error obtained when shifting the $N(\alpha_i)$ values by $-N(0)$. In this case, one may evaluate the derivative about a zero-perturbation axis, rendering the HP a singly-variate function of c_1 and the uncertainty of which may be evaluated with an analogous formula to that in Eq. (4.13).

We emphasize here that quantification of the uncertainty on the Hubbard parameters, specifically those arising from response demonstrating non-linear behavior, is a topical research query that warrants more consideration than is given in this dissertation. The definition and appropriateness of the

unbiased standard deviation in the response context, for example, is not a universally agreed-upon matter. The application of state-of-the-art statistical techniques to linear response merits its own systematic investigation that lies beyond the scope of this thesis.

4.3 The occupancy matrices

As observed in both this chapter and Section 2.5, the special ingredient in both DFT+U+J functionals and in the numerical determination of the functionals' parameters is the subspace occupancy maxtrix $\mathbf{n}^{\mathbb{i}\sigma}$ and its elements $\{n^{\mathbb{i}\sigma}_{mm'}\}$.

However, there is no mathematically rigorous or precise way to define localized electron occupancy on atoms in a multi-atom system.[4] The treatment of the Hubbard parameters under DFT+U+J-type corrective functionals is prescribed exclusively for the spatially localized correlated subspaces that require computational attention in excess of that required by the non-correlated bath surrounding those subspaces, for which the base XC functional is descriptively sufficient.[41] The machinery that isolate these treated subspaces, encapsulating their charge occupancy both for the evaluation of the Hubbard parameters themselves and in their application via the total-energy functional, are the subspace projector functions $P^{\mathbb{i}}_{mm'}$. Reliance on projector functions that are unsuitable reflections of the correct localization, either by excessive localization, unphysical discontinuities, or by excessive overlap,[40] will likely result in erroneous population analysis and, by consequence, inefficient or otherwise defective corrective protocol.[4] Thus, the utility of DFT+U+J as an error-compensation protocol is predetermined by the accuracy of the basis sets in describing the underlying physics of the system under consideration.

Often, the occupancy matrices are simply defined as

$$n^{\mathbb{i}\sigma}_{mm'} = \sum_{k,v} f^{\sigma}_{kv} \langle \psi^{\sigma}_{kv} | \phi^{\mathbb{i}}_{m'} \rangle \langle \phi^{\mathbb{i}}_{m} | \psi^{\sigma}_{kv} \rangle \,, \tag{4.33}$$

where ψ^{σ}_{kv} is the KS orbital corresponding to k-point k and band index v, and $\phi^{\mathbb{i}}_{m'}$ is the localized basis function assigned to magnetic quantum number m' on subspace $\mathbb{i}$. The f^{σ}_{kv} is the Fermi-Dirac distribution function applied to the KS orbitals, which is the mechanism that effectively fractionalizes the charge occupancy in accordance with Fermi-Dirac statistics. The Fermi-Dirac distribution function is defined as

$$f_{kv} = \frac{1}{1 + e^{\frac{\epsilon_{kv} - \mu}{\theta}}}, \tag{4.34}$$

where ϵ_{kv} is the orbital energy associated with the KS orbital, μ is the chemical potential chosen explicitly to conserve the total number of electrons, and θ is the smearing parameter used to mitigate the sharpness of the incline between states 0 and 1. The values of this function are restricted to real numbers between 0 and 1, and the sum of f_{kv} over all k-points and band indices is the total charge.[42]

The occupancy matrix in Eq. (4.33) is a generalized projection of the KS orbitals onto a particular localized basis set chosen to tailor the DFT+U+J calculation to existing DFT algorithms (e.g., Wannier functions); that choice is typically limited by the options made available by the developers of the DFT+U+J implementation in question. Comparison should be drawn from the effect of the Hubbard

parameters on observable properties, not necessarily from the parameters themselves. Moreover, we call into question the efficacy of system-independent projections and fixed Hubbard parameters at all, recognizing that transition metal centers of multiple-valence systems are often temperamental with respect to changes in charge and spin state, a sensitivity that can have macroscopic consequences on system observables.

All analyses comprising this thesis comment in some form on the projectors and how they manifest in DFT+U+J. In the next section, we introduce common projector functions that end up featuring in our studies. In particular, Chapter 10 looks at the effect of systematic modification of these projectors on the value of the Hubbard U parameters for certain molecular systems. Chapter 5 and Part III both involve the PAW method, so the PAW projectors and their influence on the occupancy matrices are examined in Section 4.3.2. The results that follow offer a solid starting block for a protocol designed to choose the appropriate projector function(s), tailored to the system under consideration, which represent well a subspace's susceptibility to SIE and/or SCE, so as to maximize the efficacy—and comparability across electronic structure theory programs—of DFT+U+J-type corrective functionals.

4.3.1 Common projector functions

Common choices of projector function include linear muffin-tin orbitals,[31,43–46] maximally localized Wannier functions,[8,47,48] and, of course, the hydrogen-like radial atomic wavefunctions,[4,49–51]

By default, QUANTUM ESPRESSO uses atomic projectors, informed by the input pseudopotentials, and optionally their ortho-normalized versions. The effect of these projectors on the Hubbard parameters features as part of the investigation in Chapter 9. The PAW method,[52] the theory of which is described in Section 3.1.4, offers comparatively direct control over the population analysis via the projector basis function. In the next section, we describe this relation in detail to prepare for Chapter 5 as well as the investigation in Part III.

Moreover, as mentioned in Section 3.2.5 (and as will become important in Chapter 10), ONETEP uses pseudoatomic orbital projections to internally generate, from the occupied KS states of neutral atoms subject to an underlying XC functional, its radial NGWFs.[53,54] These projectors can be cleanly manipulated by changing the valence subspace occupancy.[54] We demonstrate in Fig. 10.4 for the $1s$ orbital of a distended H_2^+ molecule the dismorphia of the initial radial NGWFs as the number of electrons occupying each H atom is varied between 0 and 1.

4.3.2 PAW projectors

In ABINIT, the DFT+U+J formalism is built into the program's projector-augmented wave (PAW)[52] functionality. Consequently, the population analysis relies heavily on the PAW projectors. Recall from Section 3.1.4 that the PAW projectors[52] are one of three predefined basis sets fed into DFT algorithms via the pseudopotential apparatus. These projectors are designed to isolate a spherically symmetric, element-specific region—an augmentation sphere—about each atomic site, using a relatively small cutoff radius r_c.

Within PAW, the DFT+U+J occupancy matrix elements are obtained via the pseudo- (PS) wave-

functions $\widetilde{\Psi}^{\sigma}_{kv}$ by computing

$$n^{i\sigma}_{mm'} = \sum_{k,v} f^{\sigma}_{kv} \langle \widetilde{\Psi}^{\sigma}_{kv} | \widetilde{P}^{i}_{mm'} | \widetilde{\Psi}^{\sigma}_{kv} \rangle. \tag{4.35}$$

Assuming that the charge of the subspace under scrutiny is localized about the atom, we may use the definition of a local PAW PS operator (Eq. (11) in Ref. [52]) to expand the pseudized projection operator $\widetilde{P}^{i}_{mm'}$ in terms of the KS projection operator $P^{i}_{mm'}$ and the PAW basis functions: the all-electron (AE) basis ϕ_i, the PS basis $\widetilde{\phi}_i$, and the projectors $\widetilde{p}_i$. That is

$$\begin{aligned} \widetilde{P}^{i}_{mm'} = P^{i}_{mm'} &+ \sum_{ij} |\widetilde{p}_i\rangle\langle\phi_i| P^{i}_{mm'} |\phi_j\rangle\langle\widetilde{p}_j| \\ &- \sum_{ij} |\widetilde{p}_i\rangle\langle\widetilde{\phi}_i| P^{i}_{mm'} |\widetilde{\phi}_j\rangle\langle\widetilde{p}_j|, \end{aligned} \tag{4.36}$$

where the indices i are assigned to sets of $\{a, \ell_i, m_{\ell_i}, n_i\}$), which respectively refer to the site index, angular quantum number, magnetic quantum number, and PAW partial-wave index. Similarly, an analogous set of numbers $(b, \ell_j, m_{\ell_j}, n_j)$ pertains to index j. When Eq. (4.36) is inserted into Eq. (4.35), three terms emerge, two of which cancel because a requisite in the formation of the PAW basis functions assumes that $\sum_i |\widetilde{p}_i\rangle\langle\widetilde{\phi}_i| = 1$ is maintained inside the augmentation region. Acknowledging that $\phi_i = \phi_{\ell_i m_i n_i} = \phi_{n_i} Y_{\ell_i m_i}$, we are left with

$$n^{i\sigma}_{mm'} = \sum_{ij} \rho^{\sigma}_{ij} \langle \phi_{n_i} | P^{i}_{mm'} | \phi_{n_j} \rangle, \tag{4.37}$$

where ϕ_n are the radial parts of the PAW AE basis functions, and the PAW-sphere density matrix is

$$\rho^{\sigma}_{ij} = \sum_{k,v} f^{\sigma}_{kv} \langle \widetilde{\Psi}^{\sigma}_{kv} | \widetilde{p}_i \rangle \langle \widetilde{p}_j | \widetilde{\Psi}^{\sigma}_{kv} \rangle. \tag{4.38}$$

The distribution of charge density about an atom is, in practice, oblivious to the sharp truncation of these PAW projectors at the cutoff radius; even the charge of supposedly localized orbitals often escapes beyond the confines of the augmentation sphere. Care must be taken in selecting an appropriate projector, as the selection can have far-reaching numerical implications,[55–60] which we demonstrate as part of Part III.

Four PAW occupancy matrix projector options are available in ABINIT. For simplicity and ease of reference, we refer to each option by the integer value of its ABINIT input file variable, `dmatpuopt` (Density MATrix for PAW+U OPTion), which may take on values one through four.[61] For example, when `dmatpuopt = 1`, occupancies are projections on atomic orbitals,[62] per the definition

$$n^{i\sigma}_{mm'} = \sum_{ij} \rho^{\sigma}_{ij} \left\langle \phi_{n_i} \middle| \phi_0 \right\rangle \left\langle \phi_0 \middle| \phi_{n_j} \right\rangle, \tag{4.39}$$

where ϕ_0 are normalized, bound-state atomic eigenfunctions pertaining to PAW partial wave index $n_i = 1$, drawn from the list of AE wavefunctions pertaining to the subspace in question. Importantly, the integrals $\langle \phi_{n_i} | \phi_0 \rangle$ and $\langle \phi_0 | \phi_{n_j} \rangle$ are computed within the PAW augmentation sphere.

By contrast, when `dmatpuopt = 2`, which is the default setting, occupancies are integrated in

PAW augmentation spheres of charge densities decomposed by angular momentum, per

$$n^{\mathbb{i}\sigma}_{mm'} = \sum_{ij} \rho^{\sigma}_{ij} \left\langle \phi_{n_i} \middle| \phi_{n_j} \right\rangle. \tag{4.40}$$

Again, $\left\langle \phi_{n_i} \middle| \phi_{n_j} \right\rangle$ is an integral defined only in the PAW augmentation region.[62] Eq. (4.40) may be derived from Eq. (4.35) by setting[56,63]

$$P^{\mathbb{i}}_{mm'}(\mathbf{r}, \mathbf{r}') = 1_{\circ}(\mathbf{r})\, \delta(|\mathbf{r}' - \mathbf{R}_a| - |\mathbf{r} - \mathbf{R}_a|) \times Y_{\ell m}(\hat{\mathbf{r}}) Y^{*}_{\ell m'}(\hat{\mathbf{r}}'), \tag{4.41}$$

where δ is the Dirac-Delta function that effectively counts spatial overlap, $1_{\circ}(\mathbf{r})$ is a step function equal to unity when $\mathbf{r}$ (with unit vector $\hat{\mathbf{r}}$) is inside the augmentation region and zero elsewhere, and $Y_{\ell m}$ are the spherical harmonics.

When `dmatpuopt` $\geq$ `3`, occupancies take the same form as Eq. (4.39) scaled by normalization constants. When `dmatpuopt = 3` or `dmatpuopt = 4`,

$$n^{\mathbb{i}\sigma}_{mm'} = \frac{1}{\mathcal{N}_0^{(\texttt{dmatpuopt}-2)}} \sum_{ij} \rho^{\sigma}_{ij} \langle \phi_{n_i} | \phi_0 \rangle \langle \phi_0 | \phi_{n_j} \rangle, \tag{4.42}$$

where $\mathcal{N}_0$ is a normalization constant representing the overlap between atomic wavefunctions of the bound AE basis function inside the PAW augmentation sphere, delimited by cutoff radius r_c, per

$$\mathcal{N}_0 = \int_0^{r_c} \phi_0^2(r)\, dr. \tag{4.43}$$

The use of `dmatpuopt = 3` is equivalent to Scheme o_B in Eq. (C2) in Geneste *et al.*,[55] wherein the PAW-truncated atomic orbitals ϕ_0 are effectively renormalized according to the percentage of the total orbital charge inhabiting the augmentation region. When `dmatpuopt = 4`, both the ϕ_0 and the part of the KS orbital falling inside the augmentation sphere are supposedly renormalized (only if the KS orbital matches the atomic orbital in shape), so that $\mathcal{N}_0$ is squared in the denominator.

Based on the description in Timrov *et al.*,[64] the QUANTUM ESPRESSO[65,66] uses none of these options (see Eqs. (9), (10) and (A4) in Timrov *et al.*). Instead, this schema takes the full PS atomic orbitals and augments them with an overlap operator defined in terms of the overlap of the PAW basis functions. In this way, the population analysis avoids relying on orbitals truncated at the PAW cutoff radius and is conducted without significant approximation. For this reason, in Part III, we calculate the Hubbard U via linear response first in QUANTUM ESPRESSO for use as a benchmark to determine which PAW-based population analysis involving truncated orbitals is most effective.

Chapter 5

The Abinit `lrUJ` utility

Members of the DFT+U+J family of functionals are increasingly prevalent in addressing errors intrinsic to (semi-)local XC functionals at minimum computational cost. It is mutually becoming increasingly popular to calculate the Hubbard U parameter *in situ* for given systems of interest, simulation schemes, and runtime parameters.[34,67–72] To accommodate these trends, many readily-available DFT programs have some implementation of DFT+U in different guises. Relatively few among them, however, have utilities for calculating the Hubbard parameters from first principles.

An example of a software package with both implementations is ABINIT,[73–77] an open-source electronic structure suite developed from the mid-1990s by Xavier Gonze and colleagues. The suite is equipped with a variety of *ab initio* techniques and the softwares that support them, including, but not limited to, time-dependent density functional theory, dynamical mean-field theory, density functional perturbation theory, many-body perturbation theory, electron-phonon calculations, and PAW dataset generation facilities.[59,78]

ABINIT's ground-state DFT scheme relies on a plane-wave SCF algorithm, into which developers comprehensively integrated the projector-augmented wave (PAW) method[52] in 2008.[62,79] Shortly thereafter, DFT+U+J was built on top of this PAW implementation, and programs were developed to calculate its namesake parameter, the Hubbard U, and other corrective objects *in situ* via linear response.[3,4] In preparation for the investigation undertaken in Chapter 7, we analyzed in detail the numerical performance of this linear-response implementation, originally called `UJdet`. We then extended its capability to also calculate the Hund's J parameter from first principles.

How all these formalisms—DFT+U+J, PAW, linear response, SCF algorithms—overlap in ABINIT is not trivial, and there exists a need for comprehensive, more didactic documentation making explicit the link between the programs and the theory that inspired them.[§] Furthermore, state-of-the-art Hubbard corrective techniques and practices have advanced in the 15 years since the initial implementation of the DFT+U+J and linear response utilities. For example, the Hund's exchange-coupling J and the DFT+U+J-type functionals have seen more scientific attention than before,[34,80–84] and ground has been made in calculating the Hund J via linear response.[3,4,13,40,80] ABINIT's DFT+U+J linear response

[§]In March 2021, the author of this dissertation posted a video lecture explaining the PAW formalism and its implementation in ABINIT on YouTube, linked here for convenience. In the almost four years since the video was posted, it has accumulated just over 6800 views.

implementation and support utilities were due for reevaluation and expansion.

This technical work has led to the development of what is now called the ABINIT lrUJ utility,[85,86] a renovated post-processor that enables users of ABINIT to engage easily with *in situ* Hubbard parameters and streamline their incorporation into material simulations of interest. Features of this utility, which may also interest users and developers of other DFT codes, include n-degree polynomial regression, error analysis, Python plotting facilities, didactic documentation, and avenues for further developments. The following chapter places particular emphasis on the intricacies and potential pitfalls introduced by the PAW method, SCF mixing schemes, and non-linear response, several of which are translatable to DFT+U+J implementations in other packages.

The details provided in Sections 3.1.2 (plane-wave DFT implementations), 3.1.4 and 4.3.2 (PAW method and projectors) and Chapter 2.5 (Hubbard corrective protocol and linear response) provide crucial formative information for the following description of the technical implementation of DFT+U+J in ABINIT, which is organized as follows.

First, Section 5.1.1 describes how to invoke various Hubbard parameter-related features via the ABINIT input file, followed by Section 5.1.2, which provides a closer look at ABINIT's relevant SCF mixing schemes. We then hone the focus to ABINIT's linear response functionalities in Section 5.2, explaining their recent renovations, what prompted those renovations, and clarifying their current roles in the ABINIT ecosystem. In this process, the new lrUJ utility is introduced, and so Section 5.3 provides a step-by-step tutorial on its use for determination of the Hund's J parameter, including a guide on plotting the linear response data with ABINIT's companion Python library, AbiPy. Finally, we comprehensively dissect ABINIT's linear response procedure, following a SCF calculation and documenting the algorithm that transforms potential perturbations to occupancy responses to Hubbard parameters, a chronicle recounted in Section 5.4.

5.1 Implementation of DFT+U+J in ABINIT

This and following sections are color- and font- coded for clarity. Mutable variables found in the ABINIT input file are displayed in `blue code` text. Immutable, internal ABINIT variables, functions, and subroutines are displayed in `orange code` text.

5.1.1 Running DFT+U+J in ABINIT

The DFT+U+J formalism is built inseparably into ABINIT's PAW functionality. Users have no choice but to use PAW datasets as pseudopotentials when administering a correction via the Hubbard functionals. Moreover, the Hubbard functional implementation and related utilities in ABINIT are, for the moment, restricted to the case of collinear magnetism (i.e., for which the variable `nspinor = 1`).

When DFT+U+J and PAW are simultaneously activated, the total energy becomes

$$E_{\text{DFT+U+J}} = E_{\text{DFT}} + E_{ee} - E_{\text{dc}} \,, \tag{5.1}$$

where E_{DFT} is the standard DFT energy functional, E_{ee} is the electron-electron interaction energy expanded in Eq. (1) of Ref. [62], and E_{dc} is the double-counting term, which corrects for the

interaction already encompassed in E_{DFT}.

DFT+U+J is activated via the `usepawu` input variable, a single integer which may adopt several non-zero values, each corresponding to the treatment of the double-counting term. If `usepawu = 0`, DFT+U+J is unactivated. If `usepawu = 1`, the double-counting term is assessed via the Full Localized Limit formulation proposed by Anisimov *et al.*,[33] which takes on the following form,

$$E_{\mathrm{dc}} = \frac{U}{2} N\,(N-1) - \frac{J}{2} \sum_{\sigma} N^{\sigma}\,(N^{\sigma}-1). \tag{5.2}$$

When only the Hubbard U is defined via input variable `upawu`, the Hund's J is assumed to be 0.0, and Eq. (5.2) inserted in Eq. (5.1) becomes the standard Dudarev functional (DFT+U_{eff}, discussed in Section 2.5.2).[45] When the Hund's J is set to a non-zero value via `jpawu,` Eq. (5.2) contributes to a Hubbard corrective protocol called the Liechtenstein[87] DFT+U+J functional, which is discussed in Section 2.5.1.[§] Its double-counting expression is derived from a reference system that assumes the diagonal elements of the diagonalized occupancy matrix are integers. Similarly, this expression is evaluated if `usepawu = 4`, except it is done so without spin polarization in the XC functional[88]. If `usepawu = 2`, the Around Mean-Field double-counting expression, which is found in Eq. (7) of Ref. [89], is evaluated. Other options related to DMFT and GW methods for the `usepawu` variable exist. For the standard DFT protocol with Hubbard corrections, use `usepawu = 1` corresponding to the Full Localized Limit.

Declaration of `usepawu` compels ABINIT to read three more input values: `lpawu`, `upawu` and `jpawu`. The variable `lpawu` accepts an array of integers of length `ntypat` (the number of types of atoms) to determine on which atomic subspaces we will apply U and J values. If `lpawu` is negative, no Hubbard parameters are applied. If `lpawu` is positive, ABINIT will apply a Hubbard U and Hund's J to the atomic subspace indexed by the angular quantum number of the subspace (e.g., `lpawu = 2` applies it to *d* orbitals, `lpawu = 3` to *f* orbitals). The U and J can be applied to any orbitals, including *s* orbitals. The variables `upawu` and `jpawu`, subsequently, define respectively the Hubbard U and Hund's J parameters to be applied to those subspaces. By default, `upawu` and `jpawu` are read in atomic units but can be specified in other units of energy, notably eV.

Optional variables for ABINIT's DFT+U+J implementation include `usedmatpu` and `dmatpawu`, which work together to allow the user to propose an initial density matrix to facilitate ABINIT in finding the DFT+U+J ground state.

5.1.2 Mixing schemes

ABINIT provides two mixing schemes: one that mixes the potential and one that mixes the density. Both are available in the PAW implementation, and both prove to perform equally well in efficiently achieving self-consistency (density mixing slightly outperforms potential mixing). However, density mixing is preferable when using PAW due to the degrees of freedom added to the electronic density

[§] As clarified earlier, in the literature, both the Liechtenstein and the Himmeotglu[2] functionals are, in different contexts and for purposes of conciseness, referred to as DFT+U+J. ABINIT does not have an implementation of the Himmetoglu functional, however, and so one may assume that all mentions of DFT+U+J in this chapter refer to the Liechtenstein DFT+U+J functional.

via the pseudovalence and compensation charge densities, the latter of which is directly related to the PAW occupancy matrix. (More information on the compensation charge density can be found in Appendix A5). From Ref. [75]:

> When potential mixing is activated, all parts of the total energy are computed at the same time; the total energy is thus variational with respect to the self-consistent cycle step. When density mixing is activated, parts of total energy are computed at various stages of the cycle which results in a behavior of total energy that is not variational.

The new density is computed, mixed with previous densities, then used to update the energy total alongside other contributions that are not all updated at the same place in the SCF cycle. Inside PAW, the on-site density matrix ρ_{ij}, defined explicitly in Ref. [79], is updated at the same level as the electronic density $\tilde{n} + \hat{n}$, and is then mixed at that level. Therefore, the D_{ij}, a potential term in PAW, is left unmixed by default.[79]

Density mixing is the default for ABINIT under the PAW protocol (`iscf = 17`), specifically via Pulay mixing,[90] an algorithm developed in 1980 as an efficient method of accelerating convergence of iterative sequences. Pulay mixing is used to mix ρ_j^{OUT} and the residual density $\rho_j^{\text{OUT}} - \rho_j^{\text{IN}}$ in the following iterative update of the density,

$$\rho_{i+1}^{\text{IN}} = \rho_i + \underset{j \le i}{\text{mix}} [\rho_j^{\text{OUT}}, P * (\rho_j^{\text{OUT}} - \rho_j^{\text{IN}})] \,, \tag{5.3}$$

where $P =$ `diemix` is a density preconditioning factor based on the model dielectric matrix. Here, `diemix` is the dielectric mixing constant, set to 0.7 by default for PAW calculations and 0.45 for linear response calculations.[§] The variable `iprcell` can select the function used to define the preconditioning factor.

The dielectric mixing constant `diemix`, or its magnetic analog `diemixmag`, is applied to the first SCF density after the linear response α (β) perturbation is applied but before the on-site orbital occupancies (magnetic moments) are calculated. This means that `diemix` (`diemixmag`) inadvertently scales the potential perturbation of the unscreened response matrix χ_0 (χ_{0_M}) in the determination of the Hubbard U (Hund's J) parameter. To counteract this, therefore, we must use the value of `diemix` (`diemixmag`) to unscale χ_0 (χ_{0_M}) in the Hubbard U (Hund's J) data-processing step. Based on a series of tests, we can say conclusively that changing the value of `diemixmag` does not influence the Hubbard U parameter, and analogously, changing `diemix` does not influence the Hund's J.

[§]The preconditioning factor of ABINIT's *density* mixing protocol is not a function of the wavevector k. It must be clarified that $P(k)$ is only applied in the case of *potential* mixing, where the preconditioning factor is defined, by default, as the inverse of the model dielectric matrix,

$$P(k) = \epsilon^{-1}(k) = \texttt{diemix} * \frac{\texttt{diemac}^{-1} + (\texttt{dielng} * k)^2}{1 + (\texttt{dielng} * k)^2} \,, \tag{5.4}$$

where `diemac` is the model dielectric macroscopic mixing constant (typically very large for metals or around 10 for insulators), and `dielng` is a fine-tuning parameter. To boot, the density mixing scheme used in ABINIT's PAW and DFT+U+J implementations applies the same preconditioning factor for each k-point.

5.2 Determination of the Hubbard parameters *in situ* in ABINIT

There are two ways to determine the Hubbard parameters *in situ* with ABINIT: linear response (`lrUJ` or `UJdet`), or cRPA. The cRPA protocol is beyond the scope of the present work, but the interested reader may take a look at the cRPA ABINIT tutorial in addition to Refs. [16, 20] to get started.

5.2.1 A brief history of `UJdet`

Prior to ABINIT version 9.9, only the `UJdet` internal and post-processing utilities existed as a means of calculating the Hubbard parameters via linear response in ABINIT. In the late 2000s, ABINIT developer Donat Adams, alongside Bernard Amadon and Silke Biermann, coded a utility—the U(J) Determination (`UJdet`) protocol—designed to determine the Hubbard parameters based on Cococcioni and de Gironcoli's linear response method outlined in Section 4.1. In ABINIT versions 5 to 9.9, when activated, the protocol would serially introduce two perturbations—one of strength `pawujv` (the user-specified input variable corresponding to the α or β potential perturbation) and the other of strength -1.0 × `pawujv`—to the subspace-uniform potential and harvest the resulting occupancy responses at the beginning and end of the two ensuing self-consistent cycles. The utility then had two points with which it could calculate the screened and unscreened response matrices, χ and χ_0, defined as derivatives of occupancy with respect to perturbation strength.

It is important to note that the positive value of `pawujv` was applied first, followed by its negative image. One should expect, then, that in performing two separate runs with the positive and negative values of `pawujv` should yield the same linear response. Accordingly, we produced Fig. 5.1 by performing β perturbations on a particular system (ferromagnetic NiO) and monitoring the response from both the first and second `UJdet` calculations, respectively.[§] That is, we categorized perturbation-occupancy pairs according to their place in the queue in this double-perturbation cycle.

The screened response χ in Fig. 5.1 relaxes to a reasonably similar value regardless of its status as first or second calculation. The unscreened responses, however, are different depending on which perturbation is applied first. This discrepancy contributes to Hund's J parameters differing, in this case, by several eV. The same phenomenon was observed for the α perturbations contributing to the Hubbard U. The fact that the unscreened occupancies differed depending on their place in the queue indicated that the perturbations were not being applied to the same initial ground state. Internal variables were not undergoing proper initialization, and so the second perturbation was inheriting information from the converged state of the preceding perturbative cycle.

There are a few methods available to test which χ_0 is the correct one. For instance, it is known that for the same system, where $\alpha = \beta$,

$$\frac{dN_0}{d\alpha} = \frac{dM_0}{d\beta}. \tag{5.5}$$

as discussed in Section 4.1. This requisite is fulfilled only for the first applied perturbation (i.e.,

[§] ABINIT 9.6.2 did not originally have infrastructure implemented to apply a β-perturbation as it is described in Section 5.2.1. The version of ABINIT used for these calculations was modified locally to do so. These local modifications later served as the blueprint for the official Hund's J implementation in ABINIT Version 9.10.1.

only the value supplied in pawujv, not its negative counterpart). Furthermore, it is known that when applying a potential perturbation to the spin-up channel only, the unscreened occupancy on the spin-down channel should not change. Applying a perturbation exclusively to the spin-up channel can be achieved by setting macro_uj = 2 (the macro_uj input parameter will be explained in Section 5.3.2). Running perturbations under this setting, we applied perturbations to the spin-up channel only of a Ni atom and monitored the change in unscreened occupancy on the spin-down channel of the same Ni atom. The results of this inquiry, displayed in Fig. 5.2, show that the unscreened occupancy on the spin-down channel remains constant only for the first applied perturbation, thereby corroborating the earlier conclusion that the second applied perturbation in the ABINIT cycle is unreliable. The silver lining for users of UJdet prior to ABINIT 9.10.1 is that the first perturbation data is still salvageable.

In 2022, users alerted ABINIT to the inconsistencies in its UJdet utility. For technical reasons,

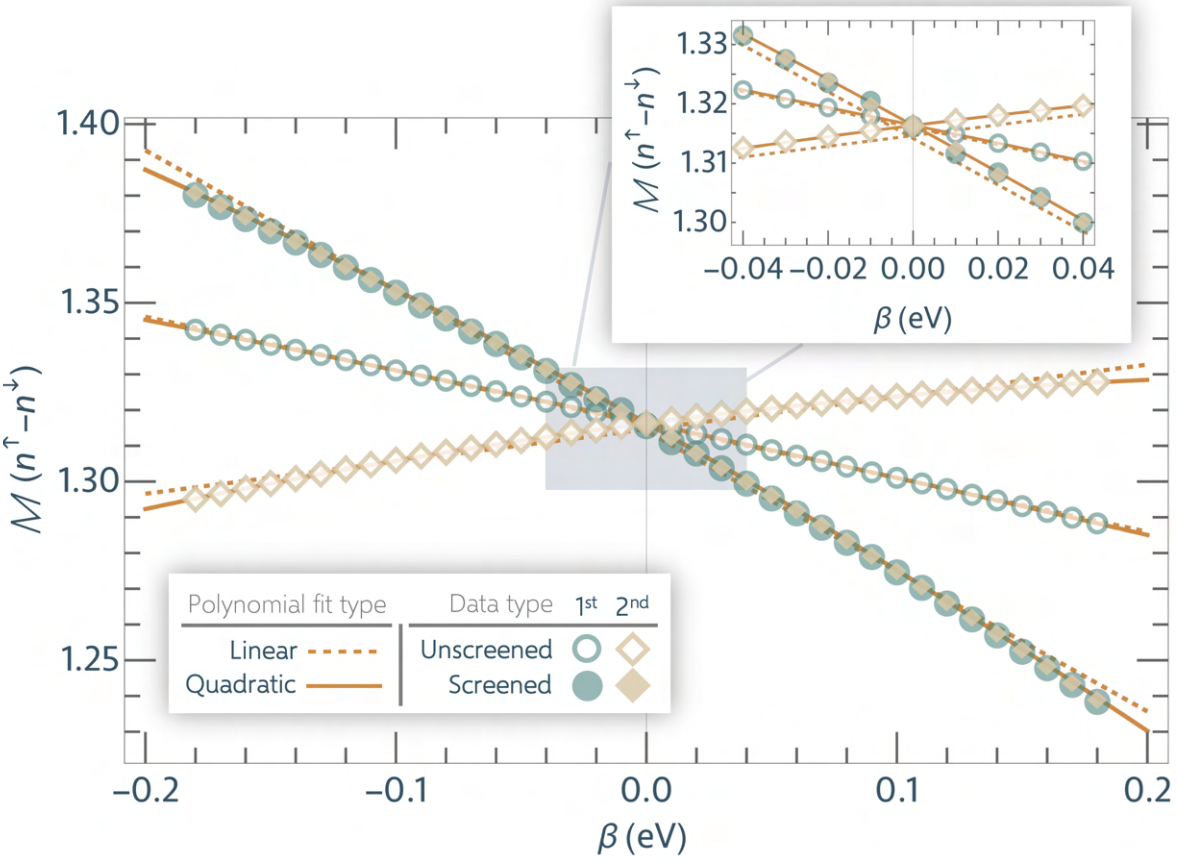

Figure 5.1: Example of the linear response procedure conducted using the now outdated rendition of UJdet *in* ABINIT *version 9.6.2 to find the Hund's* J *for* Ni *3d orbitals on ferromagnetic* NiO*. Data points are raw perturbation-magnetization pairs output by* ABINIT*, categorized according to their place in the calculation queue; that is, the SCF calculation involving the first (*1^{st}*)* β *perturbation is represented by green circles, and the SCF calculation of the second (*2^{nd}*)* β *perturbation is represented by tan diamonds. Open markers indicate unscreened response and filled markers indicate screened response. The screened response* χ *relaxes to the same value regardless of its status as first or second calculation. The unscreened responses, however, are different depending on which perturbation is applied first. This contributes to* J *parameters differing, in this case, by several* eV*. Orange lines are polynomial regressions (dashed for first-order polynomial, solid for second-order polynomial) of each set of data.*

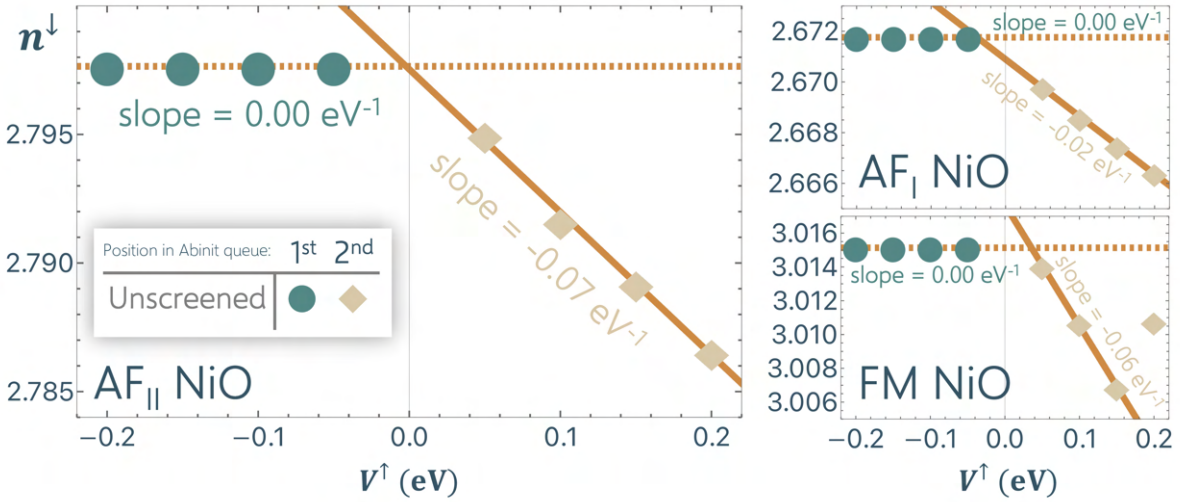

Figure 5.2: Comparison of unscreened spin-down occupancy changes in response to a perturbation $V^{\uparrow}$ applied exclusively to the spin-up 3d channel of a Ni *atom on* NiO *of various magnetic orderings, where perturbation-occupancy pairs are categorized according to their queue (first perturbation applied or second) in the full DFT cycle.*

however, these issues could not be easily remedied, and the decision was taken to decommission the `UJdet` post-processing utility and to renovate its internal functionality. As of version 9.10, the ABINIT DFT suite is equipped with both the renovated `UJdet` utility in addition to a new post-processing tool, the Linear Response U(J) (`lrUJ`) utility, which is built upon the same core `UJdet` programming. Most of `UJdet`'s data processing functionalities were preserved throughout this renovation. However, we emphasize that the functionalities of `UJdet` and `lrUJ` serve distinct purposes and implement different levels of theory, which we discuss further in the coming sections. Although older versions of ABINIT preserve the `UJdet` deprecated internal functions and post-processing utility, their use is strongly disadvized for the reasons outlined above.

5.2.2 Clarification of available linear response utilities

The primary differences between `lrUJ` and `UJdet` as implemented in current versions of ABINIT are outlined in Table 5.1. Item (2) therein highlights the most obvious difference between `UJdet` and `lrUJ`: the number of data points used to compute a linear regression of the response functions χ and χ_0. The `UJdet` utility uses only two points: the unperturbed case—in which the perturbation applied is zero and the subspace occupancies are those of the ground state—and one perturbed case, in which the potential perturbation is equal in magnitude to the value of input variable `pawujv`.

However, rigorous sampling of the $N(\alpha)$ (in the case of the Hubbard U) or $M(\beta)$ (for the Hund's J) terrains is crucial for obtention of reliable parameters. It is arguable that the two-point interpolation scheme implemented in `UJdet`, as demonstrated by the difference taken in Eqs. (5.27) and (5.28), is insufficient in terms of sampling. Furthermore, no insight into the regression error is accessible with a two-point regression. For this reason, using data from multiple perturbations is recommended.

Engineered with this in mind, the `lrUJ` utility requires, at minimum, three data points (one unperturbed case and at least two perturbations) to conduct a distinct regression analysis. With n data

	UJdet	lrUJ
1	Embedded in ABINIT core routine	Post-processor
2	Two-point linear regression	3+ point polynomial (variable degree) regression
3	χ and χ_0 responses treated as matrices; interatomic response monitored; matrices augmented by total system charge	χ and χ_0 responses treated as scalars
4	Supercell extrapolation scheme	RMS error analysis
5	Atomic Sphere Approximation projector extensions/normalizations	Outputs *LRUJ.nc NetCDF files with details of perturbative run

Table 5.1: Comparison of preserved and renovated ABINIT *linear response functionalities.*

points, the lrUJ utility computes not only a linear regression of the response functions χ and χ_0, but all polynomial regressions up to degree $n-2$, a threshold imposed to inhibit overfitting. Furthermore, the lrUJ utility conducts RMS error analysis on each fit and factors that into an approximative RMS error on the resulting Hubbard parameters.

Another crucial difference between the two utilities is item (3) of Table 5.1: the UJdet utility treats the response functions as matrices, whereas the lrUJ utility treats them as scalars. This means that the UJdet Hubbard parameters are, to some degree, informed by the Hubbard interactions on and between the other atomic subspaces of the system as well as the total charge bath. The protocol is expanded upon in Ref. [32], wherein an extrapolation scheme aiming to accelerate the determination of the Hubbard parameters is proposed. This scheme involves (i) enforcing charge neutrality by augmenting the response matrices (collecting the response functions while moving the site of perturbation) with the negative of their total response; and (ii) capitalizing on the assumption that the occupancy response to the potential perturbation attenuates for atoms further away from the site of the perturbation.[4]

By contrast, the lrUJ utility provides the scalar Hubbard parameters, informed only by the change in occupancy on the perturbed subspace. This parameter is functionally sufficient for corrective application to that subspace. For all other purposes, it can be said that lrUJ offers a simplified data processing procedure to that of UJdet, provided that the user commits to more than three response data points (i.e., at least two separate ABINIT DFT runs). By design, these data points can be run in parallel, and so the use of the lrUJ utility as an extension of the UJdet utility is strongly encouraged.

5.3 Running linear response with lrUJ

The explanation that follows is a more detailed version of the corresponding ABINIT tutorial. The ABINIT linear response procedure can be carried out in three steps:

1. Run a ground-state calculation of a supercell to generate and store its wavefunctions.

2. Run a series of perturbative calculations to generate their LRUJ.nc files.

3. Execute the lrUJ post-processing utility.

5.3.1 Ground-state calculation and generation of WFK files

It is necessary to establish a ground-state system, the subspace potential of which we can perturb. For all intents and purposes, this should be an ordinary DFT calculation, aside from a few minor modifications to the input file.

First, we choose the atom whose subspace we wish to apply a potential perturbation, as ABINIT will flag it to allow the perturbed subspace to vary its external potential independently to its kin atoms in the cell. To avail of lrUJ functions, one may choose any of the atoms listed in xred; to avail of the UJdet functions, however, such as the supercell extrapolation scheme, one should exclusively apply the linear response perturbation to the first atom listed in xred.[§]

Once the atom undergoing the perturbation is identified, it must be distinguished in the input file as a separate species by increasing ntypat by 1 and adjusting the parameters typat, znucl, lpawu, upawu, jpawu, pseudos, and all other variables dependent on ntypat, to reflect that change. These modifications will remain for Step (2), as well.

Conventionally, the input U and J values are set to zero at this point. To do this, either set all values in upawu and jpawu to 0.0, or simply deactivate DFT+U+J by setting usepawu = 0. Crucially, make sure prtwf is set to 1 so that the WFK file is printed. Once all aspects of the ground-state run are assembled, launch ABINIT with the input file. When the run converges, the wavefunctions are printed to a WFK file in the out directory.

5.3.2 Perturbative calculations and generation of LRUJ.nc files

With the reference wavefunctions in hand, one can start the linear response procedure, where ABINIT's dataset functionality is used to iteratively apply perturbations of varying strength to the chosen subspace. For now, the input variables needed to perform one such perturbation are described.

Building on top of the input file used in Section 5.3.1, linear response is further activated with one input parameter: macro_uj. This parameter's integer value, in combination with the value nsppol (the number of independent spin channels), determines how the local potential perturbation is applied and the subsequent changes in occupancy harvested. These options are organized in Table 5.2. The options macro_uj = 1 and nsppol = 1 represent the non-spin-polarized case, where total occupancies are double those of one spin channel. Importantly, note that both UJdet and lrUJ are implemented exclusively for the collinear case as the linear response theory relating to non-collinear implementation requires further consideration.[91,92]

[§]By specifying the perturbed atom as a separate species, ABINIT will only harvest the changes in occupancy of the perturbed atom. This information is sufficient for the lrUJ procedure, but not for UJdet. To avail of the supercell extrapolation technique, one must instead set the symmetry relations, symrel, explicitly. The symmetry relations are specified in terms of 3×3 matrices, and they represent the Wyckoff positions of the atoms. Making these explicit in the input will tell ABINIT that (a) the perturbed atom should vary independently to its kin, and (b) it should still collect occupancy information for all atoms containing the subspace to be treated, not just that of the perturbed atom. The UJdet utility then uses these interatomic response matrix elements to inform its Hubbard parameters.

One can generate these symmetries in a separate run, wherein the atom upon which the perturbation is to be applied is specified as a different species, in the same way described in this lrUJ tutorial. The number of symmetries (nsym), the symmetry operations (symrel), and the translation vectors (tnons) are read from the output.

	Possible Combinations				
macro_uj	1		2	3	4
nsppol	1	2	2	2	2
Parameter	Hubbard U				Hund's J
Perturbation applied to:	α on both spin-↑ and spin-↓		α on spin-↑	α on spin-↑	$+\beta$ on spin-↑; $-\beta$ on spin-↓
Response monitored on:	spin-↑ + spin-↓		spin-↑	spin-↓	spin-↑ − spin-↓

Table 5.2: Variables `macro_uj` *and* `nspden` *combinations in* ABINIT *and corresponding HP.*

It is worth highlighting that the parameter calculated using `macro_uj = 3` and `nsppol = 2` is *not* the Hund's J parameter. The Hubbard U typically requires the setting of `macro_uj = 1` and `nsppol = 2`. This setting will apply the same potential shift to both the majority- and minority-spin channels and monitor the response on the sum of occupancies on those same spin channels.

The strength of the perturbation is determined by `pawujv`. The default units for this variable are Hartree, but other units (notably eV) may also be defined. The variable `pawujat`, a single integer, specifies the atom number (the atom coordinate index listed under `xred` or `xcart`) on which the perturbation is to be applied. This must be the same atom specified as a separate species in generating the `WFK` file in Step 1.

The default settings adopted when `macro_uj` is non-zero are `tolvrs=1d-8` and `irdwfk=1`. The former dictates the tolerance on the potential residual (i.e., the difference between the input and output potentials pertaining to a particular SCF iteration). With the latter, ABINIT is instructed to read in the `WFK` files for a prior run, given the files are named according to a specific convention. Alternatively, one can specify the `WFK` file and its path by name. To do this, set the following: `getwfk_filepath`

```
getwfk_filepath="</path2file/filename_WFK>"
```

The input parameter named `dmatpuopt`, of which there are four options, selects the expression with which the density matrix elements for each subspace are calculated using PAW projectors. These options are (somewhat redundantly, for convenience to the reader) outlined in Sections 4.3.2 and 5.4.2 and their effect on the Hubbard parameters comprehensively tested in Chapter 7.

Lastly, to have the `UJdet` internal functions print out a verbose level of information as it completes its routine, the variable `pawprtvol` should be set to -3. To further manage the print volume, set `prtvol` as needed.

In changing only these variables, only one perturbative calculation is set up. This is sufficient to avail of the `UJdet` utility functionalities, which require only two data points. However, as mentioned in Section 5.2.2, in many, if not all, cases, one perturbation is inadequate to compute a good regression of the linear response data, and no error analysis can be conducted thereof. For this reason, it is recommended to conduct several (at minimum two, although the more, the better) perturbative calculations. ABINIT's inbuilt dataset function allows user to iteratively induce n perturbations by setting

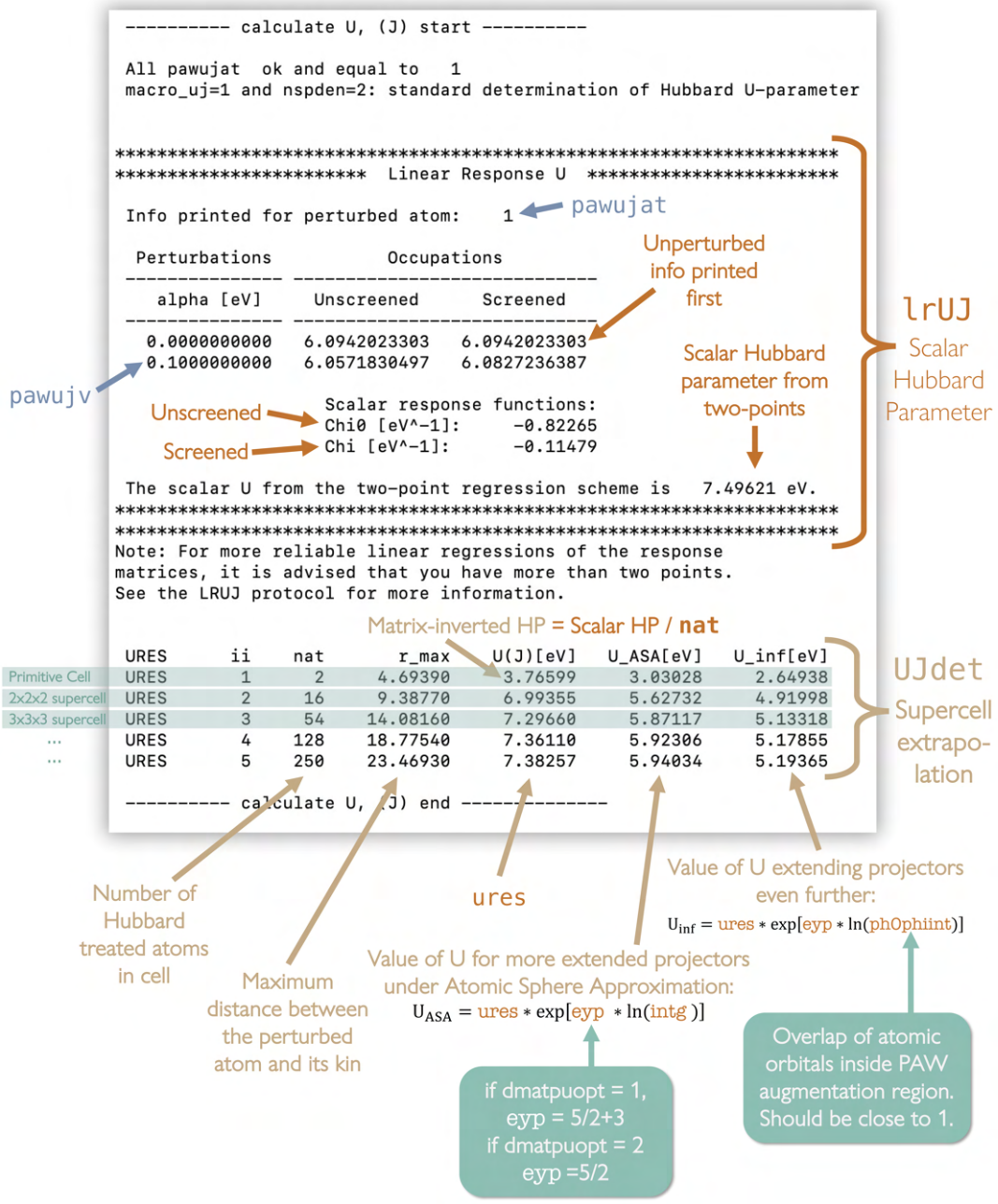

Figure 5.3: Generic output of the two-point Hubbard parameter determination functions, found in the ABINIT *output file (default suffix* `.abo`*) for a linear response DFT run. Output for the Hubbard* U *is shown here. In the case of a Hund's* J *calculation (obtained with* `macro_uj = 4`*), the labels referencing* `U`*,* `alpha`*, and* `Occupations` *will be replaced by* `J`*,* `beta`*, and* `Magnetizations`*, respectively. The unscreened response* `Chi0`*, as printed, is treated with* `diemix` *(see Sections 5.1.2 and 5.3.4 for clarification). Explanation of the* `UJdet` *supercell extrapolation output written to* `.abo` *file. See Section 5.4.4 for more information regarding the intrinsic variables. Note that the small unit cell used here is only for illustrative purposes and will not yield converged (scalar or matrix) parameters.*

`ndtset` to *n* and then specifying which perturbation strengths `pawujv1`, `pawujv2`, ... , `pawujv`*n* to apply. Once completed, launch the run.

Once the datasets have converged, the output directory will have *n* files with the suffix `LRUJ.nc`.

These files, which are NetCDF binaries,[93] contain all the internal information pertaining to the perturbations undergone. The lrUJ utility will read in a series of these files and harvest the necessary information to calculate the selected Hubbard parameter. Future developers of the lrUJ utility may find it useful to know the variables stored in LRUJ.nc: nnat, natom, ndtpawuj, nspden, nsppol, usepaw, macro_uj, pawujat, dmatpuopt, diemix, diemixmag, ph0phiint, uj_pert, luocc.

In the ABINIT output file, all information related to the two-point calculation of the scalar Hubbard parameter and all information regarding the UJdet functionalities (completed once for every dataset) can be found between the "calculate U, (J)" flags. An annotated example of the standard, scalar HP output, in addition to the output of the UJdet supercell extrapolation scheme, comprises Fig. 5.3.

5.3.3 Execution of the lrUJ post-processing utility

Once the LRUJ.nc files are printed, execute the lrUJ post-processing utility as follows:

```
lruj *_LRUJ.nc > lruj.out
```

It should take less than a second to run. If successful, the resulting output file, here named lruj.out, should resemble that shown in Fig. 5.4. The example calculation looks at the Hund's J parameter (macro_uj = 4) using results from six perturbations, the strengths of which are listed in the first table alongside the corresponding subspace magnetizations, both unscreened (for χ_{0_M}) and screened (for χ_M).

The last table gives the values for χ_0 (χ_{0_M}), χ (χ_M), the Hubbard U (Hund's J), and their RMS errors in units of eV for a consecutive series of polynomial regressions. The lrUJ utility is programmed to only calculate polynomials up to degree $n - 2$ for n data points, a tight measure implemented to avoid spurious overfitting effects. By default, then, if one reads in only two LRUJ.nc files, the maximum polynomial regression conducted will be linear; three LRUJ.nc files means maximum degree is quadratic, and so on, up to degree three (cubic). If higher polynomial order regressions are needed, and the number of data points suffices, then append -d <*maximum degree*> to the above command line to specify the maximum degree. For example, for the sample calculation with seven data points, one can bash

```
lruj *LRUJ.nc -d 5 > lruj_d5.out
```

to get parameters and errors corresponding to all polynomials of order one through five, as shown in Fig. 5.4. Other command line options for the lrUJ utility include -version and -help.

The values in eV of the Hund's J parameter according to each regression are found in column four. To assess which one is best, you'll want to use the RMS errors in column seven (more information on how the error analysis is conducted in Section 5.4.5) in addition to the visual behavior of the linear response, which can and should be plotted (see Section 5.3.4), particularly if the RMS errors seem unusually large.

At the very end of the lrUJ output file, information handy for plotting, such as the coefficients of the polynomial regression formulae, is printed in YAML format.[94]

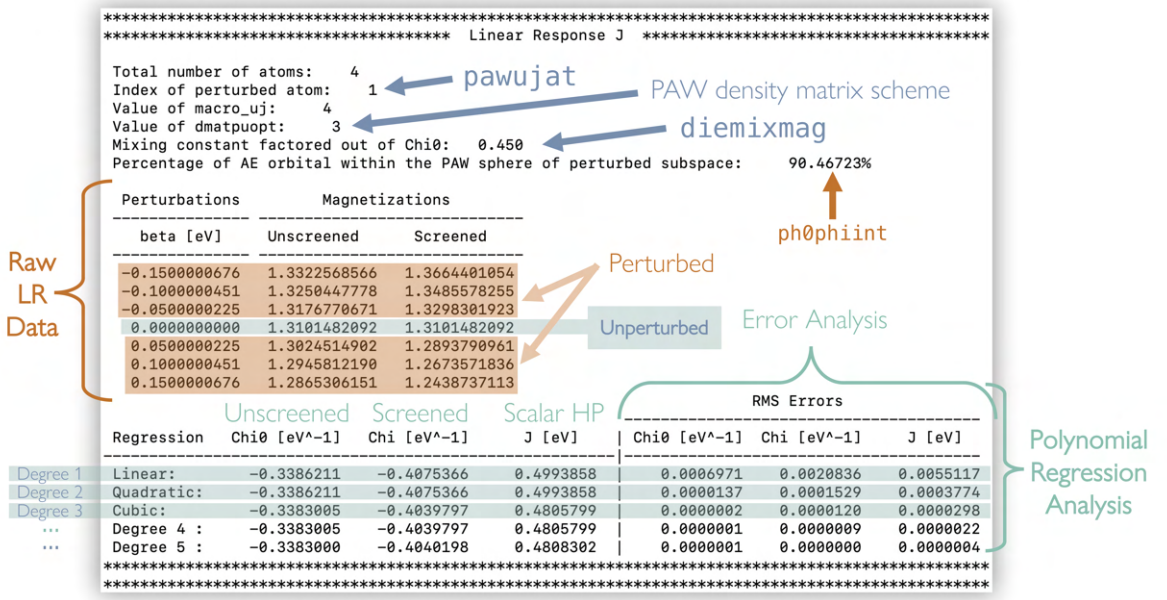

Figure 5.4: Output of the lrUJ *post-processing utility for the Hund's* J *parameter, having requested a maximum polynomial degree of five via command line. Note that this output is from* ABINIT *version 9.10.5 and so contains erroneous HP RMS errors in column seven. See Section 5.4.5 for more details.*

5.3.4 Visualization of linear response data from ABINIT

Particular care must be taken when plotting the linear response data coming from ABINIT. The lrUJ and UJdet implementations both print out the raw data, meaning that the unscreened occupancies (magnetizations) have not yet been scaled by the mixing constant diemix (diemixmag), as is necessary based on the conclusions of Section 5.1.2. If one were to directly plot this raw data, the plot would show a slope that does not match the χ_0 printed in the output file. To avoid this, we must perform a transformation on the data points, the form of which will be shown in the following proof. We assume a Hubbard U determination as an example proof, but the same conclusions may be deduced for the Hund's J parameter. We will refer to the data set of unscreened occupancies as N_0, to which some polynomial function of the perturbation strength α is fitted, producing a regression function $N_0(\alpha)$. The unscreened response function is defined as

$$\chi_0 = \frac{1}{\theta} \left. \frac{dN_0}{d\alpha} \right|_{\alpha=0} \tag{5.6}$$

where $\theta =$ diemix. In order to plot the unscreened response data with a function $p(\alpha)$ set such that χ_0 is shown with its θ-corrected slope at the zero-perturbation axis, we perform the following multiplicative transformation on $N_0(\alpha)$,

$$p(\alpha) = \gamma \cdot N_0(\alpha) \; + \; c \; , \tag{5.7}$$

where γ and c are constants. The mandatory criterion governing the shape of $p(\alpha)$ is

$$\left. \frac{dp}{d\alpha} \right|_{\alpha=0} = \chi_0 \cdot \tag{5.8}$$

It follows from Eqs. (5.6), (5.7) and (5.8) that

$$\left.\frac{dp}{d\alpha}\right|_{\alpha=0} = \gamma \left.\frac{dN_0}{d\alpha}\right|_{\alpha=0} = \chi_0 \tag{5.9}$$

$$\Rightarrow \gamma\, \theta\, \chi_0 = \chi_0 \tag{5.10}$$

$$\therefore \gamma = \frac{1}{\theta}\,. \tag{5.11}$$

In order to find the second constant c, we impose a secondary criterion on the shape of $p(\alpha)$ to ensure that $p(0) = N_0(0)$. This leads to

$$p(0) = \frac{N_0(0)}{\theta} + c = N_0(0) \tag{5.12}$$

$$\therefore\ c = \frac{N_0(0)\ (\theta - 1)}{\theta} \tag{5.13}$$

Thus,

$$p(\alpha) = \frac{1}{\theta}\ \left(N_0(\alpha) + N_0(0)\ (\theta - 1)\right). \tag{5.14}$$

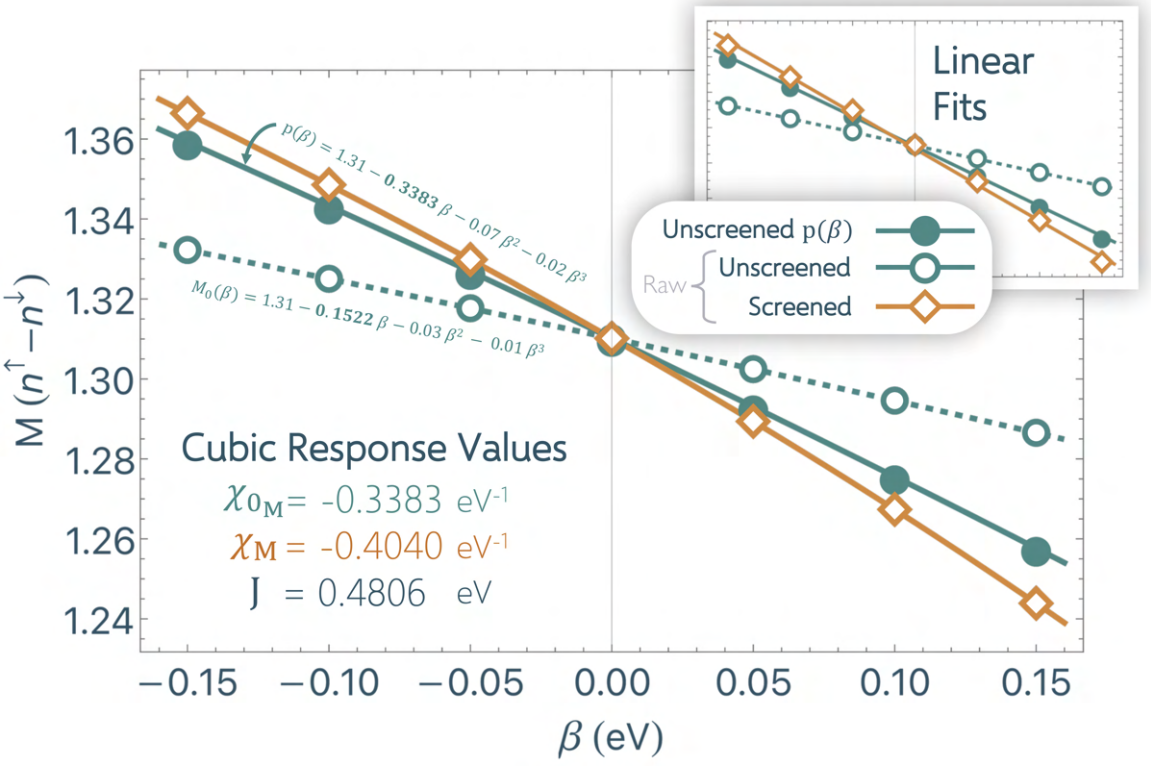

Figure 5.5: Linear response Hund's J *plot demonstrating the necessary transformation of the raw* ABINIT *unscreened data to account for the mixing constant* `diemixmag` *(or* `diemix` *in the case of the Hubbard* U*). The example data used here is the same as that of Fig. 5.4, which is more aptly fitted with a degree 3 (cubic) polynomial as opposed to a linear function. The cubic fits are shown in the main figure, and the linear fits for the same data are shown in the upper right inset for qualitative comparison. The* $p(\beta)$ *function takes the same form as Eq. (5.14), noting that we substitute* M_0 *for* N_0 *and* β *for* α *to accommodate the Hund's* J *as opposed to the Hubbard* U.

As mentioned earlier, the same conclusion can be reached assuming a β perturbation coupled with diemixmag as θ for the Hund's J parameter. Moreover, Eq. (5.14) turns out to be identical in form to the result achieved when we assume an additive transformation as opposed to a multiplicative transformation. Fig. 5.5 demonstrates the transformation in Eq. (5.14) for the raw Hund's J lrUJ data shown in Fig. 5.4.

One can customize the mixing constant-corrected linear response plot by importing the perturbation/occupancy table into one's choice graphical utility. Plot the screened occupancies as they are printed; for the unscreened occupancies, plot the function in Eq. (5.14). Fig. 5.5, for example, was generated with Mathematica.[95]

5.3.5 What AbiPy can do with a lrUJ output file

This mixing constant-corrected linear response plot can be easily generated through the AbiPy python package[96]; its version 0.9.7 is able to read in results from one's chosen `lruj.out` output file and visualize its results. To avail of this functionality, educe a python script in the same directory as that containing your `lruj.out` output. Begin the python script by importing the `LrujResults` function from the AbiPy package with the following two lines.

```
#/usr/bin/env python
from abipy.electrons.lruj import LrujResults
```

Import the `lruj.out` file using the following line.

```
lr = LrujResults.from_file("path_to_file/lruj.out")
```

The plot function may then be summoned with

```
lr.plot(ax, degrees, inset, insetdegree, insetlocale, ptcolor0,
  ptcolor, gradcolor1, gradcolor2, ptitle, fontsize)
```

where the arguments listed in blue are keywords to tailor particular characteristics of the ensuing plot. These options are described in more detail in Table 5.3, found on the next page.

Other AbiPy tools to better accommodate the linear response process in ABINIT are currently in the works. For example, under development is a suite of functions that aim to facilitate visualization of the convergence of the Hubbard parameters with respect to supercell size.

LrujResults plot utility optional arguments			
Argument	Default	Other Options	Description
ax	None	ax	Optional axes argument. If None, a new plot is generated. If ax, the figure without the axes is returned. Useful for generation of a grid of plots.
degrees	"all"	List of integers i such that $0 < i <$ maximum degree	Degrees of polynomial regressions to be included in the plot, provided as a Python list of integers (e.g., [1, 2, 3]). The maximum integer allowed is maximum degree, which is read in via the lruj.out output file
inset	True	False	Option to print inset with response information (i.e., values of χ_0, χ, the Hubbard parameter and their respective errors in units of eV). If True, information is printed for the linear regression case in the lower left corner of the plot (by default; see insetdegree and insetlocale options to tailor). If False, no inset is included.
insetdegree	1	Any integer ∈ degrees	Polynomial degree of printed response information appearing in inset.
insetlocale	"lower left"	"upper right", "center left", "lower center", "center", corresponding integers 0-10, etc.	Position of inset containing response information in standard format for matplotlib legend locations. See matplotlib documentation for all options.
ptcolor0	"k"	"r", "blue", "FF6E42", (0.1,0.9,0.54), "0.75", etc.	Color of unscreened response data point markers in any standard matplotlib color format (see matplotlib documentation for all formatting options. Default color is black. Markers themselves are open circles ○ (immutably so, for now).
ptcolor	"k"	"r", "blue", "FF6E42", (0.1,0.9,0.54), "0.75", etc.	Color of screened response data point markers in any standard matplotlib color format (see matplotlib documentation for all formatting options. Default color is black. Markers themselves are filled circles ● (immutably so, for now).
gradcolor1	"#3575D5"	Hexadecimal (HEX) code for any color	Line color of the lowest polynomial degree to be plotted (i.e., the smallest integer input via degrees argument). This color, in addition to that of gradcolor2 will inform the line colors of the intermediate polynomial degrees in a linear gradient fashion. Must be entered as a HEX code (six characters preceded by a '#'). The default color is dark blue.

gradcolor2	"#FDAE7B"	Hexadecimal (HEX) code for any color	Line color of the highest polynomial degree to be plotted (i.e., the largest integer input via degrees argument). Must be entered as a Hex code (six characters preceded by a '#'). The default color is salmon pink.
ptitle	"Linear Response for atom <*pawujat*>"	Any string	Title of plot. Incorporates input value of pawujat by default. For no title, put "".
fontsize	12	Any integer > 0	Font size in point (pt) units of the plot legend.

Table 5.3: Optional arguments and their possible values available in the plot *function implemented in the* LrujResults *import of the AbiPy package.*

5.4 Internal workings of the ABINIT U(J) determination procedures

In this section, we describe in detail the algorithm ABINIT undergoes to conduct linear response calculations. While sufficient as a launchpad for future developers of the program, this description is primarily intended to provide ABINIT users with a more transparent understanding of the linear response operations and their connection with the objects printed in the output files. This section follows the internal variables as they undergo transformations and transfer relevant information, monitoring how the potential perturbations render occupancy responses render Hubbard parameters through the lrUJ post-processor. For ease of reference, the language intrinsic to the ABINIT source code is utilized in referencing variables, functions, subroutines, modules, and programs.

5.4.1 Application of perturbation

Say a user launches an ABINIT run to determine a Hubbard parameter for subspace $n\ell_{\mathrm{U}}$ by perturbing the potential of atom pawujat by a strength pawujv.

After the variables are read from the input file and the ground-state driver is activated, the non-zero macro_uj flag sets off the self-consistent cycle driven by pawuj_drive. Here, the strength of the perturbation pawujv is read and stored in a matrix called atvshift—a nsppol $\times$ $(2\ell_{\mathrm{U}} + 1)$ array—according to the type of perturbation incited via the value of macro_uj. (For example, for the Hubbard U on a 3*d* subspace, atvshift will be a 2×5 matrix in which all elements are equal to +pawujv. Alternatively, for the Hund's J parameter, the second row of atvshift, representing the spin-down channel, will be set equal to −pawujv, keeping the first row equal to +pawujv.) Following this, the PAW density is initialized and the unperturbed occupancy matrix calculated, diagonalized, and printed. Here is where the first linear response data point, corresponding to the unperturbed ground state read in via the WFK file, is collected. The collection occurs in subroutine pawuj_red. More information on how and what information is collected is described in Section 5.4.3.

It is important to note that at this point in the code, the density (and thus the potential) is mixed according to the mixing scheme outlined in Section 5.1.2. This means that the potential perturbation applied in the first iteration of the SCF cycle will be scaled by the value of `diemix`, which is equal to 0.45 by default when `macro_uj > 0`. We must accordingly descale the unscreened response function χ_0 when the time comes.

The program then calls subroutine `pawdij`. This is where the program computes the pseudopotential strengths D_{ij} of the non-local Hamiltonian operator. The potential is defined as

$$H^{\text{PAW}} = -\frac{1}{2}\Delta + \tilde{v}_{\text{eff}} + \sum_{ij} |\tilde{p}_i\rangle \left(\hat{D}_{ij} + D^1_{ij} - \tilde{D}^1_{ij}\right) \langle \tilde{p}_j| \rangle \ , \tag{5.15}$$

where $-\frac{1}{2}\Delta$ is the kinetic energy operator and $\tilde{v}_{\text{eff}}$ is the effective one-electron potential written in the PAW formalism. As in Section 3.1.4, the indices i, j refer to congruent but distinct sets of four indices: $\{a, \ell, m_\ell, n\}$. The non-local part of the Hamiltonian mirrors the PAW energy,

$$E = \hat{E} + E^1 - \tilde{E}^1 \tag{5.16}$$

such that $\hat{D}_{ij} = \partial\hat{E}/\partial\rho_{ij}$ is the derivative of the PAW pseudized energy with respect to the density. Similarly, $D^1_{ij} = \partial E^1/\partial\rho_{ij}$ and $\tilde{D}^1_{ij} = \partial\tilde{E}^1/\partial\rho_{ij}$, where E^1 and $\tilde{E}^1$ are, respectively, the all-electron and pseudized on-site energies.

Implementing this formalism in ABINIT requires categorization of these terms into those calculated outside the SCF loop and those calculated within the SCF loop. For a more detailed derivation of this, see Ref. [79]. For now, and for our purposes, it suffices to note that the pseudopotential strengths D_{ij} of the non-local Hamiltonian operator for each spin channel are calculated inside ABINIT as the following sum of terms,

$$D_{ij} = D^0_{ij} + \hat{D}_{ij} + D^{\text{H}}_{ij} + D^{\text{xc}}_{ij} + D^{\text{U}}_{ij}, \tag{5.17}$$

where D^{U}_{ij} (labeled `dijpawu`) is the term to which the α perturbation is applied, and D^0_{ij}, D^{H}_{ij}, and D^{xc}_{ij} are, respectively, the atomic, Hartree, and XC components: all functionals of the density.[79]

Inside the `pawdij` driver, a loop over all atoms in the cell is induced, within which the subroutine `pawdiju` is summoned. Here, matrix `dijpawu` is defined as a function of the spin channel (either one for the majority or two for the minority) and of the matrix indices, which enumerate the non-core electrons by systematically combining the principle quantum number n, angular quantum number ℓ, the magnetic quantum number m_ℓ, the PAW projector index n, and the location in the matrix. In other words, the two-dimensional matrix across all sub-indices pertaining to i and j is unfolded into a one-dimensional vector.

As an example of how this works, consider the case where a perturbation α is applied to the spin-up $3d$ orbital of Ni; say, the PAW dataset for Ni in this run defines two partial waves each to describe both the p and d orbitals, only one plane wave for s orbitals, and freezes a core containing all orbitals with $n \leq 2$. For one spin channel on one atom, we are left with 18 combinations of quantum numbers $n > 2$, ℓ, m_l and PAW projector n (the $4s$ orbital of Ni contributing two electrons $\times$ one partial wave = two elements, and the $3d$ orbital contributing eight electrons $\times$ two partial waves = 16 elements).

So, the matrix `dijpawu` for each spin channel is 18×18, yielding 324 matrix elements. However, the pseudopotential strengths are symmetric across the diagonal (i.e., element $D^{\mathrm{U}}_{ij} = D^{\mathrm{U}}_{ji}$); to save memory and time, ABINIT computes the upper right triangular matrix elements only (a total of 171 in our Ni example). The matrix elements are thus enumerated from one to 171 starting from the upper left and reading left to right, top to bottom.

The D^{U}_{ij} matrix elements themselves are found to be

$$\texttt{dijpawu} = \langle \phi_{n_i} | P^{a_i}_{mm'} | \phi_{n_j} \rangle * V^{\sigma,\mathrm{U}}_{m_i m_j}. \tag{5.18}$$

Here, $P^{a_i}_{mm'}$ is the AE projection operator acting on the radial parts of the PAW AE basis functions ϕ_n. This term is discussed in detail in Section 5.4.2. The term $V^{\sigma,\mathrm{U}}_{m_i m_j}$ comprises a homogeneous potential $V^{\sigma,\mathrm{U}}$ across all m_i for a particular subspace and, if appropriate, the perturbation:

$$V^{\sigma,U}_{m_i m_j} = \begin{cases} V^{\sigma,\mathrm{U}} & m_i \neq m_j \\ V^{\sigma,\mathrm{U}} + \texttt{fatvshift} * \texttt{atvshift}(\sigma, m_i) & m_i = m_j. \end{cases} \tag{5.19}$$

The term `fatvshift` is vestigial from prior versions of the `UJdet` implementation, where a loop over values `fatvshift = 1` and `fatvshift = -1` corresponded to the positively and negatively valued perturbations of strength `pawujv`. (Now, `fatvshift = 1` only). If `pawprtvol = 3` in the input file, the entire `dijpawu` matrix will be printed in the `.log` file for all spin channels and all atoms, where one can verify that the perturbation is, indeed, being applied here. Thus ends the subroutine `pawdiju`, which returns `dijpawu` for each spin channel. Back in `pawdij`, `dijpawu` is added via matrix addition to all other pseudopotential strength matrices to calculate the total D_{ij} in accordance with Eq. (5.17).

5.4.2 Calculation of orbital occupancies via `dmatpuopt`

Calculation of the occupancy matrix, or more precisely choice of the projection operator, is dictated by the input variable `dmatpuopt`, which may take on values one through four. For the reader's convenience, we here reiterate and expand on the information provide in Section 4.3.2 due to its relevance in the current context. More information on this topic can be found in Refs. [62, 97, 98], and, once again, an evaluation of the effect of the choice of `dmatpuopt` on the magnitude of the Hubbard parameters can be found in Chapter 7. Briefly, subspace occupancies in the PAW formalism may be calculated using the AE projection operator $P^{a_i}_{mm'}$ via

$$n^{a_i\sigma}_{mm'} = \sum_{ij} \rho^{\sigma}_{ij} \langle \phi_{n_i} | P^{a_i}_{mm'} | \phi_{n_j} \rangle, \tag{5.20}$$

where ϕ_n are the radial parts of the PAW AE basis functions, and the density matrix inside the PAW augmentation region is

$$\rho^{\sigma}_{ij} = \sum_{k,v} f^{\sigma}_{kv} \langle \widetilde{\Psi}^{\sigma}_{kv} | \widetilde{p}_i \rangle \langle \widetilde{p}_j | \widetilde{\Psi}^{\sigma}_{kv} \rangle. \tag{5.21}$$

When dmatpuopt = 1, occupancies are projections on bound-state atomic orbitals ϕ_0,

$$n_{m,m\prime}^{a_i,\sigma} = \sum_{ij} \rho_{ij}^{\sigma} \left\langle \phi_{n_i} \middle| \phi_0 \right\rangle \left\langle \phi_0 \middle| \phi_{n_j} \right\rangle. \tag{5.22}$$

The ABINIT documentation for this variable is clear that the dmatpuopt = 1 option must be accompanied by a PAW dataset wherein the first atomic wavefunction of the correlated subspace (which is set to ϕ_0 when read into ABINIT) is a normalized atomic eigenfunction. To determine if a particular PAW dataset meets this criterion, one must refer to the documentation of its generator.[§]

Because many PAW datasets readily available for widespread use do not necessarily fulfill these criterion, dmatpuopt = 2 is established as the default setting. With dmatpuopt = 2, occupancies are proportional to projections of atomic orbitals onto each other,

$$n_{m,m\prime}^{a_i,\sigma} = \sum_{ij} \rho_{ij}^{\sigma} \left\langle \phi_{n_i} \middle| \phi_{n_j} \right\rangle. \tag{5.23}$$

Eq. (5.23) corresponds to a projection operator of the form

$$P_{mm'}^{a_i}(\mathbf{r}, \mathbf{r}') = 1_{\circ}(\mathbf{r})\delta(|\mathbf{r}' - \mathbf{R_i}| - |\mathbf{r} - \mathbf{R_i}|) \times Y_{\ell m}(\hat{\mathbf{r}})Y_{\ell m'}^{*}(\hat{\mathbf{r}}'),$$

where δ is the Dirac-Delta function that effectively "counts" spatial overlap, $1_{\circ}(\mathbf{r})$ is a step function equal to unity when $\mathbf{r}$ is inside the augmentation region and zero elsewhere, and $Y_{\ell m}$ are the spherical harmonics. In this way, dmatpuopt = 2 simply computes the overlap more topologically, instead of using the same theory-based assumptions that undergird the other components of DFT.

When dmatpuopt = 3 or 4,

$$n_{m,m\prime}^{a_i,\sigma} = \mathcal{N}_0^{(2-\texttt{dmatpuopt})} \sum_{ij} \rho_{ij}^{\sigma} \langle \phi_{n_i} | \phi_0 \rangle \langle \phi_0 | \phi_{n_j} \rangle, \tag{5.24}$$

where $\mathcal{N}$ is a normalization constant representing the overlap between the bound state atomic eigenfunctions inside the augmentation sphere, delimited by cutoff radius r_c,

$$\mathcal{N} = \int_0^{r_c} \phi_0^2 \, dr \, . \tag{5.25}$$

This value is computed in subroutine pawpuxinit and printed in the log file as ph0phiint(1). When dmatpuopt = 4, $\mathcal{N}$ is squared in the denominator.

[§]PAW datasets generated via the *atompaw* code[59] will always feature a normalized, bound atomic eigenfunction as the first atomic wavefunction of a PAW dataset. Step (4) on Page 2 of Ref. [78] states clearly that *atompaw* mandates the use of "atomic eigenfunctions related to valence electrons (bound states)" as the partial waves included in the PAW basis. Eigenfunctions of bound electronic states are distinguishable by their negative energies (i.e., $\epsilon < 0$). Therefore, all PAW datasets generated by *atompaw*, including the JTH sets on PseudoDojo,[99,100] have atomic eigenfunctions as the first atomic wavefunctions of the correlated subspace. Their normalization, however, depends on the pseudo-partial-wave generation scheme. The *atompaw* dataset generator provides two options for this scheme: the Vanderbilt or the Blöchl. Based on the descriptions of these schemes in Sections 1.1 and 1.2 of Ref. [78] and an ABINIT forum response in 2016, normalization of the pseudized basis functions and their corresponding projectors is guaranteed only under the Vanderbilt scheme. The JTH table of PAW datasets,[99] available on the PseudoDojo website, match all criteria as a suitable dataset with which one may use dmatpuopt = 1.

5.4.3 Extraction of changes in occupancy matrix

The outer SCF loop, declared in `pawuj_drive`, continues after the perturbation is applied; the loop symmetrizes and prints D_{ij}. If `macro_uj` > `0`, a subroutine labeled `pawuj_red` is called. The subroutine generates the mesh that directly associates the strength of the perturbation (translated from `atvshift` to a shorter variable called `vsh`), and the corresponding change in occupancy, called `occ`. This information, along with the atom and spin indices, are saved in a type called `dtpawuj`, which is made accessible to the internal `UJdet` and `lrUJ` functions after the SCF cycle. The occupancy is calculated as the trace of the occupancy matrix $n^{a_i,\sigma}_{m,m'}$ discussed in Section 5.4.2,

$$\texttt{occ}(t_i,\sigma) = \mathrm{Tr}[n^{a_i,\sigma}_{m,m'}] * (3 - \texttt{nspden}). \tag{5.26}$$

The factor $(3 - \texttt{nspden})$ accounts for the occupancy of two spin channels on a single atom if and only if we do not distinguish between the up- and down-spin channels. See Table 5.2 for clarity.

The SCF iteration concludes by calling the subroutines associated with updating the density and the Hamiltonian. It then uses those updated quantities to find the updated potential, restarts a new SCF iteration, and so on and so forth until self-consistency is achieved.

The combinatory values of `macro_uj` and `nsppol` as outlined in Table 5.2 determine how the elements of `occ` are combined and saved in a new array called `luocc`. If `nsppol = 1`, then `occ` and `luocc` are identical, complementing the application of the perturbation to the entire atomic subspace by monitoring the response on the entire atomic subspace. In the case where `nsppol = 2` and `macro_uj = 1`, $\texttt{luocc}(t_i) = \texttt{occ}(t_i,\uparrow) + \texttt{occ}(t_i,\downarrow)$. In this way, the response is monitored on the total occupancy of the subspace. By contrast, when calculating the Hund's J by setting `nsppol = 2` and `macro_uj = 4`, one monitors the subspace magnetization: $\texttt{luocc}(t_i) = \texttt{occ}(t_i,\uparrow) - \texttt{occ}(t_i,\downarrow)$.

The type `dtpawuj` saves four (`vsh`, `luocc`) pairs, indexed by integers one through four. (In the verbose `.log` file, these pairs are labeled (`vsh1`, `occ1`), (`vsh2`, `occ2`), etc.; but the `occ` printed is actually the `luocc` value.) If the pair's referential index (called `iuj`) is an odd integer, that pair's occupancy is harvested at the end of the first SCF cycle, immediately after the perturbation is applied to D_{ij} but before the Hamiltonian and the density are updated to reflect that perturbation. These points will be used by `lrUJ` and `UJdet` to calculate the unscreened response matrix χ_0. Conversely, if `iuj` is an even integer, that occupancy is harvested after self-consistency has been achieved. Following suit, these points will be used in by the `UJdet` and `lrUJ` utilities to calculate the screened response χ.

Note that the pairs (`vsh1`, `occ1`) and (`vsh2`, `occ2`) correspond to the unperturbed ground state. Because no perturbation is applied, the unscreened and screened responses are identical. That is, `vsh1` = `vsh2` = 0.0 eV, and `occ1` = `occ2`, the ground-state occupancies of the subspace in question. All (`vsh`, `luocc`) pairs for all atoms and spin channels are printed out at the end of the SCF iteration in which they are determined.

5.4.4 The Hubbard U parameter determination via `UJdet`

All subroutines constructing ABINIT's `UJdet` utility—an abbreviation of "Hubbard U and J determination"—are housed inside module `65_paw/m_paw_uj.F90`. When the SCF cycle is complete, the

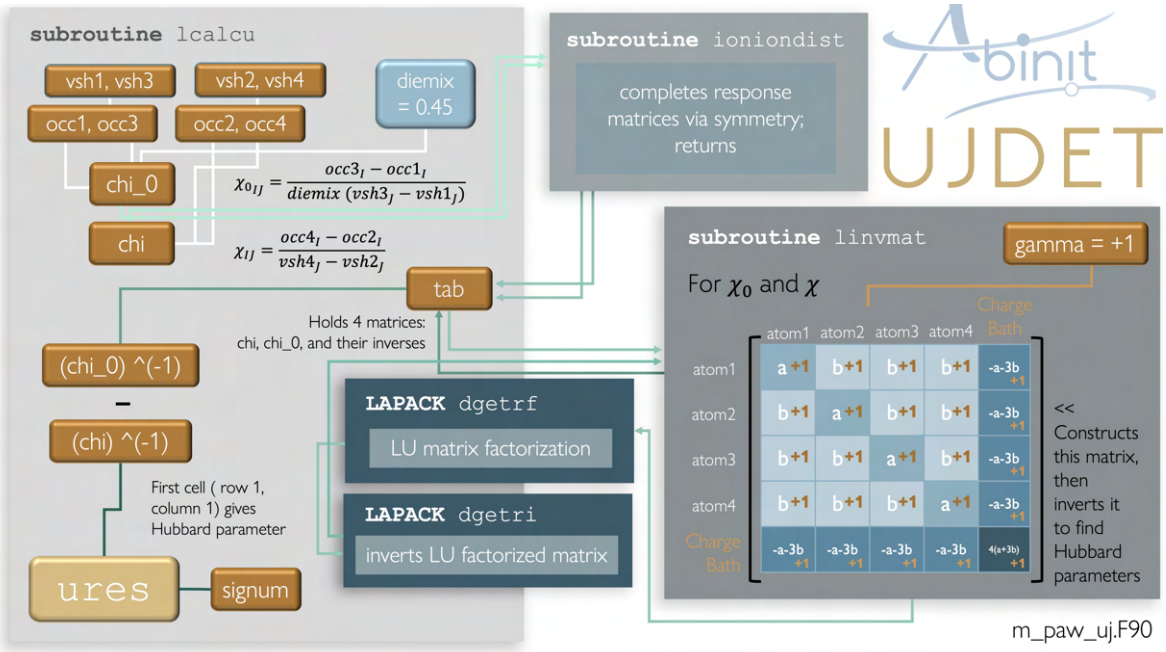

*Figure 5.6: Flowchart illustrating manipulation of (*vsh*, *occ*) pairs to determine the final Hubbard parameter,* ures*, for a transition metal Hubbard subspace.*

same subroutine that launched the SCF cycle and allocated default variables for the dtpawuj type, pawuj_drive, calls the subroutine pawuj_det.

Once called, this subroutine calculates and prints the scalar Hubbard parameter for exclusively the perturbed atom using the two data points it has (i.e., the unperturbed occupancies and those of the one perturbation applied during its run). It is here that the program creates the NetCDF file with suffix LRUJ.nc for this perturbative run, filling it with all information that the lrUJ post-processor will need to determine the choice Hubbard parameter in tandem with other perturbations. Before ABINIT wraps up its DFT run, however, the UJdet algorithm switches to the matrix prescription for calculating the Hubbard parameters. In doing so, it proceeds to calculate all elements of the response matrices using the aforementioned (vsh, luocc) pairs in the following manner:

$$\chi 0_{a_i a_j} = \frac{\texttt{luocc3}_{a_i} - \texttt{luocc1}_{a_i}}{\texttt{diemix}\,(\texttt{vsh3}_{a_j} - \texttt{vsh1}_{a_j})} \tag{5.27}$$

$$\chi_{a_i a_j} = \frac{\texttt{luocc4}_{a_i} - \texttt{luocc2}_{a_i}}{\texttt{vsh4}_{a_j} - \texttt{vsh2}_{a_j}} \tag{5.28}$$

where a_i, a_j are all atoms of the same species as the perturbed atom. (See note on symrel in Section 5.3.1 to avail of this UJdet functionality).

Once again, only the upper right triangular elements of the matrix are calculated via Eqs. (5.27) and (5.28). The matrices are then funneled, via the mother Hubbard U subroutine lcalcu, to subroutine ioniondist, where they are completed via symmetry, returned and saved into an object called tab, which holds four matrices: χ_0, χ, and their matrix inverses.

Following this, `tab` is shuffled over to subroutine `linvmat`, which calculates the inverses of not the response matrices themselves, but treated matrices designed to speed up the convergence of the Hubbard parameters with respect to supercell size. These treatments are mentioned in the “Further Considerations" section of Ref. [4], where it is posited that the perturbation on the Hubbard subspace would benefit from enhanced locality if charge neutrality in the response matrices was enforced, thereby isolating the perturbed atom from its periodic images, as one hopes to do using supercells. Following this understanding, the `UJdet` utility augments the response matrices with the negative of the sum of each row and each column, as illustrated in Fig. 5.6.

This augmented matrix is singular and thus non-invertible. To render the matrix invertible, an all-ones matrix is added to it, breaking its singularity. Note that this matrix is no longer equivalent to the input response matrices. However, Appendix A.4 of Ref. [101] demonstrates that the difference of the inverses of two non-invertible matrices—which is not possible mathematically—may be calculated indirectly by adding the same non-zero constant to each matrix element. This renders these matrices invertible, and the added constant is canceled when taking the difference of the two matrices.

Once prepped, the response matrices are funneled into the LAPACK routines `dgetrf` and `dgetri`, which respectively, LU factorize the matrices, then invert them. These inverted matrices are then saved into the last two positions of `tab` and returned back to subroutine `lcalcu`. At last, the inverted response matrices are subtracted, then scaled by a factor called `signum` (`= 1.0` for the Hubbard U and `= -1.0` for the Hund’s J). The first element of that object (row one, column one), in eV, is found to be the long-awaited Hubbard parameter, `ures`.

The `UJdet` utility does not stop here, though. The “Further Considerations" section of Ref. [4] considers an extrapolation scheme speculatively designed to converge much more quickly the Hubbard parameter with respect to supercell size. The number of Hubbard subspaces in a supercell grows linearly with the response matrix dimension. But intuition suggests that the occupancy effect of the perturbed subspace will attenuate with distance; that is, the matrix elements of the nearest neighbor atoms to that perturbed will feature most prominently in the determination of the Hubbard parameter, and those least neighborly to the perturbed atom will undergo small, if any, changes in occupancy, rendering their influence negligible. ABINIT developers took these further considerations to heart by incorporating an extrapolation scheme, wherein the response matrix elements of the primitive unit cell are used to fill out the response matrix elements of a supercell. Concisely, in ABINIT’s `UJdet` utility, the off-diagonal elements of the primitive cell response matrices are multiplied by the number of next-nearest neighbor (NNN) Hubbard atoms in the primitive cell and divided by the number of Hubbard atoms in the NNN shell of the supercell. These supercell response matrices are then inverted following the same procedure as above to approximate the Hubbard parameters for subspaces in supercells of increasing size.

5.4.5 The `lrUJ` post-processor

When the `lrUJ` post-processing utility is executed via command line, it reads in a user-specified series of NetCDF files with suffix `LRUJ.nc`. The program sorts the n files in order of perturbation strength, then reads in all necessary data related to those perturbations, including the unperturbed state (which

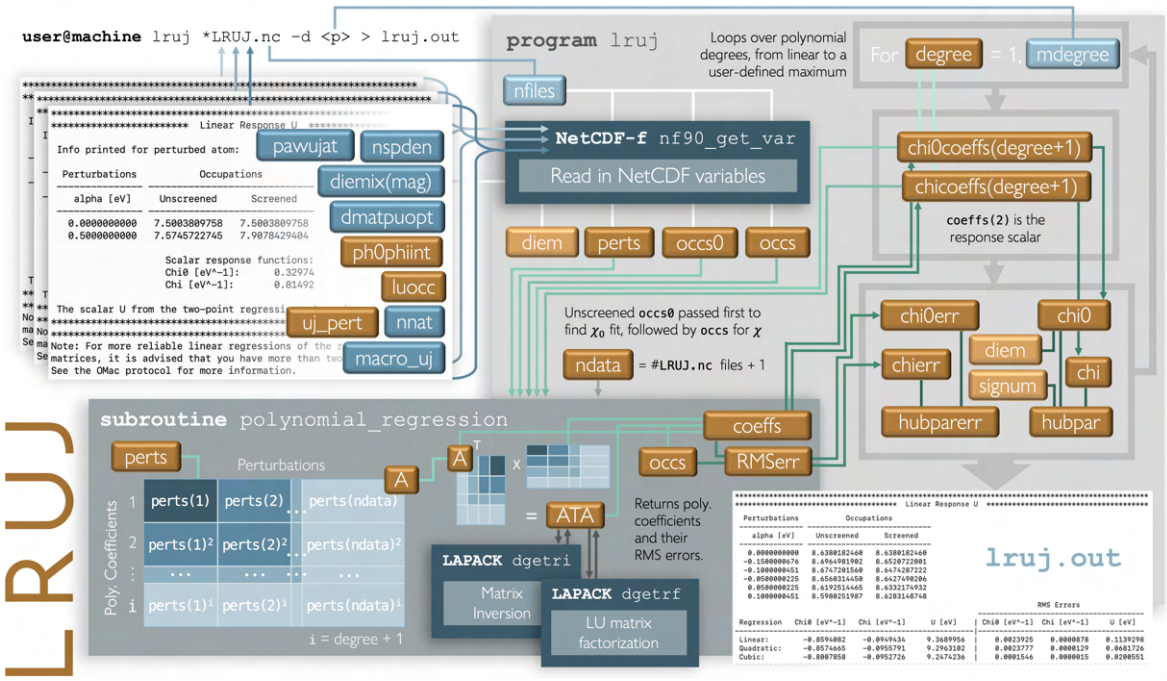

Figure 5.7: Flowchart illustrating the lrUJ algorithm.

is output in all perturbative calculations) in addition to the unscreened and screened occupancies (or spin magnetization in the case of Hund's J).

After the perturbation strengths are read from the NetCDF files, where they are reported in Ha, the lrUJ program converts them to eV. All calculations are then conducted in eV. Compatibility tests are conducted on the input information, and then the linear response procedure begins.

The lrUJ utility was engineered with the occasional non-linearity of linear response in mind. This phenomenon has been demonstrated in many of the linear response plots included thus far, for example, Figs. 5.1, 5.5, and perhaps most strikingly, Fig. 4.1. ABINIT has an inbuilt, shared subroutine that calculates the polynomial regression of any degree for any list of data points. This subroutine computes the $n + 1$ coefficients of a degree n polynomial by constructing a matrix using the fitted data points, then solving the resulting system with linear algebra. The mathematical specifics of this procedure are illustrated in Fig. 5.7 but outlined more formally on this website. As such, the polynomial_regression subroutine is dependent on the subroutines available in the widely-used linear algebra package, LAPACK.[102]

We use polynomials only in this program because of their relative simplicity and reasonably predictable RMS error behavior. In case the user wants to fit another type of function to the data, the data points are printed out in an easily copy-paste or parsable format for independent regression analysis.

To begin the regression procedure, the lrUJ program tests if the user has specified a maximum polynomial degree to calculate. If so, this degree has to be greater than or equal to two more than the number of data points (i.e., the number of incoming LRUJ.nc files plus one unperturbed state). If the user has left this information unspecified, then the maximum polynomial degree will default to cubic (degree three) UNLESS the number of input files is equal to two or three, in which cases the maximum

polynomial degree will be set to linear (degree one) or quadratic (degree two), respectively.

Once the max polynomial degree is set, the arrays storing the response information for each degree are allocated and the loop over polynomial degree begins. For every degree, the polynomial regression subroutine is called twice: once to fit the unscreened occupancies (magnetizations) and record its uncertainty, and the other to fit the screened occupancies (magnetizations) and record its uncertainty. For an N-point linear regression $f(\alpha)$, where α_i is the perturbation strength corresponding to occupancy (magnetization) μ_i, the equation the `lrUJ` utility uses to calculated the uncertainty on the response function X={χ_0, χ} models the unbiased RMS fit error, evaluated as[§]

$$\sigma_{\mathrm{X}} = \sqrt{\frac{\sum_{i=1}^{N} \left(f\left(\alpha_i\right) - \mu_i\right)^2}{N-1}}\,. \tag{5.29}$$

The error on the unscreened response, or σ_{χ_0} is scaled by an additional factor of $\frac{1}{\texttt{diemix}}$ (or $\frac{1}{\texttt{diemixmag}}$ for $\sigma_{\chi_{0_M}}$) to account for the mixing considerations outlined in Section 5.1.2. The RMS fit error, alongside the fit coefficients, are returned to the main program, where the utility uses that information to find χ and χ_0 as

$$\chi_0 = \frac{1}{\texttt{diemix}} \left.\frac{df_0(\alpha)}{d\alpha}\right|_{\alpha=0} \tag{5.30}$$

$$\chi = \left.\frac{df(\alpha)}{d\alpha}\right|_{\alpha=0}. \tag{5.31}$$

With one-dimensional polynomials as functions of α, the derivative at $\alpha = 0.0$ eV is simply the second coefficient pertaining to that polynomial function. The unscreened response χ_0 must be divided by the mixing parameter that was used in the preceding ABINIT run. This default mixing parameter is `diemix` and it is equal to 0.45, by default. However, if the value of `diemix` is changed, or if a Hund's J calculation is conducted (at which point `diemixmag` instead of `diemix` is used for the mixing constant), χ_0 is divided by that value to get the true unscreened response.

The corresponding scalar Hubbard parameter (HP) is calculated as

$$\mathrm{HP} = \texttt{signum} \cdot \left({\chi_0}^{-1} - \chi^{-1} \right) \tag{5.32}$$

where `signum` = 1 if calculating the Hubbard U or `signum` = −1 if calculating the Hund's J. The error on the Hubbard parameter, printed in column seven of the `lrUJ` output, is calculated as in Eq. (4.14).

Having executed its main function, the program concludes its operations by printing out the information in user-friendly format to the main output file (if specified in the command line; prints to terminal otherwise). An example of such an output is available in Fig. 5.4.[‡]

[§] In Chapter 7, we do not employ in practice this definition of the uncertainty on the response coefficients, opting instead to use the uncertainty defined in Eq. (4.13).

[‡] Although the `lrUJ` post-processor emerged with ABINIT version 9.10.1, important bug fixes for this utility were implemented in ABINIT version 9.10.5, and a further update using the correct form of Eq. (4.14) went into effect in Abinit version 9.11. If using prior versions of `lrUJ`, please note that the reported RMS error for the Hubbard parameter is unreliable (these versions erroneously do not square the response functions in the denominators of Eq. (4.14)).

Bibliography

[1] H. J. Kulik, M. Cococcioni, D. A. Scherlis, and N. Marzari, Phys. Rev. Lett. **97**, 103001 (2006).

[2] B. Himmetoglu, A. Floris, S. de Gironcoli, and M. Cococcioni, International Journal of Quantum Chemistry **114**, 14 (2014).

[3] W. E. Pickett, S. C. Erwin, and E. C. Ethridge, Phys. Rev. B **58**, 1201 (1998).

[4] M. Cococcioni and S. de Gironcoli, Physical Review B **71**, 035105 (2005).

[5] P. H. Dederichs, S. Blügel, R. Zeller, and H. Akai, Phys. Rev. Lett. **53**, 2512 (1984).

[6] A. K. McMahan, R. M. Martin, and S. Satpathy, Phys. Rev. B **38**, 6650 (1988).

[7] M. Shishkin and H. Sato, Phys. Rev. B **93**, 085135 (2016).

[8] K. Nakamura, R. Arita, Y. Yoshimoto, and S. Tsuneyuki, Phys. Rev. B **74**, 235113 (2006).

[9] I. V. Solovyev and M. Imada, Phys. Rev. B **71**, 045103 (2005).

[10] O. Gunnarsson, Phys. Rev. B **41**, 514 (1990).

[11] M. S. Hybertsen, M. Schlüter, and N. E. Christensen, Phys. Rev. B **39**, 9028 (1989).

[12] O. Gunnarsson, O. K. Andersen, O. Jepsen, and J. Zaanen, Phys. Rev. B **39**, 1708 (1989).

[13] E. B. Linscott, D. J. Cole, M. C. Payne, and D. D. O'Regan, Physical Review B **98**, 235157 (2018).

[14] M. Springer and F. Aryasetiawan, Phys. Rev. B **57**, 4364 (1998).

[15] T. Kotani, Journal of Physics: Condensed Matter **12**, 2413 (2000).

[16] F. Aryasetiawan, M. Imada, A. Georges, G. Kotliar, S. Biermann, and A. I. Lichtenstein, Physical Review B **70**, 195104 (2004).

[17] F. Aryasetiawan, K. Karlsson, O. Jepsen, and U. Schonberger, Physical Review B **74**, 125106 (2006).

[18] E. Şaşıoğlu, C. Friedrich, and S. Blügel, Phys. Rev. B **83**, 121101 (2011).

[19] L. Vaugier, H. Jiang, and S. Biermann, Phys. Rev. B **86**, 165105 (2012).

[20] B. Amadon, T. Applencourt, and F. Bruneval, Phys. Rev. B **89**, 125110 (2014).

[21] N. J. Mosey and E. A. Carter, Phys. Rev. B **76**, 155123 (2007).

[22] N. J. Mosey, P. Liao, and E. A. Carter, The Journal of Chemical Physics **129**, 014103 (2008).

[23] A. N. Andriotis, R. M. Sheetz, and M. Menon, Phys. Rev. B **81**, 245103 (2010).

[24] L. A. Agapito, S. Curtarolo, and M. Buongiorno Nardelli, Phys. Rev. X **5**, 011006 (2015).

[25] S.-H. Lee and Y.-W. Son, Phys. Rev. Res. **2**, 043410 (2020).

[26] I. Timrov, N. Marzari, and M. Cococcioni, Physical Review B **98**, 085127 (2018).

[27] I. Timrov, N. Marzari, and M. Cococcioni, Phys. Rev. B **103**, 045141 (2021).

[28] I. Timrov, N. Marzari, and M. Cococcioni, Computer Physics Communications **279**, 108455 (2022).

[29] K. Yu and E. A. Carter, The Journal of Chemical Physics **140**, 121105 (2014).

[30] G. Moynihan, G. Teobaldi, and D. D. O'Regan, "A self-consistent ground-state formulation of the first-principles Hubbard U parameter validated on one-electron self-interaction error," (2017), arXiv:1704.08076 [cond-mat.str-el].

[31] V. I. Anisimov and O. Gunnarsson, Phys. Rev. B **43**, 7570 (1991).

[32] M. Cococcioni, *A LDA+U study of selected iron compounds*, Physics, Scuola Internazionale Superiore di Studi Avanzati, Scuola Internazionale Superiore di Studi Avanzati (2002).

[33] V. I. Anisimov, J. Zaanen, and O. K. Andersen, Physical Review B **44**, 943 (1991).

[34] D. S. Lambert and D. D. O'Regan, Phys. Rev. Res. **5**, 013160 (2023).

[35] M. Bernardi, Journal of Physics: Condensed Matter **32**, 385501 (2020).

[36] N. S. Raju, R. Bilgic, J. E. Edwards, and P. F. Fleer, Applied Psychological Measurement **21**, 291 (1997).

[37] P. Yin and X. Fan, The Journal of Experimental Education **69**, 203 (2001).

[38] G. Shieh, Organizational Research Methods **11**, 387 (2008).

[39] J. Karch, Collabra: Psychology **6**, 45 (2020).

[40] G. Moynihan, *A self-contained ground-state approach for the correction of self-interaction error in approximate density-functional theory*, Physics, Trinity College Dublin, Trinity College Dublin, School of Physics (2018).

[41] D. D. O'Regan, M. C. Payne, and A. A. Mostofi, Phys. Rev. B **83**, 245124 (2011).

[42] J.-D. Chai, The Journal of Chemical Physics **136**, 154104 (2012).

[43] O. K. Andersen, Phys. Rev. B **12**, 3060 (1975).

[44] Hans L. Skriver, *The LMTO Method: Muffin-Tin Orbitals and Electronic Structure*, Vol. 1 (Springer, Berlin, Heidelberg, 1984) p. 286.

[45] S. L. Dudarev, G. A. Botton, S. Y. Savrasov, C. J. Humphreys, and A. P. Sutton, Phys. Rev. B **57**, 1505 (1998).

[46] V. I. Anisimov, I. V. Solovyev, M. A. Korotin, M. T. Czyżyk, and G. A. Sawatzky, Phys. Rev. B **48**, 16929 (1993).

[47] A. Ambrosetti and P. L. Silvestrelli, "Introduction to Maximally Localized Wannier Functions," in *Reviews in Computational Chemistry* (John Wiley and Sons, Ltd, 2016) Chap. 6, pp. 327–368.

[48] T. Miyake and F. Aryasetiawan, Phys. Rev. B **77**, 085122 (2008).

[49] J. Avery, *Hyperspherical Harmonics and Generalized Sturmians* (Springer, Dordrecht, 2001) p. 205.

[50] H. J. Kulik and N. Marzari, The Journal of Chemical Physics **133**, 114103 (2010).

[51] R. Pnini, Y. Peleg, E. Hecht, and E. Zaarur, *Schaum's Outline of Quantum Mechanics, Second Edition* (McGraw-Hill, US, 2010).

[52] P. E. Blöchl, Physical Review B **50**, 17953 (1994).

[53] C.-K. Skylaris, P. D. Haynes, A. A. Mostofi, and M. C. Payne, The Journal of Chemical Physics **122**, 084119 (2005).

[54] N. D. Hine, "Using the pseudoatomic solver to generate NGWFs in ONETEP," (2011), updated February 2016.

[55] G. Geneste, B. Amadon, M. Torrent, and G. Dezanneau, Physical Review B **96**, 134123 (2017).

[56] O. Bengone, M. Alouani, P. Blochl, and J. Hugel, Physical Review B **62**, 16392 (2000).

[57] M. Torrent, N. Holzwarth, F. Jollet, D. Harris, N. Lepley, and X. Xu, Computer Physics Communications **181**, 1862 (2010).

[58] N. Holzwarth, Computer Physics Communications **243**, 25 (2019).

[59] N. Holzwarth, A. Tackett, and G. Matthews, Computer Physics Communications **135**, 329 (2001).

[60] G. Kresse and D. Joubert, Physical Review B **59**, 1758 (1999).

[61] ABINIT, "PAW input variables: dmatpuopt," (2021).

[62] B. Amadon, F. Jollet, and M. Torrent, Phys. Rev. B **77**, 155104 (2008).

[63] Y.-C. Wang, Z.-H. Chen, and H. Jiang, The Journal of Chemical Physics **144**, 144106 (2016).

[64] I. Timrov, N. Marzari, and M. Cococcioni, Physical Review B **103**, 045141 (2021).

[65] P. Giannozzi, S. Baroni, N. Bonini, M. Calandra, R. Car, C. Cavazzoni, D. Ceresoli, G. L. Chiarotti, M. Cococcioni, I. Dabo, A. D. Corso, S. de Gironcoli, S. Fabris, G. Fratesi, R. Gebauer, U. Gerstmann, C. Gougoussis, A. Kokalj, M. Lazzeri, L. Martin-Samos, N. Marzari, F. Mauri, R. Mazzarello, S. Paolini, A. Pasquarello, L. Paulatto, C. Sbraccia, S. Scandolo, G. Sclauzero, A. P. Seitsonen, A. Smogunov, P. Umari, and R. M. Wentzcovitch, Journal of Physics: Condensed Matter **21**, 395502 (2009).

[66] P. Giannozzi, O. Andreussi, T. Brumme, O. Bunau, M. B. Nardelli, M. Calandra, R. Car, C. Cavazzoni, D. Ceresoli, M. Cococcioni, N. Colonna, I. Carnimeo, A. D. Corso, S. de Gironcoli, P. Delugas, R. A. DiStasio, A. Ferretti, A. Floris, G. Fratesi, G. Fugallo, R. Gebauer, U. Gerstmann, F. Giustino, T. Gorni, J. Jia, M. Kawamura, H.-Y. Ko, A. Kokalj, E. Küçükbenli, M. Lazzeri, M. Marsili, N. Marzari, F. Mauri, N. L. Nguyen, H.-V. Nguyen, A. O. de-la Roza, L. Paulatto, S. Poncé, D. Rocca, R. Sabatini, B. Santra, M. Schlipf, A. P. Seitsonen, A. Smogunov, I. Timrov, T. Thonhauser, P. Umari, N. Vast, X. Wu, and S. Baroni, Journal of Physics: Condensed Matter **29**, 465901 (2017).

[67] F. S. Hegner, J. R. Galán-Mascarós, and N. López, Inorganic Chemistry **55**, 12851 (2016).

[68] P. Gopal, R. D. Gennaro, M. S. dos Santos Gusmao, R. A. R. A. Orabi, H. Wang, S. Curtarolo, M. Fornari, and M. B. Nardelli, Journal of Physics: Condensed Matter **29**, 444003 (2017).

[69] L. A. Mariano, B. Vlaisavljevich, and R. Poloni, Journal of Chemical Theory and Computation **16**, 6755 (2020).

[70] L. A. Mariano, B. Vlaisavljevich, and R. Poloni, Journal of Chemical Theory and Computation **17**, 2807 (2021).

[71] G. C. Moore, M. K. Horton, E. Linscott, A. M. Ganose, M. Siron, D. D. O'Regan, and K. A. Persson, Phys. Rev. Mater. **8**, 014409 (2024).

[72] O. K. Orhan and D. D. O'Regan, Physical Review B **101**, 245137 (2020).

[73] X. Gonze, B. Amadon, G. Antonius, F. Arnardi, L. Baguet, J.-M. Beuken, J. Bieder, F. Bottin, J. Bouchet, E. Bousquet, N. Brouwer, F. Bruneval, G. Brunin, T. Cavignac, J.-B. Charraud, W. Chen, M. Côté, S. Cottenier, J. Denier, G. Geneste, P. Ghosez, M. Giantomassi, Y. Gillet, O. Gingras, D. R. Hamann, G. Hautier, X. He, N. Helbig, N. Holzwarth, Y. Jia, F. Jollet, W. Lafargue-Dit-Hauret, K. Lejaeghere, M. A. L. Marques, A. Martin, C. Martins, H. P. C. Miranda, F. Naccarato, K. Persson, G. Petretto, V. Planes, Y. Pouillon, S. Prokhorenko, F. Ricci, G.-M. Rignanese, A. H. Romero, M. M. Schmitt, M. Torrent, M. J. van Setten, B. V. Troeye, M. J. Verstraete, G. Zérah, and J. W. Zwanziger, Comput. Phys. Commun. **248**, 107042 (2020).

[74] A. H. Romero, D. C. Allan, B. Amadon, G. Antonius, T. Applencourt, L. Baguet, J. Bieder, F. Bottin, J. Bouchet, E. Bousquet, F. Bruneval, G. Brunin, D. Caliste, M. Côté, J. Denier, C. Dreyer, P. Ghosez, M. Giantomassi, Y. Gillet, O. Gingras, D. R. Hamann, G. Hautier, F. Jollet, G. Jomard, A. Martin, H. P. C. Miranda, F. Naccarato, G. Petretto, N. A. Pike, V. Planes, S. Prokhorenko, T. Rangel, F. Ricci, G.-M. Rignanese, M. Royo, M. Stengel, M. Torrent, M. J. van Setten, B. V. Troeye, M. J. Verstraete, J. Wiktor, J. W. Zwanziger, and X. Gonze, J. Chem. Phys. **152**, 124102 (2020).

[75] X. Gonze, B. Amadon, P. M. Anglade, J. M. Beuken, F. Bottin, P. Boulanger, F. Bruneval, D. Caliste, R. Caracas, M. Côté, T. Deutsch, L. Genovese, P. Ghosez, M. Giantomassi, S. Goedecker, D. R. Hamann, P. Hermet, F. Jollet, G. Jomard, S. Leroux, M. Mancini, S. Mazevet, M. J. T. Oliveira, G. Onida, Y. Pouillon, T. Rangel, G. M. Rignanese, D. Sangalli, R. Shaltaf, M. Torrent, M. J. Verstraete, G. Zerah, and J. W. Zwanziger, Computer Physics Communications 40 YEARS OF CPC: A celebratory issue focused on quality software for high performance, grid and novel computing architectures, **180**, 2582 (2009).

[76] X. Gonze, C.-O. Almbladh, A. Cucca, D. Caliste, C. Freysoldt, M. Marques, V. Olevano, Y. Pouillon, and M. Verstraete, Computational Materials Science **43**, 1056 (2008).

[77] X. Gonze, J.-M. Beuken, R. Caracas, F. Detraux, M. Fuchs, G.-M. Rignanese, L. Sindic, M. Verstraete, G. Zerah, F. Jollet, M. Torrent, A. Roy, M. Mikami, P. Ghosez, J.-Y. Raty, and D. Allan, Computational Materials Science **25**, 478 (2002).

[78] N. A. W. Holzwarth, "Notes for revised form of atompaw code," (2010).

[79] M. Torrent, F. Jollet, F. Bottin, G. Zérah, and X. Gonze, Computational Materials Science **42**, 337 (2008).

[80] B. Himmetoglu, R. M. Wentzcovitch, and M. Cococcioni, Phys. Rev. B **84**, 115108 (2011).

[81] S. Ryee and M. J. Han, Scientific Reports **8**, 9559 (2018).

[82] O. K. Orhan and D. D. O'Regan, Phys. Rev. B **101**, 245137 (2020).

[83] A. Albavera-Mata, S. B. Trickey, and R. G. Hennig, The Journal of Physical Chemistry Letters **13**, 12049 (2022).

[84] A. C. Burgess, E. Linscott, and D. D. O'Regan, Phys. Rev. B **107**, L121115 (2023).

[85] L. MacEnulty, M. Giantomassi, B. Amadon, G.-M. Rignanese, and D. D. O'Regan, Electronic Structure **6**, 037003 (2024).

[86] L. MacEnulty and D. J. Adams, "Hubbard U and Hund's J parameters with Cococcioni and de Gironcoli's approach: Determine the Hund's J for Ni 3d in NiO with LRUJ," (2023).

[87] A. I. Liechtenstein, V. I. Anisimov, and J. Zaanen, Phys. Rev. B **52**, R5467 (1995).

[88] H. Chen and A. J. Millis, Phys. Rev. B **93**, 045133 (2016).

[89] M. T. Czyżyk and G. A. Sawatzky, Phys. Rev. B **49**, 14211 (1994).

[90] P. Pulay, Chemical Physics Letters **73**, 393 (1980).

[91] L. Binci and N. Marzari, Phys. Rev. B **108**, 115157 (2023).

[92] G. C. Moore, M. K. Horton, E. Linscott, A. M. Ganose, M. Siron, D. D. O'Regan, and K. A. Persson, Phys. Rev. Mater. **8**, 014409 (2024).

[93] Unidata, "Netcdf 4," (2024), Boulder, CO, USA: UCAR/Unidata Program Center.

[94] I. döt Net, T. Müller, P. Antoniou, E. Aro, T. Smith, C. C. Evans, and O. Ben-Kiki, "YAML Ain't Markup Language, Version 1.2.2," (2024).

[95] Wolfram Research, Inc., "Mathematica, Version 14.0," (2024), champaign, IL, 2024.

[96] M. Giantomassi and the AbiPy Group, "Abipy, Version 0.9.7," (2024), Louvain-la-Neuve, BE.

[97] L. MacEnulty and D. D. O'Regan, Phys. Rev. B **108**, 245137 (2023).

[98] G. Geneste, B. Amadon, M. Torrent, and G. Dezanneau, Phys. Rev. B **96**, 134123 (2017).

[99] F. Jollet, M. Torrent, and N. Holzwarth, Computer Physics Communications **185**, 1246 (2014).

[100] M. J. van Setten, M. Giantomassi, E. Bousquet, M. J. Verstraete, D. R. Hamann, X. Gonze, and G. M. Rignanese, Computer Physics Communications **226**, 39 (2018).

[101] E. B. Linscott, *Accounting for Strong Electronic Correlation in Metalloproteins*, Physics, University of Cambridge, Corpus Christi College, England (2019).

[102] E. Anderson, Z. Bai, C. Bischof, L. S. Blackford, J. Demmel, J. Dongarra, J. Du Croz, A. Greenbaum, S. Hammarling, A. McKenney, and D. Sorensen, *LAPACK Users' Guide*, 3rd ed. (Society for Industrial and Applied Mathematics, 1999).

Part III

Optimization Strategies for Magnetic NiO in Abinit

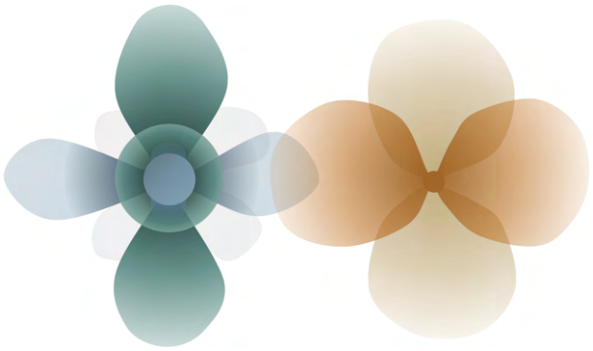

Chapter 6

A magnetic model of NiO

Nickel is a prototypical first-row transition metal and a suitable candidate for many sustainable technologies. Its monoxide, NiO, is promising as a p-type semiconductor with multiple technological applications: in photocathodes,[1–3] lithium-ion battery cathodes for electric vehicles,[4] OH- carrier battery cathodes for portable electronics,[5] efficiency enhancers in solar cells,[6] among others. It is relatively non-toxic and structurally stable, with a wide and tunable band gap (around 3.5-4.0 eV).[6–9]

NiO crystallizes above the Néel temperature (523 K) in the rocksalt structure (space group *Fm3m*) with an experimental lattice parameter consistently estimated at around 4.17 Å (7.88 a_0) across a variety of diffraction studies.[10–18] Other experiments indicate that Ni sites in bulk NiO take on magnetic moments between 1.96 μ_B[15] and 2.2 μ_B.[18–21] While under certain conditions the TMO can be observed in other magnetic orderings, its ground-state magnetic ordering (MO) is AF_{II}, the isomagnetic planes of which alternate antiferromagnetically in the [111] direction (see schematic in Fig. 6.1).[10–12] NiO AF_I and FM MOs yield experimental lattice parameters of 4.168 and 4.171 Å, respectively.[22]

Bulk NiO is a well-studied system with a wealth of literature attesting to its total energy difference parameters, properties of material systems that, as we discussed in Section 2.4, lie just beyond bare DFT's realm of accuracy. The status of NiO as the prototypical Mott-Hubbard insulator renders it a good benchmark system through which to observe the effect of SIE corrective techniques on total energies. To date, relatively little is known of the effects of fully first-principles Hubbard corrective protocol on magnetism-related interactions and parameters in NiO.

This chapter is a discussion on the complexities of structuring a magnetic model of NiO using DFT-accessible objects, beginning with a description of the challenge that transition metal oxides pose for DFT simulations. It features an introduction to our chosen model for magnetism and magnetic energies, the Heisenberg-Dirac-van Vleck (HDvV) effective spin Hamiltonian, a sophisticated semi-classical representation of macroscopic magnetism in material systems. The origins of the HDvV effective spin Hamiltonian are briefly described, followed by its dissection to reveal the physical basis for each of its mathematical components. Finally, commonly employed assumptions regarding spin-vector treatment and occupancy analysis in the mapping of the HDvV Hamiltonian onto approximative DFT results are dismantled and reconsidered, opening the possibility of further interpretations of the HDvV Hamiltonian that could improve KS DFT's accuracy.

6.1 Challenges of modeling magnetic transition metal oxides

Antiferromagnetic transition metal oxides (TMOs) are increasingly vital constituents of many technologies, from high-performance battery cathodes,[23–27] to water-splitting catalysts,[28,29] to efficient photovoltaic devices for sustainable energy storage.[30–32] Understanding the macroscopic magnetic properties of this class of material requires a sophisticated description of the competing spin-related energies relevant at microscopic scales.

In nickel oxide specifically, the Ni^{2+} ions find themselves in octahedral coordination environments, which break the degeneracy of the Ni $3d$-orbitals and have the effect of suppressing the orbital contribution to the magnetic moment. As such, Ni atoms in NiO act like Curie paramagnets, i.e., they respond in a temperature-dependent fashion to magnetic field exposure. Each Ni atom thus acts like a magnetic center with which we may associate a localized magnetic moment.[33]

Magnetic interactions in systems with local magnetic moments arise from static and dynamic electron-electron correlation effects. A relativistic formalism is ultimately necessary to obtain a comprehensive description of the electronic structure of these magnetic systems. However, it is possible, and often more feasible, to achieve reasonable accuracy through the deployment of non-relativistic, effective Hamiltonians, eventually incorporating scalar relativistic effects locally and *ad hoc*.[33,34] A variety of simulation techniques exist to carry out such calculations, such as DMFT,[35–38] quantum Monte Carlo[39–42] and coupled cluster methods,[43–45] to name only a few.

Each method comes with its own strengths and weaknesses, regimes of applicability, and computational cost and scaling.[46] The principle challenge to physical accuracy lies in the correct definition of the different spin states. Recall from Chapter 1 that the non-relativistic, many-body electronic Hamiltonian $\hat{H}_e$ does not act on the spin coordinates of electrons; spin-symmetry requirements and adherence to the PEP are instead satisfied by imposing anti-symmetry and other spin restrictions on the wavefunction. Only true eigenstates of the square of the total spin $\mathbf{S}^2$ have a well-defined total spin

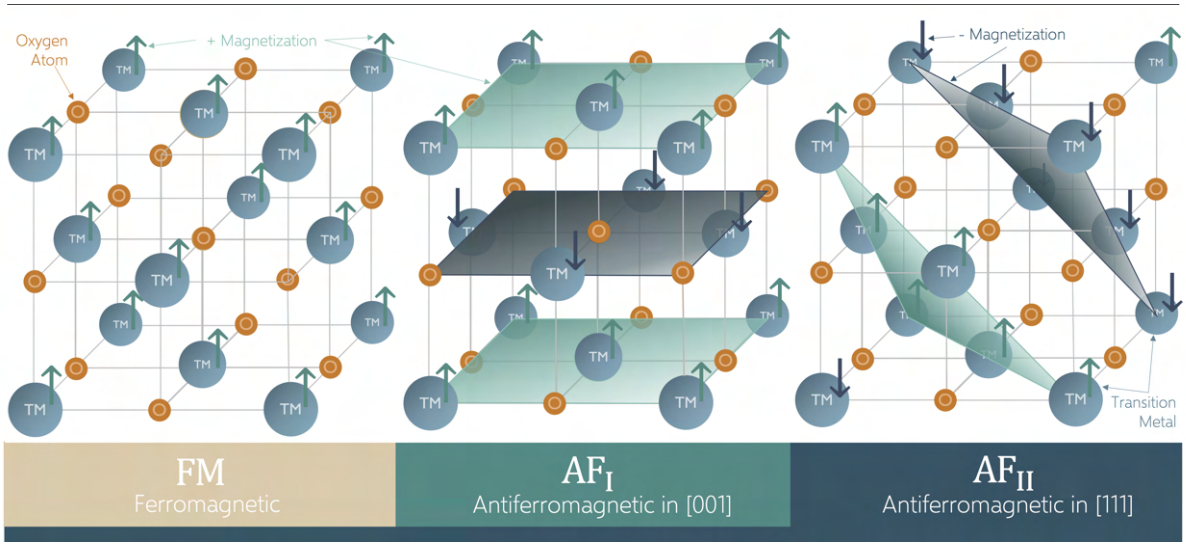

Figure 6.1: The magnetic orderings of monoxide ground-state antiferromagnetic TMOs crystallizing in the rocksalt structure, oxygen atoms (orange) and TMs (blue). Isomagnetic planes represented by color gradients: spin-up (green) and spin-down (navy).

quantum number S and thus commute with $\hat{H}_e$. For example, the ferromagnetic state of any system, which can in general be written in terms of a single determinant, is an eigenstate of $\mathbf{S}^2$, corresponding to the maximum eigenvalue $S = S_{\text{max}}$.[33] The antiferromagnetic state written with one Slater determinant, however, is only an eigenstate of the S_z, not of $\mathbf{S}^2$.[33] Adequate description of any eigenstate of $\mathbf{S}^2$ is obtainable through multi-reference formalisms,[47] which can be quite time-consuming and resource intensive.[46] DFT formalisms that impose the $\mathbf{S}^2$ eigenvector requirements are based on either spin-restricted KS DFT (like spin-restricted open-shell KS or spin-restricted ensemble-referenced KS) or time-dependent DFT, the latter of which attempts to construct a reference configuration that produces both singlet and triplet states through single excitations.[46,48]

Spin-unrestricted KS DFT, while only making use of only one Slater determinant, is often used to model magnetic properties all the same. In principle, only the ferromagnetic state is accessible to these implementations. With other spin states, it becomes impossible to satisfy spin and spatial symmetry requirements, leading to broken symmetry solutions that are not necessarily eigenstates of $\mathbf{S}^2$.[49,50] Mapping effective spin Hamiltonians to spin-polarized KS-DFT total energies is controversial, as the extracted magnetic parameters can be ambiguous, erroneous, or physically meaningless.[48] Care must be taken in dealing with the broken symmetry states and their corresponding total energies.

If the exact XC functional were known exactly, DFT would be able to find the exact ground state for any magnetic configuration. It follows, then, that the broken symmetry solutions result from the approximations made to the XC functional.[51] As described in Section 2.4, it is well-documented that the (semi-)local XC functional approximations to DFT struggle to accurately describe the strongly correlated electron systems for which the TMO class is prototypical.[52–58] A challenge thus emerges for DFT+U+J functionals in spin-unrestricted KS DFT; fix the spin-based total energies (or, more feasibly, total energy differences between magnetic orderings) to obtain accurate magnetic parameters.

Within the context of Hubbard-corrected DFT, much scientific attention is directed towards understanding the effect of the corrective functionals and their parameters upon bond distances, band gap predictions,[59–61] total energy differences,[62–68] and other parameterized spectroscopic properties. Meanwhile, comparatively few studies have probed how DFT+U+J and related functionals impact metrics of magnetism, such as the magnetic exchange parameters in the Heisenberg model.[68,69] When calculated using total energy differences, these parameters become valid ground-state DFT quantities and thus concise indicators of the reliability of DFT+U+J total energies. Magnetic exchange parameters constitute expedient indicators of the quality of first-principle DFT+U+J total energy differences, which are often supposed to be within the method's regime of reliable applicability, albeit without much concrete literature evidence of that to date. It is essential, and even more so due to its widespread adoption, to work to establish the regime of reliability of first principles for DFT+U+J total-energy differences, and to explore and delineate its remaining weaknesses and ambiguities.

6.2 Effective spin Hamiltonians

In a groundbreaking 1921 paper, Hendrika Johanna van Leeuwen completed the derivation of what was to become known as the Bohr-van Leeuwen theorem, a pivotal discovery that exposed the need for a quantum mechanical description of magnetism.[70] Building on that work, and simultaneously

seeking a theoretical description for magnetic phase transitions, the physicist Wilhelm Lenz and later his pupil Ernst Ising in 1924 developed a semi-classical model describing exchange interactions of a one-dimensional lattice of integer spins, which could take on binary, scalar values of +1 or -1 corresponding to the conventional up and down orientations.[71] Ising's thesis represented one of the first attempts at describing macroscopic magnetism in materials via an accumulation of microscopic quantum spin-based phenomena and became known as the Ising model.[72]

The Ising model fell just shy of modeling the interactions of the elementary units of magnetism, principally because the theory of quantum mechanics, in its adolescence in 1924, had not developed enough to tackle spin in terms of vectors, much less Pauli matrices.[72] By 1928, however, the spin operator had matured enough to allow Werner Heisenberg to develop the quantum Heisenberg Hamiltonian,[73] the simplified version of which indeed reduces to the one-dimensional Ising model and its three-dimensional analog (the classical Heisenberg model).

These models are used to interpret experimental phenomena that demonstrate magnetic properties of materials, which are documented through a variety of experimental techniques. One such method is inelastic neutron scattering (INS) spectroscopy, which harnesses the magnetic dipole interaction that occurs between the spin of a neutron and that of an electron in a magnetic solid. This interaction causes a neutron to both flip its spin and excite the dipole moment of the atom it encounters, as well as all neighboring atoms, into synchronized precession that can be described by a spin wave (or magnon). The path of the outgoing neutron is deflected in a manner related to the energy it lost during its interaction with the magnon. It is this dispersion relation, which emerges after directing a steady stream of neutrons at the sample material, that reveals information about the material's interatomic magnetic interactions, including the numerical values of the relevant exchange-coupling constants, which we will discuss later. A similar experimental method involves Raman scattering spectroscopy, which relies on the inelastic scattering of photons instead of neutrons. Upon irradiation (usually by a laser), the system will transition from its ground state to an excited state signaled by a change in magnetic quantum number.[74,75] The final photon, spawned from the interaction of the incident photon with the magnon of the material, will be lower in energy, resulting in a measurable Raman shift that appears on spectra as an intensity peak. The nature of this peak (or peaks, as there may be several magnons) reveals information about the material's magnetic interactions.[76,77]

Such experiments rely on effective spin Hamiltonians to interpret their measurements. Spin Hamiltonians act exclusively on spin variables, and they give rise to eigenvalues that match the spectra of magnetic systems through proper parametrization.[78,79] Similarly, one may map electronic states (solutions to the electronic many-body eigenvalue equation) onto these effective spin Hamiltonians to obtain descriptive parameters of magnetic properties.

The simplest of these effective spin Hamiltonians is that of Heisenberg, Dirac, and van Vleck (HDvV), which assumes that the magnetic moments of electrons are localized, thus defining a Hamiltonian of the form

$$\hat{H} = -\sum_{ij} J_{ij} \hat{\mathbf{S}}_i \cdot \hat{\mathbf{S}}_j, \tag{6.1}$$

where i and j represent all magnetic centers of the system under consideration, and $\hat{\mathbf{S}}_i$ and $\hat{\mathbf{S}}_i$ are, respectively, vector spin operators for magnetic centers i and j. The dot product between them is short-hand for a quantum mechanical operator expression[80,81]

$$\hat{\mathbf{S}}_i \cdot \hat{\mathbf{S}}_j = \hat{S}_{i,x}\hat{S}_{j,x} + \hat{S}_{i,y}\hat{S}_{j,y} + \hat{S}_{i,z}\hat{S}_{j,z} \,, \tag{6.2}$$

where $\hat{S}$ are the spin operators (subscripts indicate Cartesian directions and magnetic center indices), and they are combined as Kronecker tensor products. For $S = 1/2$ systems, the spin operators are simply Pauli matrices; for $S = 1$ systems like Ni^{2+}, however, the spin operators are

$$\hat{S}_x = \frac{\hbar}{\sqrt{2}}\begin{bmatrix} 0 & 1 & 0 \\ 1 & 0 & 1 \\ 0 & 1 & 0 \end{bmatrix} \qquad \hat{S}_y = \frac{i\hbar}{\sqrt{2}}\begin{bmatrix} 0 & -1 & 0 \\ 1 & 0 & -1 \\ 0 & 1 & 0 \end{bmatrix} \qquad \hat{S}_z = \hbar\begin{bmatrix} 1 & 0 & 0 \\ 0 & 0 & 0 \\ 0 & 0 & -1 \end{bmatrix} . \tag{6.3}$$

The quantum operator expression $\hat{\mathbf{S}}_i \cdot \hat{\mathbf{S}}_j$ is evaluated inside a given combined (nine-dimensional) Hilbert space through algebraic manipulation of the above spin operators. Ultimately, this yields a 9×9 matrix that, when placed back into Eq. (6.1) and the whole expression diagonalized, yields eigenvalues corresponding to magnetic excitation energies.[47] It's this energy spectrum that can be compared with energy spectral data from experimental techniques like INS, Raman scattering, electron paramagnetic resonance (EPR), or magnon frequencies.

In mapping onto KS DFT energies, however, one can instead take the semi-classical or mean-field approach, evaluating the expectation value of Eq. (6.1) for particular long-range magnetic configurations of spins. The expectation value is inherited by the spin operators. Here, a simplification emerges for collinear spin states: $\left\langle \hat{\mathbf{S}}_i \cdot \hat{\mathbf{S}}_j \right\rangle = \left\langle \hat{S}_i \right\rangle \cdot \left\langle \hat{S}_j \right\rangle$. That is, we may conduct the mapping with classical vectors, obtaining the semi-classical HDvV Hamiltonian

$$\hat{H} = -\sum_{ij} J_{ij}\mathbf{S}_i \cdot \mathbf{S}_j \,. \tag{6.4}$$

We will discuss these spin vectors further in Section 6.2.3. In the literature there is no unique formulation of Eq. (6.4), and variation exists based on the definition of the exchange-coupling parameters J_{ij} and the constants (i.e., -1, 2, 1/2) that they absorb. Table 6.1 outlines these variations in convention and how they relate to that used here.

Convention	$J_{ij}^{\dagger}$
$\hat{H} = -\sum_{ij} J_{ij}^{\dagger}\,\mathbf{S}_i \cdot \mathbf{S}_j$	J_{ij}
$\hat{H} = \gamma \sum_{ij} J_{ij}^{\dagger}\,\mathbf{S}_i \cdot \mathbf{S}_j$	$\frac{-1}{\gamma} J_{ij}$
$\hat{H} = \gamma \sum_{\langle ij \rangle} J_{ij}^{\dagger}\,\mathbf{S}_i \cdot \mathbf{S}_j$	$\frac{-2}{\gamma} J_{ij}$
$\hat{H} = \gamma \sum_{i>j} J_{ij}^{\dagger}\,\mathbf{S}_i \cdot \mathbf{S}_j$	$\frac{-2}{\gamma} J_{ij}$

Table 6.1: Exchange-coupling parameters $J_{ij}^{\dagger}$ across various conventions of the HDvV effective spin Hamiltonian in terms of the kinetic exchange-coupling parameters J_{ij} used here, where $J_{ij}^{\dagger}$ are the parameters and γ the real constant pertaining to that particular convention. The HDvV convention used here (orange) assumes that there is no interaction between one magnetic site and itself. Sometimes this assumption is made explicit by replacing the sum over ij with that over $i \neq j$. The use of angle brackets denotes a set of all pairs $\{i, j\}$ excluding $\{j, i\}$. A similar table may be found in He et al.[82]

Additional terms are often tacked onto Eqs. (6.1) and (6.4) to include anisotropic or antisymmetric interactions arising from spin-orbit coupling.[33,83] Among these contributions are, for example, the Dzyaloshinskii-Moriya interaction[84,85] (also known as the asymmetric exchange interaction) or the single-ion anisotropy.[78] Generally, but not always, the anisotropic or antisymmetric types of energy contributions are overpowered by those of the HDvV Hamiltonian,[33,78,86,87] sometimes called the symmetric or isotropic exchange interaction. In structuring our investigation for ease of comparison with similar magnetic mappings of spin-polarized KS DFT in past works, we opt to use the minimalistic HDvV Hamiltonian in Eq. (6.4). In doing so, we do not necessarily aim to replicate experimentally obtained Heisenberg exchange-coupling parameters J_{ij}, noting that many experiments incorporate anisotropic effects in their mapping Hamiltonians.[86,88,89]

We dissect Eq. (6.4) in the following sections to further deduce how it may best operate in a DFT context. But first, we clarify the meaning of the exchange-coupling parameters J_{ij} from basic quantum mechanical principles.

6.2.1 Kinetic exchange

There exists a mathematical relation between the indistinguishability of particles and their antisymmetry. Fermions are antisymmetric, because when one switches the positions (in time and in space) of two indistinguishable electrons, the resulting wavefunctions are negative images of the initial wavefunctions. Bosons, by contrast, are symmetric, because the initial and final wavefunctions of switched particles are identical.

As demonstrated in Section 1.1.2, the aptly-named *exchange* terms arise when deriving the behavior of indistinguishable particles—whose positions we exchange mathematically—in the formal language of quantum mechanics. The signature move of these exchange terms is that they enforce a difference between the expectation values for symmetric and antisymmetric wavefunctions. Consider, for example, the expectation value of the square of the distance between two indistinguishable particles; the more their paths overlap, the more they attempt to avoid each other, and thus the higher this expectation value's exchange terms become.

In satisfying the PEP, electrons with the same spin tend to avoid each other more, i.e., the ex-

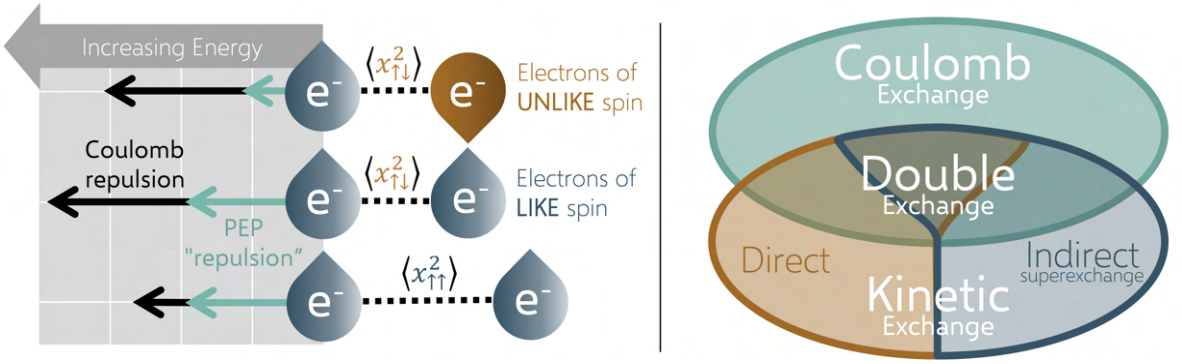

Figure 6.2: [Left] Illustration of energy character arising from Coulomb exchange between electrons of like-spin (blue) and electrons of unlike-spin (orange). Reprint of Fig. 1.1. [Right] Venn diagram illustrating the types of exchange.

pectation value of the square of the distance between aligned electrons is higher than that between anti-aligned electrons. It follows, then, that the electrostatic repulsion, which is inversely related to the distance between electrons, is smaller for electrons with parallel spin and thus more energetically favorable. This spin-based coupling of electrons, illustrated in Fig. 6.2, is called **Coulomb exchange**. Coulomb exchange is the basis of Hund's first rule, which favors FM alignment of spins.

A second, more long-range type of exchange, dubbed **kinetic exchange**, describes the coupling arising from a (virtual) electron transfer (a hop) from one atomic site to a neighboring atomic site. By the constraints imposed and enforced by the Pauli exclusion principle (PEP), the electrons may hop from one site to another only if the destination site is void of an electron with the same spin; thus, kinetic exchange also gives rise to spin-based coupling, one that often favors AF alignment. The *exchange energy* is the difference in energy between states with parallel spins and states with antiparallel spins.

There are two types of kinetic exchange prominent in materials: direct and indirect. The former classifies the exchange terms arising from overlapping electronic orbitals on neighboring atoms. It is expected that the t_{2g} states of the $3d$ orbitals on nearest-neighbor Ni atoms in NiO give rise to a robustly AF direct exchange. This antiferromagnetic disposition is mitigated, however, by a primarily FM 90° oriented indirect exchange, also known as superexchange. This round-the-corner superexchange mechanism is strongly mediated by the intra-atomic Coulomb exchange between orthogonal $2p$ orbitals on the pivotal oxygen atom. Within this framework, the 90° oriented indirect exchange is mutually classified as double exchange—exchange with both kinetic and Coulombic influences.

By orbital orientation, superexchange between magnetic sites in NiO exclusively comprises interactions between Ni^{2+} e_g states, which are half-filled, and O^{2-} $2p$ states. It starts when one e_g orbital accepts a transfer from the $2p$ ligand orbital it overlaps. Because the e_g orbital is already half-filled, the incoming electron must adopt the opposite spin, leaving a vacancy in the oxygen valence orbital with spin parallel to that of the Ni atom to which it just transferred its electron. The second Ni atom (a nearest neighbor [NN] of the first in the case of 90° oriented superexchange or a next-nearest neighbor [NNN] in the case of 180° oriented superexchange) also transfers an e_g electron to the corner O, but of which spin? For 90° oriented superexchange, we require a spin parallel to that of the initial Ni atom, because the $2p$ orbital the second Ni overlaps is orthogonal to that overlapping the first Ni's orbital, activating the ligand's much more dominant preference for FM intra-atomic exchange (see light green dynamics in Fig. 6.3 for illustration). By contrast, with 180° oriented superexchange, no such activation is possible—the transferred $2p$ electrons must come from the same orbital: one spin-up, the other spin-down (see teal dynamics in Fig. 6.3). Adjacent Ni atoms must thereby adopt opposing magnetic moments to host these electrons without violating the PEP.

6.2.2 Exchange-coupling parameters

The Heisenberg model quantifies the phenomenon of interatomic exchange, described earlier as an effective long-range manifestation of the PEP, which forbids doubly occupied quantum states. Exchange in the intra-atomic short-range, by contrast, leads to Hund's rules and is several orders of magnitude stronger than its interatomic counterpart.[90] The exchange-coupling parameters $\boldsymbol{J}_{ij}$ between magnetic

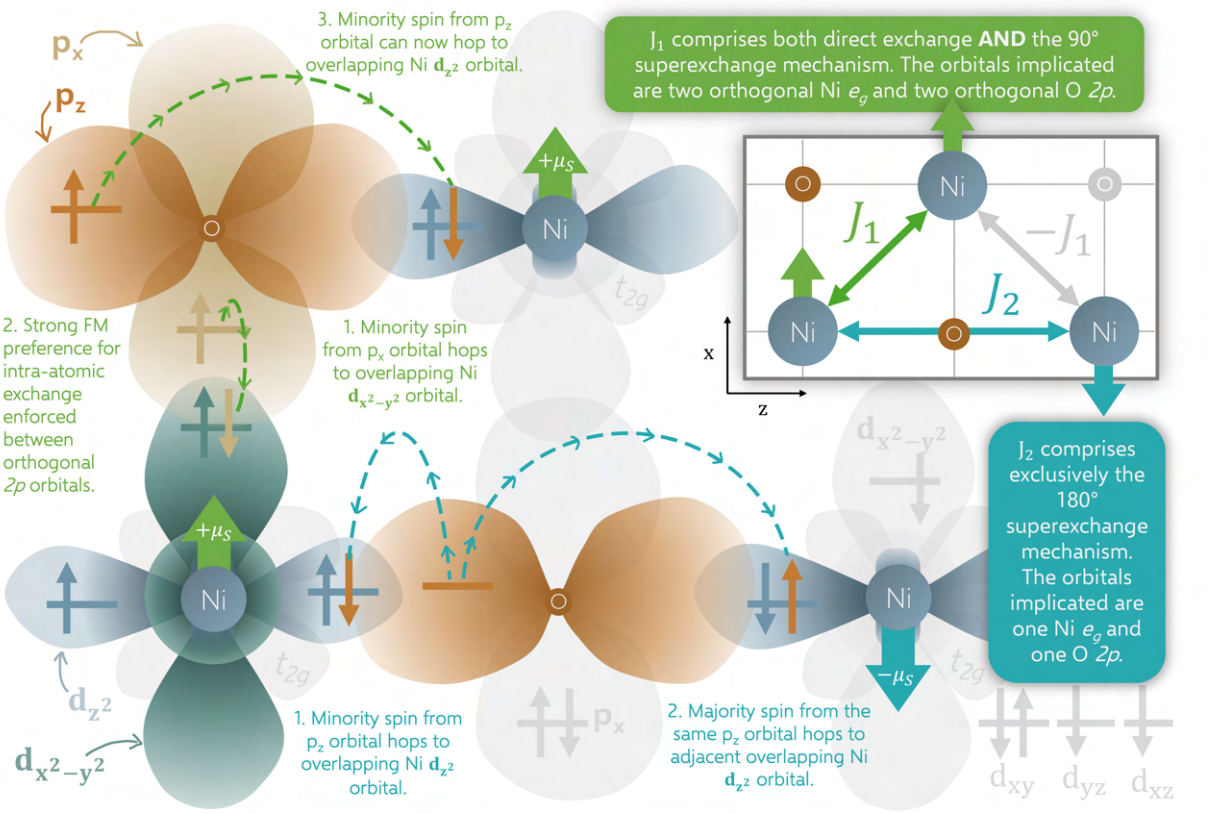

Figure 6.3: Schematic of xz-plane (y = 0) of AF_{II} NiO *in the rocksalt structure, demonstrating how the crystal-field splitting influences the preferred orientation of the Heisenberg interatomic exchange-interaction parameters* J_1 *(green) and* J_2 *(teal) corresponding, respectively, to the interactions between nearest neighbor transition metal sites and next-nearest neighbor TM sites. More information is provided in Section 6.2.*

atom centers can be considered spin-based measures of repulsion between electrons on neighboring atoms. When $J_{ij} > 0$, a ferromagnetic interaction is preferred, meaning the atoms will adopt the same spin orientation, while $J_{ij} < 0$ indicates the atomic spins would rather oppose each other in an antiferromagnetic ordering. For simplicity, we take into consideration only the two most dominant exchange terms—those describing interactions between nearest and next-nearest neighbors—of an expansion that, in theory, includes energetic contributions from all neighbor-to-neighbor interactions, even those infinitely separated from one another. Such a strategy is common for this type of study,[91–93] as energetic contributions from magnetic interactions beyond those of NNN magnetic centers are perhaps outside of DFT's realm of accuracy.

The first interaction is exchange between NN Ni atoms (J_1), wherein the overlap of the t_{2g} states of the 3*d* orbitals on NN Ni atoms gives rise to a strongly AF direct exchange. This antiferromagnetic disposition is mitigated, however, by a primarily FM 90°-oriented superexchange. As illustrated in the schematic in Fig. 6.3, we expect this superexchange to favor ferromagnetic alignment and to overpower the AF direct exchange, meaning that J_1 will adopt a positive value overall. The schematic also illustrates why we expect J_2, a quantifier of NNN exchange interactions separated by 180°, to adopt a profoundly negative value, indicating strong preference for AF alignment.

With these phenomena in mind, we map the electronic Hamiltonian onto the HDvV effective spin

Hamiltonian and look at J_1 and J_2 of NiO. We opt to compute the exchange-coupling parameters using total energy differences per Ni-O pair resulting from relaxing different magnetic configurations of the same NiO solid in the rocksalt structure. Taking the form of Eq. (6.4), J_1 and J_2 may be computed as

$$J_1 = \frac{1}{16}(E_{\mathrm{AF_I}} - E_{\mathrm{FM}})\,, \quad \text{and} \tag{6.5}$$

$$J_2 = \frac{1}{48}(4E_{\mathrm{AF_{II}}} - E_{\mathrm{FM}} - 3E_{\mathrm{AF_I}})\,, \tag{6.6}$$

where the E_{MO} are the total energies per Ni-O pair achieved by relaxing NiO in each of its three main stable or meta-stable magnetic configurations. These orderings are depicted in Fig. 6.1. A similar figure can be found in Ref. [94].

An INS experiment conducted on NiO by Hutchings *et al.*[86]—which, it is necessary to point out, incorporated out-of-plane and in-plane anisotropic contributions in their effective spin Hamiltonian mapping,[89] finding small but nonetheless reportable values for both—found $J_1 = 0.69$ eV and $J_2 = -9.50$ eV. Magnon frequency experiments conducted on NiO by Lockwood *et al.*[88], which also incorporated some anisotropic effects in the mapping, found $J_1 = 0.69$ eV and $J_2 = -9.61$ eV. Raman scattering experiments by Dietz *et al.*[95] found $J_2 = -9.18$ eV, although it is unclear whether anisotropic effects were taken into account. Shanker *et al.*[87] consider anisotropic effects to be negligible in conducting their own fitting.

6.2.3 Spin parametrization and magnetic moment

From Section 1.1.1: An electron with quantum numbers (n,ℓ,m_ℓ,m_s) will have spin magnetic moment $\boldsymbol{\mu}_s = -g_e\mu_B\boldsymbol{s}$, where $g_e \approx 2.002319$ is the g-factor for a free electron and $\mu_B = \frac{e\hbar}{2m} = \frac{1}{2}$ [a.u.] is the Bohr magneton.[96,97] The total spin magnetic moment is the sum of spin magnetic moments of all electrons on that atom. That is, $\boldsymbol{\mu}_{\mathbf{S}} = -g_e\mu_B\mathbf{S}$ (where $\mathbf{S}$ is the summation over electrons).[79,97] Referencing atomic magnetic moments in units of μ_B, then, $\mathbf{S}\ [\mu_B] = -\boldsymbol{\mu}_{\mathbf{S}}/g_e$. In atomic units, by contrast, $\mathbf{S}$ [a.u.] $= -2\boldsymbol{\mu}_{\mathbf{S}}/g_e$.

In a conventional spin-unrestricted KS DFT context, the $\mathbf{S}_i$ of Eq. (6.4) are considered (a) projections $(\mathrm{S}_z)_i$ of the quantum spin vector $\mathbf{S}_i$ on the quantization axis, and (b) of unit magnitude in accordance with nickel's expected oxidation state of +2, corresponding to an atomic magnetic moment of +2 μ_B (= 1 in atomic units, hence $\boldsymbol{\mu}_S^2 \approx 1$). In effect, these two conditions cause the mapping to bear closer resemblance to the Ising effective spin Hamiltonian rather than that of HDvV. We seek to reevaluate these conventions given the multitude of DFT-accessible population analyses that can influence, to a large degree, the predicted magnetic moment on Ni atoms.

For example, recall from Section 4.3.2 that the PAW population analysis extends naturally to a definition of the magnetic moment that is both atom-centered and restricted to the augmentation sphere (AS). That is, for magnetic centers, we take

$$(\mathrm{S}_z^{\mathrm{AS}})_i = \int_{|\mathbf{r}|=0}^{r_c} (\rho^{\uparrow}(\mathbf{R}_i + \mathbf{r}) - \rho^{\downarrow}(\mathbf{R}_i + \mathbf{r}))\, d\mathbf{r}. \tag{6.7}$$

However, because the PAW augmentation spheres do not envelop all the charge in the system,

leaving some interstitial charge uncounted, this option is expected to produce moments smaller than expected. We may address this by normalizing the subspace occupancies via the projector, as in Section 4.3.2, and calculating

$$(\mathrm{S}_z^{\mathrm{PAW}})_i = \sum_m n_{m,m}^{i,\uparrow} - n_{m,m}^{i,\downarrow}, \tag{6.8}$$

which, by consequence, encodes the choice of PAW projector. Alternatively, we may obtain magnetic moments via the extraction of S_z from the entire spin density (SD), by using

$$(\mathrm{S}_z^{\mathrm{SD}})_i = \frac{1}{N_{\mathrm{Ni}}} \int |\rho^{\uparrow}(\mathbf{r}) - \rho^{\downarrow}(\mathbf{r})| \; d\mathbf{r}, \tag{6.9}$$

where N_{Ni} is the number of Ni atoms in the system. While it produces larger magnetic moments, this method is accompanied by the particular limitation that atom-specific magnetic moments are no longer resolved, and any moments formed near the oxygen atoms are absorbed into those of the magnetic centers.

It is conventional in the relevant literature to consider oxygen atoms as mere extensions or mediators of the magnetic character of the TM magnetic centers, thereby restricting assessment of exchange interactions to those between Ni atoms. After all, the magnetic moment on oxygen, if it exists at all (our calculations found no discernible oxygen moment in $\mathrm{AF_{II}}$ NiO), is at least an order of magnitude overpowered by the moment on Ni. In principle, however, there exist TM-O exchange interactions in FM and $\mathrm{AF_I}$ NiO, which effectively renormalize the TM-TM exchange-interaction parameters.

A similar study conducted in Ref. [92] investigated the incorporation of the oxygen magnetic moment and found that the resulting effective NN exchange interaction decreases noticeably when the moment on oxygen is considered distinct from that of the magnetic centers in FM NiO. The methodology used to obtain these exchange parameters—the magnetic force theorem, an alternative HDvV mapping problem involving Green's functions—is in theory translatable to our own preferred total energy method but lies beyond the scope of our already quite multi-dimensional investigation. In using Eq. (6.9), we follow this study's (and generally conventional) treatment of the oxygen magnetic moment as indistinct from that of the TM center.

It should be noted, however, that the HDvV Hamiltonian in Eq. (6.4) calls for the use of the quantum spin vectors $\mathbf{S}_i$, as opposed to their scalar and DFT-accessible counterparts, the expectation values of the z-axis projection of the spin angular momentum S_z. Suppose we instead consider an approximate quantum model in which $|\mathbf{S}| = \sqrt{\langle \mathbf{S}^2 \rangle}$. Coupling the spins on each magnetic site such that $s = 1$ for the two unpaired spins on Ni together, the expectation value of the spin angular momentum of an atomic system is

$$\begin{aligned} |\mathbf{S}| = \sqrt{\langle \mathbf{S}^2 \rangle} &= \hbar \sqrt{s(s+1)} \mathrm{S}_z \\ &= \sqrt{2}\, \mathrm{S}_z \text{ [a.u.]}. \end{aligned} \tag{6.10}$$

That is, in a sort of crude quantum approximation, we scale the DFT-accessible magnetic moments, which may be thought of as time-averages of precessing, canted spins, by a factor of $\sqrt{2}$. To our

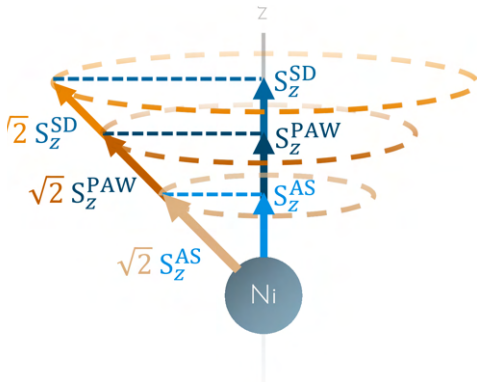

Figure 6.4: Schematic of Ni *spin-vector quantification schemes investigated in this work.*

knowledge, this approximation has been made to magnetic properties in other contexts—such as in the works of Harrison,[98] Kotani *et al.*,[99] and Wan *et al.*[100]—but not tested systematically against other DFT-accessible spin objects for NiO.

All six spin vector treatment schemes are depicted in Fig. 6.4. Once we settle on an appropriate treatment of the spin vector, we can examine how it factors into the numerical calculation of the exchange-coupling parameters. Eqs. (6.5) and (6.6) can be considered simplifications of a more generalized set of total energy difference equations under the HDvV Hamiltonian, derived by considering all NN and NNN of one Ni atom (or Ni-O pair) in the cell. They are solutions to a system of linear equations mapping the total energy of each MO onto the HDvV Hamiltonian (bearing notable resemblance to the Ising model), solutions that simplify when we impose assumptions that the spin magnetic moments of all atoms are a) integers and b) the same regardless of the cell's magnetic environment. That is, the magnitudes of the atomic magnetic moments are $|S_{FM}| = |S_{AF_I}| = |S_{AF_{II}}| = 1$ in

$$\begin{aligned} E_{FM} &= E_0 - 12J_1S_{FM}^2 - 6J_2S_{FM}^2 \\ E_{AF_I} &= E_0 + 4J_1S_{AF_I}^2 - 6J_2S_{AF_I}^2 \\ E_{AF_{II}} &= E_0 + 6J_2S_{AF_{II}}^2\,. \end{aligned} \tag{6.11}$$

Suppose we assume instead that $|S_{FM}| \neq |S_{AF_I}| \neq |S_{AF_{II}}| \neq 1$. Since DFT uses the non-integer spin degree of freedom to deepen the total energy well of each MO, and since that relaxed magnetization is accessible, we can perhaps explicitly use the final magnetization to better weight the energetic contributions of each MO to the exchange coefficients. Then the system of linear equations in Eqs. (6.11), solved for J_1 and J_2, becomes

$$J_1 = \frac{E_{AF_{II}}(S_{AF_I}^2 - S_{FM}^2) + E_{AF_I}(S_{AF_{II}}^2 + S_{FM}^2) - E_{FM}(S_{AF_I}^2 + S_{AF_{II}}^2)}{4\left[3S_{AF_{II}}^2S_{FM}^2 + S_{AF_I}^2\left(S_{AF_{II}}^2 + 4S_{FM}^2\right)\right]}, \quad \text{and} \tag{6.12}$$

$$J_2 = \frac{E_{AF_{II}}(S_{AF_I}^2 + 3S_{FM}^2) - 3E_{AF_I}S_{FM}^2 - E_{FM}S_{AF_I}^2}{6\left[3S_{AF_{II}}^2S_{FM}^2 + S_{AF_I}^2\left(S_{AF_{II}}^2 + 4S_{FM}^2\right)\right]}. \tag{6.13}$$

Note that if we set $|S_{FM}| = |S_{AF_I}| = |S_{AF_{II}}| = 1$ then Eqs. (6.12) and (6.13) reduce to Eqs. (6.5) and (6.6).

Exchange-coupling parameters that incorporate differences in magnetization across MOs are not immediately comparable to those reported in previous works. We find this is not so much an artefact of the assumption that $|S_{FM}| = |S_{AF_I}| = |S_{AF_{II}}| = \sigma$ (where σ is a constant) so much as it reflects the assumption that $\sigma = 1$. As a comparative intermediary, therefore, we look at the exchange-interaction parameters when the sum of electrons in a Ni atom corresponds directly to the magnitude of the Ni magnetic moment in the ground-state magnetic configuration of NiO (i.e., when $\sigma^2 = S^2_{AF_{II}}$ [a.u.]). Under this approach, Eqs. (6.12) and (6.13) reduce to

$$J_1 = \frac{1}{16\, S^2_{AF_{II}}} \left(E_{AF_I} - E_{FM}\right), \quad \text{and} \tag{6.14}$$

$$J_2 = \frac{1}{48\, S^2_{AF_{II}}} \left(4E_{AF_{II}} - 3E_{AF_I} - E_{FM}\right). \tag{6.15}$$

For the purposes of clarity, we will refer to the first method of calculating exchange-interaction parameters, those embodied by Eqs. (6.5) and (6.6), as Method A. Similarly, Eqs. (6.14) and (6.15) are henceforth referenced as Method B, and Eqs. (6.12) and (6.13) are Method C. [§]

[§]Eqs. (6.12 - 6.15) are true only in atomic units, where $\mu_B = 1/2$ and the numerical value of these units is absorbed into the other constants of the equations. Thus, total energies expressed in eV must each be multiplied by a factor of four for Eqs. (6.12 - 6.15) to hold true.

Chapter 7

Error-corrected exchange-coupling parameters in NiO

Given the context recounted in Chapter 6, we undertook a multi-pronged investigation designed to systematically unscramble the complexities of the HDvV Hamiltonian, first-principles Hubbard corrective functionals, intra-atomic spin-parametrization schema, and the PAW method for the prototypical antiferromagnetic TMO, nickel oxide. We draw heavily on lessons learned on linear response in Chapters 4 and 5 while focusing specifically on the intricacies of the PAW formalism as laid out in Section 3.1.4 and projectors for population analysis in Section 4.3.2.

Due to the diversity of population analysis methodologies in the PAW formalism, described in Section 4.3.2, we examine in Section 7.2.1 the sensitivity of the *in situ* calculated Hubbard parameters U and J with respect tio the projector used to distinguish the Hubbard manifold. To distinguish the Hund's J from the exchange-coupling $\boldsymbol{J}_i$, we denote the former as $\mathrm{J_H}$ for the remainder of this chapter.

With Hubbard parameters defined, we map select points in the energy-magnetization landscape of bulk NiO onto the HDvV Hamiltonian by calculating its electronic structure in its $\mathrm{AF_I}$, $\mathrm{AF_{II}}$, and FM orderings (see Fig. 6.1). We then proceed to extract Heisenberg (interatomic) exchange-coupling parameters in terms of strict density-functional-accessible total energy differences between these magnetic configurations.

In Sections 7.2.2 and 7.2.3, we explore the possibility of incorporating not only total energies but also local moments in the mapping onto the HDvV Hamiltonian, and we assess several ways to perform this. In doing so, we effectively reevaluate Heisenberg exchange-coupling calculation conventions and scrutinize a variety of moment estimation techniques, both classical and semi-classical, as outlined in Section 6.2.3. Adopting this framework enables a direct and rigorous assessment of the efficacy of 6+ corrective Hubbard functionals via the quality of the Heisenberg exchange-coupling parameters as compared to both experiment (i.e., magnon frequencies or inelastic neutron scattering) and ostensibly more comprehensive theory (e.g., hybrid functionals). We relay this comparative analysis in Sections 7.2.4-7.2.6, finishing with a closer look at the effect of Hubbard corrective treatment on the O-2p sites in Section 7.2.7.

7.1 Computational details

We use different runtime parameters for computing the Hubbard parameters and applying them due to the different simulation cell and attendant Brillouin zone sizes needed for each task. This information, for all parameters that varied across tasks and MO (FM, AF_I, and AF_{II}), are laid out in Table 7.1.

Otherwise, consistent across all calculations, we use the Perdew-Burke-Ernzerhof (PBE) GGA [101] XC functional and the Jollet-Torrent-Holzwarth PBE PAW pseudopotentials (Version 1.1) [102,103] generated via *atompaw*. [104] Derived from those pseudopotentials, the PAW augmentation sphere cutoff radius r_c used in, for example, the projector of Eq. (5.24) or the magnetic moment of Eq. (6.7), is 1.81 a_0 for Ni and 1.41 a_0 for O. We use the experimental lattice parameters (LPs) pertaining to each MO of NiO specified in Table 7.1, and for those that have metallic character, we use the Marzari-Vanderbilt smearing scheme [105] with 0.005 Ha broadening. Furthermore, we enforce a cutoff energy of 33.1 Ha (44.1 Ha on the PAW atom augmentation sphere). In terms of the magnetic moment, we extract S_z in accordance with Eq. (6.9) using C2x. [106] Representative input files are included in Appendix B1.

Which Hubbard functional, and which subspaces require numerical attention in excess of the underlying XC functional, are both topical inquiries that this investigation does not directly address for NiO. For brevity, we test six widely recognizable Hubbard functionals: DFT+U^d, DFT+$U^{d,p}$, DFT+U^d_{eff}, DFT+$U^{d,p}_{\text{eff}}$, DFT+ U^d+J^d_H, DFT+$U^{d,p}$+$J^{d,p}_H$. More precisely, we use three forms of Hubbard functional—the Dudarev *et al*. DFT+U and DFT+U_{eff} = U - J_H of Ref. [107], and the Liechtenstein *et al*. DFT+U+J functional of Ref. [108]—where the Hubbard corrections are applied to different combinations of valence subspaces, denoted by the italicized superscripts (i.e., *d* refers to the Ni 3*d* subspace and *p* refers to the O 2*p* subspace).

	DFT LR Calculations			DFT+ U (± J_H) Exchange Calculations		
	FM	AF_I	AF_{II}	FM	AF_I	AF_{II}
# Atoms		64			4	
Experimental LP (Å)	4.171[a]	4.168[b]	4.170[b]	4.171[a]	4.168[b]	4.17[b]
Lattice Vectors		[2, 0, 0] [0, 2, 0] [0, 0, 2]		[½, ½, 0] [0 , 0 , 1] [½, −½, 0]	[½, ½, 0] [0 , 0 , 1] [½, −½, 0]	[½, ½, 1] [1, ½, ½] [½, 1, ½]
Energy Tolerance (Ha)		1×10^{-7}			1×10^{-12}	
***k*-Point Sampling**	3 × 3 × 3	3 × 3 × 3	5 × 5 × 5	40 × 20 × 40	40 × 20 × 40	30 × 30 × 30
Insulating Character	metal	metal	insulator	insulator	insulator	insulator
U^d | J^d_H (eV)	0.0 | 0.0	0.0 | 0.0	0.0 | 0.0	6.91 | 0.18	6.74 | 0.55	5.58 | 0.47
U^p | J^p_H (eV)	0.0 | 0.0	0.0 | 0.0	0.0 | 0.0	11.64 | 1.55	11.30 | 1.87	11.37 | 1.82

[a] Refs. [10–18] [b] Ref. [22]

Table 7.1: Calculation parameters specific to each MO of NiO *for both the calculation and application of the Hubbard parameters, respectively. We include here number of atoms, experimental lattice parameter (*LP*), lattice vectors, converged energy tolerance, k-point sampling, insulating character, and Hubbard parameters* U *and* J_H *calculated for the* Ni 3*d* *and* 2*p* *subspaces respectively, calculated with the population analysis schema of Eq. (4.42) (see Section 4.3.2 for a discussion of population analysis schemes).*

Furthermore, we seek to understand if total energy differences between MOs are most comparable when calculated using Hubbard parameters that are (i) specific to each MO, or (ii) the same across MOs. To test (i), we apply each of the aforementioned Hubbard functionals with MO-specific Hubbard parameters (HPs) to its respective magnetically ordered version of NiO (that is, FM HPs applied to FM NiO via each functional, AF_I HPs to AF_I NiO, and so on). To test (ii), we apply the U and J_H from the ground-state AF_{II} MO to every MO of NiO via each of the aforementioned Hubbard functionals (that is, AF_{II} HPs applied to FM NiO via each functional, AF_{II} HPs to AF_I NiO, and so on).

7.1.1 Linear response calculations

We conduct ABINIT linear response calculations via what is now its intrinsic `lrUJ` algorithm[109,110] (described further in Chapter 5) to determine the Hubbard parameters U and J_H for both the *3d* Ni and *2p* O orbitals (SCF procedure described in Section 4.1). For each U (J_H) parameter, at least five perturbations, one of which is the unperturbed state, between $\alpha = \pm 0.2$ eV ($\beta = \pm 0.1$ eV) are applied to one of the 64 atoms in the supercells of each MO of NiO. Depending on how well these calculations converged, additional perturbations were undertaken.

As described at the end of Section 4.3.2, QUANTUM ESPRESSO augments the pseudized wavefunctions with core contributions without truncating at the PAW cutoff radius. Therefore, we further undertook QUANTUM ESPRESSO linear response calculations for the Hubbard U on Ni and O across all MOs to use as reference values.

For each U parameter calculated with QUANTUM ESPRESSO, five equally spaced perturbations (including the unperturbed state) between $\alpha = \pm 0.2$ eV were applied to one of the 64 atoms in the supercells of each MO of NiO. Runtime parameters remain the same as those for ABINIT except the following: The energy is relaxed self-consistently to within a threshold tolerance of 10^{-9} Ha, and a kinetic energy of 25 Ha for wavefunctions is administered alongside an energy cutoff of 250 Ha for the density. For all MOs, we use Monkhorst-Pack[111] grid k-point sampling of $2 \times 2 \times 2$. See Fig. 4.1 for examples.

7.2 Results and discussion

7.2.1 PAW projectors and the Hubbard parameters

Switching between PAW population analysis schemes induces noticeable numerical differences in the resulting Hubbard parameters for both Ni $3d$ orbitals and O $2p$ orbitals (see Table 7.2). It is encouraging that the unscreened response functions χ_0 and χ_{0_M}, pertaining to each projector choice, are reasonably alike. This is expected in accordance with the Corollary in Section 4.1.2.

The Hubbard parameters U and J_H resulting from `dmatpuopt=2` and `dmatpuopt=3` are consistently similar, whereas `dmatpuopt=1` yields the largest of these parameters and `dmatpuopt=4` yields the smallest in magnitude. These phenomena are concordant with our understanding of the make-up of the response matrices. That is, extrapolations of occupancies beyond the PAW radius increase the overall occupancy (magnetization), thereby decreasing the inverse of the response matrices and reducing U (J_H).

			Ni Linear Response Parameters						O Linear Response Parameters					
			U			J_H			U			J_H		
MO	$n^{t,\sigma}_{m,m'}$		χ_0	χ	U^d	χ_{0_M}	χ_M	J^d_H	χ_0	χ	U^p	χ_{0_M}	χ_M	J^p_H
FM	ABINIT	1	-0.8064	-0.1024	**8.53**	-0.8054	-0.9829	**0.22**	-0.0856	-0.0264	**26.16**	-0.0856	-0.1216	**3.46**
		2	-0.9856	-0.1359	**6.34**	-0.9854	-1.1746	**0.16**	-0.1901	-0.0595	**11.55**	-0.1901	-0.2697	**1.55**
		3	-0.9858	-0.1262	**6.91**	-0.9826	-1.1892	**0.18**	-0.1914	-0.0593	**11.64**	-0.1914	-0.2719	**1.55**
		4	-1.2010	-0.1610	**5.38**	-1.2010	-1.3887	**0.11**	-0.4281	-0.1314	**5.28**	-0.4280	-0.6075	**0.69**
	QE		-0.5008	-0.1178	**6.49**				-0.1176	-0.0530	**10.36**			
AF_I	ABINIT	1	-0.9219	-0.1064	**8.31**	-0.9449	-2.5779	**0.67**	-0.0923	-0.0277	**25.27**	-0.0927	-0.1545	**4.31**
		2	-1.1289	-0.1347	**6.54**	-1.1577	-3.3259	**0.56**	-0.2054	-0.0601	**11.52**	-0.2060	-0.3363	**1.88**
		3	-1.1259	-0.1311	**6.74**	-1.1547	-3.2044	**0.55**	-0.2068	-0.0620	**11.30**	-0.2073	-0.3390	**1.87**
		4	-1.3750	-0.1583	**5.59**	-1.4107	-3.1137	**0.39**	-0.4634	-0.1417	**4.90**	-0.4643	-0.7652	**0.85**
	QE		-0.6299	-0.1244	**6.45**				-0.1144	-0.0516	**10.64**			
AF_{II}	ABINIT	1	-0.3104	-0.0998	**6.80**	-0.3104	-0.3870	**0.64**	-0.0803	-0.0264	**25.49**	-0.0799	-0.1181	**4.04**
		2	-0.3791	-0.1248	**5.37**	-0.3790	-0.4737	**0.53**	-0.1784	-0.0593	**11.27**	-0.1779	-0.2640	**1.83**
		3	-0.3793	-0.1218	**5.58**	-0.3795	-0.4621	**0.47**	-0.1798	-0.0590	**11.37**	-0.1793	-0.2661	**1.82**
		4	-0.4644	-0.1428	**4.85**	-0.4634	-0.5206	**0.24**	-0.4024	-0.1320	**5.09**	-0.4017	-0.5953	**0.81**
	QE		-0.2607	-0.0998	**6.18**				-0.1247	-0.0537	**10.59**			

Table 7.2: PAW-based occupancy determination methods (variations itemized by `dmatpuopt` *integer for brevity:* 1 *refers to Eq. (4.39),* 2 *refers to Eq. (4.40), and* 3 *and* 4 *refer to Eq. (4.42)) compared with that of* QUANTUM *ESPRESSO* (QE) *in terms of the effect induced on Hubbard parameters,* U *and* J_H*, as well as their bare (χ_0) and screened (χ) response function components. Numbers gathered via linear response procedures implemented on both* Ni *and* O *across all magnetic orderings* (MO) *of the 64-atom* NiO *supercell.*

For Ni, which has well-localized valence electrons, the range of Hubbard parameters is not very wide; by our calculations, 90.47% of the $3d$ atomic wavefunctions lie inside the PAW augmentation sphere. For O $2p$ orbitals, however, this overlap is significantly smaller, around 66.87%, and thus the range of achievable Hubbard parameters by various population analysis schemes is significantly larger for O than for Ni. It is important, therefore, in treating O $2p$-orbitals, to select an occupancy matrix calculation scheme that is normalized inside the PAW augmentation sphere.

In terms of numerical similarity with the QUANTUM ESPRESSO-derived U, only `dmatpuopt=2` and `dmatpuopt=3` remain viable candidates, with `dmatpuopt=2` slightly outperforming `dmatpuopt=3` based on numerical nuances. Not only does `dmatpuopt=4` systematically underestimate U, from a theoretical standpoint (described in Section 4.3.2), using the integral of ϕ_0 to renormalize the AE basis function is an approximation that is not entirely justified. While the first AE partial wave listed in a PAW dataset for a particular treated subspace, which ABINIT selects as ϕ_0, is required to be a normalized atomic eigenfunction, the second (or third or fourth, etc.) AE basis functions have no such constraints. There's no guarantee that these functions are localized in the PAW augmentation region to the same extent as ϕ_0. By contrast, based on the systematic overestimation of U via `dmatpuopt=1`, it is clear that at least some normalization is necessary, especially for the oxygen $2p$ states.

For these reasons, we focus our attention on the subtle differences between `dmatpuopt=2` and `3`. It is worth mentioning that, outside of convergence difficulties arising from the J_H calculations for the FM and AF_I MOs, `dmatpuopt=3` marginally outperforms `dmatpuopt=2` in terms of quality of linear response and ease of numerical convergence. The metrics used to evaluate this quality were (a) similarity of unscreened response functions χ_0 and χ_{0_M}; (b) average number of SCF cycles needed to converge perturbative calculations; (c) average regression order (i.e., how often did the response functions demonstrate linearity over higher order polynomial regressions), and; (d) the error on the Hubbard parameter, calculated as in Eq. (4.14).

For `dmatpuopt=3`, the average $\sigma_U(\sigma_{J_H})$ across all HPs is $\bar{\sigma}_U = 0.93\%$ ($\bar{\sigma}_{J_H} = 1.50\%$), which is slightly better than `dmatpuopt=2`'s $\bar{\sigma}_U = 1.01\%$ ($\bar{\sigma}_{J_H} = 2.73\%$). All in all, `dmatpuopt=3` outperforms its competitor in three of the four aforementioned metrics ((b), (c) and (d), to be precise).

There is a case to be made in opposition to `dmatpuopt=2` from a theoretical standpoint. Its projection operator, Eq. (5.24), is defined using a Heaviside step function, which operationally "counts," so to speak, the overlap between two PAW radial basis functions by brute-force. The ground-state eigenfunction basis for `dmatpuopt=3` is underpinned by the same assumptions and approximations

	(eV)	FM	AF_I	AF_{II}
Ni	U^d	6.91 ± 0.08	6.74 ± 0.03	5.58 ± 0.15
	J_H^d	0.18 ± 0.01	0.55 ± 0.01	0.471 ± 0.004
O	U^p	11.64 ± 0.02	11.30 ± 0.11	11.37 ± 0.03
	J_H^p	1.55 ± 0.01	1.87 ± 0.02	1.82 ± 0.02

Table 7.3: In situ Hubbard parameters calculated via linear response for FM, AF_I *and* AF_{II} NiO *and associated errors, calculated via Eq. (4.14), reported in* eV. *Projectors of choice used to calculate these parameters correspond to* `dmatpuopt=3`.

that are used in the definition of the bound PAW AE partial waves. The renormalization of projections of all partial waves with a bounded, truncated AE wavefunction reintroduces a crucial, physics-based safeguard into the definition of the occupancy matrix. For this reason, we select `dmatpuopt=3` as our preferred PAW population analysis. We report the Hubbard parameters pertaining to this population analysis scheme as well as their associated errors in Table 7.3.

7.2.2 Intra-atomic spin moment

Having solidified the *in situ* Hubbard parameters, we must give due consideration to the most appropriate Hubbard functional (among the six tested using the AF_{II} HPs), intra-atomic spin moment calculation (AS, PAW or SD, permutated across S_z and $|\mathbf{S}|$), and MO-based spin-parametrization method (Methods A, B, or C). Table 3 in Appendix B (also published in the Supplemental Material (SM) of Ref. [112]) provides all of this raw data. To make the process of elimination simpler, however, we'll focus on identifying the most effective combination of spin treatments by averaging across all six Hubbard functionals the percent RMS deviation (% RMSE) of our results for J_1 and J_2 from those of one particular experiment (exp), specifically

$$\%\ \mathrm{RMSE} = \sqrt{\frac{1}{2}\left(\left(\frac{J_1}{J_1^{\mathrm{exp}}}\right)^2 + \left(\frac{J_2}{J_2^{\mathrm{exp}}}\right)^2\right)}. \tag{7.1}$$

We semi-arbitrarily select the inelastic neutron scattering experiment of Hutchings *et al.*[86] as our benchmark for this analysis. After averaging Eq. (7.1) across the six Hubbard functionals, Table 3 in Appendix B3 reduces to Table 7.4, where the darker shades of gray-blue represent lower errors.

We notice immediately that the % RMS error is smaller when approximately treating intra-atomic spin as a quantum vector. Compared with its z-axis projection, $|\mathbf{S}|$ diminishes differences across population analysis schemes, such that $|\mathbf{S}^{\mathrm{AS}}|$ is only subtly favored over other candidates. The preferable MO-based spin-parametrization method depends crucially on the use of the quantum vector over the z-axis projection; under the latter treatment, Method A obtains exchange parameters more in line with experiment by a clear margin, indicating a preference for total energy differences with idealized spin-moment values. By contrast, if the magnetic moments are amplified by a factor of $\sqrt{2}$ as with

	S_z			$\lvert\mathbf{S}\rvert$		
%RMSE	A	B	C	A	B	C
AS	50.2	105.1	89.8	50.2	29.7	29.4
PAW	50.2	96.3	86.4	50.2	30.3	30.4
SD	50.2	76.9	100.0	50.2	33.1	36.3

Table 7.4: Percent RMS errors (%RMSE). AS *spin moments refer to those calculated in atom-centered augmentation spheres (Eq. (6.7));* PAW *refers to cumulative differences in PAW occupancy matrix elements (Eq. (6.8));* SD *refers to use of the global spin-density difference (Eq. (6.9)). Cell hue represents error magnitude; the darker the gray-blue, the smaller the error.*

the quantum vector approximation, Methods B and C, which weight the total energies from each MO according to various combinations of their atomic magnetic moments, win out.

To understand this behaviour, we recall that DFT-derived Ni magnetic moments on AF NiO do not typically exceed 2 μ_B (see Fig. 7.1(a)). So, the coefficients by which the AF total energies are weighted exceed unity, thereby amplifying the total energy differences to which the exchange-interaction parameters are proportional. Most underlying Hubbard functionals, in and of themselves, generate total energy differences that are too large anyway, so the modifications provided by these magnetic moments are almost always counterproductive in obtaining results that more closely resemble experiment. The only exceptions to this trend occurred when we applied Hubbard functionals using parameters exceeding those calculated via linear response by several eV. Overestimation of the exchange parameters continues as long as DFT underestimates the magnetic moment of Ni on NiO.

According to Fig. 7.1(a), experimentally consistent AF moments are out of reach for all population analysis techniques. The additional $\sqrt{2}$ factor accompanying $|\mathbf{S}|$ serves to approximately compensate where DFT falls short, lending itself to overcompensation when coupled with the population analysis techniques that typically predict higher Ni magnetic moments by default (like PAW and SD). For this reason, we see that a relatively underestimated population analysis, like that coming from AS, coupled

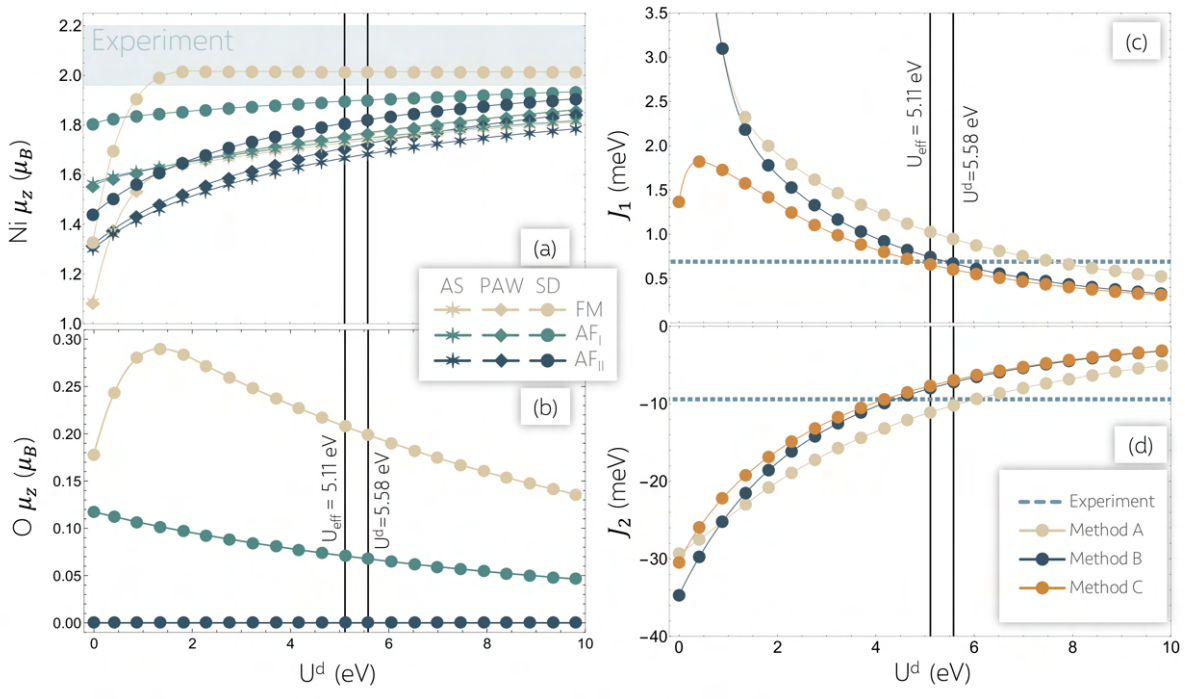

Figure 7.1: The effect of treating Ni *3d orbitals in the* DFT+U^d *functional with varying magnitude of the* AF$_{II}$ $U^d_{eff} = U^d - J^d_H$ *(same HPs across all MOs). Plot* (a) *and* (b) *show average nickel and oxygen site magnetic moments* μ_z*, projected on the z-axis and resolved via magnetic ordering (*FM *for ferromagnetic,* AF$_I$ *for antiferromagnetic I and* AF$_{II}$ *for antiferromagnetic II), for each population analysis described in Section 6.2.3;* AS = *augmented sphere (Eq. (6.7)),* PAW = *PAW occupancies (Eq. (6.8)), and* SD = *total spin density (Eq. (6.9)). Plots* (c) *and* (d) *show, respectively, nearest-neighbor and next-nearest neighbor Heisenberg exchange-interaction parameters, calculated via different spin-parametrization methods, where intra-atomic spin is calculated as* $|\mathbf{S}^{AS}| = \sqrt{2}\, S^{AS}_z$.

with the overestimation attributed to the $\sqrt{2}$ factor from $|\mathbf{S}|$ can balance out to yield minimized errors.

This explanation, of course, is not a glowing theoretical testimonial for either technique, especially since S_z^{AS} performs rather poorly compared to its PAW and SD counterparts. However, the results in and of themselves, independent of their justification, offer concrete, actionable insights to the reader in terms of which spin treatment is best for NiO exchange. Certainly, Table 7.4 offers more organized navigation of a few available DFT-tractable, spin-based objects and their influence on the Heisenberg exchange constants, and the numerical forgiveness awarded by these techniques should not be overlooked. For the purposes of further analysis, therefore, we take Table 7.4 at its face value and both select and recommend $|\mathbf{S}^{AS}| = \sqrt{2}\, S_z^{AS}$ as the preferred intra-atomic spin moment calculation method. Further data pertaining to the S_z calculations across all population analysis methods tested is provided in Appendix B3.

7.2.3 Comparison of spin-parametrization methods

In Table 7.5, we resolve our $|\mathbf{S}^{AS}|$ results to the level of the individual Hubbard functional and spin-parametrization method. Principally, we report obtained values for J_1 and J_2. Secondarily, for visual comparison, the final column shows the range of RMS errors obtained by comparing the best pair of coefficients from that functional to each of the four experiments listed at the bottom of the table. To clarify, for each functional, we take the best $\{J_1, J_2\}$ pair of the three spin-parametrization methods and calculate their percent RMS error with respect to each of the four experiments via Eq. (7.1). We then report the minimum (leftmost bar), range (stacked bar) and maximum (digit) of all those errors to compare across other functionals. The bar color corresponds to the spin-parametrization method used to obtain that best $\{J_1, J_2\}$ pair (tan for Method A, blue for Method B and orange for Method C).

We prepare an identical error analysis scheme in Table 7.6, where we compare the exchange-interaction parameters J_1 and J_2 reported in the literature to our own results, obtained from the various spin-parametrization methods proposed in Section 6.2. For values reported in the literature, we reverse engineered the exchange-interaction parameters for Methods B and C based on those reported for Method A (the conventional method) in addition to the reported values for the Ni magnetic moment for each configuration.

It should be clarified that we use RMS error in Tables 7.4, 7.5, and 7.6 as a measure of proximity to the reported values of the four different experiments cited. The RMS error is not asserting the proximity of our computed parameters to the true, physical values of these parameters. For example,

Table 7.5: Comparison of exchange-coupling parameters from various Hubbard functionals, where $U_{eff} = U - J_H$. *The "*AF_{II} NiO Parameters*" header refers to functionals tested using the Hubbard parameters arising from linear response on the ground-state* AF_{II} *magnetic ordering of* NiO *(i.e., column 4 in Table 7.3). "*MO-Specific Parameters*" refers to the use of the Hubbard parameters pertaining specifically to each magnetic ordering (i.e.,* FM *HPs applied to* FM *ordering via Hubbard functional,* AF_I *parameters applied to* AF_I *ordering, etc.). Histogram shows minimum (leftmost bar), range (stacked bar) and maximum (digit) of all %* RMS errors *with respect to* $\{J_1, J_2\}$ *pairs from each of the four experiments listed above. Color of bar corresponds to spin-parametrization method used to obtain that best* $\{J_1, J_2\}$ *pair (i.e., tan for* Method A*, blue for* Method B *and orange for* Method C*).*

	Method A		Method B		Method C	
	$S_{FM} = S_{AF_I} = S_{AF_{II}} = 1$		$S_{FM} = S_{AF_I} = S_{AF_{II}}$		$S_{FM} \neq S_{AF_I} \neq S_{AF_{II}}$	
Functional	J_1 (meV)	J_2 (meV)	J_1 (meV)	J_2 (meV)	J_1 (meV)	J_2 (meV)
DFT (PBE)	8.23	-29.32	9.73	-34.68	1.37	-30.48
AF_{II} NiO Parameters						
DFT + U^d	0.95	-10.20	0.67	-7.22	0.60	-6.95
DFT + $U^{d,p}$	1.53	-7.11	1.07	-5.00	1.00	-4.88
DFT + U^d_{eff}	1.03	-11.10	0.74	-8.00	0.66	-7.68
DFT + $U^{d,p}_{eff}$	1.52	-8.41	1.09	-6.04	1.00	-5.86
DFT + U^d + J^d_H	0.96	-10.24	0.69	-7.31	0.62	-7.04
DFT + $U^{d,p}$ + $J^{d,p}_H$	1.00	-7.35	0.71	-5.22	0.66	-5.09
MO-Specific Parameters						
DFT + U^d	-2.60	-43.53	-1.84	-30.79	-1.72	-29.27
DFT + $U^{d,p}$	-18.01	-41.77	-12.67	-29.38	-11.96	-28.28
DFT + U^d_{eff}	-10.19	-45.89	-7.35	-33.09	-6.54	-31.29
DFT + $U^{d,p}_{eff}$	-40.63	-46.36	-29.15	-33.26	-26.75	-31.79
DFT + U^d + J^d_H	-19.24	-44.87	-13.73	-32.01	-12.39	-30.40
DFT + $U^{d,p}$ + $J^{d,p}_H$	-49.96	-45.16	-35.48	-32.07	-32.83	-30.81
Experiment						
INS | Hutchings (1972)[86]	0.69	-9.50				
Thermo | Shanker (1973)[87]	-0.69[§]	-8.66				
Magnon | Lockwood (1992)[88]	0.69	-9.61				
Magnon | Dietz (1971)[95]	—	-9.18				

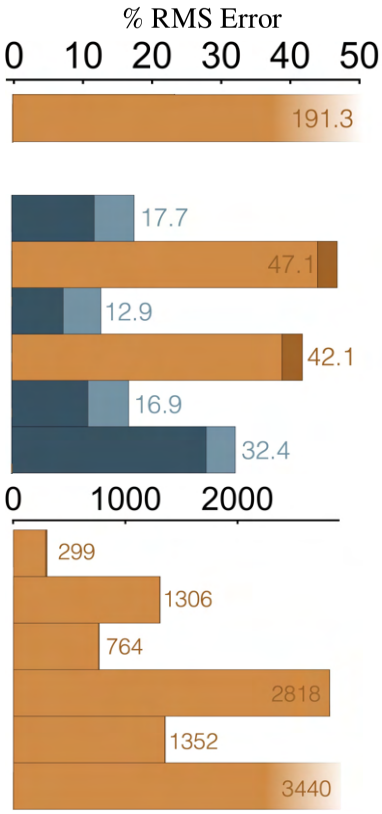

§ Ref. [87] reports a preference for antiferromagnetic alignment for both J_1 and J_2.

a % RMS error of 20% on $J_1 = 0.7$ meV does not mean we claim to know the value of J_1 to within ± 0.14 meV on the basis of calculations.

All Hubbard functionals we tested produced exchange-coupling parameters that are highly competitive with those from other techniques. Generally, however, the literature reports a wide range of values for this particular magnetic property, in part due to large variation in calculation of the magnetic moments (approximately half use some form of the total spin-density difference integrals, others use atom-centered sphere integration up to inconsistent maximum radii; all use S_z). Only a few computations use PAW, and many calculate the exchange coefficients with methods other than that involving total energy differences. It is crucial to recognize that the variation in spin moment integrations severely limits the reliability of any comparison across works of literature, and it is these incongruities in procedure that reinforce our inclination to benchmark with experiment.

Now for the analysis; referencing Tables 7.4 and 7.5, for converged total energies and their corresponding magnetic moments, we find that spin-parametrization Methods B and C generally predict exchange-interaction values smaller in magnitude, and closer to experiment, than the method that uses idealized values for Ni magnetization. This much is also demonstrated by the curves (the exchange parameters as functions of AF_{II} U^d variation) in Figs. 7.1(c) and (d) as U^d approaches its *in situ* values of $U^d = 5.58$ eV and $U^d_{\text{eff}} = 5.11$ eV.

Table 7.5 shows that Method C routinely predicts exchange parameters smaller in magnitude than those from Methods B and A. This may be attributed to the presence of and a heavy reliance on a strong magnetic moment on FM NiO—that, or the AF_{II} moment is comparatively too weak. Whatever the explanation, the message is clear; if the spin moments are large enough, then it is well worth the effort to weight the total energies with them, as spin-parametrization Methods B and C predict exchange parameters more closely in line with experiment. That much is also evident in the % RMSE in Row 1 of Table 7.4. The same AS data demonstrate a slight preference for Method B over Method C, however, the difference is minute.

The same conclusions cannot be drawn from Table 7.6. While J_2 is consistently smallest in magnitude under Method C, J_1 actually performs best under Method A. This is consistent with our own data, recalling that the literature analyzed here exclusively calculates the magnetic moment as a projection on the z-axis, whereas values from our own Hubbard functionals reported in Table 7.5 use $|\mathbf{S}^{\text{AS}}|$ as per the conclusions of Section 7.2.2.

If we better align our calculations with the literature by using S_z^{AS}, we can see from Table 7.4 that indeed, Method A minimizes the error compared to the other spin-parametrization methods. This demonstrates the sensitivity of the interplay between the magnetic moments and total energies of each MO of NiO. Under our preferred spin treatment procedure, our results indicate that Methods B and C are, somewhat interchangeably, the most reliable in obtaining realistic exchange-interaction parameters for NiO.

7.2.4 Effect of MO-specific Hubbard functional calculations

Going back to Table 7.5, we see the uncorrected PBE XC functional predicts, at best, $J_1 = 1.37$ meV under Method C and $J_2 = -29.32$ meV under Method A, values which are far from corroborated

by our experimental benchmarks of $J_1 = 0.69$ meV and $J_2 = -9.50$ meV.[86] The error arising from parametrization schemes B and C can be attributed in part to PBE's incorrect prediction of the Ni magnetic moments under the AS population analysis (wherein $\mu_{\mathrm{FM}} = 1.09\ \mu_B$, $\mu_{\mathrm{AF_I}} = 1.56\ \mu_B$, $\mu_{\mathrm{AF_{II}}} = 1.30\ \mu_B$).

PBE nonetheless correctly predicts the preference for ferromagnetic alignment in J_1 and antiferromagnetic alignment in J_2, unlike all functionals incorporating MO-specific parameters (center of Table 7.5). These performed poorly, not only quantitatively—note the inflated % RMS error scale, dilated by two orders of magnitude—but qualitatively, as they failed to predict the correct magnetic alignment for J_1. This decisively answers the query posed earlier; while the U and $\mathrm{J_H}$ for a particular subspace in FM NiO differ from those calculated for other MOs (see Tables 7.2 and 7.3), the total energies resulting from the application of these magnetic ordering-specific parameters to their corresponding system are not necessarily comparable to one another. We must emphasize, however, that this will not necessarily be the case for any and all Hubbard functionals; there remain quite a few functionals untested in this article, and further testing is needed to determine if this deficiency is an intrinsic property of Hubbard corrective protocol.

This finding is unexpected. The MO of a particular material system influences the magnitude of its atomic magnetic moments, as is demonstrated in Figs. 7.1(a) and (b). These moments are direct functions of valence subspace occupancies, and so changing the magnetic moments in turn alters the amount of self-interaction intrinsic to each subspace and, therefore, the Hubbard parameters and the efficacy of their host Hubbard functionals. If the total energies of each system are individually more accurate by application of a Hubbard corrective functional, then is it not expected that the total energy differences between these systems become more accurate, as well?

The linearity condition of linear response is based heavily on the quadratic nature of SIE (i.e., the deviation from piecewise linearity of the total energy with respect to fractional charge). It is worth noting, however, that the response behavior in the first-principles calculation of the Hubbard parameters for certain Ni *3d* subspaces—notably upon application of the beta perturbation to the FM and $\mathrm{AF_I}$ MOs—noticeably deviated from linearity. This non-linear response suggests that the SIE in these systems may require a correction of order higher than quadratic, possibly as a result of the added complexity in enforcing the system's non-ground-state MOs.

We might be tempted to conclude then that applying different sets of Hubbard parameters to these systems is akin to changing its functional entirely, to the degree that the resulting total energies are no longer comparable (i.e., asserting that a DFT+$\mathrm{U}^d = 5.58$ eV functional is inherently different to a DFT+$\mathrm{U}^d = 6.91$ eV functional). However, this justification is not compatible with our understanding of the Hubbard parameters as intrinsic, ground-state properties of the degree to which SIE and SCE infect the system. In maintaining the integrity of this understanding, then, it is more plausible that we have simply not found/tested a Hubbard-like functional adequately equipped to deal with long-range magnetic ordering of this nature. In applying the same Hubbard parameters inside this particular set of functionals to all structures, its possible that the results benefit from a black-box cancellation of errors that manifests in the total energy difference domain. Whatever the case, it is clear that calculating and applying MO-ordering specific Hubbard parameters is a disadvantageous complexity for deriving the exchange-coupling parameters for magnetic NiO, at least for the six Hubbard functionals tested here.

			Method A		Method B		Method C		
			$S_{FM} = S_{AF_I} = S_{AF_{II}} = 1$		$S_{FM} = S_{AF_I} = S_{AF_{II}}$		$S_{FM} \neq S_{AF_I} \neq S_{AF_{II}}$		
	U	J_H	J_1	J_2	J_1	J_2	J_1	J_2	% RMS Error
Ref | XC	(eV)	(eV)	(meV)	(meV)	(meV)	(meV)	(meV)	(meV)	0 100 200
PBE			8.23	-29.32	9.73	-34.68	1.37	-30.48	191.3
PBE+U^d	5.58		0.95	-10.20	0.67	-7.22	0.60	-6.95	17.7
PBE+U^d_{eff}	5.58	0.47	1.03	-11.10	0.74	-8.00	0.66	-7.68	12.9
PBE+U^d+J^d_H	5.58	0.47	0.96	-10.24	0.69	-7.31	0.62	-7.04	16.9
[92] | PBE+U	6.30	1.00	**1.10**	**-11.90**	1.66	-17.96	2.05	-17.83	49.7
[91] | PBE			**0.60**	**-22.25**	1.32	-48.95	2.32	-44.02	111.3
[91] | HSE			**1.15**	**-10.5**	1.69	-15.46	1.34	-14.52	49.5
[91] | PSIC			**1.65**	**-12.35**	2.55	-19.10	2.37	-18.40	102.9
[113] | SIC-LSD*			**1.15**	**-6.0**	1.89	-9.88	1.53	-9.12	54.1
[93] | GGA+U	6.30	1.00	**0.87**	**-9.54**	1.23	-13.55			19.8
[114] | LDA			**5.95**	**-35.65**	17.13	-102.65			582.4
[114] | UHF			**0.4**	**-2.3**	0.44	-2.53			58.1
[114] | Fock-35			**0.95**	**-9.85**	1.24	-12.90			28.4
[114] | Fock-50			**0.75**	**-5.3**	0.92	-6.49			32.3
[114] | B3LYP			**1.2**	**-13.35**	1.73	-19.19			64.8
[115] | LSIC			**1.42**	**-6.95**	2.02	-9.87			77.3
[115] | LSIC*			**0.15**	**-6.92**	0.21	-9.83			50.1
[36] | LSDA*			**0.54**	**-21.50**	0.64	-25.18			105.9
[36] | LSDA+U*	8.2	0.95	**-0.03**	**-6.80**	-0.03	-7.97			74.8
[36] | LSDA+DMFT*			**-0.04**	**-6.53**	-0.05	-7.65			77.2
[99] | LDA*			**0.3**	**-28.3**	0.82	-77.50			165.3
[68] | PBE+$U^{d,p}$	7.63[a]		**2.36**	**-25.15**	4.25	-45.42			217.8
[68] | LDA+$U^{d,p}$	7.49[b]		**1.48**	**-20.04**	4.05	-54.86			123.2
[116] | LDA+U	8.0	0.95	**2.4**	**-28.0**					235.9
[117] | LDA+U*	8.0	0.9	**0.2**	**-9.4**					50.6
			Experiment						
[86] | INS			**0.69**	**-9.50**					
[87] | Thermo			**-0.69**	**-8.66**					
[88] | Magnon			**0.69**	**-9.61**					
[95] | Magnon			—	**-9.18**					

[a] Applied $U^d = 7.63$ eV and $U^p = 3.00$ eV.
[b] Applied $U^d = 7.49$ eV and $U^p = 2.60$ eV.

Table 7.6: Comparison of exchange-interaction parameters from different XC functionals (or experiment) across literature works for each spin-parametrization method. Parameters for Methods B *and* C *are reverse engineered from past works based on reported values for MO-dependent magnetization on* Ni *atoms and J_1 and J_2 values, translated according to Hamiltonian conventions outlined in Table 6.1. Reported values from each work are in bold. Histogram shows minimum (leftmost bar), range (stacked bar) and maximum (digit) of all %* RMS errors *with respect to J_1, J_2 pairs from each of the four experiments listed. Color of bar corresponds to spin-parametrization method used to obtain that best J_1, J_2 pair (i.e., tan for* Method A, *blue for* Method B *and orange for* Method C*). Asterisk (*) indicates that these exchange parameters were calculated via a method other than that using total energy (i.e., Green's Functions).*

7.2.5 Effect of Hubbard functional choice

Whatever ails the MO-specific functionals does not affect the Hubbard functionals employing only the AF_{II} NiO parameters, in which the same Hubbard functionals are applied to all structures regardless of MO. Like PBE, these functionals correctly predict the preference for ferromagnetic alignment in J_1 and

antiferromagnetic alignment in J_2. This remains true as long as the Hubbard parameters are reasonable in magnitude, as demonstrated in Figs. 7.1(c) and (d); under the standard DFT+U^d functional, both the NN and the NNN exchange interactions gradually weaken with increasing U^d, coinciding with experimental values around the first-principles value of U^d.

In particular, the DFT+U^d_{eff} yields J_1 and J_2 coefficients strikingly in line with experimental values under the Method B spin-parametrization scheme, contributing to shared RMS errors ranging from 7.4-12.9%. It is closely followed in performance by the same functional under Method C spin parametrization (8.6-14.5% error), and then by the Liechtenstein DFT+U^d+J^d_{H} functional—in which we apply both HPs to the Ni *3d* subspace only–under Method B (11.0-16.9% error). This ranking remains stable even as the intra-atomic spin-population analysis technique varies, although only when considering $|\mathbf{S}|$. When using S_z, the Liechtenstein DFT+U^d+J^d_{H} under Method A performs best.

The $\{J_1, J_2\}$ pairs from these Hubbard functionals are highly competitive with those from other semi-local or hybrid functionals reported in the literature. Looking back at Table 7.6, the best DFT prediction for J_1 on NiO remains that from Fock-35 results of Ref. [114], with an individual parameter RMS error of 8.7%. For J_2, the best predictions are held by the GGA+U_{eff} = 5.3 eV calculation of Ref. [93] (J_2 RMS errors ranging from 0.4% to 10.2%) and the LDA+U^d_{eff} = 7.1 eV conducted in Ref. [117] (J_2 errors 1.1-8.6%). In terms of pairwise performance, however, the *in situ* Hubbard functionals monopolize the best error minimization rankings, reflecting positively on the error compensation and spin-parametrization techniques. At minimum, this demonstrates that the Hubbard functionals are competitive with the more costly hybrid functionals in achieving total energy difference results that reflect experiment.

7.2.6 Mechanics of the Hubbard functional

It is possible to rationalize the dependence of J_1 and J_2 on the choice of Hubbard functional and parameter strength in a relatively simple way. To see this, we start with the energy expressions for Method B, Eqs. (6.14) and (6.15). Taking the former, J_1, we first note that a sufficient U^d will change the FM and AF_I systems from metallic to insulating. This will tend to reduce the relevant total energy difference; the total energy of the metallic state depends significantly, through the kinetic energy, on the Fermi densities of the two systems, whereas in the insulating systems, it will primarily depend on weaker differences of exchange and correlation effects. As we can see from Fig. 7.1(a), the local moments become more similar in the two states at larger U values, which moderates the tendency for the different Hubbard energy contributions to increase. As these local moments increase with U^d, furthermore, so too the denominator in Eq. (6.14) increases quadratically, which further brings down the J_1. Thus, we can visualize how increasing U^d tends to bring down the predicted J_1. Of course, that effect is moderated in the Dudarev scheme when U^d is reduced to U^d_{eff} by an increasing J^d_{H}.

Meanwhile, it is interesting that the exchange parameters arising from DFT+U^d and the Liechtenstein DFT+U^d+J^d_{H} are so similar. In fact, the similarity between the exchange parameters arising from either functional is tenacious, remaining even as we vary U^d and J^d_{H} (keeping the first-principles ratio between U^d and J^d_{H} constant). The relative agnosticism of the inter-atomic, Heisenberg exchange parameters to the addition of a non-zero J_{H} parameter suggests that the spin localization facilitated

by the U^d term is already quite robust. The addition of U^p_{eff} largely mitigates the effect of U^d_{eff} on J_1, and not in a beneficial way when using the first-principles parameters. We return to discuss this effect further in the next section.

As for the substantial moderation of J_2 by the addition of U^d, the same arguments and trends largely hold. The total energy differences in Eq. (6.15) are reduced when all three systems are insulating. Once again, as the moments are increased with increasing U^d_{eff}, so the J_2 decreases due to the quadratic expression in the denominator. This effect is weakened by J^d_{H} in the Dudarev functional, by definition, and beneficially so when J_2 is compared against experiment. The effects of J^d_{H} and J^p_{H} are much more weak in the Liechtenstein functional, where it is also more difficult to interpret. The main difference in the trends observed between J_1 and J_2 is a different sign in the change with the addition of finite U^p_{eff}, so that increasing U^p_{eff} reduces the magnitude of J_2, as we go on to discuss further. Once again, however, the addition of the first-principles U^p_{eff} is detrimental to the quality of J_2.

7.2.7 Effect of Hubbard parameters on oxygen

Introduction of HPs on the oxygen *2p* orbitals, across all Hubbard functionals, seems to have the effect of strengthening the NN ferromagnetic exchange while simultaneously weakening the antiferromagnetic coupling between layers, similar to how HSE and PSIC perform compared to raw PBE.[91] For example, relative to DFT+U^d+J^d_{H}, the additional U^p and J^p_{H} in DFT+$U^{d,p}$+$J^{d,p}_{\text{H}}$ increase J_1 to 1 meV, but bring J_2 down in magnitude to -7.35 meV. These are typically unwelcome modifications under Methods B and C, for both J_1 and J_2, since the latter is chronically underestimated by a large margin and the former hovers tightly around the experimental value of 0.69 eV.

Nonetheless, the regularity of the phenomenon is intriguing and worth some discussion. In the much simplified picture of Eq. (6.11), the spin dependence of the AF_{II} total energy is informed exclusively by J_2 interactions, and the FM total energy is informed heavily, although not exclusively, by J_1 interactions. Moreover, as discussed in Section 6.2.2, the crystal-field splitting of orbitals is heavily implicated in the direct exchange and superexchange mechanisms that collectively give rise to interatomic exchange. We can perhaps look for clues in the FM and AF_{II} NiO density of states (DOS) plots, shown in Fig. 7.2 as functions of U^p, keeping $U^d = 5.58$ eV constant.

In FM NiO, the occupied minority-spin states on oxygen and the unoccupied minority-spin states on Ni are shifted higher in energy with increasing U^p, although the former at a faster rate than the latter. By itself, this means we should expect the exchange energy, and thus J_1, to gradually reduce in magnitude. However, simultaneous to this feature, we notice two pivotal details about the shifting occupancies (i) the t_{2g} states are decreasing in occupancy, so the Coulombic repulsion that contributes to a strong AF exchange interaction is weakening; and (ii) the oxygen $2p$ orbitals are increasing in occupancy, as demonstrated by the gradually inflating area underneath the PDOS curve as well as the inset graphs in Fig. 7.2. Thus, the intra-atomic Coulomb repulsion grows, strengthening the FM preference of the superexchange mechanism. Because intra-atomic exchange overwhelms its interatomic counterpart by several orders of magnitude, we expect these local oxygen dynamics to eclipse the gradual reduction in exchange energy coming from the evolution of the minority-spin PDOS. Collectively,

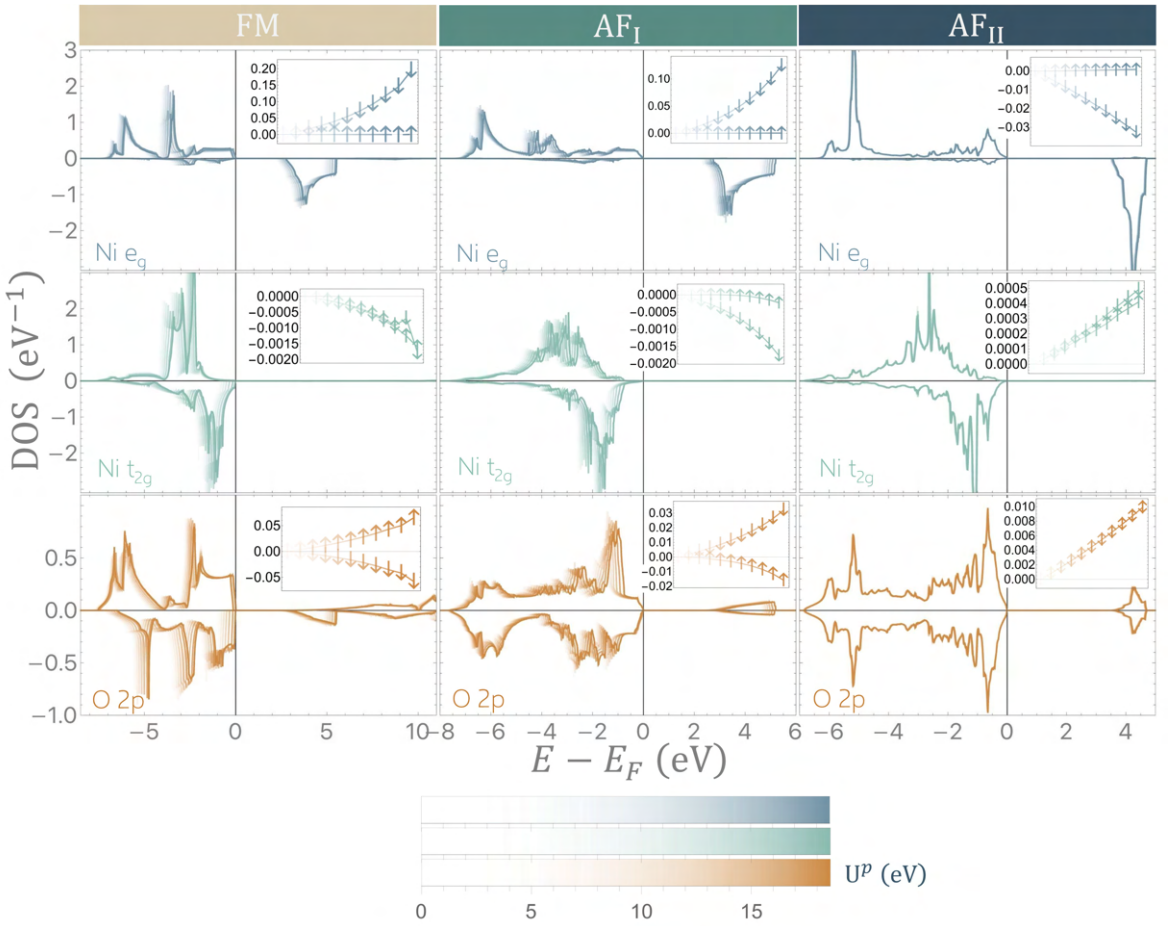

Figure 7.2: Overlaid atomic (AE) orbital projected density of states (PDOS) on two particular atoms of the four-atom unit cell, resolved by crystal-field-splitting characterization on Ni *(e_g blue, top row; t_{2g} light green, middle row) and* O *(2p orbital orange, bottom row) for each magnetic ordering (*FM *left column;* AF$_I$ *middle column;* AF$_{II}$ *right column) of* NiO*. Positive values indicate majority-spin DOS, negative values indicate minority-spin. Only the component within the PAW augmentation sphere cutoff r_c for each species is included, with no interstitial contributions, hence the relatively sharp (atomic-like) features of the PDOS. Moreover, only the conduction band edge position should be interpreted here, as the Kohn-Sham basis is not thought to be complete for the conduction band for all MOs in the energy range shown. Insets show corresponding relative changes in majority-spin ($\sigma = \uparrow$) and minority-spin ($\sigma = \downarrow$) occupancies $\Delta n^\sigma = 100(n^\sigma|_{U^p} - n^\sigma|_{U^p=0.45})/n^\sigma|_{U^p=0.45}$ as a function of* U^p [eV] *for that particular MO and crystal-field characterization. Opacity of plot is a function of* U^p (eV) *in the Dudarev et al.* DFT+U^{d,p} *functional, where* U^d = 5.58 eV *is kept constant and applied to all MOs. Variations in the* AF$_{II}$ *case are present but barely discernible.*

these justifications point to an overall increasing FM preference for J_1.

For the AF$_{II}$ NiO case, the Ni and O subspace occupancies both become more integer-like upon application of HPs on O in addition to those already applied on Ni—more integer-like and, thus, more localized spatially. As the orbitals cling more closely to their respective nuclei, there is less overlap between neighboring atomic orbitals. In the NNN case, less orbital overlap translates to a decrease in virtual hopping and therefore a weaker exchange bridge; by consequence, J_2 decreases in magnitude. Yet, unlike in 180° superexchange, the 90° superexchange is mediated by the Coulombic exchange between orthogonal orbitals on the same oxygen atom (see Fig. 6.3). As orthogonal orbitals

on the same atom become more localized, the exchange increases in magnitude, thereby intensifying the ferromagnetic preference embodied by J_1. So, J_1 increases in magnitude and J_2 decreases in magnitude, precisely as observed. In this way, it is possible that the application of the oxygen HPs on top of those applied on Ni serves to partially relocalize the atomic orbitals.

In Fig. 7.2, it is interesting that the AF_{II} PDOS character varies almost imperceptibly with changes in oxygen's U^p, which changes only E_F in a manner rigidly linear with the magnitude of the Hubbard parameter. We mention this to preemptively assuage concerns that it belies a plotting error and tentatively propose that the phenomenon is related to the fact that the oxygen atoms in AF_{II} NiO have absolutely no net magnetic moment. When we set U^p to a large, finite number, the DOS undergoes significant changes. We refer the reader to Appendix B2 for an analogous figure to Fig. 7.2, where instead the U^d is varied.

To complete our foray into NiO's electronic structure, we briefly comment on the aptitude of our obtained DFT+U PDOS. To this end, we provide Fig. 7.3, which shows the total DOS with no PAW sphere truncation for the best performing functional that used $U^d_{\text{eff}} = 5.11$ eV. We emphasize here that the PDOS shown in Figs. 7.2 and 7.3, in addition to Fig. B.1 of the Appendix, are truncated within the PAW augmentation spheres, with no interstitial contribution, based on the PAW population analysis. It therefore exhibits sharper, more atomic-like features than would be observed experimentally. An increased smearing would be needed for comparison to experiment. Furthermore, only the conduction

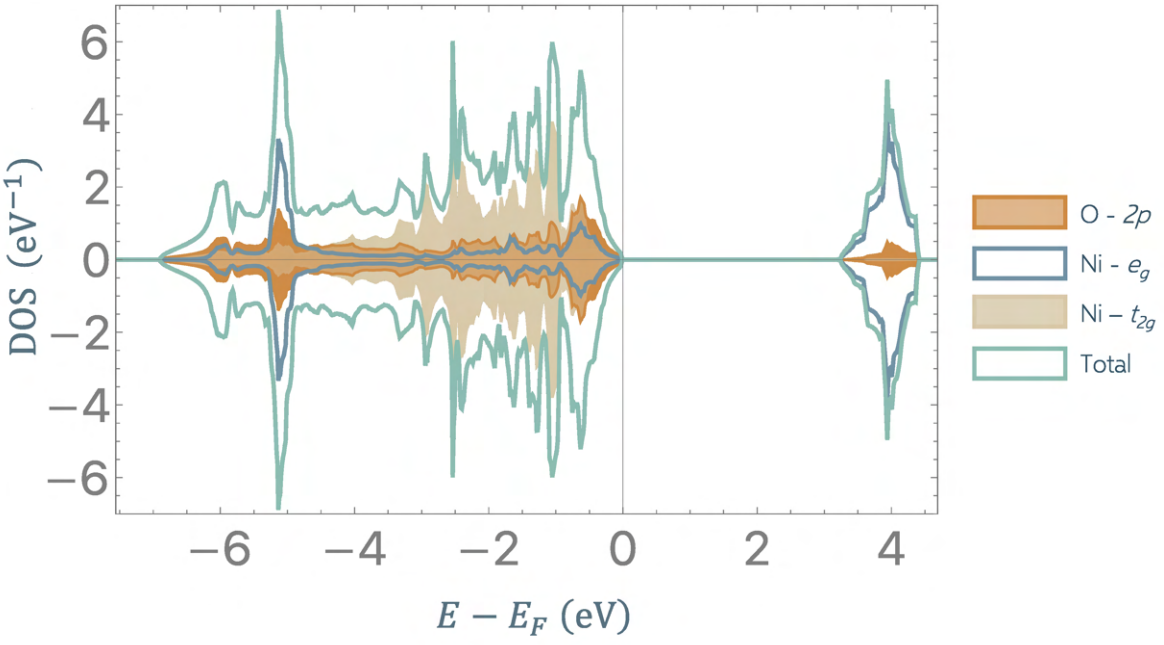

Figure 7.3: PDOS resolved by crystal-field-splitting characterization, summed over all atoms in the unit cell, Ni *(e_g blue; t_{2g} tan) and* O *(2p orange) of* NiO. *Calculated with the Dudarev functional* $U^d_{eff} = 5.11$ *eV. Only the component within the PAW augmentation sphere cutoff* r_c *for each species is included, with no interstitial contributions, hence the relatively sharp (atomic-like) features of the PDOS. The Total DOS (light green) is also shown, which is not restricted to the PAW augmentation sphere region and does include all contributions. In all cases, only the conduction band edge position should be interpreted here, as the Kohn-Sham basis is not thought to be complete for the conduction band for all MOs in the energy range shown.*

band edge should be interpreted, and features no higher in energy thereof, due to insufficient basis resolution. Our objective here is to understand the mechanisms of inter-atomic exchange interactions.

Despite these limitations, our AF_{II} NiO PDOS does not deviate significantly in its features from those of prior DFT+U calculations.[118–123] The upper band is clearly of primarily Ni e_g character, whereas the lower band edge is characterized by the O $2p$, followed by non-negligible contributions of Ni t_{2g} and e_g character. The failure of DFT+U-like methods to replicate other features of the experimental PDOS is well-documented across the literature. For example, our oxygen $2p$ spectrum exhibits a two-peaked structure (with edges at -5.1 eV and 0.6 eV) instead of the broad peak feature attributed to oxygen from angle-resolved photoemission spectra.[124,125] This result is at odds with the results of DFT+DMFT calculations.[37,38] The width of the valence band Ni $3d$ spectrum is also narrower overall than might be expected, as well as appearing sharper for the aforementioned reasons. However, the same experiments also indicate that the NiO valence-band spectrum has two distinct peaks, one around -2 eV and the other around -5 eV, a behavior reflected in our own plots, where the peak-to-peak splitting across the Fermi energy is approximately 4.6 eV, a value comparable to that derived from experiment (4.3 eV)[126,127] and DMFT.[37,38] Fig. 7.3 in particular displays more clearly the low-energy peak at -5.1 eV of primarily Ni e_g character, which has the distinct sharpness as the spectral feature attributed to Ni in experiment.

7.3 Summary and conclusions

In this work, we analyzed the NN and NNN Heisenberg exchange-coupling coefficients of the prototypical Mott-Hubbard insulator NiO, calculating its electronic structure in its three main enforceable magnetic configurations (FM, AF_I, and AF_{II}) in a Hubbard corrected DFT context, for comparison with experiment. First, we examined the sensitivity of the first-principles Hubbard parameters U and J_H to the PAW projectors. Here, we found that `dmatpuopt = 3`, the population analysis corresponding to the once-normalized projection of the PAW basis functions on bound AE atomic eigenfunctions and truncated at the PAW augmentation radius, renders a numerically well-behaved linear response procedure that yields robust Hubbard parameters. These go on to provide experimentally relevant J_1 and J_2 exchange pairs once applied to NiO via a range of host Hubbard functionals.

Our results highlight just how valuable to the simulation of NiO and its total energetic properties are its *in situ*-derived U and J_H. We report rigorously defined PBE Hubbard parameters U and J_H for the Ni *3d* and O *2p* subspaces of NiO. The technical platform on which we build these investigations, the open-source plane-wave DFT suite ABINIT,[128,129] allowed us to at once assess the numerical performance of the code's linear-response implementation for calculating the Hubbard U and to extend its utility to also calculate the intra-atomic exchange-coupling corrective parameter J_H from first principles. The details of this implementation are itemized in Chapter 5.

We continued to probe the minutiae of population analysis procedures to reevaluate conventions pertaining to spin parameterization, both inter- and intra-atomic, in the HDvV Hamiltonian. In doing so, we systematically charted a particular region of DFT-accessible spin-moment parameter space to make navigation of these techniques more manageable for scientists. Our optimization of this parameter space corresponds to the particular combination of (i) a rudimentary-quantum, atomic-sphere-

restricted intra-atomic spin moment ($|\mathbf{S}^{\mathrm{AS}}| = \sqrt{2}\,\mathrm{S}_z^{\mathrm{AS}}$), and (ii) a spin-parametrization scheme that assumes $|\mathrm{S_{FM}}| = |\mathrm{S_{AF_I}}| = |\mathrm{S_{AF_{II}}}|$. We recommend this particular spin treatment for magnetic properties and total energy differences pertaining to NiO, given that the resulting $\{J_1, J_2\}$ exchange pairs give % RMS errors (with respect to experiment) as low as 13%, a considerable improvement on state-of-the-art DFT simulations conducted thus far. Regardless of the Hubbard functional used, this spin treatment produced exchange-coupling constants that are satisfactorily in line with experiment and highly competitive with other, more computationally taxing hybrid functionals, which were methodically categorized in a comprehensive literature review.

Throughout these investigations are implicit suggestions towards best practices in calculating Hubbard parameters and use of Hubbard functionals for non-ground-state magnetic orderings of TMOs. Notably, we highlight the fact that the Hubbard functionals tested here, despite the bespoke nature of these parameters to their respective magnetic environments, did not result in comparable total energies, so we generally disadvise their use for such comparisons in NiO. Alternatively, these results highlight the need for more advanced Hubbard functionals designed to accommodate differences in magnetic environment. Notwithstanding, it is clear from Table 7.5 that use of the $\mathrm{J_H}$ parameter on both the Ni and the O is critical for reducing % RMSE of the Heisenberg exchange-coupling parameters in NiO with standard functionals.

Lastly, through extensive testing of a suite of 6+ different corrective Hubbard functionals, we draw attention to the effect of the O *2p* Hubbard parameter pairs on the NiO exchange-coupling coefficients and provide a justification for the phenomenon thereabouts based on the crystal-field resolved DOS and occupancy analyses.

Bibliography

[1] K. L. Materna, A. M. Beiler, A. Thapper, S. Ott, H. Tian, and L. Hammarström, ACS Applied Materials & Interfaces **12**, 31372 (2020).

[2] R. A. Wahyuono, M. Braumüller, S. Bold, S. Amthor, D. Nauroozi, J. Plentz, M. Wächtler, S. Rau, and B. Dietzek, Spectrochimica Acta Part A: Molecular and Biomolecular Spectroscopy **252**, 119507 (2021).

[3] C.-Y. Hsu, W.-T. Chen, Y.-C. Chen, H.-Y. Wei, Y.-S. Yen, K.-C. Huang, K.-C. Ho, C.-W. Chu, and J. T. Lin, Electrochimica Acta **66**, 210 (2012).

[4] X. Xia, L. Fu, Z. Luo, J. Zhu, W. Yang, D. Li, and L. Zhou, Electrochemistry Communications **134**, 107185 (2022).

[5] A. Manthiram, Nature Communications **11** (2020).

[6] M. D. Irwin, D. B. Buchholz, A. W. Hains, R. P. H. Chang, and T. J. Marks, Proceedings of the National Academy of Sciences **105**, 2783 (2008).

[7] H. Yang, Q. Tao, X. Zhang, A. Tang, and J. Ouyang, Journal of Alloys and Compounds **459**, 98 (2008).

[8] M. Shi, T. Qiu, B. Tang, G. Zhang, R. Yao, W. Xu, J. Chen, X. Fu, H. Ning, and J. Peng, Micromachines **12** (2021).

[9] J. Hugel and C. Carabatos, Journal of Physics C: Solid State Physics **16**, 6713 (1983).

[10] A. P. Cracknell and S. J. Joshua, Mathematical Proceedings of the Cambridge Philosophical Society **66**, 493 (1969).

[11] W. L. Roth, Phys. Rev. **111**, 772 (1958).

[12] W. L. Roth, Phys. Rev. **110**, 1333 (1958).

[13] T. Eto, S. Endo, M. Imai, Y. Katayama, and T. Kikegawa, Phys. Rev. B **61**, 14984 (2000).

[14] A. M. Balagurov, I. A. Bobrikov, J. Grabis, D. Jakovlevs, A. Kuzmin, M. Maiorov, and N. Mironova-Ulmane, IOP Conference Series: Materials Science and Engineering **49**, 012021 (2013).

[15] A. M. Balagurov, I. A. Bobrikov, S. V. Sumnikov, V. Y. Yushankhai, J. Grabis, A. Kuzmin, N. Mironova-Ulmane, and I. Sildos, physica status solidi (b) **253**, 1529 (2016).

[16] N. Smith, Journal of the American Chemical Society **58**, 173 (1936).

[17] M. A. Peck and M. A. Langell, Chemistry of Materials **24**, 4483 (2012).

[18] A. K. Cheetham and D. A. O. Hope, Physical Review B **27**, 6964 (1983).

[19] V. Fernandez, C. Vettier, F. de Bergevin, C. Giles, and W. Neubeck, Physical Review B **57**, 7870 (1998).

[20] W. Neubeck, C. Vettier, V. Fernandez, F. de Bergevin, and C. Giles, Journal of Applied Physics **85**, 4847 (1999).

[21] E. Brok, K. Lefmann, P. P. Deen, B. Lebech, H. Jacobsen, G. J. Nilsen, L. Keller, and C. Frandsen, Physical Review B **91**, 014431 (2015).

[22] Y. Shimomura, M. Kojima, and S. Saito, Journal of the Physical Society of Japan **11**, 1136 (1956).

[23] A. Chakraborty, M. Dixit, and D. T. Major, npj Computational Materials **4**, 60 (2018).

[24] K. Saritas, E. R. Fadel, B. Kozinsky, and J. C. Grossman, The Journal of Physical Chemistry C **124**, 5893 (2020).

[25] J. Shu, T.-F. Yi, M. Shui, Y. Wang, R.-S. Zhu, X.-F. Chu, F. Huang, D. Xu, and L. Hou, Computational Materials Science **50**, 776 (2010).

[26] Y. S. Meng and M. E. Arroyo-de Dompablo, Energy & Environmental Science **2**, 589 (2009).

[27] M. Shishkin and H. Sato, The Journal of Physical Chemistry C **125**, 1531 (2021).

[28] F. S. Hegner, J. R. Galán-Mascarós, and N. López, Inorganic Chemistry **55**, 12851 (2016).

[29] A. Aziz, *Electronic structure simulations of energy materials: chalcogenides for thermoelectrics and metal-organic frameworks for photocatalysis*, Chemistry, University of Reading, United Kingdom (2017).

[30] S. Siebentritt and S. Schorr, Progress in Photovoltaics: Research and Applications **20**, 512 (2012).

[31] A. Polman, M. Knight, E. C. Garnett, B. Ehrler, and W. C. Sinke, Science **352** (2016).

[32] C. Yan, K. Sun, J. Huang, S. Johnston, F. Liu, B. P. Veettil, K. Sun, A. Pu, F. Zhou, J. A. Stride, M. A. Green, and X. Hao, ACS Energy Letters **2**, 930 (2017).

[33] A. Bencini and F. Totti, Journal of Chemical Theory and Computation **5**, 144 (2009).

[34] F. Illas, I. de P. R. Moreira, J. M. Bofill, and M. Filatov, Theoretical Chemistry Accounts **116**, 587 (2006).

[35] L. Zhang, P. Staar, A. Kozhevnikov, Y.-P. Wang, J. Trinastic, T. Schulthess, and H.-P. Cheng, Phys. Rev. B **100**, 035104 (2019).

[36] Y. O. Kvashnin, O. Granas, I. Di Marco, M. I. Katsnelson, A. I. Lichtenstein, and O. Eriksson, Physical Review B **91**, 125133 (2015).

[37] S. Mandal, K. Haule, K. M. Rabe, and D. Vanderbilt, npj Computational Materials **5**, 115 (2019).

[38] J. Kuneš, V. I. Anisimov, S. L. Skornyakov, A. V. Lukoyanov, and D. Vollhardt, Phys. Rev. Lett. **99**, 156404 (2007).

[39] S. Tanaka, Journal of the Physical Society of Japan **64**, 4270 (1995).

[40] S. Zhang, F. D. Malone, and M. A. Morales, The Journal of Chemical Physics **149**, 164102 (2018).

[41] C. Mitra, J. T. Krogel, J. A. O. Santana, and F. A. Reboredo, Journal of Chemical Physics **143** (2015).

[42] K. Saritas, J. T. Krogel, P. R. C. Kent, and F. A. Reboredo, Physical Review Materials **2**, 085801 (2018).

[43] Y. Gao, Q. Sun, J. M. Yu, M. Motta, J. McClain, A. F. White, A. J. Minnich, and G.-L. Chan, Phys. Rev. B **101**, 165138 (2020).

[44] H. Takaki, S. Inoue, and Y. Matsumura, Chemical Physics Letters **774**, 138624 (2021).

[45] D. Hait, N. M. Tubman, D. S. Levine, K. B. Whaley, and M. Head-Gordon, Journal of Chemical Theory and Computation **15**, 5370 (2019).

[46] J. P. Malrieu, R. Caballol, C. J. Calzado, C. de Graaf, and N. Guihéry, Chemical Reviews **114**, 429 (2014).

[47] F. Illas, I. de P. R. Moreira, C. de Graaf, and V. Barone, Theoretical Chemistry Accounts **104**, 265 (2000).

[48] F. Illas, I. de P. R. Moreira, J. M. Bofill, and M. Filatov, Phys. Rev. B **70**, 132414 (2004).

[49] L. Noodleman, The Journal of Chemical Physics **74**, 5737 (1981), https://pubs.aip.org/aip/jcp/article-pdf/74/10/5737/18928366/5737_1_online.pdf.

[50] L. Noodleman and D. A. Case (Academic Press, 1992) pp. 423–470.

[51] I. Rudra, Q. Wu, and T. Van Voorhis, The Journal of Chemical Physics **124**, 024103 (2006).

[52] A. Schron, C. Rodl, and F. Bechstedt, Physical Review B **82**, 165109 (2010).

[53] M. Cococcioni and N. Marzari, Physical Review Materials **3**, 033801 (2019).

[54] W. Zhang, D. G. Truhlar, and M. Tang, Journal of Chemical Theory and Computation **10**, 2399 (2014).

[55] A. J. Cohen, P. Mori-Sánchez, and W. Yang, Science **321**, 792 (2008).

[56] P. Mori-Sánchez, A. J. Cohen, and W. Yang, The Journal of Chemical Physics **125**, 201102 (2006).

[57] E. B. Isaacs, S. Patel, and C. Wolverton, Physical Review Materials **4**, 065405 (2020).

[58] A. Georges, L. d. Medici, and J. Mravlje, Annual Review of Condensed Matter Physics **4**, 137 (2013).

[59] V. I. Anisimov, J. Zaanen, and O. K. Andersen, Physical Review B **44**, 943 (1991).

[60] V. I. Anisimov and O. Gunnarsson, Phys. Rev. B **43**, 7570 (1991).

[61] V. I. Anisimov, I. V. Solovyev, M. A. Korotin, M. T. Czyżyk, and G. A. Sawatzky, Phys. Rev. B **48**, 16929 (1993).

[62] Y.-C. Wang, B.-L. Liu, Y. Liu, H.-F. Liu, Y. Bi, X.-Y. Gao, J. Sheng, H.-Z. Song, M.-F. Tian, and H.-F. Song, "The underestimation of high pressure in dft+u simulation for the wide range cold-pressure of lanthanide metals," (2021).

[63] M. Yu, S. Yang, C. Wu, and N. Marom, npj Computational Mathematics **6**, 180 (2020).

[64] B. Dorado, B. Amadon, M. Freyss, and M. Bertolus, Phys. Rev. B **79**, 235125 (2009).

[65] B. Dorado, G. Jomard, M. Freyss, and M. Bertolus, Phys. Rev. B **82**, 035114 (2010).

[66] D. A. Tompsett, D. S. Middlemiss, and M. S. Islam, Phys. Rev. B **86**, 205126 (2012).

[67] C. E. Patrick and K. S. Thygesen, Phys. Rev. B **93**, 035133 (2016).

[68] P. Gopal, R. D. Gennaro, M. S. dos Santos Gusmao, R. A. R. A. Orabi, H. Wang, S. Curtarolo, M. Fornari, and M. B. Nardelli, Journal of Physics: Condensed Matter **29**, 444003 (2017).

[69] O. Le Bacq, A. Pasturel, C. Lacroix, and M. D. Nunez-Regueiro, Phys. Rev. B **71**, 014432 (2005).

[70] B. Savoie, Reviews in Mathematical Physics **27**, 1550019 (2015).

[71] E. Ising, *Beitrag zur Theorie des Ferro- und Paramagnetismus*, Physics, University of Hamburg, Bochum, Hamburg, Germany (1924).

[72] T. Ising, R. Folk, R. Kenna, B. Berche, and Y. Holovatch, Journal of Physical Studies **21**, 3002 (2017).

[73] W. Heisenberg, Zeitschrift für Physik **49**, 619 (1928).

[74] Y. R. Shen and N. Bloembergen, Phys. Rev. **143**, 372 (1966).

[75] A. Stasch, Journal of Raman Spectroscopy **5**, 145 (1976).

[76] P. A. Fleury, S. P. S. Porto, L. E. Cheesman, and H. J. Guggenheim, Phys. Rev. Lett. **17**, 84 (1966).

[77] R. Elliott and R. Loudon, Physics Letters **3**, 189 (1963).

[78] H. Xiang, C. Lee, H.-J. Koo, X. Gong, and M.-H. Whangbo, Dalton Trans. **42**, 823 (2013).

[79] X. Li, H. Yu, L. Feng, F. J.S., M.-H. Whangbo, and H. Xiang, Molecules **26**, 803 (2021).

[80] E. M. da Silva Wheeler, *Neutron Scattering from Low-Dimensional Quantum Magnets*, Ph.D. thesis, University of Oxford, Oxford, UK (2007).

[81] S. Tóth and B. Lake, Journal of Physics: Condensed Matter **27**, 166002 (2015).

[82] X. He, N. Helbig, M. J. Verstraete, and E. Bousquet, Computer Physics Communications **264**, 107938 (2021).

[83] J. Jensen and A. R. Mackintosh, *Rare Earth Magnetism: Structures and Excitations*, International Series of Monographs on Physics, Vol. 81 (Clarendon Press, Oxford, 1991) reprinted edition, 2023.

[84] I. Dzyaloshinsky, Journal of Physics and Chemistry of Solids **4**, 241 (1958).

[85] T. Moriya, Phys. Rev. **120**, 91 (1960).

[86] M. T. Hutchings and E. J. Samuelsen, Phys. Rev. B **6**, 3447 (1972).

[87] R. Shanker and R. A. Singh, Phys. Rev. B **7**, 5000 (1973).

[88] D. J. Lockwood, M. G. Cottam, and J. H. Baskey, Journal of Magnetism and Magnetic Materials Proceedings of the International Conference on Magnetism, Part II, **104-107**, 1053 (1992).

[89] M. E. Lines and E. D. Jones, Phys. Rev. **139**, A1313 (1965).

[90] R. Skomski, *Simple Models of Magnetism* (Oxford University Press, 2008).

[91] T. Archer, C. D. Pemmaraju, S. Sanvito, C. Franchini, J. He, A. Filippetti, P. Delugas, D. Puggioni, V. Fiorentini, R. Tiwari, and P. Majumdar, Physical Review B **84**, 115114 (2011).

[92] R. Logemann, A. N. Rudenko, M. I. Katsnelson, and A. Kirilyuk, Journal of Physics: Condensed Matter **29**, 335801 (2017).

[93] W.-B. Zhang, Y.-L. Hu, K.-L. Han, and B.-Y. Tang, Physical Review B **74**, 054421 (2006).

[94] P. Garcia-Fernandez, J. C. Wojdel, J. Iniguez, and J. Junquera, Physical Review B **93**, 195137 (2016).

[95] R. E. Dietz, W. F. Brinkman, A. E. Meixner, and H. J. Guggenheim, Physical Review Letters **27**, 814 (1971).

[96] V. R. Eisberg and R. R. J. Wiley, *Quantum Physics of Atoms, Molecules, Solids, Nuclei and Particles* (John Wiley & Sons, 1976) pp. 127–128.

[97] J. Coey and J. Coey, *Magnetism and Magnetic Materials*, Magnetism and Magnetic Materials (Cambridge University Press, 2010).

[98] W. A. Harrison, Physical Review B **76**, 054417 (2007).

[99] T. Kotani and M. van Schilfgaarde, Journal of Physics: Condensed Matter **20**, 295214 (2008).

[100] X. Wan, Q. Yin, and S. Y. Savrasov, Physical Review Letters **97**, 266403 (2006).

[101] J. P. Perdew, K. Burke, and M. Ernzerhof, Phys. Rev. Lett. **77**, 3865 (1996).

[102] F. Jollet, M. Torrent, and N. Holzwarth, Computer Physics Communications **185**, 1246 (2014).

[103] M. J. van Setten, M. Giantomassi, E. Bousquet, M. J. Verstraete, D. R. Hamann, X. Gonze, and G. M. Rignanese, Computer Physics Communications **226**, 39 (2018).

[104] N. Holzwarth, A. Tackett, and G. Matthews, Computer Physics Communications **135**, 329 (2001).

[105] N. Marzari, *Ab initio Molecular Dynamics for Metallic Systems*, Physics, University of Cambridge, Pembroke College, University of Cambridge (1996).

[106] M. Rutter, Computer Physics Communications **225**, 174 (2018).

[107] S. L. Dudarev, G. A. Botton, S. Y. Savrasov, C. J. Humphreys, and A. P. Sutton, Phys. Rev. B **57**, 1505 (1998).

[108] A. I. Liechtenstein, V. I. Anisimov, and J. Zaanen, Phys. Rev. B **52**, R5467 (1995).

[109] L. MacEnulty, M. Giantomassi, B. Amadon, G.-M. Rignanese, and D. D. O'Regan, Electronic Structure **6**, 037003 (2024).

[110] L. MacEnulty and D. J. Adams, "Hubbard U and Hund's J parameters with Cococcioni and de Gironcoli's approach: Determine the Hund's J for Ni 3d in NiO with LRUJ," (2023).

[111] H. J. Monkhorst and J. D. Pack, Phys. Rev. B **13**, 5188 (1976).

[112] L. MacEnulty and D. D. O'Regan, Phys. Rev. B **108**, 245137 (2023).

[113] D. Kodderitzsch, W. Hergert, W. M. Temmerman, Z. Szotek, A. Ernst, and H. Winter, Physical Review B **66**, 064434 (2002).

[114] I. d. P. R. Moreira, F. Illas, and R. L. Martin, Physical Review B **65**, 155102 (2002).

[115] G. Fischer, M. Dane, A. Ernst, P. Bruno, M. Lueders, Z. Szotek, W. Temmerman, and W. Hergert, Physical Review B **80**, 014408 (2009).

[116] A. Jacobsson, B. Sanyal, M. Lezaic, and S. Blugel, Physical Review B **88**, 134427 (2013).

[117] D. M. Korotin, V. V. Mazurenko, V. I. Anisimov, and S. V. Streltsov, Physical Review B **91**, 224405 (2015).

[118] G. Trimarchi, Z. Wang, and A. Zunger, Phys. Rev. B **97**, 035107 (2018).

[119] M. J. Han, T. Ozaki, and J. Yu, Phys. Rev. B **73**, 045110 (2006).

[120] I. Naz, F. Ahmad, J. Jang, and J. Y. Rhee, AIP Advances **8**, 125216 (2018).

[121] K. O. Egbo, C. P. Liu, C. E. Ekuma, and K. M. Yu, Journal of Applied Physics **128**, 135705 (2020).

[122] J. A. Dawson, Y. Guo, and J. Robertson, Applied Physics Letters **107**, 122110 (2015).

[123] W. B. Zhang, N. Yu, W. Y. Yu, and B. Y. Tang, The European Physical Journal B **64**, 153 (2008).

[124] Z.-X. Shen, C. K. Shih, O. Jepsen, W. E. Spicer, I. Lindau, and J. W. Allen, Phys. Rev. Lett. **64**, 2442 (1990).

[125] Z.-X. Shen, R. S. List, D. S. Dessau, B. O. Wells, O. Jepsen, A. J. Arko, R. Barttlet, C. K. Shih, F. Parmigiani, J. C. Huang, and P. A. P. Lindberg, Phys. Rev. B **44**, 3604 (1991).

[126] G. A. Sawatzky and J. W. Allen, Phys. Rev. Lett. **53**, 2339 (1984).

[127] O. Tjernberg, S. Söderholm, G. Chiaia, R. Girard, U. O. Karlsson, H. Nylén, and I. Lindau, Phys. Rev. B **54**, 10245 (1996).

[128] X. Gonze, B. Amadon, P. M. Anglade, J. M. Beuken, F. Bottin, P. Boulanger, F. Bruneval, D. Caliste, R. Caracas, M. Côté, T. Deutsch, L. Genovese, P. Ghosez, M. Giantomassi, S. Goedecker, D. R. Hamann, P. Hermet, F. Jollet, G. Jomard, S. Leroux, M. Mancini, S. Mazevet, M. J. T. Oliveira, G. Onida, Y. Pouillon, T. Rangel, G. M. Rignanese, D. Sangalli, R. Shaltaf, M. Torrent, M. J. Verstraete, G. Zerah, and J. W. Zwanziger, Computer Physics Communications 40 YEARS OF CPC: A celebratory issue focused on quality software for high performance, grid and novel computing architectures, **180**, 2582 (2009).

[129] B. Amadon, F. Jollet, and M. Torrent, Phys. Rev. B **77**, 155104 (2008).

Part IV

Spin-State Energetics of Molecular Spin-Crossover Systems

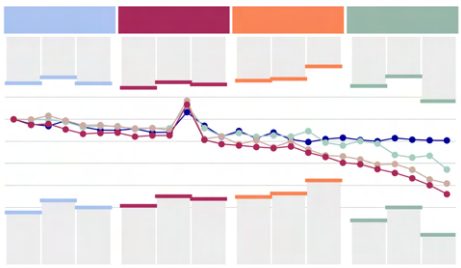

Chapter 8

Spin-crossover energetics and trends

Prussian Blue and its chemical analogues are materials of perpetual fascination for the physics and chemistry communities. These metal-hexacyanometallates—transition metals linked by magnetically asymmetric cyanide bridges—are easily synthesized and comprise elements that are both cheap and abundant, awarding this emergent class of materials high potential for renewable energy and eco-friendly functions[1–3]: as sodium-ion battery anodes[4] and cathodes,[5–10] water-splitting catalysts,[11] magnetic switches,[11–16] radioactive waste detection,[17], carbon capture,[18,19] and, of course, paint.

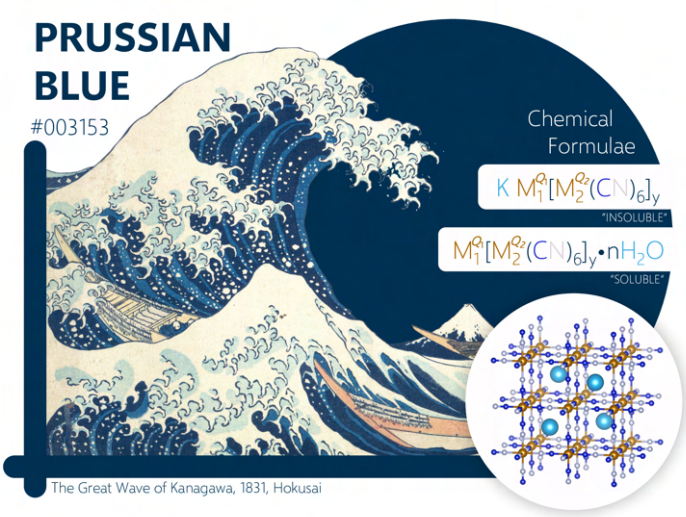

Prussian Blue (PB) and its analogues (PBAs) can adopt primarily two ideal stoichiometries: (i) the alkali A-intercalated "insoluble" $AM_1^{Q_1}[M_2^{Q_2}(CN)_6]_y$, or (ii) the "soluble" $M_1^{Q_1}[M_2^{Q_2}(CN)_6]_y \cdot nH_2O$ inundated by n water molecules. Here, M_1 and M_2 are transition metals (typically Fe, Mn, Ni, Co, Cu, or Zn) in oxidation states Q_1 and Q_2, respectively. Occasionally, M_1 is a combination of TMs, or $M_1 = M_2$, as is the case for PB (for which $M_1 = M_2 =$Fe). The constituent atoms arrange into FCC symmetry (space group Fm-3m), forming cages that harbor intercalants (like potassium ions) as shown in the above illustration, which also depicts the usage of PB in a familiar, historic painting. The spin state of the two metal sites is enforced by their coordination environments; the low-spin (LS) TM is surrounded by a strong ligand field comprising six carbon atoms and the high-spin (HS) TM by a weak ligand field of six nitrogen atoms. These spin states can switch with changes in pressure,[20,21] temperature,[14,22] irradiation,[16,21] guest molecules,[3] electric field,[22] and other stimuli.

The mechanisms that give rise to Prussian Blue's bewitching blue pigment and technological versatility—notably, the electron transfer between its ferrous $M_1^{Q_1}$ = Fe(II) and ferric $M_2^{Q_2}$ = Fe(III) metallic centers—foster an exciting environment in which to test DFT+U+J methodologies. The presence of two differently magnetized d subspaces on Fe centers in the same ground state could offer clarity

on the surprisingly incomparable energetics between NiO magnetic orderings in Section 7.2.4. For example, past studies on PBAs do not agree on the use of one U^d value for all magnetic centers, regardless of magnetic ordering.[23–30] Moreover, the appropriateness of the Hund's J as it is situated in both well-studied and emergent Hubbard-type energy functionals can be further evaluated in this highly spin-polarized environment due to the sensitive crossover susceptibility of the magnetic centers.

However, the large simulation cell, the degeneracy of magnetic configurations, and the diversity of stoichiometries render first-principles simulation of PBAs a cumbersome, laborious quest. Our approach, therefore, is to test our proposed DFT+U+J methodologies on molecular systems that resemble multi-atomic components of PB, then scale up. This chapter prepares the reader for this approach, which features a series of fictitious, yet theoretically well-studied, octahedrally-coordinated Fe(II) SCO molecules that span the ligand field strength spectrum. Ligand field theory for octahedral complexes is reviewed, following which the phenomenon and pertinent metrics of spin crossover are discussed.

8.1 Ligand field theory for octahedrally coordinated Fe(II) molecules

Ligand field theory is a combination of crystal-field theory and molecular orbital theory. It seeks to explain the magnitude of the energy separation between molecular orbitals of TMs surrounded by ligands. The effect of the ligand donor's electrons on the energetics of the TM *d* orbitals depends heavily on the coordination geometry of the complex due to alignment with or against the bond axes. For simplicity in guiding the current study, we focus on the description of Fe(II)-centered octahedrally coordinated complexes.

On its own, the Fe(II) ion (also written Fe^{2+}) has four electrons distributed across five degenerate energy levels in the 3*d* valence subshell. When placed in an octahedrally coordinated ligand field, the energy levels are subjected to repulsive forces that reorganize the *d* orbital occupancies in an effort to

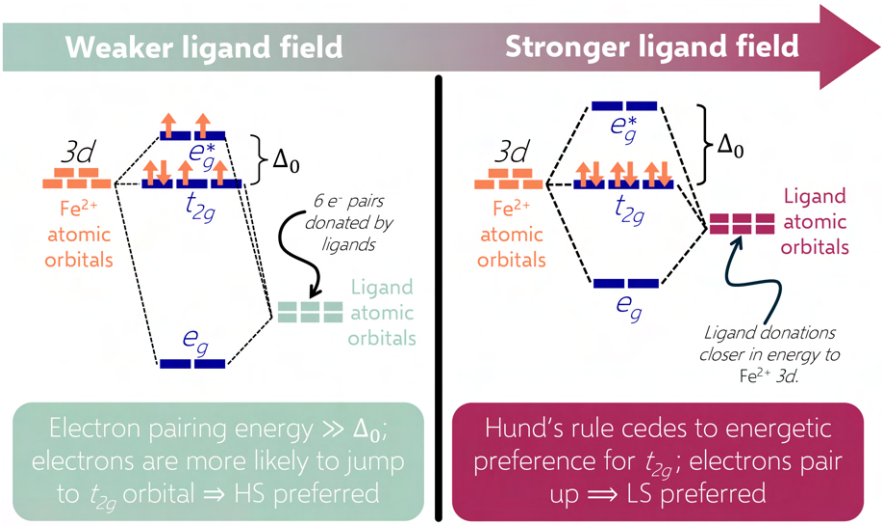

Figure 8.1: Orbital diagrams for octahedrally coordinated Fe(II) *molecular complexes of various ligand field strengths and spin states.*

minimize electrostatic repulsion. The $3d$ splits into two levels: (i) a doubly degenerate higher energy e_g state (d_{z^2} and $d_{x^2-y^2}$), the orbitals of which have on-axis nodes that can overlap with the ligand's p_x, p_y and p_z and are thus active in the bonding process, and (ii) a triply degenerate lower energy t_{2g} state (d_{xy}, d_{xz}, and d_{yz}). These states are not axially aligned and so cannot contribute to bonding. They are destabilized by the presence of the ligand lone pairs and are the most metallic in nature (i.e., the electrons that occupy them come primarily from the Fe(II) atomic states). Since the e_g bonding orbitals are closer in energy to the ligand lone pairs (which are generally lower in energy as they have less electrons), the e_g bonding state has a more ligand-like character, and the anti-bonding e_g^* is more metallic in character.

The relevant energy difference, called Δ_0 and shown in Fig. 8.1, lies between the most metal-like orbitals: the anti-bonding e_g^* and the t_{2g} states. This Δ_0 has two contributions: a spherical part, which homogeneously shifts all energy levels of the free ion, and an asymmetric contribution, which is applied unevenly to each crystal-field level. The competition that emerges here is between Hund's rules (preference for coexistence of like spins and subsequent maximization of subshell magnetization) and the energetic preference for the lower t_{2g} state. When Δ_0 is less than the energetic cost of electron pairing, we get the HS state; when Δ_0 is larger than the electron pairing energy, we get the LS state. It is the ligand field strength, a qualitative metric asserting how strong is the interatomic repulsion compared to the electron pairing energy, that contributes to rendering the magnitude of Δ_0.

When the ligand and Fe(II) atomic orbitals are closer in energy—inducing a stabilization of the t_{2g} due to the reinforcing π bonds—the ligand field is said to be strong. Δ_0 increases in magnitude. Rather than jumping to the higher energy level, the electrons find it energetically favorable to pair in the t_{2g} state, resulting in a LS ground state. Examples of ligand complexes with strong fields are CO^-, CN^- and NO_2.

By contrast, when the ligand field is weak, Δ_0 several orders of magnitude smaller than the electron pairing energy. The electrons are more likely to spread out, resulting in an overall HS state. Examples of ligand complexes with weak fields are OH^- and H_2O, which have lone pairs perpendicular to the metal-ligand bond axes. Alternatively, when the ligand field strength is comparable in magnitude to the electron pairing energy—as is the case for the intermediate field splitting ligand NH_3—even small external perturbations can engender a spin crossover.

8.2 Spin crossover

Spin crossover (SCO) is the phenomenon by which material systems may reversibly switch spin states from their low-spin (LS) to their high-spin (HS) configurations and vice versa. The switch may be stimulated by various environmental changes, including the presence of guest molecules, magnetic and electric fields, temperature, pressure, and light irradiation. SCO can be understood from a thermodynamic framework as the competition between enthalpy, which prefers the ground state of a material, and the entropy, which prefers maximally disordered systems. Systems will undergo several, dramatic physical and chemical changes upon SCO, which rendered the phenomenon rather visible by a variety of experimental techniques, so attempts at modeling its mechanisms began early.

Many of the early theories for SCO focused on justifying and replicating experimental behavior,

effects described best in macroscopic and thermodynamic terms. Thermodynamic properties of a SCO system are described using the Gibb's free energy (G) difference between the HS and LS states of a collection of N molecules in contact with thermal bath T, isobaric and isothermal:

$$\Delta G = \Delta H - T\Delta S\,, \tag{8.1}$$

where $\Delta H = H_{\mathrm{HS}} - H_{\mathrm{LS}}$ is the enthalpy variation and $\Delta S = S_{\mathrm{HS}} - S_{\mathrm{LS}}$ is the entropy variation. The equilibrium temperature $T_{1/2}$ is reached when half of the N molecules are in the LS state and the other half in the HS state, at which point ΔG is zero, and

$$T_{1/2} = \frac{\Delta H}{\Delta S}. \tag{8.2}$$

When considering the mixing entropy (i.e., the entropy arising from neither the HS molecules nor the LS molecules, but from the mixing of the two in complementary fractions in the system), the temperature changes to

$$T = \frac{\Delta H}{R\ln(\frac{1-n_{\mathrm{hs}}}{n_{\mathrm{hs}}}) + \Delta S}, \tag{8.3}$$

where R is the ideal gas constant, and n_{hs} is the fraction of molecules in the HS state. This precision is necessary to predict abrupt SCO changes, which is related to the emission or absorption of a latent heat produced and governed exclusively by the interactions of the SCO compounds.[31]

ΔH has primarily two contributions: an electronic part, which is not dependent on temperature, and a temperature-dependent vibrational part. In other words, $\Delta H = \Delta E_{\mathrm{HL}} + \Delta H_{\mathrm{vib}}$.[32] To compare magnitudes of these terms, the dominant ΔE_{HL} contributions for small compounds in Ref. [32] seem to be on the order of 1 kcal m^{-1}, while ΔS is on the order of 10^{-3} kcal m^{-1} K^{-1}, leaving T on the order of 10^2 K. The contributions to the entropy, by contrast, are four-fold:

$$\Delta S = \Delta S_{\mathrm{el}} + \Delta S_{\mathrm{vib}} + \Delta S_{\mathrm{trans}} + \Delta S_{\mathrm{rot}}, \tag{8.4}$$

corresponding, respectively, to the electronic, vibrational, translational, and rotational entropies. The vibrational term, ΔS_{vib} is, by far, the greatest contribution to the entropy, considering that ΔS_{el}, the electronic contribution arising from the change of spin multiplicity, is kept constant at 13.38 $\frac{J}{Kmol}$. Since the rotation and translation of the SCO compounds are not necessarily reliant on the spin state, their HS-LS differences are minor corrections to the entropy.[33]

The electronic entropy variation can be further decomposed into the orbital and spin contributions and arises from the difference of orbital (L) and spin (S) momenta degeneracy between the LS and HS states. Thus,

$$\Delta S_{\mathrm{el}} = R\ln(\frac{2 * L_{\mathrm{HS}} + 1}{2 * L_{\mathrm{LS}} + 1}) + R\ln(\frac{2 * S_{\mathrm{HS}} + 1}{2 * S_{\mathrm{LS}} + 1}). \tag{8.5}$$

The electronic entropy usually favors the HS state, but the vibrational entropy is usually the dominant contribution to the global entropy.[31]

As quantum theories of materials became more refined and significant technological advancements facilitated the manipulation of isolated molecules, it became necessary to describe SCO in terms of

what was happening at the chemical bond and molecular level. As described in Section 8.1, when Hund's rules manage to oust the electron pairing energy by way of external stimulus, a SCO occurs from LS to HS. The metal-ligand distances can increase by around 10% (0.2 Å), leading to an approximate 25% increase in volume, enough to notify IR and Raman spectroscopists (i.e., vibrational modes are larger in the LS state than in the HS by 10-90%).[31]

SCO materials have gained traction as candidates for storage and sensor devices and molecular spintronics. Designers of such devices are interested in various properties: the critical temperature $T_{1/2}$, light absorption, and interaction with other materials in proximity. Furthermore, engineers and materials scientists look to discover idealized SCO materials, for which the properties must be predicted entirely *ab initio*. For this reason, simulation software built on the quantum theory of materials are sought, DFT among them.[34]

Chapter 9

Breakdown of and potential remedies for DFT+U+J in SCO complexes

Enthalpy terms, chief among them the electronic ΔE_{HL}, are the dominant contributors to the critical SCO temperature $T_{1/2}$ (*vide supra*).[32] However, ΔE_{HL} is also one of the more challenging quantities to predict in approximate DFT. The semi-local XC functionals underestimate the exchange energy, thus overstabilizing the LS state of SCO complexes and rendering ΔE_{HL} too positively valued.[34] Hartree-Fock does the opposite, overstabilizing the HS state and rendering ΔE_{HL} too negatively valued. Modulating the amount of exact exchange in the XC functional can therefore achieve an accurate prediction, albeit at more computational expense.

Alternatively, DFT+U+J methods have demonstrated remarkable versatility in addressing the shortcomings of semi-local functionals, mainly with electronic structure and spectroscopic metrics such as band gaps, not necessarily in energetics. A steadily increasing body of DFT+U+J literature provides strategies to overcome the challenges pertaining to spin-related total-energy metrics through efficient navigation of parameter space.[35–37] The inclusion of the Hund's J, as a mitigator of the Hubbard U or as a penalizing term in its own right, is further untested territory here.

In a similarly designed study to that of Chapter 7, we dig into fully first-principles Hubbard-like DFT+U+J corrective protocol and its potential to achieve high-precision densities of state and adiabatic energy differences ΔE_{HL}. After describing the computational details in Section 9.1, we calculate and analyze trends of the *in situ* Hubbard U and Hund's J for all valence subspaces in a series of octahedrally-coordinated Fe(II) SCO molecules that span the ligand field strength spectrum. The geometries, chemical formulae, and reference ΔE_{HL} for each molecule are shown in Fig. 9.1.

For two of such molecules, we calculate all parameters near-identically across three open-source DFT programs (ABINIT, ONETEP, and QUANTUM ESPRESSO) to compare the potency of the basis set projector functions in available linear response methods. This analysis is undertaken in Section 9.2.1 and prompts a further statistical investigation into the effect of the projectors on the Hubbard U and Hund's J, a discussion undertaken in Section 9.2.2. After a brief description in Section 9.2.4 of the electronic structure properties obtained by various functionals, in Section 9.2.5, we methodically apply the ONETEP parameters (analyzed in Section 9.2.3) via a select range of both common and

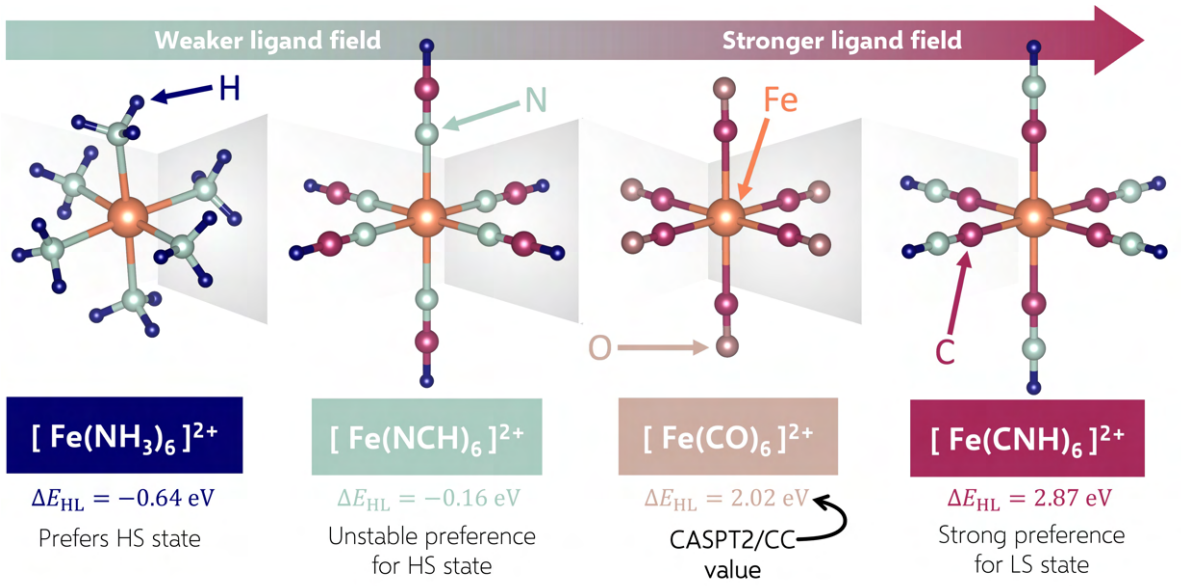

Figure 9.1: Geometries, chemical formulae, and reference CASPT2/CC ΔE_{HL} values for the featured series of fictitious molecules spanning the middle to upper range of the ligand field strength spectrum.

experimental Hubbards functionals in search of the simplest combination to yield reliable electronic structures and spin-state energetic properties. Conclusions from these discussions are then summarized in Section 9.3.

9.1 Computational details

We conduct our investigation on a series of four octahedrally coordinated Fe(II) complexes that span the ligand field strength spectrum (see Fig. 9.1): $[Fe(NH_3)_6]^{2+}$, $[Fe(NCH)_6]^{2+}$, $[Fe(CO)_6]^{2+}$ and $[Fe(CNH)_6]^{2+}$. We simulate separately each molecule in their $^1A_{1g}$ LS and $^5T_{2g}$ HS states, the geometries of each of which were determined using the TPSSh functional (more details on this calculation in the SI of Ref. [35]). As a benchmark method for calculating adiabatic energy differences, we use the coupled cluster-corrected CASPT2 (CASPT2/CC) ΔE_{HL} values from Refs. [35] and [36], which follow Refs. [38–40] in successful employing the method to remove CASPT2's well-known bias towards the HS states.

All calculations (linear response and Hubbard functional) are spin polarized and the total charge of the system set to +2. The spin state of the Fe^{2+} ion is encouraged by setting iron's starting magnetization to +4 (HS) or 0 (LS). We use the Perdew-Burke-Ernzerhof (PBE) GGA[41] XC functional. When PAW datasets are required, we use Jollet-Torrent-Holzwarth (JTH) PBE PAW pseudopotentials (Version 1.0)[42] generated via *atompaw*.[43] Derived from those pseudopotentials, the PAW augmentation sphere cutoff radius r_c used is 1.51 a_0 for C 2*p*, 2.01 a_0 for Fe 3*d*, 0.99 a_0 for H 1*s*, 1.20 a_0 for N 2*p*, and 1.41 a_0 for O 2*p*.

DFT+U+J functional calculations are, due to the sensibility of the parameters (discussed in Section 9.2.1), performed with the Order N Electronic Total Energy Package (ONETEP)[44] using PBE

and the PAW method[45] to describe the XC functional. Each complex is placed at the center of a cubic vacuum of side-length 75.59 a_0 (40 Å). For ease of comparison with prior investigations,[35] a psinc basis set (see Section 3.26) is selected to resemble a plane-wave basis set with a cutoff kinetic energy of 40 Ha and a fine-grid energy cutoff of 160 Ha. We encourage convergence by enabling Ensemble DFT with 0K smearing. The central Fe atom is described with a total of 26 non-generalized Wannier functions (NGWFs) limited to a radius of 14 a_0; all *p*-block elements (i.e., N, C, O) are allotted eight NGWFs limited to a radius of 12 a_0, and H receives two NGWFs extending maximally to 10 a_0. The NGWFs were initialized in split-norm pairs (see Section 3.2.5), not least in order to afford more variational freedom in such spin-polarized systems. Total energies are converged to within 2.7211×10^{-5} eV (1.0×10^{-6} Ha). To correct for spurious electrostatic interactions between periodic images of the molecules, we use the Martyna-Tuckerman (MT)[46] minimum image convention (MIC) with cutoff of 7.0 a_0 following the suggestions of Hine *et al.*[47]

9.1.1 Linear response calculations

The Hubbard U and Hund's J for $[Fe(NCH)_6]^{2+}$ and $[Fe(CO)_6]^{2+}$ are determined via linear response across three technical platforms, the details of which are outlined below. Example input files for each are included in Appendix C2. Each complex is placed at the center of a cubic vacuum of side-length 37.79 a_0 (20 Å). The total energy is relaxed self-consistently to within a threshold tolerance of 2.7211×10^{-8} eV (1×10^{-9} Ha). To evaluate projector effects, we compare the use of GBRV ultrasoft pseudopotentials[48] versus JTH PAW datasets[42] in QUANTUM ESPRESSO and ONETEP.

- ABINIT: The plane-wave kinetic energy cutoff is set to 40 Ha. Only the gamma *k*-point is sampled. As the DFT+U+J protocol are built into the PAW implementation, we use a fine-grid energy cutoff of 160 Ha on each PAW augmentation sphere and `dmatpuopt = 3`, corresponding to once-normalized projections onto bound state atomic orbitals as the projector functions (see Section 7.2.1 for related discussion). Six evenly-spaced linear response perturbations (SCF method; see Section 4.1) ranging from -0.15 to 0.15 eV were applied and used alongside the zero-perturbation data point to calculate the Hubbard parameters with the `lrUJ` utility (see Chapter 5).

- ONETEP: All runtime parameters are the same as those used for functional calculations described above, except the cell size is set to 37.79 a_0. Four evenly-spaced linear response perturbations (minimum-tracking method; see Section 4.2) ranging from -0.10 to 0.10 eV were applied to calculate the Hubbard parameters. The zero perturbation was also considered in the regression. Due to formatting limitations, the GBRV pseudopotentials fed into ONETEP are also PAW datasets. In order to include the response of the HXC contribution of the PAW effective potential, $V^{\sigma}_{\mathrm{PAW}}$ have been added to $V^{\sigma}_{\mathrm{hxc}}$ in the minimum-tracking definitions of U and J, shown in Eq. 4.29.

- QUANTUM ESPRESSO: The plane-wave algorithm (pw.x) is used with kinetic energy and density cutoffs of 40 Ha and 400 Ha, respectively. Only the gamma *k*-point is sampled. The Makov-Payne correction to the total energy is used to compensate for spurious electrostatic interactions

between periodic images of the molecules.[49] The use of GBRV ultrasoft pseudopotentials versus the JTH PAW datasets are compared in Section 9.2.1. The use of atomic projectors versus orthogonalized atomic projectors for the population analysis of the Hubbard manifold for these molecules is also investigated in Section 9.2.2. Eight evenly-spaced linear response perturbations (SCF method; see Section 4.1) ranging from -0.10 to 0.10 eV were applied and used alongside the zero-perturbation data point to calculate each Hubbard parameter for d and p-block valence subspaces (for the H s subspace, the perturbations ranged from -0.05 to 0.05 eV).

Polynomial regressions and their errors up to degree-three (cubic) regressions were calculated for all response datasets. Most subspace responses were very well-behaved, and either quadratic or cubic regressions were chosen to represent responses depending on the unbiased root mean squared errors (RMSE) associated with the fit, calculated as in Eq. (4.31).

9.2 Results and discussion

9.2.1 Hubbard parameters across three programs

Despite the similarities in implementation and theory, ABINIT, QUANTUM ESPRESSO, and ONETEP yield unusually different LR Hubbard parameters for similar systems, in this case, the moderate and strong field ligand molecules $[Fe(NCH)_6]^{2+}$ (Table 9.1) and $[Fe(CO)_6]^{2+}$ (Table 9.2), respectively. Classic box-and-whisker plots are used to visualize the distribution of the parameters. For almost all subspaces outside the central Fe^{2+} $3d$, ABINIT finds the largest parameter by far, whereas ONETEP typically predicts the lowest.

The minor discrepancies between ONETEP parameters calculated with JTH versus GBRV PAW datasets can be attributed to different mesh densities, PAW cutoff radii—the GBRV sets typically have smaller PAW cutoff radii—shape functions, and other dataset generation minutiae. The pseudopotential dependence in ONETEP is almost nil compared to that in QUANTUM ESPRESSO, whose values vary widest for the N $2p$ subspaces in $[Fe(NCH)_6]^{2+}$ and the Fe $3d$ subspaces in both molecules tested. The N $2p$ parameters seem to be most sensitive to the type of projector used, APs yielding a U ∼2.5-3 eV larger (and a J just shy of 1 eV larger) than their orthogonalized counterparts. Moreover, the OAPs augment the sensitivity to the use of a PAW dataset, but only for the Hubbard U (the Hund's J is similarly sensitive to the PAW method across both projector types). This fits into the broader trend for ligand $2p$ subspaces (the use of the word ligand here refers to the atom immediately neighboring the iron ion), where, across both molecules, the sensitivity of the U to the PAW method more than doubles when OAPs are used as opposed to APs. Both the OAPs and the PAW augmentation sphere have the effect of reducing the amount of charge nominally counted in the Hubbard manifold. More discussion on the use of APs versus OAPs can be found in Section 9.2.2.

For the Fe $3d$ subspaces, we find that across both molecules and both spin states, a higher QUANTUM ESPRESSO U is correlated with a lower screened response χ. This remains true even if we vary the projector and pseudopotential, although the GBRV pseudopotentials generally correspond to larger values of χ and thus larger values of Fe $3d$ U. In the HS case specifically, the QUANTUM ESPRESSO U is also anti-correlated with the number of spin-down electrons in the PBE ground state;

the more spin-down electrons, the smaller the magnetization, both of which coincide with a lower U. Simultaneously, however, the ground-state 3*d* occupancies become less integer, which may have the indirect effect of prompting a lower corrective coefficient. This is not the case for the LS states, where there are no consistent, noticeable trends in the occupancy distribution that would have a bearing on the values of the Hubbard parameters. In LS $[Fe(NCH)_6]^{2+}$, the t_{2g} orbitals experience a noticeable increase in occupancy correlated with a decreasing value of U.

Parameters for subspaces beyond the iron center and its immediate neighbor are similar in magnitude regardless of the molecule's spin state, meaning the time-pressed investigator need only calculate a {U, J} pair for one such spin configuration for each subspace. The technical platforms tend to agree better (in some cases, only marginally) on the parameters for LS, especially for Fe 3*d*, indicating that linear response is better suited to non-spin-polarized and/or non-magnetic systems.

The C 2*p* parameters do not change as much with respect to coordination environment, indicating that the Hubbard parameters are, in these molecular cases, more sensitive to intra-atomic interactions and coordinations as opposed to inter-atomic ones. We do observe fairly dramatic differences between LS Fe 3*d* Hubbard U across the two molecules; notably, the QUANTUM ESPRESSO U calculated with PAW atomic projectors is 2.9 eV greater in $[Fe(CO)_6]^{2+}$ than in $[Fe(NCH)_6]^{2+}$, conveying an acute sensitivity of SIE in that subspace to ligand field strength. Curiously, that sensitivity is not shared by the HS state of the same molecules. SIE is perhaps exacerbated somehow by the presence of electrons with anti-aligned spins in the same orbital or energetic degeneracies.

There is substantial disagreement on even what order of magnitude the H 1*s* Hubbard parameters should adopt; the U ranges anywhere from 0.65 eV to over 14 eV depending on the platform and LR methodology used. We don't observe as many fluctuations in QUANTUM ESPRESSO numbers as for other atoms; QUANTUM ESPRESSO is capable of appropriately treating the PAW augmentation sphere in full without approximation. In ABINIT, only 30% of the AE H 1*s* orbital lies within the PAW augmentation sphere, and the projectors severely underestimate the total charge attributable to hydrogen's 1*s* orbital. One could cursorily deduce that lower occupancies induce a rigidity in the response and thus inflated parameters. However, both ABINIT and the QUANTUM ESPRESSO ortho-atomic projectors predict the H 1*s* orbital to hold close to half an electron (0.48 e^- and 0.70 e^-, respectively), whereas QUANTUM ESPRESSO atomic projectors and ONETEP both assert the occupancy to be just over 1.5 electrons. Despite this, QUANTUM ESPRESSO finds similar Hubbard parameters regardless of the projector used, and ONETEP and ABINIT predict opposingly extreme values. Thus, the rigidity of the response, and therefore the magnitude of the Hubbard parameter, is not entirely related to the number of electrons occupying the subspace. Nevertheless, while the `dmatpuopt = 3` option renormalizes once for the localized augmentation sphere, it appears at first glance that the twice renormalized `dmatpuopt = 4` option would result in less extremized parameters. (Recall from Section 4.3.2 that this projector function renormalizes both the bound atomic orbital and the KS orbital onto which it is projected). In fact, when we apply the `dmatpuopt = 4` projector to all subspaces, most ABINIT parameters (with the exception of the HS Fe 3*d* J) deflate to QUANTUM ESPRESSO levels.

It is precisely the exception to the trend, the Hund's J for HS Fe 3*d*, that is cause for the most scrutiny. Hubbard projectors are known to inflate or deflate parameter values but not reverse the

corrective curvature. The phenomenon is not, per se, illicit. It emerges when the unscreened response χ_{0_M} is smaller in magnitude than the screened response χ_M (i.e., the unscreened system responds less enthusiastically to perturbation than the screened system). The necessity for the unscreened response arises when considering the effects of varying the site occupancy unrelated to the system's linear change in energy, for example, modifications to the radial extent of the Fe atom's $4s$ and $3p$ orbitals as a result of changing the $3d$ occupancy, or the rehybridization of the localized subspace with bath degrees of freedom.[50,51] It is assumed that the curvature of these unrelated effects are well described

$[Fe(NCH)_6]^{2+}$			QUANTUM ESPRESSO APs (eV)		QUANTUM ESPRESSO OAPs (eV)		ABINIT (eV)	ONETEP (eV)	
HP	at	ss	GBRV	JTH	GBRV	JTH	JTH	GBRV	JTH
U	Fe	HS	6.83	2.32	8.72	4.06	6.65	5.70	5.34
		LS	8.16	5.09	9.03	6.15	7.69	6.42	6.27
	N	HS	11.24	10.91	8.63	7.37	14.59	3.99	3.98
		LS	10.01	10.00	7.77	6.78	14.24	4.36	4.34
	C	HS	6.99	6.30	6.58	5.48	10.66	2.29	2.29
		LS	6.84	6.82	6.17	5.80	10.77	2.61	2.61
	H	HS	5.78	5.62	5.88	5.38	14.16	0.67	0.65
		LS	5.61	5.58	5.77	5.45	14.50	0.86	0.85
J	Fe	HS	-0.89	-1.72	-0.58	-1.49	0.005	0.51	0.51
		LS	0.72	0.75	0.70	0.70	0.65	0.51	0.51
	N	HS	2.71	2.49	1.86	1.70	3.81	0.73	0.72
		LS	2.73	2.51	1.83	1.68	3.76	0.76	0.76
	C	HS	1.94	1.84	1.77	1.65	3.24	0.61	0.60
		LS	1.91	1.79	1.67	1.55	3.20	0.61	0.60
	H	HS	4.56	4.54	4.42	4.47	11.63	1.78	1.81
		LS	4.66	4.61	4.51	4.58	11.71	1.77	1.79

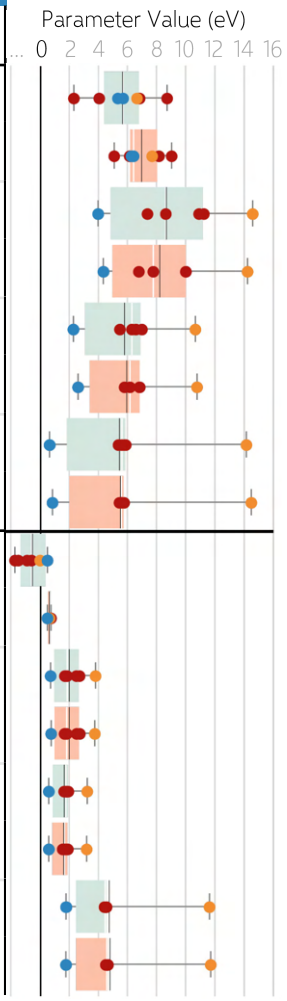

Table 9.1: Hubbard parameters (eV) for all valence subspaces in HS/LS $[Fe(NCH)_6]^{2+}$, calculated via LR similarly in QUANTUM ESPRESSO (SCF), ABINIT (SCF), and ONETEP (minimum-tracking). Either PBE GBRV[48] or JTH PAW[42] pseudopotential sets used, which alter the projectors (either APs or OAPs in QUANTUM ESPRESSO, normalized projections on bound atomic states for ABINIT, and in-house atomic for ONETEP). PAW datasets are underlined. Classic box-and-whisker plots show mean (black vertical line), median (white vertical line), range between the lower and upper quartile (shaded box), and extrema of the parameter distribution, onto which are superimposed the data points (marker color corresponding to code used; red for QUANTUM ESPRESSO, blue for ONETEP , or orange for ABINIT).

by a system of non-interacting electrons with KS band structure. As far as we are aware, this concept has never been tested systematically in the literature and may provide a numerical justification for the observed incongruencies of linear response methodologies.

Consider, however, an approximative DFT energy landscape with multiple, perhaps shallow or clustered local maxima corresponding to (approximately degenerate) magnetic configurations. The ground-state configuration of the DFA system in question could lie on a local minimum between two such maxima. Linear response perturbations from that well would thus elicit magnetic responses contouring a convexity, registering a negatively valued Hund's J. Such system pathologies could require a Hubbard-like corrective functional encouraging spin pairing to effectively compress the peak and neutralize the erroneous concavity.

Response definitions aside, a negative Hund's J—a measure of the local curvature of the subspace energy with respect to subspace magnetization—indicates that the approximate functional is net over-interacting with respect to $\boldsymbol{M}$ in the subspace. (Semi-)Local XC functionals tend to over-delocalize the subspace magnetization, breaking the constancy condition with respect to subspace magnetization by introducing erroneous concavity, wherein the energetically preferred coordination is that which maximally magnetizes the subspace. In the Himmetoglu DFT+U+J corrective functional, then, a positive

$[Fe(CO)_6]^{2+}$			QUANTUM ESPRESSO				ABINIT	ONETEP	
			Atomic (eV)		Ortho (eV)		(eV)	(eV)	
HP	at	ss	GBRV	JTH	GBRV	JTH	JTH	GBRV	JTH
U	Fe	HS	6.74	2.42	8.07	4.30	6.73	5.19	5.16
		LS	9.46	7.99	9.22	7.81	7.67	7.50	7.61
	C	HS	6.38	6.59	7.26	6.86	11.88	1.53	1.55
		LS	5.17	5.23	5.89	5.57	10.88	1.98	1.97
	O	HS	13.65	13.63	8.37	8.29	13.62	6.78	6.64
		LS	13.59	13.50	8.42	8.08	13.61	6.78	6.78
J	Fe	HS	-0.74	-2.00	-0.42	-1.31	0.08	0.55	0.56
		LS	0.79	1.05	0.71	0.78	0.68	0.55	0.55
	C	HS	1.61	1.52	1.70	1.56	3.23	0.57	0.56
		LS	1.64	1.53	1.65	1.51	3.08	0.63	0.61
	O	HS	3.23	2.99	1.95	1.82	2.48	0.85	0.85
		LS	3.11	2.90	1.84	1.72	2.39	0.85	0.85

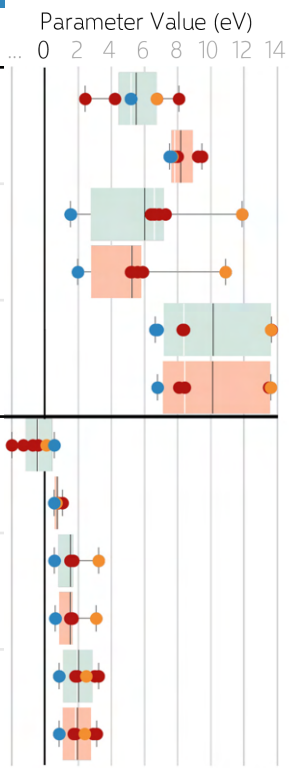

Table 9.2: Hubbard parameters (eV) *for all valence subspaces in HS/LS* $[Fe(CO)_6]^{2+}$*, calculated via LR similarly in* QUANTUM *ESPRESSO (SCF),* ABINIT *(SCF), and* ONETEP *(minimum-tracking). For further details, see caption for Table 9.1.*

J, which scales the (positively valued) term penalizing anti-aligned spins, is expected to exacerbate the constancy condition. There is emerging literature suggesting that a negative J term may actually benefit system energetics. In order to neutralize the concavity, we'd need a negatively valued J preceding a penalty that maximally penalizes equal occupancies of anti-aligned spins ($^1/_2$ spin up and $^1/_2$ spin down). A modern addition to the family of Hubbard functionals, BLOR (see Appendix A4), has demonstrated success at correcting total energies, which the authors attributed to the fact that the term addressing SCE (scaled by J) is negative and therefore cancels the added effect of the SIE terms. Most other corrective functionals do not have this feature as the corrective SCE term is positive in value, abetted by a positive Hund's J. This framework leads to the assertion that if one were to make the value of J negative in employing the Himmetoglu DFT+U+J functional, thereby reversing the effect of the minority spin and SCE terms, a similar cancellation of errors would occur and something closer to the exact corrective energy recovered.[52]

It's not obvious which platform, if any, yields the most reliable set of parameters. It's evident enough that pathologies particular to these molecular systems have exposed a breakdown in the presumed equivalence of our linear response methodologies. The SCF and minimum-tracking LR methods have hitherto produced congruent *in situ* parameters across a variety of subspaces belonging to a variety of molecular and solid systems, technical discrepancies notwithstanding. The data in Tables 9.1 and 9.2 have, at the very least, revealed a need to revisit the formalisms of these methodologies and the assumptions on which they are built. The reasonability of the ONETEP parameters, particularly the positively valued Fe 3*d* J and the relative independence with respect to pseudopotential choice, provides a suitable basis on which to build the rest of our investigation. For Section 9.2.3, we calculate *in situ* and analyze trends among ONETEP Hubbard parameters across all four Fe(II) octahedrally coordinated molecules.

9.2.2 Statistical assessment of all LR conducted on these systems

We use these additional Hubbard parameters—as well as another dataset of QUANTUM ESPRESSO atomic and ortho-atomic parameters for two further molecules in their HS and LS states, $[Fe(NH_3)_6]^{2+}$ and $[Fe(CNH)_6]^{2+}$, also with state-dependent geometries, generated in the backend of this investigation—to engage in a brief but stimulating statistical analysis across the different projectors. We seek to understand, via statistical means, how (i) the response functions behave with respect to changes in ground-state occupancy, diversely quantified, and (ii) the Hubbard parameters behave with respect to changes in their constituent response functions. In total, we analyzed 140 Hubbard U-Hund's J parameter pairs calculated across ABINIT, ONETEP, and QUANTUM ESPRESSO, which, when divvied up according to molecule, subspace, and spin state, yield sub-datasets of either three HP pairs (for $[Fe(NH_3)_6]^{2+}$ and $[Fe(CNH)_6]^{2+}$) or seven (for $[Fe(CO)_6]^{2+}$ and $[Fe(NCH)_6]^{2+}$) spanning a range of projectors.

A variety of ground-state occupancy metrics prove useful for these queries: the total subspace occupancy $N = N^{\uparrow} + N^{\downarrow}$, the total magnetization $M = N^{\uparrow} - N^{\downarrow}$, the summation term

$$\Sigma = \sum_{\sigma}^{\uparrow,\downarrow} \sum_{m} n_{mm}^{\sigma} - (n_{mm}^{\sigma})^2, \tag{9.1}$$

—a metric that, when averaged across m and σ as $\bar{\Sigma} = \Sigma/(2(2\ell + 1))$, effectively describes how integer-like are the subspace occupancies (i.e., the larger the $\bar{\Sigma}$, the less integer are the occupancies for the $m = m_\ell = \{-\ell, -\ell - 1, ...0, ..., \ell - 1, \ell\}$ orbitals). When scaled by U/2, Σ is also the penalty term in many Hubbard energy functionals. Analogously, we look at the spin product term

$$\Pi = \sum_{\sigma}^{\uparrow,\downarrow} \sum_{m} n^{\sigma}_{mm} n^{\bar{\sigma}}_{mm} \tag{9.2}$$

—a metric effectively describing how similar are the spin-resolved subspace occupancies to eachother on average (i.e., the larger the $\bar{\Pi} = \Pi/(2(2\ell + 1))$, the closer $n^{\uparrow} - n^{\downarrow}$ is to zero, and the larger the occupancies are); here, $\bar{\sigma}$ is the opposite spin to σ). When scaled by J, Π is the spin-pairing penalty applied via the Himmetoglu functional (see Section 2.5.3).

The response behavior can also be characterized by various quantifiers outside of its screened and unscreened, magnetic or non-magnetic varieties. Of course, the steepness of the response functions relative to the horizontal axis—a property we dub "rigidity" for convenience (i.e., the smaller the magnitude of χ or χ_0, the more rigid its response is)—plays an important role in determining the value of the HP. Typically, subspaces that rigidly transact with the surrounding electron bath correspond to larger HPs; alternatively, subspaces that more flexibly accept electrons from or donate electrons to the surrounding bath correspond to smaller HPs. But the difference between the unscreened and screened response functions plays an equally important role in the value of the HP; the larger the difference, the larger the HP, typically. How much larger depends on the response rigidity. If the subspace only rigidly transacts with the surrounding electron bath, then one can obtain a large U value with only slight differences between the interacting and non-interacting response functions. Alternatively, if the subspace is flexible in accepting electrons from or donating electrons to the surrounding bath, the non-interacting response function must adopt a value several times larger than its interacting counterpart in order to achieve a large value of U. Concisely, the more rigid the response, the more important $\chi - \chi_0$ ($\chi_M - \chi_{0_M}$) becomes in determining the magnitude of U (J).

There are limitations to a statistical analysis in this arena. HPs and their building blocks are metrics of XC functional-, subspace-, even platform- and projector-specific pathologies, and as such they should be compared apprehensively. At the same time, it is important to try to understand the nature of SIE and SCE in terms of properties intrinsic to any subspace, for any XC functional, program, or projector. The following analyses use statistical tools to better identify these global variables. Treating the projectors on equal footing, as effectuators of change in subspace population, can yield more generalizable insight into how response changes as a function of occupancy and, more broadly, how the Hubbard parameters effectively measure the erroneous nature of the DFA in localized subspaces.

For brevity, we refer to the various projectors tested with the following indices: ABINIT with JTH PAW datasets = A; AP with JTH PAW datasets = aj; AP with GBRV pseudopotentials = ag; OAP with JTH PAW datasets = oj; OAP with GBRV pseudopotentials = og; ONETEP with JTH PAW datasets = 1j; ONETEP with GBRV pseudopotentials = 1g.

How occupancy metrics influence response

In our dataset, the projector influences the population of the Hubbard manifold in a very clear-cut fashion. For the $2p$ and $1s$ subspaces, the projectors adopt values of N in this order: $N_{\mathrm{A}} < N_{\mathrm{og}}$ or N_{oj} (ordering varies) $< N_{\mathrm{ag}}$, N_{aj}, $N_{1\mathrm{g}}$, or $N_{1\mathrm{j}}$ (ordering varies). For the Fe $3d$ subspaces, $N_{\mathrm{A}} < N_{\mathrm{og}}$ $< N_{\mathrm{ag}}$ or N_{oj} (ordering varies) $< N_{1\mathrm{g}}$ or $N_{1\mathrm{j}}$ (ordering varies) $< N_{\mathrm{aj}}$. The ordering of projectors with respect to N does not translate to $\bar{\Sigma}$; higher occupancies only translate to higher fractionalization when subspace occupancies are, on average, less than half full.

The rigidity of the subspace response—in other words, the willingness of a subspace to transact with the surrounding electron bath—is a property that has been said to correlate with common chemical properties such as electronegativity[53] and more recently, in the context of linear response HPs, chemical hardness.[54] Under identical screening conditions, subspaces that rigidly transact with the surrounding electron bath, demonstrating chemical hardness, correspond to larger HPs; alternatively, subspaces that more flexibly accept electrons from or donate electrons to the surrounding bath, demonstrating chemical softness, correspond to smaller HPs. Generally speaking, electronegativity increases and chemical hardness decreases as one moves to the right of the periodic table. It is tempting to conjecture, then, that subspaces with smaller ground-state valence occupancies would respond more rigidly to perturbation.

Our dataset vaguely demonstrates this trend as an atomic phenomenon. In Fig. 9.2, the H $1s$ subspaces, with their small occupancies, have the most rigid responses on average, and the heavily occupied Fe $3d$ subspaces tend toward the more flexible response. But the other subspaces range widely in their response rigidity and total occupancies. What's clear is that the aforementioned subspace-specific N ordering does not bear exclusive influence over the rigidity of the response functions. For example, in LS $[Fe(CO)_6]^{2+}$, the ABINIT projector in the Fe $3d$ subspace yields the most flexible (lowest) χ but the most rigid (highest) χ for C and O $2p$, despite the fact that the ABINIT projector in all three cases delivers the lowest N for each subspace. As outlined in Table 9.2, this translates to maximal U and J values for the $2p$ subspaces but some of the lower U and J values for $3d$ among the projectors tested. Concisely, there is no concrete correlation between the total occupancy of the

Figure 9.2: Screened response χ versus total occupancy N of all Fe(II) *LR data across* ABINIT, ONETEP, *and* QUANTUM ESPRESSO. *Point color (orange for* Fe $3d$, *pink for* C $2p$, *green for* N $2p$, *brown for* O $2p$, *and blue for* H $1s$*) indicates the atomic subspace for which* U *was calculated. The pseudopotential used for each LR calculation is indicated by the shape of the point marker (circle for JTH PAW and diamond for GBRV).*

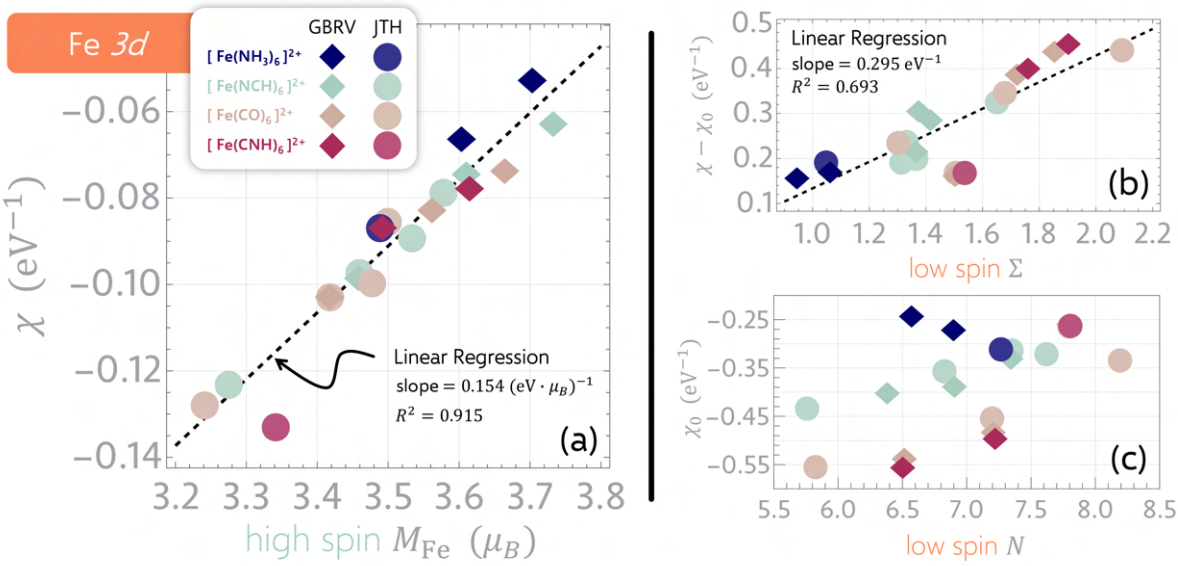

Figure 9.3: Notable trends in the change of various response quantifiers with respect to changes in various occupancy metrics for the Fe 3*d subspace across all* Fe(II) *complexes (blue for* $[Fe(NH_3)_6]^{2+}$*, green for* $[Fe(NCH)_6]^{2+}$*, light brown for* $[Fe(CO)_6]^{2+}$*, and pink for* $[Fe(CNH)_6]^{2+}$*), calculated across* ABINIT, ONETEP, *and* QUANTUM ESPRESSO. *The figures show (a) screened response* χ *as a function of magnetic moment on HS-coordinated complexes; (b)* $\chi - \chi_0$ *difference as a function of summation term* Σ *(Eq. (9.1)) for all complexes in the LS state; (c) unscreened response* χ_0 *as a function of total* 3*d subspace occupancy* N *for all complexes in the LS state. The pseudopotential used for each LR calculation is indicated by the shape of the point marker (circle for JTH PAW and diamond for GBRV).*

subspace and its (screened or unscreened) response values. The projectors are influencing more than simply the total charge counted. There may be some emphasis, for example, on what charge is counted, be it interstitial or ionic. Although it's difficult to quantify precisely, we can intuit that the shape of the projector functions influences what type of charge is counted in the Hubbard manifold. Furthermore, the projectors hold sway over the level of screening to which each subspace is subjected, a property which can be understood, to some degree, as the willingness of the electron bath to transact with the Hubbard manifold.

The response functions of the Fe 3*d* subspace often display trends that responses for other subspaces do not follow. This makes sense in some cases; as the Fe 3*d* is the only orbital with clearly non-zero magnetic moment (see Fig. 9.3(a)), it demonstrates a (comparatively crisp) linear relation between χ and increasing HS magnetic moment. In the absence of any strong trend in the difference between χ and χ_0 as a function of M_{Fe}—as is the case here—we expect a more rigid screened response to raise the value of U, which is precisely what we observe on the ligand field strength spectrum. The weaker ligand field complexes tend to have larger magnetic moments (see Fig. 9.9)—manifested primarily by a lower $N^{\downarrow}$, since $N^{\uparrow}$ hovers around 5 e^{-}—but smaller U parameters (see Table 9.3). It is worth noting that the opposite correlation was observed for the NiO HPs (see Table 7.3 and Figs. 7.1(a) and (b) in Chapter 7), where FM NiO had the largest HPs despite harboring the largest magnetic moments on both Ni and O.

Given their characteristic lack of any magnetic moment on Fe, the LS states of the molecules

cannot claim the same justification despite a similar tendency: lower U with respect to weaker ligand field. Instead, certain response quantifiers of the Fe 3*d* orbitals on the LS state complexes demonstrate some sensitivity to two other occupancy metrics: N and Σ. An increase in the former sees to a subtle monotonic change in the rigidity of the unscreened response function χ_0 (albeit at different rates for different LS complexes; see Fig. 9.3(c)), whereas an increase in the latter corresponds loosely to an increase in $\chi - \chi_0$ (Fig. 9.3(b)). The bonds between the Fe and the ligand have more covalent character in stronger ligand fields, resulting in more fractional (but overall larger) occupancies as the electrons are shared. These characteristics lead to a more rigid response and (although it's not clear why) a larger screening effect, both of which result in larger U values. Which of these properties—the response rigidity or screening magnitude—carries more importance in this subspace, however, is highlighted by the weak field ligand complex $[Fe(NH_3)_6]^{2+}$. In Fig. 9.3(c), $[Fe(NH_3)_6]^{2+}$ shows the opposite trend; the Fe 3*d* response becomes less rigid with increasing N, indicating that its overall smaller occupancies would instead have the effect of increasing U. Since this is not the case (i.e., $[Fe(NH_3)_6]^{2+}$ still has the smallest Fe 3*d* U of all complexes tested), it seems that the difference between χ and χ_0 carries more weight in determining the value of the U for this subspace.

There emerges a sense, especially in the LS state, that across all subspaces, the value of χ_0 is correlated with the integerness of the m_ℓ-resolved occupancies. That is, χ_0 (as well as the difference between χ and χ_0) increases in magnitude as the subspaces become less integer. Interestingly, the magnetic response functions are also sensitive to $\bar{\Sigma}$. In Fig. 9.4(b), we observe χ_M and χ_{0_M} locked in step; raising one typically raises the other, which in conjunction with Fig. 9.4(a) indicates that both the

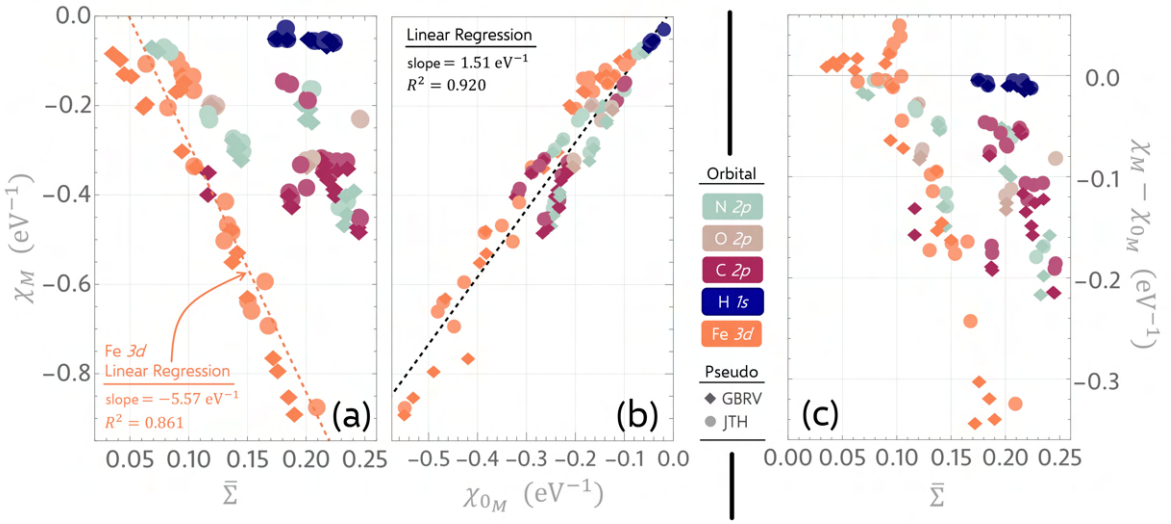

Figure 9.4: Potent trends in the magnetic response functions for J *among all subspaces for all* Fe(II) *complexes, calculated across* ABINIT, ONETEP, *and* QUANTUM ESPRESSO*; (a) the screened magnetic response χ_M as a function of average summation term $\bar{\Sigma}$, with a linear regression (orange dashed line) performed on the* Fe 3*d data only; (b) χ_M as a function of unscreened magnetic response χ_{0_M} with linear regression (black dashed line) performed on all data; (c) the difference between the two responses as a function of $\bar{\Sigma}$. Point color (orange for* Fe 3*d, pink for* C 2*p, green for* N 2*p, brown for* O 2*p, and blue for* H 1*s) indicates the atomic subspace for which* J *was calculated. The pseudopotential used for each LR calculation is indicated by the shape of the point marker (circle for JTH PAW and diamond for GBRV).*

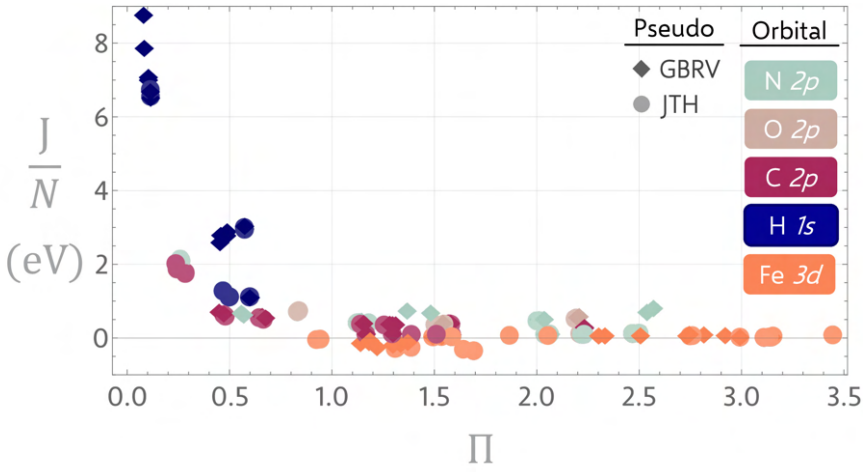

Figure 9.5: The Hund's J *correction per electron plotted against the spin-product term* Π *(non-averaged). Point color (orange for* Fe 3*d, pink for* C 2*p, green for* N 2*p, brown for* O 2*p, and blue for* H 1*s) indicates the atomic subspace for which* U *was calculated. The pseudopotential used for each LR calculation, calculated across* ABINIT, ONETEP, *and* QUANTUM ESPRESSO*, is indicated by the shape of the point marker (circle for JTH PAW and diamond for GBRV).*

screened and unscreened magnetic response functions are likely to become less rigid as the subspaces become, on average, less integer. This will tend to increase the value of J, as will the trend in Fig. 9.4(c), where more fractional subspaces (like those of the strong ligand field complexes) correspond to larger $\chi_M - \chi_{0_M}$ differences. Indeed, this is exactly what we observe in Table 9.3.

In the analogy, however, if the response metrics of χ and/or χ_0 are related somehow to the summation term Σ, then the magnetic response metrics of χ_M and/or χ_{0_M} should be responsive in some fashion to Π. Some cryptic pattern emerges as J itself is plotted against Π—a series of concentric lines emanating from an unclear origin. However, when we divide a subspace's J by its total occupancy N, as in Fig. 9.5, a clearer relation appears. The Hund's J correction per electron in the subspace seems strongly and exponentially anti-correlated with the (non-averaged) spin-product term Π. When a regression of the form $\frac{\mathrm{J}}{N} = a + \frac{b}{\Pi + c}$ is performed, the resulting best fit ascertains an adjusted R^2 value of 0.97, although there's no hint at the physical meaning of the constants $a = 0.417$, $b = 0.119$, or $c = -0.040$. There are exceptions to the trend; the H 1s values predicted by QUANTUM ESPRESSO atomic projectors noticeably jut out around $\frac{\mathrm{J}}{N} = 3.0$ eV and $\Pi = 0.5$, and the negatively valued Fe 3d J diverge from the decay pattern for Π between 1.0 and 2.0. While the source of or reasoning behind the pattern is unknown, it seems to suggest that less spin-polarized subspaces, where $n^{\uparrow}$ is similar in magnitude to $n^{\downarrow}$, require less correction per electron. The differences between the J in the HS and LS states for each subspace in Table 9.3 do not necessarily corroborate this assertion.

How response metrics influence the Hubbard parameters

The effect of the projector on the value of U may be evaluated by looking at its response components, which carry different signatures under variation. Across all projectors, molecules, codes, and subspaces, the screened response χ carries a significantly smaller standard deviation than the unscreened

response χ_0 (defined differently for minimum-tracking LR versus SCF). Suppose this relative agreement on χ across platforms allows us to make the assumption that χ is known and relatively constant. It follows from Eq. (4.10) that U as a function of χ_0 will follow a particular pattern, demonstrating logarithmic decay with respect to increasing (less negative) χ_0, the curvature of which swings upwards, approaching verticality as the magnitude of χ approaches a very small $|\chi_0| << 0$ before disappearing entirely into the asymptote at $\chi = 0$. This pattern is demonstrated in Fig. 9.6, which plots the LR Hubbard U versus the unscreened response χ_0 superimposed on graphs of $U(\chi_0,\chi)$ with constant χ taking on various values corresponding to statistical metrics taken across all projector/platform/pesudopotential data available in each subspace.

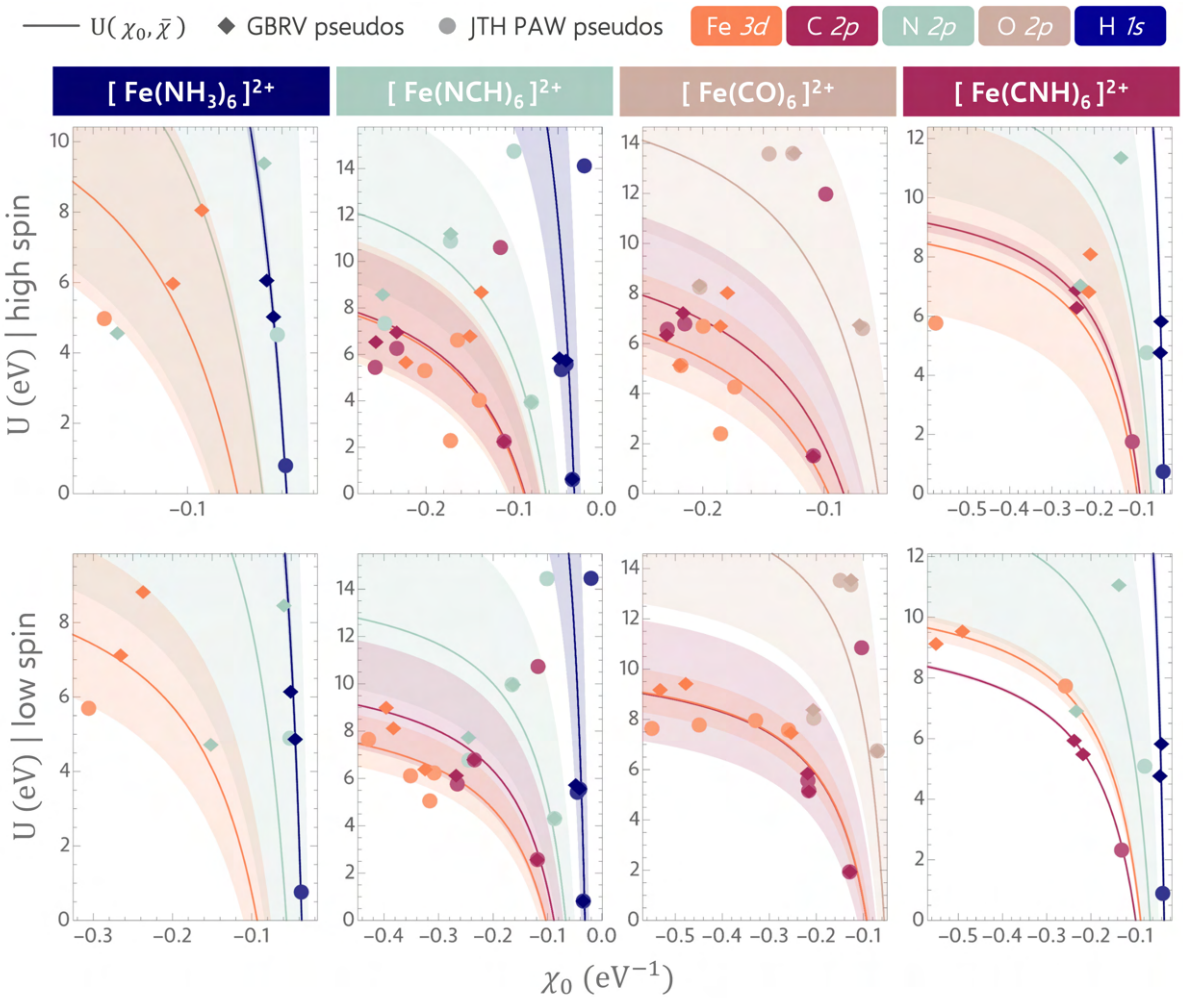

Figure 9.6: Linear response Hubbard U*, calculated across* ABINIT*,* ONETEP*, and* QUANTUM ESPRESSO*, plotted versus its corresponding unscreened response χ_0, superimposed on graphs of* $U(\chi_0,\bar{\chi})$*, where $\bar{\chi}$ is the mean screened response (line; range of* $U(\chi_0,\bar{\chi}\pm\sigma)$*, where σ is one standard deviation, is visualized with shaded area) across all projector/platform/pesudopotential types for the delineated subspace in the spatially-delineated system. That is, the color of components (orange for* Fe 3*d, pink for* C 2*p, green for* N 2*p, brown for* O 2*p, and blue for* H 1*s) indicates the atomic subspace for which* U *was calculated, and the row and column to which the figure pertains indicates the spin state (upper row for HS and lower row for LS) of the molecular complex (in labeled columns ordered by increasing ligand field strength). The pseudopotential used for each LR calculation is indicated by the shape of the point marker (circle for JTH PAW and diamond for GBRV).*

Analogously, J as a function of increasing (less negative) χ_{0_M} for constant χ_M will show exponential growth, the curvature of which swings downwards, approaching verticality as the magnitude of χ_M approaches a very small $|\chi_{0_M}| << 0$ before disappearing entirely into the asymptote at $\chi_M = 0$. This pattern is demonstrated in Fig. 9.7.

What's striking about these plots is how they contextualize the disagreement on the unscreened response in light of the agreement for the screened response. For example, χ for the C $2p$ in LS $[Fe(CNH)_6]^{2+}$ is, it is agreed across all platforms, exceptionally well-known. So, too, are the χ for the H $1s$ subspace across all molecules. Despite this, the projectors with either U or χ_0 that fall outside of this agreement most commonly are QUANTUM ESPRESSO OAPs with GBRV pseudopotentials and the ABINIT PAW projectors. (ABINIT projectors tend to have $\{\chi_0, U\}$ that lie outside a range of even two standard deviations for C and H).

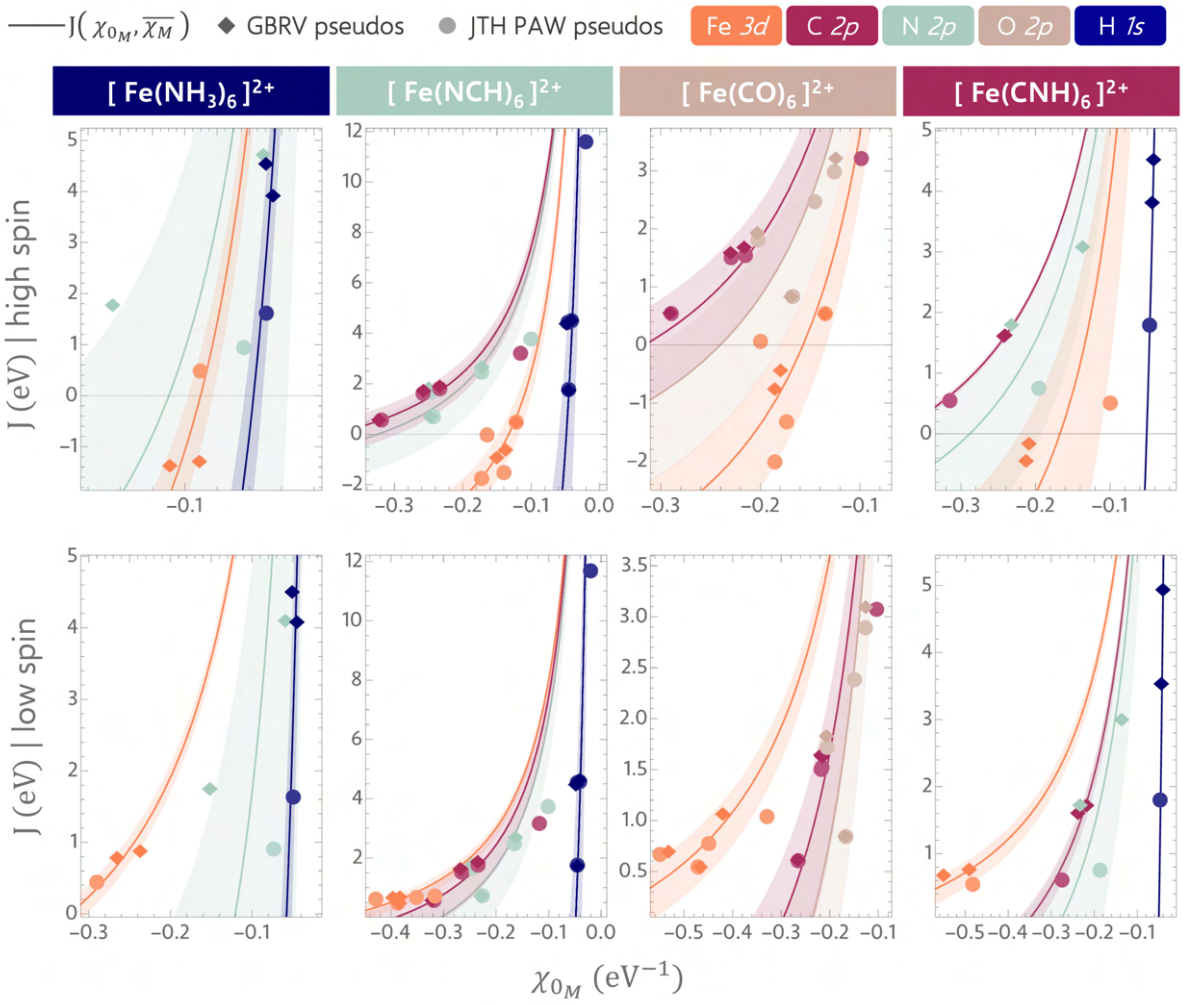

Figure 9.7: Linear response Hund's J, *calculated across* ABINIT, ONETEP, *and* QUANTUM ESPRESSO, *plotted versus its corresponding unscreened magnetic response* χ_{0_M}, *superimposed on graphs of* $J(\chi_{0_M}, \bar{\chi}_M)$, *where* $\bar{\chi}_M$ *is the mean screened magnetic response (line; range of* $J(\chi_{0_M}, \bar{\chi}_M \pm \sigma)$, *where* σ *is one standard deviation, is visualized with shaded area) across all projector/platform/pesudopotential types for the delineated subspace in the spatially-delineated system. See caption in Fig. 9.6 for more details.*

We would expect not necessarily that the agreement in the unscreened response should be reflected in the patterns that the U and χ_0 data points follow—this reasoning relies too heavily on the premise that there should be agreement in χ at all—but rather that there should be statistical variety in the data points that deviate from this agreement.

We do not observe such statistical variety. Out of the 40 points that lie outside one standard deviation of χ, 17 come from QUANTUM ESPRESSO OAPs with GBRV pseudopotentials and nine from ABINIT. For the magnetic response, 39 points lie outside one standard deviation of χ_M; 17 come from QUANTUM ESPRESSO OAPs with GBRV pseudopotentials and 12 from ABINIT. Across both magnetic and non-magnetic responses, ONETEP GBRV projectors never deviate from the expected range. These statistical anomalies indicate that something is anomolous with how QUANTUM ESPRESSO OAPs and ABINIT calculate the unscreened response. Another possibility is that the SCF definition of or approach to the unscreened response is in some way flawed or at least numerically more fraught.

It is also intriguing that for the HS states as well as the weak-field ligands in the LS state the Fe $3d$ subspace is particularly loathe to follow these contextualizing patterns for U. First, there is broad disagreement in χ for these systems. Not so for J, as χ_M seems particularly well-defined across systems and χ_{0_M} typically falls well within expected range. This could indicate that LR J is benefitting from a cancellation of errors in the spin-resolved population analysis.

Atomic versus ortho-atomic projectors

To really crystallize the projector's unique influence on Hubbard corrective protocol, we briefly hone our focus to the QUANTUM ESPRESSO atomic projectors (APs) versus ortho-atomic projectors (OAPs) curiosity. The atomic projectors are identical in both cases, drawn from the pseudopotentials, and are said to be well-suited for systems with pronounced atomic character.[55] Essentially by definition, however, OAPs count less electrons than APs do in the same subspaces and for the same pseudopotentials. The orthogonality between interatomic projector functions, enforced via Löwdin orthogonalization in QUANTUM ESPRESSO (see Eq. (6) in Ref. [55]), curtails the double counting of interstitial charge arising from overlapping AP orbital "tails." The understanding here is that the Hubbard correction is applied twice to this region when APs are used.

Our analysis of the 84 QUANTUM ESPRESSO HPs in our dataset, and their application via several common Hubbard functionals, found that this overlap does not necessarily translate to a double energy correction. In some cases, the Hubbard energy correction administered when OAPs are used exceeds that administered when APs are used. For example, consider the standard Dudarev DFT+U functional, where energy penalties are applied to all valence orbitals of the LS $[Fe(CO)_6]^{2+}$ molecule. The C $2p_z$ subspace defined by APs, which LR found to require a U = 5.17 eV, is occupied by $n^{\uparrow}_{mm} = n^{\downarrow}_{mm} = 0.836$ electrons,[§] in which the charge of the overlapped region is counted. That charge is also counted in the O $2p_z$ subspace, where APs prescribe a very high U = 13.59 eV coupled with comparatively full occupancies ($n^{\uparrow}_{mm} = n^{\downarrow}_{mm} = 0.927$). The total Hubbard correction applied, then—having twice incorporated the overlapped charge of the interstitial region—sums to $E_{\mathrm{U}} = 1.629$ eV. Consider now

[§]Here, we use the uncorrected ground state occupancies, which amounts to a sizable approximation as the Hubbard corrected electron density is very different from that relaxed by the underlying DFA. As such, these back-of-the-envelope calculations are used principally for illustrative purposes.

a situation in which the interstitial charge is considered exclusively part of the O $2p_z$ OAP manifold. The OAPs prescribe a much smaller U = 8.42 eV and find $n^{\uparrow}_{mm} = n^{\downarrow}_{mm} = 0.804$, smaller in magnitude, but much more fractionalized. It's these occupancies that inflate the summation term Σ and render a large Hubbard correction $E_{\mathrm{U}} = 1.737$ eV, greater than that prescribed by the APs.

It is challenging, and maybe not particularly instructive, to think about Hubbard corrections in terms of spatial distribution. Applying Hubbard corrections influences the local potential, which in turn encourages or discourages charge to occupy that subspace. Which charge (be it interstitial or closer to the atomic center) is not *a priori* identifiable. However, the interstitial charge being counted twice—once for each of two separate, overlapping Hubbard manifolds—will have the effect of inflating the Hubbard energy correction on one subspace only if that subspace is less than half full. As a result, we can envision, and indeed have witnessed, a situation in which the Hubbard energy correction being applied to those interstitial regions is larger when OAPs are used over APs. We see this across a variety of common Hubbard functionals, particularly when corrections are applied to non-TM subspaces. When a U correction is only applied to the Fe $3d$ subspace, the Hubbard energy term is typically larger when APs are used as opposed to OAPs. However, as soon as correction terms are applied to the ligand $2p$ subspace (in addition to the Fe $3d$), the tables turn, often drastically: the OAPs yield much larger Hubbard corrections than APs do. For example, in the case of the DFT+U functional applied to Fe $3d$ and the N $2p$ for HS $[Fe(NCH)_6]^{2+}$ (GBRV pseudopotentials), the Hubbard penalty jumps to 36.40 eV from 27.28 eV using OAPs versus APs respectively, and this despite the fact the OAPs lower the Hubbard U for the N $2p$ subspace to 8.63 eV from AP's 11.24 eV. This jump in penalty term largely derives from the N $2p$ occupancies, which are much more fractionalized for OAPs than for APs, and the fact that there are six N $2p$ subspaces across the molecule compared to the one Fe $3d$, the penalty for which lowers slightly with OAPs.

Conclusively, OAPs invariably count less charge in the Hubbard manifold of both the ground-state PBE (see Fig. 9.8(c)) and density-corrected systems, but that charge is not necessarily more integer. This affects not only Σ in the application of a Hubbard corrective functional, but also the magnitude of the U parameter upon determination via linear response.

To analyze this more closely, we look again at the dataset of 84 QUANTUM ESPRESSO {U, J} pairs determined via LR for all valence subspaces of this series of octahedrally coordinated Fe(II) complexes. Of these 84, half were determined with APs and the other with OAPs; 56 were computed using GBRV pseudopotentials and 28 with JTH PAW datasets. We compared like with like. Specifically, we looked at the differences in U or J induced by the use of OAPs over APs (i.e., $\Delta\mathrm{HP} = \mathrm{HP}^{\mathrm{OA}}\text{-}\mathrm{HP}^{\mathrm{A}}$). In five cases, ΔHP fell within the corresponding range of RMS errors calculated for those parameters. Of the remaining 79 data points, the use of OAPs decreased the HP ($\Delta\mathrm{HP} < 0$) in 45 cases and raised it ($\Delta\mathrm{HP} > 0$) in 34 others. Regardless of the projector used, regression on U tends to skew quadratic and that on J cubic, although APs tended to have marginally less well-behaved LR as measured by the HP regression error (Eq. (4.31)); average error $\sigma_{\mathrm{U}} = 0.048$ eV and average $\sigma_{\mathrm{J}} = 0.030$ eV for APs, compared to average $\sigma_{\mathrm{U}} = 0.040$ eV and average $\sigma_{\mathrm{J}} = 0.020$ eV for OAPs.

There are a few powerful relationships that emerge from this analysis. Fig. 9.8(b) shows a striking relation between $\Delta\chi$ and ΔU across all subspaces; an off-hand linear regression renders $R^2 = 0.847$. It's not as clear cut—what with a strange forking of the trend at the origin attributable to the mutiny

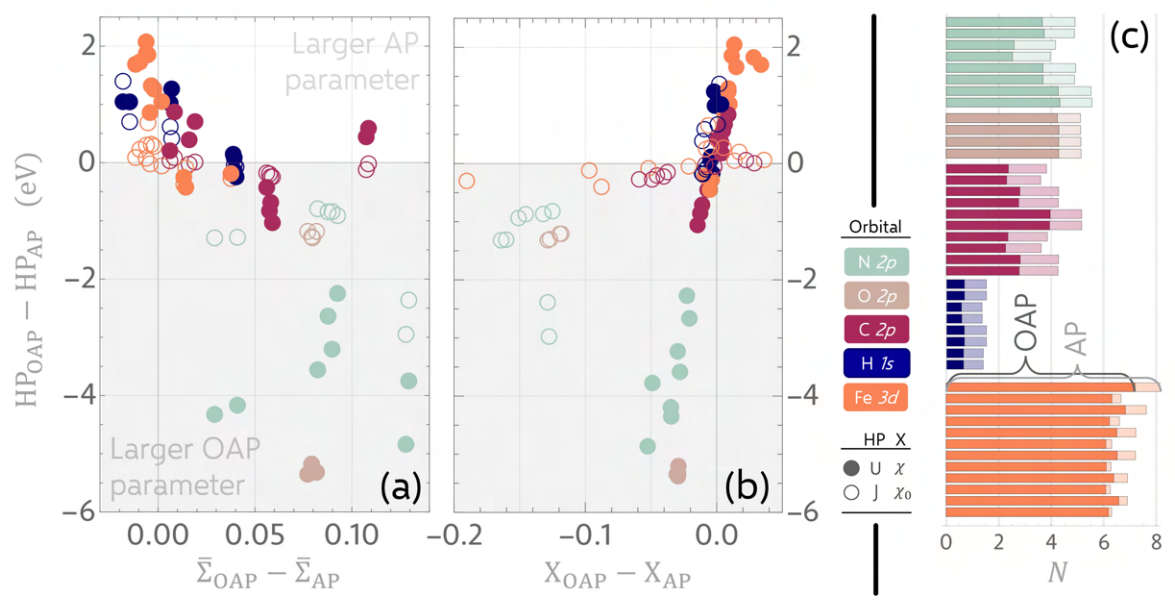

Figure 9.8: Trends in a dataset of 84 QUANTUM *ESPRESSO* {U, J} *pairs determined via LR for all valence subspaces of this series of octahedrally coordinated* Fe(II) *complexes, half with APs and the other with OAPs. Left figures show the difference in Hubbard parameters (closed circle markers for* HP = U *and open circle markers for* HP = J*) determined via OAPs versus APs as a function of (a) the OAP to AP difference in average summation term (see Eq. (9.1)) or (b) the corresponding difference in screened response (*χ *for* U, χ_M *for* J*). The overlayed (not stacked) bar chart in (c) shows total subspace occupancy N for all datapoints, the darker bar being that yielded by OAPs and the lighter that from APs. All plots use color to differentiate between subspaces;* Fe 3*d* → *orange;* C 2*p* → *pink;* N 2*p* → *green;* O 2*p* → *brown;* H 1*s* → *blue.*

of the negative Js—but at a lesser slope, $\Delta\chi_M$ and ΔJ also display a similar tendency. This seems to indicate that OAP HPs are larger than AP HPs at least partially by virtue of their less rigid screened response. On the level of occupancies, as shown in Fig. 9.8(a), OAPs tend to make occupancies more fractional on average, and as they do so, the corresponding value of U drops, sometimes substantially (O can fluctuate by ∼5 eV depending on the projector used). This highlights the unique propensity for fractionalized occupancies to contribute to the Hubbard corrective energy, that even despite a lower parameter, OAPs manage to inflate (not necessarily artificially) the corrective term.

9.2.3 ONETEP Hubbard parameters

With a better understanding of how the projectors influence the LR HP values, we transition to the set of HPs to be used for the adiabatic energy difference investigation: the ONETEP JTH PAW parameters, tabulated in Table 9.3. Recall that in order to include the response of the HXC contribution of the PAW effective potential, V^{σ}_{PAW} have been added to V^{σ}_{hxc} in the minimum-tracking definitions of U and J, shown in Eq. 4.29. Even so, all response was well-behaved, resulting in low regression errors across the board. Overall, errors are substantially lower than the state-of-the-art thus far.

Across all molecules, straightforwardly for the LS and imperfectly for the HS, the Hubbard parameters on the iron center tend to increase with strengthened ligand field. These phenomena are linked to trends in occupancy metrics, described in elaborate detail in Section 9.2.2.

In all cases except for that of H on $[Fe(NH_3)_6]^{2+}$, the U is larger in the LS state as opposed to the HS. (Ref. [56] found a similar differential between spin states for U on Fe in $[Fe(CO)_6]^{2+}$; Ref. [57] found U_{Fe}=8.5 eV for LS $[Fe(CO)_6]^{2+}$). This could come from the slightly different geometries used for each spin state; Ref. [58] showed that increasing the Fe-O interatomic distance in the FeO^+ molecule decreased the value of U. The same trend is present for this series of Fe(II) molecules, for which the HS state has 10%-20% larger metal-ligand bond lengths than in the LS state. Exchange mechanics could also factor into this observation. Electrons of like-spin, in experiencing less Coulomb repulsion due to exchange, are more likely to find themselves further from each other. Thus, electrons of like-spin are more delocalized by nature, an effect that is already well replicated by approximate (semi-)local exchange-correlation functionals and therefore demanding of less correction. Counterintuitively, then, most subspace occupancies (especially the d-orbitals of the iron centers, for which the differences between U_{hs} and U_{ls} are greatest) are more integer-like when the molecules are in the LS state. J exhibits very subtle, if any, relation to the molecule's spin state.

The HPs on the carbon ligand follow suit (where the use of the word ligand here refers to the atom immediately neighboring the iron ion), but not so the nitrogen ligands, which decrease with respect to increasing ligand field strength.

The magnitude of the Hund's J for the p-block elements seems correlated with its uncorrected DFT total occupancy, hovering consistently around 0.14-0.18 eV per electron. Such correlations have not been studied intensively, if at all; although a high-throughput study of Hubbard parameters on transition metal oxides found no exclusive relation between the location of the d-block element in the periodic table and its corresponding Hund's J value (Table 1(b) of Ref. [59]). In a separate trend, with the exception of $[Fe(NH_3)_6]^{2+}$, the further the atom is from the molecular center, the larger the Hund's J.

It's fairly standard across the literature to find a large U value coupled with a small J, which renders the hydrogen U to J ratio of these molecules surprising; the hydrogen J is consistently around twice its U value. Under the standard Dudarev DFT+U-J functional, then, the H 1s subspace will receive a negatively valued correction. This phenomenon seems to be ONETEP specific, as QUANTUM ESPRESSO and ABINIT both prescribe a U value greater than the corresponding J for H 1s in $[Fe(NCH)_6]^{2+}$. While the minimum-tracking method does not rely on the unscreened and screened responses to calculate the U (J), we can calculate χ (χ_M), and with it, reverse engineer χ_0 (χ_{0_M}), using the screened ONETEP occupancies. With ONETEP, we note that χ_0 and χ_{0_M} are noticeably dissimilar to each other. This reiterates that the minimum-tracking and SCF linear response methodologies are not equivalent for these molecular systems, chiefly in approach to calculating the unscreened response.

Another interesting analysis involves focusing on the total of corrective constants for $[Fe(NCH)_6]^{2+}$ and $[Fe(CNH)_6]^{2+}$, molecules with the same atomic constituents configured slightly differently. The latter seems to demand as much as 2 eV more corrective power. Most valence subspaces see an increase in their parameter values when carbon is closest to the iron center, all except C 2p, whose values decrease not unsubstantially. But the largest contributor to the discrepancy in corrective power between these two similar molecules comes from the Fe 3d subspace, which is accompanied by a small, but noticeable, increase in occupancy. Also contributing is the movement of the N 2p further away from the iron center, making the molecule more prone to SIE (and localized SCE) from the linear

	Molecule	Subspace	U $\pm$ error [eV]		J $\pm$ error [eV]	
			HS	LS	HS	LS
Iron center	$[Fe(CNH)_6]^{2+}$	Fe 3*d*	5.80 $\pm$ 0.14	7.760 $\pm$ 0.002	0.52 $\pm$ 0.04	0.555 $\pm 4\times10^{-6}$
	$[Fe(CO)_6]^{2+}$	Fe 3*d*	5.16 $\pm$ 0.14	7.609 $\pm 2\times10^{-4}$	0.556 $\pm 4\times10^{-6}$	0.553 $\pm 2\times10^{-8}$
	$[Fe(NCH)_6]^{2+}$	Fe 3*d*	5.34 $\pm$ 0.02	6.271 $\pm$ 0.013	0.513 $\pm 9.6\times10^{-4}$	0.510 $\pm 5\times10^{-10}$
	$[Fe(NH_3)_6]^{2+}$	Fe 3*d*	4.999 $\pm$ 0.007	5.721 $\pm$ 0.005	0.501 $\pm 4\times10^{-4}$	0.455 $\pm 1.3\times10^{-6}$
Ligand	$[Fe(CNH)_6]^{2+}$	C 2*p*	1.79 $\pm$ 0.06	2.351 $\pm 1.0\times10^{-4}$	0.561 $\pm 3\times10^{-5}$	0.620 $\pm 2\times10^{-6}$
	$[Fe(CO)_6]^{2+}$	C 2*p*	1.55 $\pm$ 0.04	1.969 $\pm 3\times10^{-5}$	0.557 $\pm 3\times10^{-5}$	0.614 $\pm 7\times10^{-7}$
	$[Fe(NCH)_6]^{2+}$	N 2*p*	3.984 $\pm$ 0.002	4.340 $\pm 7\times10^{-5}$	0.725 $\pm 7\times10^{-5}$	0.755 $\pm 5\times10^{-7}$
	$[Fe(NH_3)_6]^{2+}$	N 2*p*	4.54 $\pm$ 0.02	4.918 $\pm 2\times10^{-5}$	0.960 $\pm 7\times10^{-5}$	0.920 $\pm 4\times10^{-6}$
Intermediary	$[Fe(CNH)_6]^{2+}$	N 2*p*	4.792 $\pm 6\times10^{-4}$	5.116 $\pm 3\times10^{-4}$	0.766 $\pm 5\times10^{-6}$	0.766 $\pm 5\times10^{-6}$
	$[Fe(CO)_6]^{2+}$	O 2*p*	6.64 $\pm$ 0.02	6.782 $\pm 3\times10^{-5}$	0.852 $\pm 2\times10^{-4}$	0.851 $\pm 2\times10^{-7}$
	$[Fe(NCH)_6]^{2+}$	C 2*p*	2.295 $\pm 2\times10^{-4}$	2.610 $\pm 2\times10^{-6}$	0.597 $\pm 5\times10^{-6}$	0.600 $\pm 1.1\times10^{-6}$
Hydrogen	$[Fe(CNH)_6]^{2+}$	H 1*s*	0.778 $\pm 3\times10^{-4}$	0.923 $\pm$ 0.003	1.806 $\pm 3\times10^{-4}$	1.816 $\pm$ 0.002
	$[Fe(NCH)_6]^{2+}$	H 1*s*	0.651 $\pm 4\times10^{-4}$	0.855 $\pm 2\times10^{-4}$	1.806 $\pm 8\times10^{-4}$	1.788 $\pm 2\times10^{-4}$
	$[Fe(NH_3)_6]^{2+}$	H 1*s*	0.823 $\pm 3\times10^{-5}$	0.785 $\pm 2\times10^{-5}$	1.632 $\pm 1.4\times10^{-4}$	1.646 $\pm 6\times10^{-5}$

Table 9.3: ONETEP Hubbard Parameters U *and* J *and their uncertainties for all spin states (HS or LS) and all molecular systems, grouped in terms of position in the molecule and ordered by ligand field strength. Cell color is a function of parameter magnitude relative to all other parameters (i.e., the lighter the orange, the smaller the parameter).*

response perspective. Coordination environment carries some weight, therefore, in the amount of SIE afflicting the TM subspace. For more analysis on the LR components and their influence on the HPs, please consult Section 9.2.2.

As mentioned earlier, the reasonability of the ONETEP parameters provides a suitable basis on which to build our energetics investigation, particularly as we thereby circumvent, for now, the employment of the negatively valued Hund's Js, a phenomenon we have yet to understand as more than a SCF LR methodological pathology.

9.2.4 Relevant electronic structure properties

In depth analysis of the electronic structure of these molecules lies beyond the scope of the current investigation. We briefly relay data on the band gaps and magnetic moments, however, for documentation purposes and to demonstrate the (already well-documented) impact that Hubbard-like functionals have on these properties, which become relevant for certain assumptions in the energetics analysis of

Section 9.2.5. For more detailed analyses on the effect of DFT+U on the density of these molecules, we refer the readers to Refs. [35] and [36].

Any Hubbard functional with *in situ* correction applied to, at minimum, the Fe 3*d* orbital widens the PBE band gap, according to Fig. 9.10. Band gaps are larger in the LS state, mainly attributable to the lowering of the highest occupied molecular orbitals (HOMO), although some changes in the lowest unoccupied molecular orbitals (LUMO) are also visible. The difference between the LS and HS band gaps increases with increasing ligand field strength.

The magnetic moments on iron in the HS state coordination of the molecules are shown in Fig. 9.9. PBE largely underestimates the magnetic moment, and while all Hubbard functional manage to increase the moment, predictions still fall short of the intuitive 4 μ_B (bearing in mind that the global moment is fixed to 4 μ_B). The moments decrease consistently with increasing ligand field strength somewhat linearly at a rate that depends on the functional. This rate, for example, does not change with a mitigating J term in Dudarev functional. The rate noticeably decreases when J correction is added via the Himmetoglu DFT+U+J functional, but increases when the J term is made negative. Adding corrections to subspaces beyond the Fe 3*d* will forcibly increase the moment.

9.2.5 Energetics of common Hubbard functionals

We compare the energetics deriving from a variety of Hubbard functionals. Adiabatic energy differences ΔE_{HL} pertaining to the commonly implemented Dudarev DFT+U(−J) functional and the Himmetoglu DFT+U+J we present in Table 9.4. We also compare the results to an experimental version of the Himmetoglu functional, in which we apply a negatively valued Hund's J to effectively switch the sign of the Hund's J corrective term as a proof of principle testing the reasonability of the abnormalities encountered in Section 9.2.1.

For each functional, we examine the effect of corrective application to select permutations of valence subspaces—to the iron 3*d* alone (Fe), to iron and its neighboring ligand 2*p* (Fe+L), or to all valence subspaces (All). Then, for each such permutation, we use either the spin-state-specific Hubbard parameters for each spin state (*in situ*) or the same Hubbard parameters for both the LS and

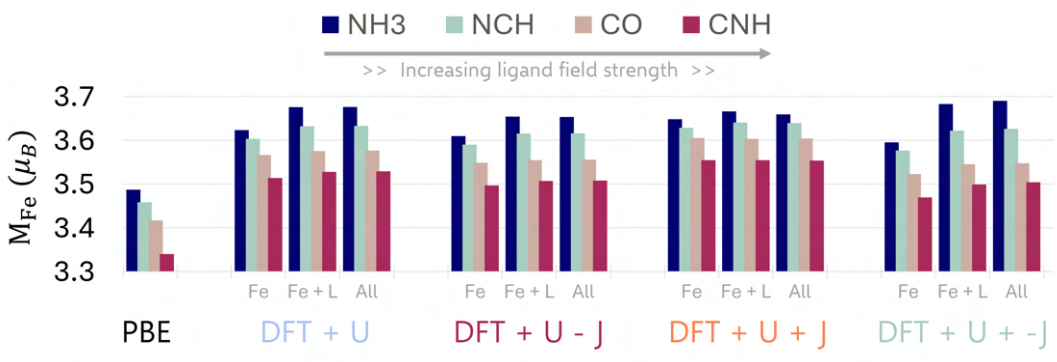

Figure 9.9: The moment on the Fe(II) *atom for each molecule in its high-spin-state configuration as it changes with the Hubbard corrective functional. In situ Hubbard corrections are applied to the valence states of the metal only (label:* Fe*), the metal and the ligand (label:* Fe+L*), or all atoms in the molecule (label:* All*).*

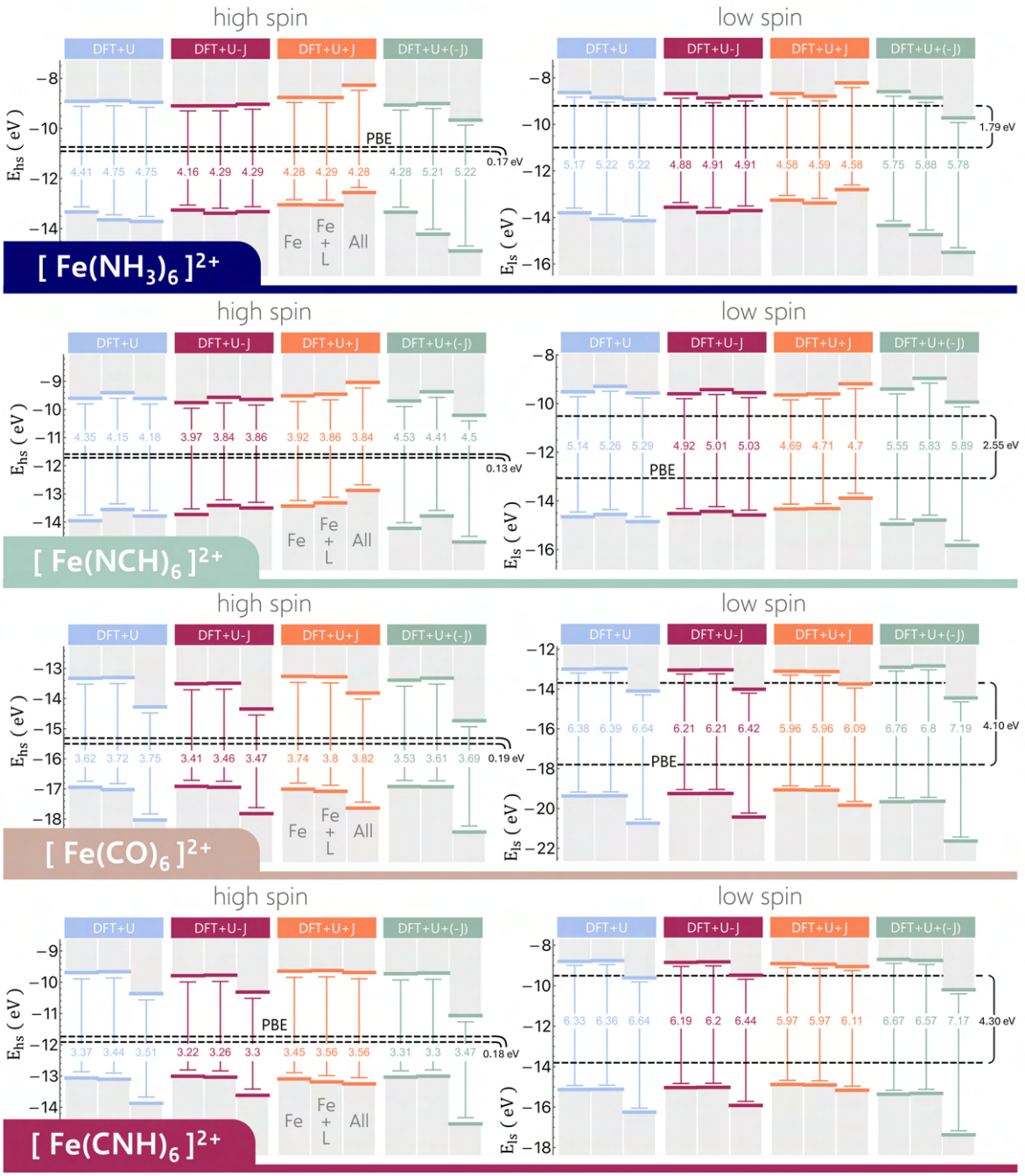

Figure 9.10: HOMO and LUMO energy levels as well as gaps of all molecules, in HS [left] or LS [right] state, as determined by PBE (black dashed lines) and all tested Hubbard functionals (colored lines); correction is applied to Fe 3*d alone (*Fe*), *Fe *and its immediate neighboring* 2*p (*Fe+L*), or all valence subspaces (*All*).*

HS states of the molecules (HS, as we opt semi-arbitrarily to use the smaller HS parameters following the success of the DFT+U−J functional, *vide infra*) the latter method having shown promise for energy differences between magnetic orderings of NiO in Chapter 7.

Compared to the reference, uncorrected PBE yields an average MAE magnitude of 1.233 eV across all molecules by overstabilizing the LS state, resulting in positively valued ΔE_{HL} across the board.

Each functional including PBE manages to reconstruct the gradual increase of the adiabatic energy differences with respect to ligand field strength. However, Table 9.4 demonstrates that the use of spin-state-specific parameter pairs does not manage, under any corrective permutation, to outperform PBE; the Hubbard functionals, and in particular the strong field ligand molecules, suffer instead from overstabilization of the HS state. Just as in Section 7.2.4 of the NiO investigation, this behavior points towards an exact cancellation of errors in those functionals involving the same Hubbard parameter

	HP specs		ΔE_{HL} (eV)				Error wrt CASPT2/CC (eV)	
Functional	Atoms	{U, J}	NH3	NCH	CO	CNH	-8 -6 -4 -2 0 2	Avg. MAE
CASPT2/CC	–	–	-0.64	-0.16	2.02	2.87		0.000
U + (-J)	All	HS	-1.079	-0.191	1.996	2.361		0.251
U + (-J)	Fe+L	HS	-1.256	-0.196	2.336	2.454		0.346
U + (-J)	Fe	HS	-0.769	-0.404	1.903	1.964		0.349
U-J	Fe	HS	-1.345	-0.855	1.474	1.556		0.815
U-J	Fe+L	HS	-1.621	-0.781	1.498	1.631		0.841
U-J	All	HS	-1.636	-0.768	1.331	1.653		0.878
U	Fe	HS	-1.493	-1.062	1.198	1.301		1.037
U	Fe+L	HS	-1.83	-0.968	1.228	1.408		1.063
U	All	HS	-1.813	-0.958	1.017	1.408		1.109
PBE	–	–	0.005	1.094	3.715	4.209		1.233
U + (-J)	Fe	*in situ*	-1.218	-0.942	0.246	1.007		1.249
U+J	Fe	HS	-2.222	-1.721	0.467	0.63		1.734
U-J	Fe	*in situ*	-1.701	-1.412	-0.242	0.502		1.736
U+J	Fe+L	HS	-2.354	-1.736	0.107	0.364		1.927
U	Fe	*in situ*	-1.825	-1.61	-0.503	0.255		1.943
U+J	All	HS	-2.462	-1.717	0.004	0.413		1.963
U + (-J)	Fe+L	*in situ*	-2.7	-1.233	-0.718	-0.146		2.222
U+J	Fe	*in situ*	-2.436	-2.274	-1.255	-0.541		2.649
U + (-J)	All	*in situ*	-2.313	-2.53	-1.343	-1.061		2.834
U-J	Fe+L	*in situ*	-2.518	-2.119	-1.613	-1.2		2.885
U	Fe+L	*in situ*	-2.631	-2.363	-2.083	-1.643		3.203
U-J	All	*in situ*	-2.339	-3.392	-2.04	-2.001		3.466
U	All	*in situ*	-2.477	-3.623	-2.549	-2.471		3.803
U+J	Fe+L	*in situ*	-2.543	-3.465	-3.42	-3.105		4.156
U+J	All	*in situ*	-2.559	-4.709	-3.795	-3.905		4.765

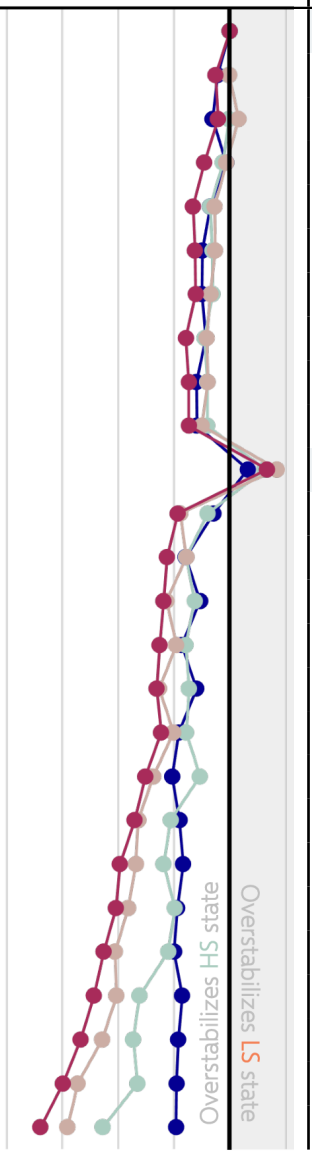

Table 9.4: Ranking of common Hubbard functionals in terms of mean average errors (MAE) *for adiabatic energy differences* ΔE_{HL}*, averaged across all complexes, with respect to CASPT2/CC reference across all molecules (first row).*[35,36] *Histogram shows signed error with respect to CASPT2/CC values.* {U, J} *column delineates use of either HS state* HP *pairs or in situ pairs for each respective spin state. "*Atoms*" column indicates to which subspaces corrections were applied (*Fe = Fe 3*d only,* Fe+L = Fe 3*d and ligand* 2*p,* All = *all valence subspaces in molecule).*

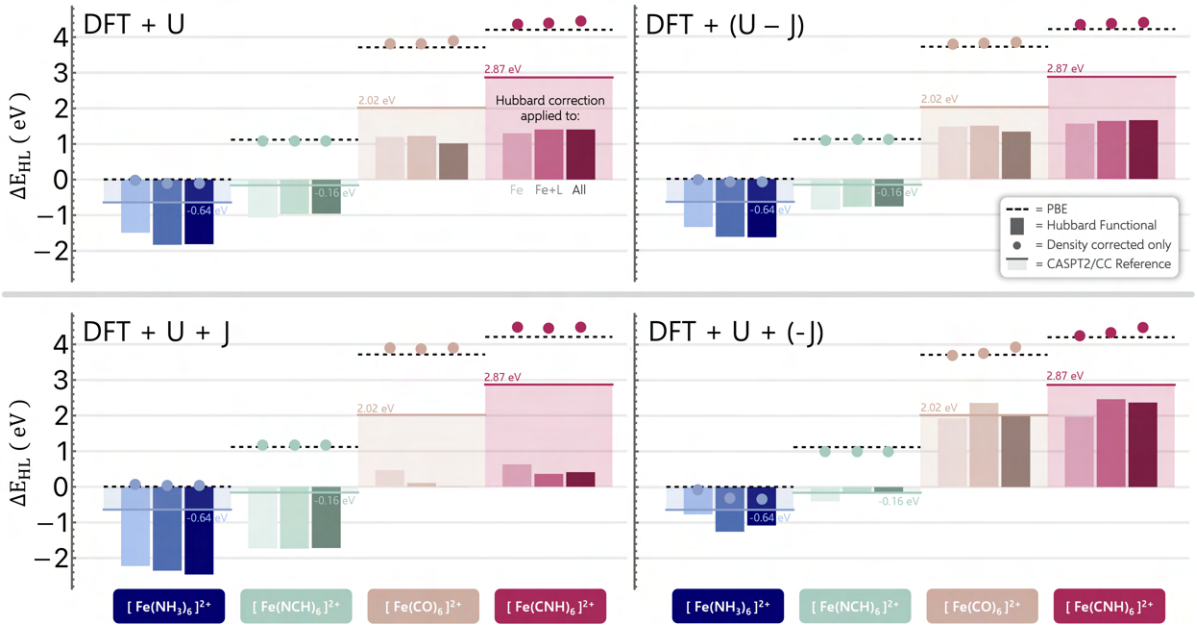

*Figure 9.11: Adiabatic energy differences ΔE_{HL} for all molecules obtained via the denoted Hubbard functional (*DFT+U *upper left;* DFT+U−J *upper right;* DFT+U+J *lower left;* DFT+U+(-J) *lower right), where correction is applied to some combination of subspaces (*Fe = Fe 3*d only,* Fe+L = Fe 3*d and ligand* 2*p,* All = *all valence subspaces in molecule) with the* {U, J} *parameter pairs coming from the HS state (non-spin-state-specific parameters), compared to uncorrected DFT (PBE XC functional; black dashed lines) and CASPT2/CC reference values (solid color line with shading). "*Density-corrected*" values (data points) are total energies converged with the denoted Hubbard functional, but Hubbard energy corrections are removed non-self-consistently.*

values. If *in situ* {U, J } pairs are used, however, there is redemption for the energetics in that the density has been corrected by the SCF use of the Hubbard functionals. Using only this density-corrected PBE@PBE+U (labelled PBE[U] in Ref. [36]), where the Hubbard energy terms are effectively removed non-self-consistently, yields slightly better ΔE_{HL} values than bare PBE if corrections are applied to the TM and the ligand only. A comparison of these density-corrected values to the Hubbard functionals themselves can be found in Figs. 9.11 and C.1, where the PBE@f ΔE_{HL} for all Hubbard functionals f are similar to those of PBE and thus far from the CASPT2/CC reference values.

We note that this result, particularly concerning those PBE@f values obtained with *in situ* parameters as displayed in Fig. C.1 of Appendix C1, counter those of Ref. [36], which found that the energetics relative to the same CASPT2/CC reference values are best with PBE[U] and starkly dissimilar to those with PBE. Thinking this could attest to erroneous execution of our methodology, we performed tests on $[\mathrm{Fe(NCH)_6}]^{2+}$ to find the source of this discrepancy. We saw no qualitative or otherwise major deviations between reasonably identical PBE and PBE+U^d runs on QE (using APs) and ONETEP. The most notable energetic discrepancy comes from the Hubbard terms ($E_{\mathrm{U,HS}} - E_{\mathrm{U,LS}} = -2.615$ eV in ONETEP versus -2.384 eV in QE), which in turn factors dominantly in the discrepancy between the corresponding PBE+U and PBE@PBE+U functionals. Having used the same value of U^d in our test, this discrepancy of $\sim$ 0.23 eV ($\sim$ 0.44 eV when using OAPs in QUANTUM ESPRESSO) attests to the considerable impact of the Hubbard projector function in determining subspace occupancies.

We managed, in constructing this experiment, to identify the two most potent differences between

our methodology and that of Ref. [36]: (i) the use of atomic-like versus OAPs, and (ii) the use of PAW JTH[42] versus GBRV pseudopotentials. Item (ii) is anticipated to account for energy differences on the order of 10^{-2} eV (the difference between the PBE ΔE_{HL} using JTH versus GBRV pseudopotentials), while energy differences arising from item (i) account for much larger discrepancies, on the order of 1 eV. OA or equivalent types of projectors are not implemented in ONETEP at this stage. The use of OAPs to find Hubbard subspace occupancies in Ref. [36] is likely the major factor contributing to the fact that their PBE[U] total energies are unlike the authors' PBE results. Columns 4-7 of Table 9.1 further corroborate this explanation. As measures of change in subspace occupancy in and of themselves, the *in situ* Hubbard parameters are highly sensitive to the Hubbard projectors, varying as much as 3 eV when OAPs are used as opposed to the default APs.

The best overall option, according to Table 9.4, is to use the same HPs regardless of spin state. In availing of a black box cancellation of errors in the structure of the Hubbard functional, the overstabilization of the HS state is mitigated and we observe most Hubbard functionals making a remarkable improvement on PBE. The best-performing physically derived Hubbard functional is the Dudarev PBE+U-J, which reduces the average MAE by 34% with respect to PBE, with correction applied exclusively to Fe $3d$. The use of the J in mitigating the magnitude of U on any subspace is beneficial here as DFT+U yields a mere 16% improvement on PBE. This indicates that the values of U prescribed by linear response are too large and contribute in a monotonic fashion to the overstabilization of the HS states. Incidentally, this also highlights the reason why we selected the HS HP parameters, as they are smaller than both their LS counterparts and the average of the LS and HS parameters.[§] The results are clear in that there is no value in applying correction to any subspace beyond the TM valence, although doing so is unlikely to change the adiabatic energy differences drastically.

For convenience in the remaining discussion, we recall from Section 2.5.3 in Chapter 2 that the U and J energy corrections for the Himmetoglu DFT+U+J functionals can be written, respectively, as

$$E_{\mathrm{U}} = \frac{\mathrm{U}}{2}\Sigma \tag{9.3}$$

$$E_{\mathrm{J}} = \frac{\mathrm{J}}{2}C_{\mathrm{J}} = \frac{\mathrm{J}}{2}(2\Pi - \Sigma), \tag{9.4}$$

where Σ and Π are defined in Eqs. (9.1) and (9.2), respectively. In Fig. 9.11 and Table 9.4, we see that DFT+U+J egregiously undershoots the target CASPT2/CC reference for each molecule. We observe 80% improvement on PBE, however, when reversing the concavity of E_{J} in the DFT+U+J functional, a maneuver with no physical justification in and of itself. Under DFT+U+(-J), the molecules show no particular tendency to overstabilize the low- or high-spin states, and where there is bias, it is not correlated with ligand field strength. These properties of DFT+U+(-J)—in addition to the fact that the best ΔE_{HL} are obtained when correction is applied to all valence subspaces in the molecule, not just the Fe $3d$—are strong indications that the incorporation of intra-atomic exchange in the Himmetoglu functional may be flawed and that the structure of the Hubbard functional itself requires revision.

[§]Assuming the density itself is rather well-corrected at its base and thus unperturbed by small changes in the magnitude of the Hubbard parameter, we tested non-self-consistently different {U, J} pairs on the adiabatic energy differences. The set of parameters obtained by averaging those of the HS and LS states yielded slightly worse MAEs, as did the LS state set of parameters. To confirm, we applied the HS parameters via the Hubbard functionals self-consistently, however, to obtain the data represented in Table 9.4.

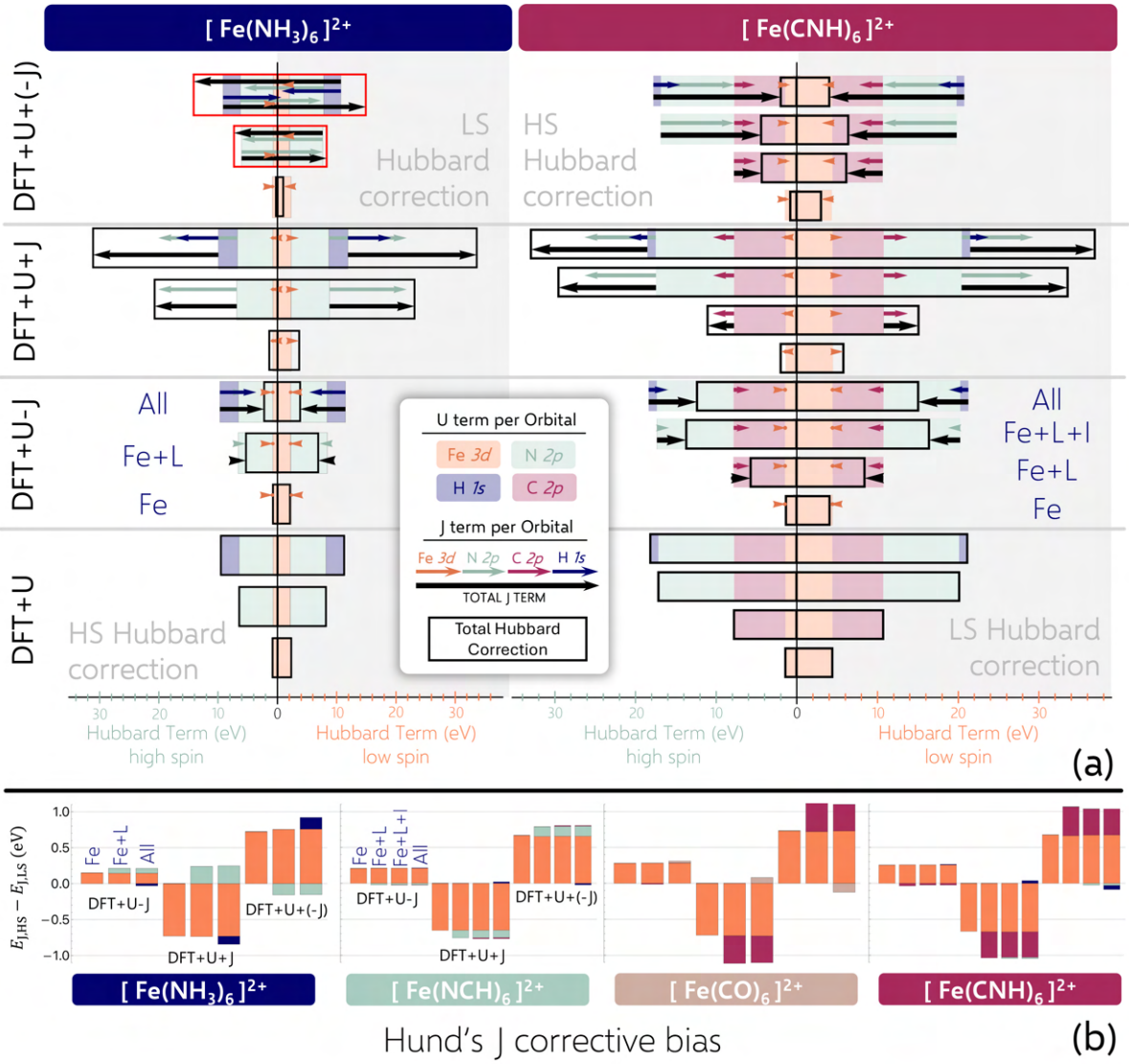

Figure 9.12: Corrective energy terms. The plot in (a) is split in terms of those preceded by the Hubbard U *(colored bars), Hund's* J *(colored arrows; total* J *correction, which amounts to the sum of the colored arrows, is denoted by black arrow), and then the total of the two (black-rimmed rectangles) for (top left)* $[Fe(NH_3)_6]^{2+}$ *and (top right)* $[Fe(CNH)_6]^{2+}$ *across all Hubbard functionals. Corrections applied to the* Fe 3*d orbital denoted by orange hues,* N 2*p by green hues,* C 2*p by pink hues, and* H 1*s by blue hues. Red-rimmed rectangles signal that total Hubbard correction applied via that functional is negatively valued. The left side of each paired bar chart is HS state of the molecule and the right is the LS. Plot in (b) shows the Hund's* J *corrective bias.*

As found with prior investigations, the tendency for E_U to overstabilize the HS state comes from an inflated penalty applied to the LS state, rendering $E_{U,HS} - E_{U,LS}$ negatively valued in a manner increasing in magnitude as one moves to the right of the spectrochemical series. In Fig. 9.12(a), we see that E_U for each valence subspace stays approximately the same magnitude regardless of the functional used, where the bias in penalizing the LS state comes primarily from the Fe 3*d* term. It's the J term that changes noticeably with respect to spin state for all subspaces, particularly on the Fe 3*d* and the ligand 2*p*. These changes accumulate and manage to reduce the penalty bias against the LS state, amplify it, or augment the penalty bias against the HS state.

From Fig. 9.12(b), the necessity of a negative J term in reducing the bias against the LS state

becomes clear. The N and C 2p corrections, largely canceling themselves out when not immediately neighboring the Fe atom, only contribute anywhere from 25%-50% of the Fe 3d bias, the direction of which is highly dependent on the functional used. For example, in in $[Fe(NH_3)_6]^{2+}$, the J correction on N bolsters whatever bias the 3d orbital demonstrates in DFT+U−J but mitigates it in the Himmetoglu functional (and it's -J variant), only to be canceled, in part or in full, by a H 1s J correction almost always demonstrating the opposing bias. The only time the 1s and N 2p corrections compound their bias is in the DFT+U+(-J) functional on $[Fe(CNH)_6]^{2+}$, where they encourage LS bias, rather futilely considering that together they make up less than 10% of the 3d and C 2p correction that collectively penalize the HS state more than the LS. Coincidentally, that N 2p is the only subspace whose correction doesn't flip its bias going from DFT+U+J to DFT+U+(-J); in both functionals, the N contributes to the bias towards the LS state. Coincident to that, the $[Fe(CNH)_6]^{2+}$ N 2p is the only subspace of all the molecules tested for which the *in situ* J value is the exact same in both the HS and LS states. The N 2p subspace in $[Fe(CNH)_6]^{2+}$ is highly spin-polarized and almost fully occupied, featuring the second largest J-scaled energy correction of any subspace (the first being the N 2p in $[Fe(NH_3)_6]^{2+}$); the spin state does not alter this much at all. What's significant is that it is the only subspace for which $C_{J,HS} - C_{J,LS}$ switches sign when the Hund's J sign is switched in the Himmetoglu functional. That is, in DFT+U+J, the HS C_J is smaller than the LS C_J, whereas in DFT+U+(-J), the opposite is true.

To understand why this is happening, we look at the six sets of N $2p_y$, $2p_z$, and $2p_x$ occupancies in $[Fe(CNH)_6]^{2+}$ (18 orbitals in total) for each functional. For all orbitals, DFT+U+(-J) renders larger spin-up and spin-down occupancies than DFT+U+J, especially for those orbitals that lie off the bond axes. This makes the on-axis contributions to C_J 50-60% larger than those from the off-axis orbitals (for DFT+U+J, for example, the average C_J for on-axis orbitals is 1.719 in the HS and 1.717 in the LS, compared to 1.063 and 1.068 respectively for the off-axis orbitals). But the on-axis C_J contributions, which tend to lightly penalize the LS state over the HS state, are resilient to changes in spin state. Thus, the $E_{J,HS} - E_{J,LS}$ term we see in Fig. 9.12(b) mainly comprises contributions from the off-axis orbitals. This is from where the phenomenon described above is derived. In DFT+U+J, most off-axis orbitals not only penalize the LS state but do so strongly, rendering $C_{J,HS} - C_{J,LS} < 0$. By contrast, in DFT+U+(-J), only half of the off-axis orbitals manage only to weakly penalize the LS state, rendering $C_{J,HS} - C_{J,LS} > 0$.

What's also interesting on both $[Fe(CNH)_6]^{2+}$ and $[Fe(CO)_6]^{2+}$ is that the C 2p corrective bias noticeably lessens when corrections are applied to their outer 2p neighbor (either N or O). This reflects a larger difference in Π between the HS and the LS states, impulsed by a reducing Π on both spin states but the LS faster than the HS. Because the magnetic moment in the LS state of these molecules is not increasing, this suggests that the J correction on the neighboring 2p is causing more of its charge to transfer, in equal parts spin-up and spin-down, to the C 2p. This is a testament to how much the J correction is affected by the spin degree of freedom, not necessarily the magnitude of the magnetic moment. The strong covalency of the systems perhaps amplifies this.

Across all molecules, the DFT+U−J functional lightly counters the larger LS U penalty with a larger J correction on the HS 3d orbital, a bias toward the HS state often minimally mitigated by the C 2p correction only to be lightly bolstered by other subspace corrections. By contrast, the C 2p correction compounds the bias of the Fe 3d corrections in the Himmetoglu-type functionals. With

DFT+U+J, that bodes poorly for the energetics; the main J correction greatly amplifies the LS state bias, pushing the total energy further away from the CASPT2/CC reference. This is precisely the behavior that is flipped on its head with DFT+U+(-J); the difference in correction largely remain the same magnitude for 3*d* and C 2*p*, but it administers the penalty to the HS state instead of the LS, thereby countering the LS bias in DFT+U and resulting in adiabatic energy differences more in line with the CASPT2/CC expectations.

9.3 Summary and conclusions

The versatility of SCO technologies continues to captivate interest among the chemical physics community. High-throughput materials discovery and design has served to shift the focus of that interest from SCO's thermodynamic and macroscopic mechanisms to its more microscopic manifestations, on the level of molecular energetics and electronic structure. In principle, this realm is accessible to DFAs in the available computationally tractable local or semi-local functionals. Building on literature in the area, this investigation sought to unearth the nitty-gritty of fully first-principles Hubbard-like DFT+U+J methods and their potential to achieve high-precision adiabatic energy differences.

We calculated and analyzed trends of the linear response-derived Hubbard U and Hund's J for all valence subspaces in a series of highly covalent octahedrally-coordinated Fe(II) SCO molecules, adopting either the $^1A_{1g}$ low-spin or $^5T_{2g}$ high-spin state, spanning the ligand field strength spectrum. In Section 9.2.1, we confirmed priorly documented phenomena, including the larger values of U in the LS as opposed to the HS states and certain dependencies on the ligand field strength of the molecules. Chiefly, however, we unveiled surprising differences between the U and J parameters calculated near-identically across three open-source DFT programs—ABINIT, ONETEP, and QUANTUM ESPRESSO—pointing not only to the potency of the basis set projector functions in the linear response method and to the dependence on pseudopotential choice, but to a breakdown in the equivalence of the SCF and minimum-tracking linear response methodologies. These observations prompted discussion on potential methodological failures and/or system pathologies that could give rise to, in particular, the negatively valued Hund's J for the Fe 3*d* subspaces of $[Fe(NCH)_6]^{2+}$ and $[Fe(CO)_6]^{2+}$ in their HS orientation and the striking differences in all parameters when calculated with PAW or ultrasoft pseudopotentials. There arise, then, clear avenues for future evaluation of this problem, not least of which is a revisitation of the determination of the unscreened response function in available linear response methodologies. It is probable that direct comparison will be necessary, involving the implementation of minimum-tracking LR into a plane-wave SCF program or SCF LR into a linear-scaling algorithm. Such an undertaking would enable the projector-based differences to be detached from the methodology-based differences in the population analysis of the Hubbard manifold.

Incidentally, we evaluated at length such projector-based differences on various components of the *in situ* U and J, approaching the issue from a data-driven, subspace- and system-independent statistical framework in Section 9.2.2. Such discussion surfaced a need for more efficient language and reformulation of certain occupancy and response metrics. We thus introduced the concepts of 'rigidity' and 'flexibility' to describe subspace transactions with the charge bath, and $\bar{\Pi}$ or $\bar{\Sigma}$ as defined in Eqs. (9.1) and (9.2). We found that the projector influences the occupancy magnitude of the Hubbard

manifold in a very clear-cut fashion, but that this clarity did not necessarily translate to particular ordering in response rigidity or screening magnitude. In other words, the projector functions influence more than the total charge counted in the Hubbard manifold; what charge is counted—be it interstitial, off-axis, core, etc.—bears weighted influence over the unscreened and screened response functions, as well. Further research on this topic could include, for example, a careful evaluation of the shape of the projector functions on the response. A scaled version of the musings in Chapter 10 could serve as an excellent basis for such a project. We refer the reader to Section 9.2.2 for other interesting, but not necessarily generalizably conclusive, trends in this arena.

We then proceeded to highlight statistical anomalies in the influence of the response functions on their corresponding U or J parameters, which further evidenced a need to revisit the formulation of the unscreened response and how it is calculated in practice. Our findings may be helpful in contributing to a reevaluation of the incorporation of exchange mechanics in the Hubbard energy functional. To wrap up the Hubbard parameter discussion, we honed our focus specifically to the QUANTUM ESPRESSO atomic and ortho-atomic projectors in an effort to further isolate the ways in which the projector functions influence linear response. This discussion surfaced an important distinction, that while OAPs invariably count less charge in the Hubbard manifold of both the ground-state PBE and density-corrected systems, that charge is not necessarily more integer, thus leading to, in some subspaces, higher corrective penalties than those applied with APs.

Given these findings, we took the ONETEP HPs and methodically applied them via a select range of common Hubbard functionals in search of the simplest combination to yield reliable spin-state energetic properties with respect to those obtained by our chosen reference: the CASPT2/CC wavefunction method provided by our collaborators at the Université Grenoble-Alpes. A brief check on electronic structure properties revealed anticipated corrections to the density, which gave us ground on which to build an energetics analysis. Following this, we found a somewhat counterintuitive failure of the *in situ* HPs, and in particular a positively valued Hund's J, in furthering DFT+U's already robust capacity to obtain reasonable adiabatic energy differences via the Dudarev and Himmetoglu functionals. We explained contradictions in our results with respect to those obtained priorly in Refs. [35] and [36] , suggesting that the value of PBE@f-type density-corrected functionals can be useful depending on the type of projector used. Similar to the conclusions of Chapter 7, it appears best practice to use the same Hubbard parameter values regardless of the molecule's spin state and to reduce the corrective coefficient in the Dudarev energy penalty as much as is permissible within the *ab initio* realm of possibilities; this latter suggestion attests to the tendency for Hubbard functionals to more strongly penalize the LS state as opposed to the HS state, a reversal from and overcompensation for Hartree-Fock exact exchange corrections. Ultimately, however, this investigation called for the construction of more appropriate DFT+U+J-type functionals to account for the unique static-correlation phenomena at play in strongly covalent systems. We refer the reader to Appendix C4 for a discussion on the BLOR functional, which may provide some insight into why the J term in the Himmetoglu functional appears to be incorrect (or more precisely, that the J term needs to be different, and not simply through a change in sign).

It is worth recalling that this project initially aspired to an accurate description of Prussian Blue's electronic structure and energetics in order to design chemical analogues that optimize and tailor func-

tionality while simultaneously minimizing, if not eliminating, impracticalities. Along the way, we have inadvertently stumbled upon the simple material systems for which first-principles DFT+U+J and linear response break down, and in doing so, we were able to map previously uncharted limitations of the method and precisely highlighted the areas for improvement therein. As a result, we have massively boiled down the search space across Hubbard-like methodologies, which is a necessary preliminary step (one lacking in the literature to date) to tackling a complicated system like PB. Future work and extensions to this project, then, involve applying these conclusions to ferrous-hexacyanometallate systems for which these molecules are localized and periodically repeating constituents. Getting DFT+U+J to work on such challenging systems would amount to considerable progress in computationally feasible materials simulation.

Bibliography

[1] A. A. Karyakin, Electroanalysis **13**, 813 (2001).

[2] N. R. de Tacconi, K. Rajeshwar, and R. O. Lezna, Chemistry of Materials **15**, 3046 (2003).

[3] Y. Xie, R.-B. Lin, and B. Chen, Advanced Science **9**, 2104234 (2022).

[4] P. Nie, L. Shen, H. Luo, B. Ding, G. Xu, J. Wang, and X. Zhang, J. Mater. Chem. A **2**, 5852 (2014).

[5] M. Pasta, R. Y. Wang, R. Ruffo, R. Qiao, H.-W. Lee, B. Shyam, M. Guo, Y. Wang, L. A. Wray, W. Yang, M. F. Toney, and Y. Cui, Journal of Materials Chemistry A **4**, 4211 (2016).

[6] X. Guo, Z. Wang, Z. Deng, X. Li, B. Wang, X. Chen, and S. P. Ong, Chemistry of Materials **31**, 5933 (2019).

[7] B. Wang, Y. Han, X. Wang, N. Bahlawane, H. Pan, M. Yan, and Y. Jiang, iScience **3**, 110 (2018).

[8] K. Hurlbutt, F. Giustino, M. Pasta, and G. Volonakis, Chemistry of Materials **33**, 7067 (2021).

[9] Q. Wang, J. Li, H. Jin, S. Xin, and H. Gao, InfoMat **4**, e12311 (2022).

[10] G. Oh, J. Kim, S. Kansara, H. Kang, H.-G. Jung, Y.-K. Sun, and J.-Y. Hwang, Journal of Energy Chemistry **93**, 627 (2024).

[11] F. S. Hegner, J. R. Galán-Mascarós, and N. López, The Journal of Physical Chemistry Letters **13**, 4104 (2022).

[12] V. Escax, A. Bleuzen, C. Cartier dit Moulin, F. Villain, A. Goujon, F. Varret, and M. Verdaguer, Journal of the American Chemical Society **123**, 12536 (2001).

[13] A. Bleuzen, C. Lomenech, V. Escax, F. Villain, F. Varret, C. Cartier dit Moulin, and M. Verdaguer, Journal of the American Chemical Society **122**, 6648 (2000).

[14] T. Yokoyama, T. Ohta, O. Sato, and K. Hashimoto, Physical Review B **58**, 8257 (1998).

[15] M. Cammarata, S. Zerdane, L. Balducci, G. Azzolina, S. Mazerat, C. Exertier, M. Trabuco, M. Levantino, R. Alonso-Mori, J. M. Glownia, S. Song, L. Catala, T. Mallah, S. F. Matar, and E. Collet, Nature Chemistry **13**, 10 (2021).

[16] O. Sato, T. Iyoda, A. Fujishima, and K. Hashimoto, Science (New York, N.Y.) **272**, 704 (1996).

[17] Y. Matos-Peralta and M. Antuch, Journal of The Electrochemical Society **167**, 037510 (2019).

[18] P. K. Thallapally, R. K. Motkuri, C. A. Fernandez, B. P. McGrail, and G. S. Behrooz, Inorganic Chemistry **49**, 4909 (2010).

[19] F. Karadas, H. El-Faki, E. Deniz, C. T. Yavuz, S. Aparicio, and M. Atilhan, Microporous and Mesoporous Materials **162**, 91 (2012).

[20] D. Papanikolaou, W. Kosaka, S. Margadonna, H. Kagi, S.-i. Ohkoshi, and K. Prassides, The Journal of Physical Chemistry C **111**, 8086 (2007).

[21] H. L. B. Boström, A. B. Cairns, L. Liu, P. Lazor, and I. E. Collings, Dalton Transactions **49**, 12940 (2020).

[22] O. Sato, T. Kawakami, M. Kimura, S. Hishiya, S. Kubo, and Y. Einaga, Journal of the American Chemical Society **126**, 13176 (2004).

[23] J. C. Wojdeł, I. de P. R. Moreira, S. T. Bromley, and F. Illas, The Journal of Chemical Physics **128**, 044713 (2008), publisher: American Institute of Physics.

[24] J. C. Wojdeł, I. d. P. R. Moreira, and F. Illas, The Journal of Chemical Physics **130**, 014702 (2009).

[25] F. S. Hegner, J. R. Galán-Mascarós, and N. López, Inorganic Chemistry **55**, 12851 (2016).

[26] J. H. Lee, S. Kattel, Y. Wang, B. M. Tackett, Z. Xie, S. Hwang, S. R. Denny, W. Xu, and J. G. Chen, Journal of Catalysis **393**, 390 (2021).

[27] E. Targholi, S. M. Mousavi-Khoshdel, M. Rahmanifara, and M. Yahya, Chemical Physics Letters **687**, 244 (2017).

[28] J. Peng, J. Wang, H. Yi, W. Hu, Y. Yu, J. Yin, Y. Shen, Y. Liu, J. Luo, Y. Xu, P. Wei, Y. Li, Y. Jin, Y. Ding, L. Miao, J. Jiang, J. Han, and Y. Huang, Advanced Energy Materials **8**, 1702856 (2018).

[29] X. Su, Y. Wang, J. Zhou, S. Gu, J. Li, and S. Zhang, Journal of the American Chemical Society **140**, 11286 (2018).

[30] H. M. Le, T.-T. Pham, V. D. Dat, and Y. Kawazoe, Journal of Physics D: Applied Physics **50**, 035004 (2016).

[31] W. Nicolazzi and A. Bousseksou, Comptes Rendus Chimie **21**, 1060 (2018).

[32] D. Vidal, J. Cirera, and J. Ribas-Arino, Dalton Trans. **50**, 17635 (2021).

[33] J. Wu, C. Sousa, and C. de Graaf, Magnetochemistry **5** (2019).

[34] A. Droghetti, D. Alfè, and S. Sanvito, The Journal of Chemical Physics **137**, 124303 (2012).

[35] L. A. Mariano, B. Vlaisavljevich, and R. Poloni, Journal of Chemical Theory and Computation **16**, 6755 (2020).

[36] L. A. Mariano, B. Vlaisavljevich, and R. Poloni, Journal of Chemical Theory and Computation **17**, 2807 (2021).

[37] L. MacEnulty and D. D. O'Regan, Phys. Rev. B **108**, 245137 (2023).

[38] K. Pierloot, Q. M. Phung, and A. Domingo, Journal of Chemical Theory and Computation **13**, 537 (2017).

[39] M. Radoń, Phys. Chem. Chem. Phys. **21**, 4854 (2019).

[40] M. Radoń, G. Drabik, M. Hodorowicz, and J. Szklarzewicz, Chem. Sci. **15**, 20189 (2024).

[41] J. P. Perdew, K. Burke, and M. Ernzerhof, Phys. Rev. Lett. **77**, 3865 (1996).

[42] F. Jollet, M. Torrent, and N. Holzwarth, Computer Physics Communications **185**, 1246 (2014).

[43] N. Holzwarth, A. Tackett, and G. Matthews, Computer Physics Communications **135**, 329 (2001).

[44] C.-K. Skylaris, P. D. Haynes, A. A. Mostofi, and M. C. Payne, The Journal of Chemical Physics **122**, 084119 (2005).

[45] P. E. Blochl, Physical Review B **50**, 17953 (1994).

[46] G. J. Martyna and M. E. Tuckerman, The Journal of Chemical Physics **110**, 2810 (1999).

[47] N. D. M. Hine, J. Dziedzic, P. D. Haynes, and C.-K. Skylaris, The Journal of Chemical Physics **135**, 204103 (2011).

[48] K. F. Garrity, J. W. Bennett, K. M. Rabe, and D. Vanderbilt, Computational Materials Science **81**, 446 (2014).

[49] G. Makov and M. C. Payne, Phys. Rev. B **51**, 4014 (1995).

[50] V. I. Anisimov and O. Gunnarsson, Phys. Rev. B **43**, 7570 (1991).

[51] M. Cococcioni and S. de Gironcoli, Physical Review B **71**, 035105 (2005).

[52] A. C. Burgess, E. Linscott, and D. D. O'Regan, Phys. Rev. B **107**, L121115 (2023).

[53] X. Dong, A. R. Oganov, H. Cui, X.-F. Zhou, and H.-T. Wang, Proceedings of the National Academy of Sciences **119**, e2117416119 (2022).

[54] G. C. Moore, M. K. Horton, E. Linscott, A. M. Ganose, M. Siron, D. D. O'Regan, and K. A. Persson, Phys. Rev. Mater. **8**, 014409 (2024).

[55] I. Timrov, N. Marzari, and M. Cococcioni, Computer Physics Communications **279**, 108455 (2022).

[56] Q. Zhao, E. I. Ioannidis, and H. J. Kulik, The Journal of Chemical Physics **145**, 054109 (2016).

[57] Y. Cytter, A. Nandy, A. Bajaj, and H. J. Kulik, The Journal of Physical Chemistry Letters **13**, 4549 (2022).

[58] H. J. Kulik and N. Marzari, The Journal of Chemical Physics **135**, 194105 (2011).

[59] G. C. Moore, M. K. Horton, E. Linscott, A. M. Ganose, M. Siron, D. D. O'Regan, and K. A. Persson, Phys. Rev. Mater. **8**, 014409 (2024).

Part V

The Derivative of U with Respect to The Projector

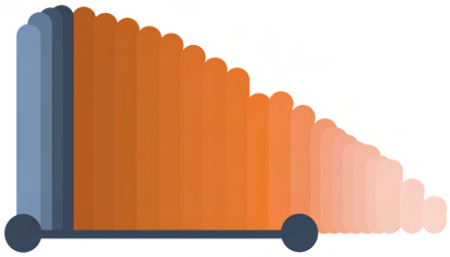

Chapter 10

A feasibility study on Hubbard projector dynamics

Former chapters have revealed how pivotal are the projector functions in determining the efficacy of DFT+U+J corrective schema. An undercurrent of the science in Parts III and IV keeps tabs on the Hubbard U and Hund's J as functions of the projectors characteristic to each electronic structure platform: those confined to and renormalized by the PAW augmentation sphere in ABINIT (Section 7.2.1), the atomic orbitals versus their orthonormalized counterparts in QUANTUM ESPRESSO (Section 9.2.2), or the pseudoatomic orbitals of ONETEP, the latter of which we investigate more thoroughly in the coming sections. Overall, we observe the projector's capacity to envelop the subspace charge, precisely or imprecisely, is heavily implicated in determining the strength of the Hubbard parameters as well as their application via their respective penalizing energy terms.

Now, we call into question the efficacy of static projections and fixed Hubbard parameters at all, recognizing that transition metal centers of multi-valence systems are often temperamental with respect to changes in charge and spin state, a sensitivity that can have macroscopic consequences on system observables. Here, we operate on the premise that the Hubbard U correction changes as we contract, dilate, transpose, or even transform the representation of the subspace for which the parameter is derived and on which the penalty is to be applied. The utility of this exercise, however, hinges on the existence of a local extremum. That is, we need to know whether or not the Hubbard parameters can be maximized or minimized as we change the projection operator. Accordingly, we conduct a preliminary investigation to determine, for a given projector, whether the Hubbard U parameter for a valence subspace obtains an extremum and, if so, under what occupancy conditions.

The broader aim of this proof-of-concept study is to design a protocol for choosing the appropriate projector function(s), tailored to the system under consideration, which represents well the subspaces undergoing interrogation for their susceptibility to SIE and SCE, so as to maximize the efficacy and provide critical comparative documentation of DFT+U+J-type corrective functionals across electronic structure theory programs. While increasing consideration has been given to the projectors that define the Hubbard manifold in recent years,[1–8] only Ref. [9], to our knowledge, has attempted a critical mathematical evaluation of projector dynamics.

In Sections 10.1 and 10.2, we derive a theoretical basis for this project, following which we set up a simple investigation to test its assertions. The computational details of the feasibility study are described in Section 10.3 and its results relayed and discussed in Section 10.4. We present our conclusions in Section 10.5.

10.1 The hydrogen-like radial atomic wavefunctions as projectors

A logistical question we are faced with is how to evolve the projector functions continuously while maintaining their structural comparability. Within the proof-of-concept framework, we restrict our assessment to rudimentary variations in the hydrogen-like, radially symmetric, hydrogen-like atomic wavefunctions,[10–16] themselves solutions to the wavefunction equation for a single atom and defined as a function of distance from the nucleus r for orbital $n\ell$,

$$R_{n\ell}^{(Z_{\text{eff}})}(r) = \sqrt{\frac{1}{4\pi}\left(\frac{2Z_{\text{eff}}}{n}\right)^3 \frac{(n-\ell-1)!}{2n\,[(n+\ell)!]}}\, e^{\frac{-rZ_{\text{eff}}}{n}} \left(\frac{2rZ_{\text{eff}}}{n}\right)^{\ell} \mathcal{L}_{n-\ell-1}^{2\ell+1}\left(\frac{2rZ_{\text{eff}}}{n}\right), \tag{10.1}$$

where Z_{eff} is the effective nuclear charge of the atom, and $\mathcal{L}_{n-\ell-1}^{2\ell+1}\left(\frac{2rZ_{\text{eff}}}{n}\right)$ are generalized Laguerre polynomials. The factor of $1/\sqrt{4\pi}$ is present to ensure that $\int 4\pi[rR_{n\ell}^{(Z_{\text{eff}})}(r)]^2\, dr = 1$. By assuming $\ell = n-1$, Eq. (10.1) simplifies to

$$R_{n,n-1}^{(Z_{\text{eff}})}(r) = \sqrt{\frac{Z_{\text{eff}}^3}{\pi n^4\,[(2n-1)!]}}\, e^{\frac{-rZ_{\text{eff}}}{n}} \left(\frac{2rZ_{\text{eff}}}{n}\right)^{n-1}. \tag{10.2}$$

Eq. (10.2), alongside its derivative and radial probability distribution, is plotted in Fig. 10.1

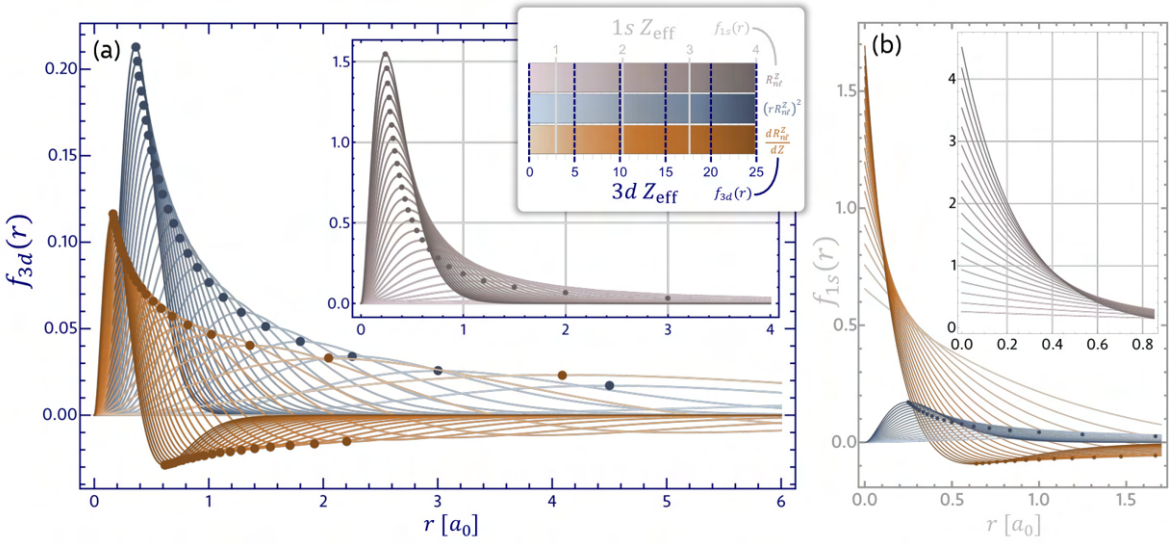

Figure 10.1: Hydrogen-like atomic projectors $R_{n\ell}^{(Z_{\text{eff}})}(r)$ (inset, grey), their radial probability distribution (blue), and their derivatives with respect to atomic nuclear charge Z_{eff} (orange), all as functions of Z_{eff}. Left plot shows these functions for 3d orbitals (dark blue numbers) and the right plot for 1s (gray numbers). Extrema are pinpointed with circular markers. Note the different Z_{eff} and axis scales.

for a variety of Z_{eff} values for the $1s$ and $3d$ states. While elementary, this class of orbitals can be used as projectors that are functions of one parameter: the effective nuclear charge Z_{eff}. The Z_{eff} variable can be thought of as an indirect measure of the occupancy matrix of a Hubbard-treated orbital. A more flexible and dramatic change would perhaps stretch the orbital in a spherically symmetric manner along the atomic radius, as this would alter the expectation radii of the electronic subspaces and, by extent, the charge localization. Even more sophisticated projector choices include molecular orbitals or Wannier functions. For now, we opt to use these radial atomic orbitals for their relative simplicity. Moreover, a technical convenience of the hydrogen-like atomic orbitals as functions of Z_{eff} stems from their reciprocal-space implementation in a once-obsolete ONETEP subroutine. We propose, and indeed have already embarked on, expansion of this functionality by coding up a similar subroutine featuring the derivative of these projectors with respect to Z_{eff}, details of which can be found in Appendix D1.

10.2 The variation of U as a function of the projector

Theorem: Consider a projector $\hat{P}$, of the form in Eq. (10.1) and thus a function of Z_{eff}, that extremizes the total electronic occupancy $N = n^{\uparrow} + n^{\downarrow}$ of a subspace orbital. We are concerned with the derivative of U with respect to effective nuclear charge. Via the chain rule,

$$\frac{d\mathrm{U}}{dZ_{\text{eff}}} = \mathrm{Tr}\left[\frac{d\mathrm{U}}{d\hat{P}}\frac{d\hat{P}}{dZ_{\text{eff}}}\right]. \tag{10.3}$$

For this system, $\frac{d(n^{\uparrow}+n^{\downarrow})}{dZ_{\text{eff}}} = 0$ if and only if $\frac{d\mathrm{U}}{dZ_{\text{eff}}} = 0$.

Proof: We bifurcate the proof into the following two lemmata to show $\frac{d(n^{\uparrow}+n^{\downarrow})}{dZ_{\text{eff}}} = 0 \iff \frac{d\mathrm{U}}{dZ_{\text{eff}}} = 0$.

1. Lemma: $\frac{d(n^{\uparrow}+n^{\downarrow})}{dZ_{\text{eff}}} = 0 \implies \frac{d\mathrm{U}}{dZ_{\text{eff}}} = 0$.

   We can see from Eq. (10.3) that, in applying the chain rule to $\frac{d\hat{P}}{dZ_{\text{eff}}}$,

   $$\frac{d\mathrm{U}}{dZ_{\text{eff}}} = \mathrm{Tr}\left[\frac{d\mathrm{U}}{d\hat{P}}\frac{d\hat{P}}{d(n^{\uparrow}+n^{\downarrow})}\frac{d(n^{\uparrow}+n^{\downarrow})}{dZ_{\text{eff}}}\right] = \frac{d(n^{\uparrow}+n^{\downarrow})}{dZ_{\text{eff}}}\mathrm{Tr}\left[\frac{d\mathrm{U}}{d\hat{P}}\frac{d\hat{P}}{d(n^{\uparrow}+n^{\downarrow})}\right], \tag{10.4}$$

   which necessarily demands that when $\frac{d(n^{\uparrow}+n^{\downarrow})}{dZ_{\text{eff}}} = 0$, $\frac{d\mathrm{U}}{dZ_{\text{eff}}} = 0$ as well.

2. Lemma: If $\frac{d\mathrm{U}}{dZ_{\text{eff}}} = 0$ then $\frac{d(n^{\uparrow}+n^{\downarrow})}{dZ_{\text{eff}}} = 0$.

   We start with the chain rule

   $$\frac{d\mathrm{U}}{dZ_{\text{eff}}} = \frac{d\mathrm{U}}{d(n^{\uparrow}+n^{\downarrow})}\frac{d(n^{\uparrow}+n^{\downarrow})}{dZ_{\text{eff}}}. \tag{10.5}$$

   To demonstrate that the only way Eq. (10.5) can hold true is if $\frac{d(n^{\uparrow}+n^{\downarrow})}{dZ_{\text{eff}}} = 0$, we must first show that, in all physically relevant contexts, $\frac{d\mathrm{U}}{d(n^{\uparrow}+n^{\downarrow})} \neq 0$. In a proof by contradiction, we take the

minimum-tracking definition of U in Eq. (4.29) and set it equal to 0:

$$\frac{d\mathrm{U}}{d(n^{\uparrow}+n^{\downarrow})} = \frac{1}{2}\frac{d}{d(n^{\uparrow}+n^{\downarrow})}\left[\frac{d(V_{\mathrm{hxc}}^{\uparrow}+V_{\mathrm{hxc}}^{\downarrow})}{d(n^{\uparrow}+n^{\downarrow})}\right] = \frac{1}{2}\frac{d^2(V_{\mathrm{hxc}}^{\uparrow}+V_{\mathrm{hxc}}^{\downarrow})}{d(n^{\uparrow}+n^{\downarrow})^2} = 0. \tag{10.6}$$

For reasonable systems and subspaces with approximative functionals, $(V_{\mathrm{hxc}}^{\uparrow}+V_{\mathrm{hxc}}^{\downarrow})$ has curvature, and thus its second derivative with respect to N will never be zero. Therefore, ad absurdum, $\frac{d(n^{\uparrow}+n^{\downarrow})}{dZ_{\mathrm{eff}}}$ has to be 0 if $\frac{d\mathrm{U}}{dZ_{\mathrm{eff}}} = 0$.

By lemmata 1 and 2, the proof holds, and $\frac{d(n^{\uparrow}+n^{\downarrow})}{dZ_{\mathrm{eff}}} = 0$ if and only if $\frac{d\mathrm{U}}{dZ_{\mathrm{eff}}} = 0$. □

We demonstrate that a subspace's Hubbard U as a function of the projector is extremized for the same projector that either minimizes or maximizes the subspace occupancy. This relation could greatly simplify the process of determining the optimal U for a particular subspace. In the next sections, we test this theory on a series of molecular systems, looking particularly to verify that such extrema exist in subspaces and that they are accessible (i.e., energetically stable configurations).

10.3 Computational details

We perform our calculations in the Order N Electronic Total Energy Package (ONETEP)[17] due to its versatile projector implementation, which may be cleanly manipulated in the input file via the atomic solver. Recall from Section 3.2.5 that the atomic solver uses pseudoatomic orbital projections to internally generate, from the occupied KS states of the specified neutral atom subject to an underlying XC functional, its radial NGWFs.[17,18] The shape of the pseudoatomic orbital may then be cleanly manipulated by varying the fraction of electrons $n_{n\ell}$ residing therein, which, in turn, influences the shape of the orbital.

As a proof-of-principle, we first explore the dihydrogen cation H_2^+, the simplest one-electron system exhibiting self-interaction error (SIE) arising only from the underlying XC functional and entirely decoupled from the similarly diagnosed static-correlation error. The H_2^+ molecule modeled at its dissociation limit is often used to demonstrate pure SIE[19,20] due to its relatively non-overlapping $1s$ subspaces and accurate population analysis. We model the diatomic molecule at its dissociation limit with a stretched bond length of 8.5 a_0 at the center of a $40\times31\times31$ a_0 cell using ONETEP spin DFT, activating its minimum-tracking linear response implementation. In performing similar calculations, Ref. [21] observed odd behavior in the U at dissociated bond lengths in addition to numerical instabilities. The body of response monitoring only changes in the spin-up channel, however, was found to provide seamless total-energy corrections for neutral projectors. For this reason, instead of looking at the U as defined in Eq. (16) of Ref. [22], we look at changes in

$$\mathrm{U}^{\uparrow} = \frac{dV_{\mathrm{hxc}}^{\uparrow}}{dn^{\uparrow}}, \tag{10.7}$$

which we call the '1×1' $U^{\uparrow}$ to follow the same article's naming conventions.

A norm-conserving PBE pseudopotential generated by Opium[23–25] (generative input file from Ref. [26] and reprinted in Appendix D2), in conjunction with a PBE XC functional[27] were used alongside a 14 a_0 NGWF cutoff radius to generate one initial NGWF for each $1s$ subspace. Cubic psinc spacing was constructed to imitate a plane-wave cutoff radius of $\sim$ 22 Ha (600 eV). Total energies were converged self-consistently to within a threshold tolerance of $\sim 3.675\times10^{-8}$ Ha (1.0×10^{-6} eV). To correct for spurious electrostatic interactions between periodic images of the molecules, we used the Martyna-Tuckerman (MT)[28] minimum image convention (MIC) with cutoff of 7.0 a_0 following the suggestions of Hine *et al.*[29]

For H_2^+, $n_{1s}^{\uparrow}$ was varied in the pseudoatomic solver between 0 and 1. For each value of $n_{1s}^{\uparrow}$, five evenly-spaced α perturbations between $\pm$0.1 eV, including the non-perturbed state at 0.0 eV, were applied to the spin-up channel of one H atom only. If and once relaxed, we harvested total occupancies and Hartree and exchange-correlation potentials from the same spin-up channel to which the perturbation was applied. Many single-point calculations did not converge, especially those at particularly low or high values of $n_{1s}^{\uparrow}$. Recognizing that there is no physical reason to expect non-linear or erratic behavior and that numerical instabilities are common at this chosen bond-length interval because of the degeneracy of the KS eigenstates,[26] $(n^{\uparrow}, V_{\mathrm{hxc}})$ pairs obfuscating the linear trend from which the response may be gleaned were considered outliers and discounted. For this molecule, we only conducted first-degree polynomial (linear) regressions. An example input file for this simulation is provided in Appendix D2.

Having obtained encouraging results, we performed similar tests on the (actual) U of both the high- and low-spin states of two octahedrally-coordinated Fe(II) molecules from Chapter 9: $[Fe(NH_3)_6]^{2+}$ and $[Fe(CNH)_6]^{2+}$. Computational details for these molecules are identical to those elaborated in Section 9.1.1 save the following differences: (i) the MT electrostatic correction within the MIC with cutoff of 7.0 a_0 is used for all LR calculations; (ii) the simulation cell size is extended to $75.59\times75.59\times75.59$ a_0; (iii) the charge and spin of the central Fe atom are not initialized in the atomic solver; and (iv) for the LS state on each molecule, perturbations of strength α were applied only to the spin-up channel (in order to simultaneously obtain U and J via the simple 2x2 method[22] for this non-spin-polarized system[30]). The PAW formalism[31] is incited here, and with it JTH PBE PAW datasets[32] are used. Bearing in mind the aforementioned differences, example input files for these runs are provided in Appendix C2. For these molecules, our standard polynomial regression procedure outlined in Chapter 4 for determination of the Hubbard parameters was employed.

10.4 Results and discussion

10.4.1 Dissociated H_2^+

Following this methodology we built Fig. 10.2, where plot (a) shows the linear-response regressions and plot (b) the resulting $U^{\uparrow}$ values as a function of varying n_{1s} for H_2^+ at the dissociation limit (bond length 8.5 a_0). The same behavior (more smooth, even) is noted for the molecule at 3 a_0, although the $U^{\uparrow}$ are smaller; see Fig. 10.3(a). This much is expected, because the $n^{\uparrow}$ occupancies on one H atom

are less fractionalized, resulting in less SIE.

We emphasize that n_{1s} is a measure of the charge state implicated in the construction of the radial $1s$ NGWF projector, whereas n^σ (where $\sigma = \{\uparrow, \downarrow\}$) is the final spin-resolved occupancy of the perturbed H $1s$ orbital, ultimately itself a function of the projector via the density kernel. To hit this home, we show in Fig. 10.4 the influence of n_{1s} on the radial distribution functions of the initial radial NGWFs $\psi(r)$ coming from the atomic solver. Note that at a certain low value of n_{1s}, the shape is maximally dilated, at which point the trend doubles back on itself.

A total of five α perturbations were attempted for each value of n_{1s}. For the 8.5 a_0 bond length, several points were discarded due to numerical instabilities, which are common at this extended bond length. No LR calculation, for either bond length, converged when $n_{1s} = 0.0$. When $n_{1s} = 1.0$ was tested on the molecule at 8.5 a_0 bond length, four of the five points converged, but the response was unpredictably non-linear. For the other 35 data points (23 for 3.0 a_0), the average error on $\mathrm{U}^\uparrow$—calculated via Eq. (4.31) and discounting the $\sigma_{\mathrm{U}}^\uparrow = 0.0$ eV for $n_{1s} = 0.1$ (for which only two perturbations converged)—was found to be $\bar{\sigma}_{\mathrm{U}}^\uparrow = 0.02$ eV ($\sigma_{\mathrm{U}}^\uparrow = 0.008$ eV for 3.0 a_0), on par with other minimum-tracking parameters we've obtained (i.e, the Fe $3d$ subspaces in the Fe(II) molecular series; see Table 9.3). We indeed observe that $\mathrm{U}^\uparrow$ reaches a maximum of approximately 4.84 eV when $n_{1s} \approx 0.118$. Remarkably, approximately simultaneous to $\mathrm{U}^\uparrow$ reaching a maximum, $n^\uparrow$ reaches a minimum around 0.501 (for 3 a_0 bond length, maximal $\mathrm{U}^\uparrow = 2.14$ for minimized $n^\uparrow = 0.634$). In fact, upon discovery

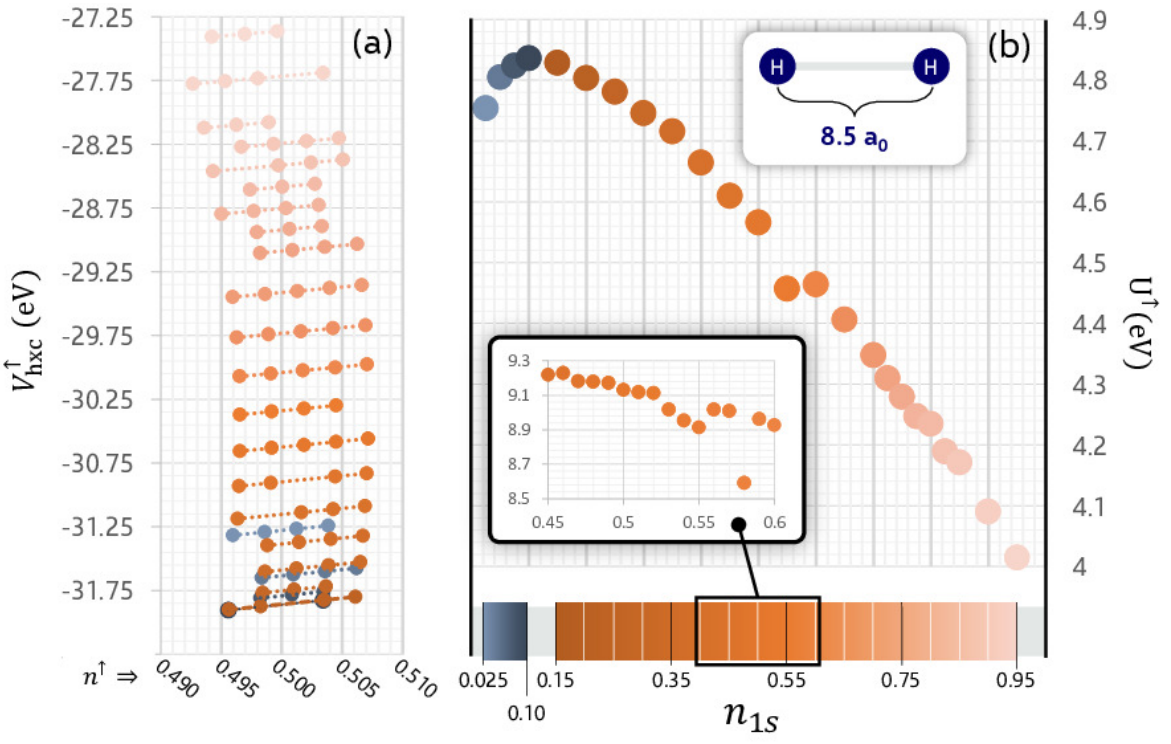

Figure 10.2: (a) Minimum-tracking linear response plots (see Section 4.2) at different values of n_{1s} on H *atom of H_2^+ (bond length* 8.5 a_0*) juxtaposed with (b) their corresponding values of* $\mathrm{U}^\uparrow$ (eV) *(with inset expanding between $n_{1s} = 0.45$ and* 0.6*. Color gradient of n_{1s} is used for clarity. The maximum value of* $\mathrm{U}^\uparrow$ *calculated explicitly was* 4.84 *eV at $n_{1s} = 0.1$.*

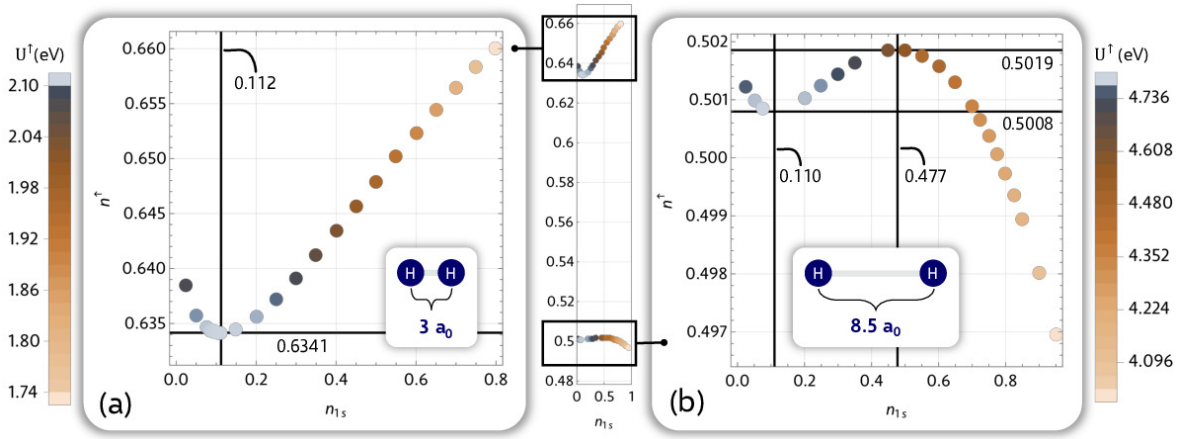

Figure 10.3: Converged occupancy versus projector metric n_{1s} for the H_2^+ molecule with a bond length of (a) 3 a_0 and (b) 8.5 a_0. Extrema coordinates indicated with black lines. Color of marker indicates the $U^\uparrow$ value corresponding to each $\{n_{1s}, n^\uparrow\}$ point.

of this pattern, we promptly looked to the formalism and confirmed that

$$\frac{d(n^\uparrow + n^\downarrow)}{dn_{1s}} = 0 \iff \frac{dU}{dn_{1s}} = 0. \tag{10.8}$$

The resulting proof can be found in Section 10.2. This result remarkably demonstrates that $U^\uparrow$ is, indeed, linked with the total charge of the subspace, albeit in a counterintuitive inverse manner (i.e., $U^\uparrow$ maximizes as n_{1s} minimizes). Albeit without much direct evidence to date, a relation between subspace charge and U has been suspected in the literature, for example, with the atomic versus ortho-atomic projectors[5] or the assertion that U may be related to standard electronic properties like electronegativity[33] or chemical hardness.[34] Recall that we also touched on this relation in the statistical analysis of Section 9.2.2.

Further inspection reveals more extrema. The projectors corresponding to these extrema are itemized in Table 10.1. Across both bond lengths, $U^\uparrow$ is maximized and the $n^\uparrow$ minimized for approximately the same value of n_{1s}, which also roughly corresponds to the most localized radial NGWF, colored light pink in Fig. 10.4. By localized, we refer to the projector's shape, i.e., how quickly it decays with respect to r and how high its peak at $r = 0$ is—a property we describe in Table 10.1 as $\max(\psi)$. The more localized projectors decay quickly before reaching the interstitial region, but reach a higher peak at $r = 0$. According to Fig. 10.4, there's a limit for how localized a projector can be, or more precisely, a limit to the localization of the finite plane-wave basis that we can resolve and beyond which the results are no longer necessarily reliable. There is no physical reason, however, to expect there to be a limit for how delocalized it can be.

It is approximately at this localized limit that $U^\uparrow$ reaches a global maximum. At least in the case of a 3.0 a_0 bond length, this relation can be explained by the fact that $n^\uparrow$ is the most fractionalized for the maximally localized projector and thereby demanding of a more aggressive energy correction. But this justification does not hold at the dissociation limit of 8.5 a_0 bond length because the most localized projector does not, in fact, correspond to the most fractionalized $n^\uparrow$ occupancy. We must

conclude, then, that some other property of the projector function is at least partially implicated in the value of U. One explanation for this relation could be that as the projector delocalizes, it begins to cut into the $1s$ orbital at lower r, leaving some charge unaccounted for.

A clue to this end may come from the curious presence of a $n^{\uparrow}$ maximum at $n_{1s} = 0.477$ for the molecule at 8.5 a_0 bond length, a maximum not present in the 3.0 a_0 case, as shown in Fig. 10.3. Knowing now that the $d\mathrm{U}/d\hat{P}$ environment is mapped onto the $dN/d\hat{P}$ environment, we hypothesized that this maximum could be somehow related to the aberration at $n_{1s} \approx 0.550$ in Fig. 10.2(b). We more finely resolved the region, resulting in the (numerically noisy) inset to Fig. 10.2(b). While unlikely that the $n^{\uparrow}$ maximum at $n_{1s} = 0.477$ corresponds to another, more subtle $\mathrm{U}^{\uparrow}$ extremum, a saddle point in either $\frac{d\mathrm{U}^{\uparrow}}{dn_{1s}}$ or $\frac{dn_{1s}}{dn^{\uparrow}}$ is possible.

	n_{1s}	
Bond length (a_0) ⇒	**3.0**	**8.5**
$\mathrm{U}^{\uparrow}$ maximizes	0.118	0.113
$n^{\uparrow}$ minimizes	0.112	0.110
$n^{\uparrow}$ maximizes	—	0.477
$\max(\psi(r))$ maximizes	0.121	0.121

Table 10.1: Values of n_{1s} corresponding to listed extrema for H_2^+ at either 3.0 or 8.5 a_0 bond length. Numbers obtained from interpolated fits of the data (23 single-point calculations for 3.0 a_0 or 24 for 8.5 a_0).

We propose yet another tentative explanation for the maximum in Fig. 10.3(b). In s-orbital cases, the projector can be thought of as a weighting function; the larger its value at a certain r, the more importance it affords the charge located at that r. That begs the question, why don't we just use a normalized step function to award all charge equal weight? We could hypothetically do this with hydrogen without consequence on the population count, but only because it has one orbital. The electron density is distributed across a system with no regard for which atomic orbital it pertains to. In a system with multiple overlapping subspaces, there's no way to distinguish which charge belongs to which orbital. This is why we need shaped projectors and why those projectors mimic the wavefunction distributions of atomic orbitals—to efficiently discern how much of the charge in a particular region of space belongs to which valence subspace.

Taking the projector's weighting property into consideration would explain why H_2^+ at the dissociation limit behaves as such. Note, again in Fig. 10.4, that at the origin the projector is maximal when $n_{1s} \approx 0.121$ and minimal when $n_{1s} \to 1.0$. In other words, the most localized projector corresponding to lower n_{1s} is better weighting those radii where the charge is expected to be. By contrast, the delocalized projectors, corresponding to $n_{1s} \to 1.0$, lend slightly more weight to the interstitial region, where there is little to no charge, at the expense of the weight applied to the radii with higher density. As n_{1s} increases, the resulting more delocalized projectors are counting less and less of the charge at peak density, thus accounting for the stagnation and decrease in $n^{\uparrow}$ in Fig. 10.3. This is not an issue for H_2^+ at 3.0 a_0 bond length because there is substantial interstitial charge, allowing $n^{\uparrow}$ to keep increasing as the projector functions gradually delocalize.

The observed extrema, particularly the simultaneous maximization of $\mathrm{U}^{\uparrow}$ and $n^{\uparrow}$, are not necessarily occurring at physically reasonable values of the atomic orbital filling. The important takeaway here is this unique link between U and $n^{\uparrow}$. Should it scale to more relevant subspaces and systems,

this finding would render the process of maximizing U significantly more practical. The fact that there exists at all a projector for which the Hubbard U may be maximized is crucial to understanding how to address SIE dynamically.

10.4.2 Fe(II) molecules

The encouraging results from the H_2^+ case are not necessarily applicable to more relevant SIE-ridden subspaces, so we escalate our investigation to the Fe $3d$ orbitals of LS or HS coordinated $[Fe(NH_3)_6]^{2+}$ and $[Fe(CNH)_6]^{2+}$. As shown in Figs. 10.5 and 10.6, these subspaces demonstrate some extrema with respect to variations in the projector as manipulated by changing the fraction of occupancy n_{3d} considered by the atomic solver in constructing the projectors. However, there are extra complexities of these calculations worth highlighting.

For example, for simplicity we tested only variations in n_{3d} between 3.0 and 8.0, setting the Fe n_{4s} to 0.0, meaning we cannot necessarily compare our results to those provided in Chapter 9 since there the projectors have Fe $n_{4s} = 2.0$. The 3.0 and 8.0 range was obtained through trial and error; any occupancy outside of that range did not converge due to numerical instabilities. As in Chapter 9, we use (i) the PAW method in these systems, (ii) the split-valence approach in the atomic solver (see Section 3.2.5), and (iii) technically, we're testing the method on four separate systems: each molecule in both its high- and low-spin-state coordinations. Item (i) is expected to have influence on the projectors even though we cannot, due to technical constraints, visualize how via the projectors in Fig. 10.5, which

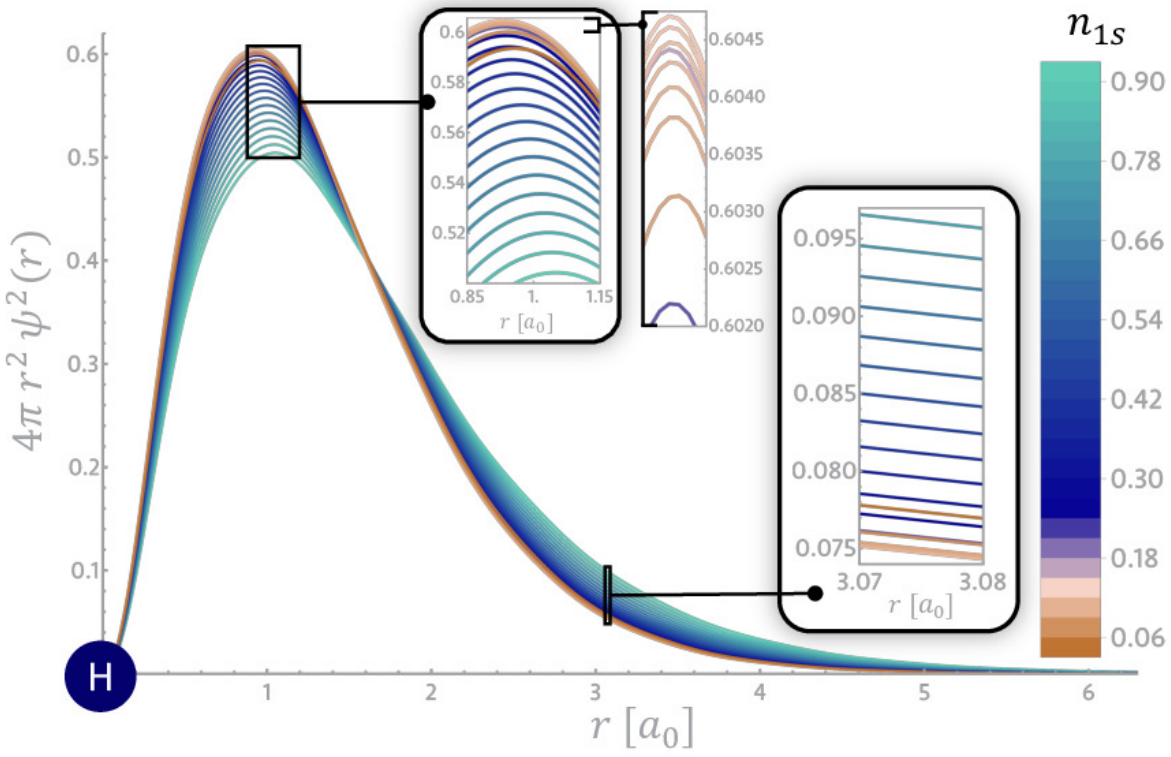

Figure 10.4: Radial distribution functions for the initial radial NGWFs $\psi(r)$ generated by ONETEP *for the* H *atom in* H_2^+ *as* n_{1s} *is varied between 0.025 and 0.95 on both* H *atoms. Color gradient selected for clarity.*

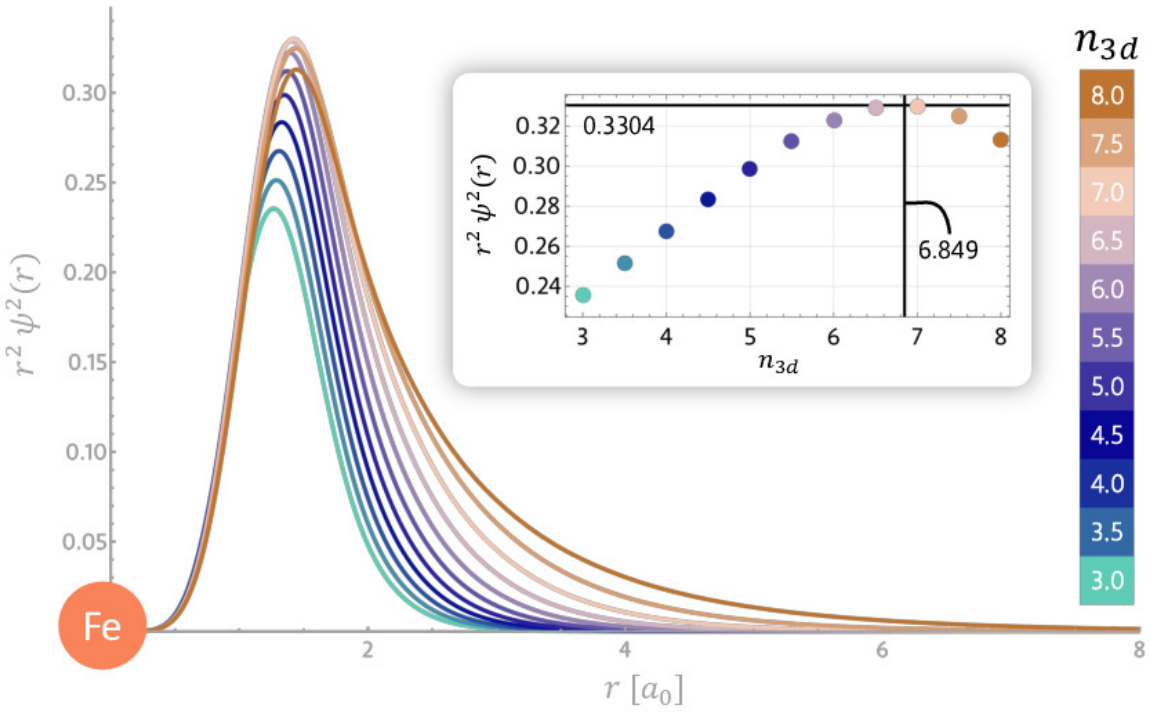

Figure 10.5: Radial distribution functions for the initial radial NGWFs $\psi(r)$ generated by ONETEP *for the neutral* Fe *atom as its* 3d *occupancy n_{3d} is varied between 3.0 and 8.0 (while the* 4s *occupancy is set to 0.0 in the atomic solver). Inset shows the vertical axis coordinate of the peak of each projector as a function of n_{3d}, the maximum of which, indicated by the labeled black lines, is obtained through interpolation of the data set. Color gradient selected for clarity.*

consider only the pseudo-orbitals. As a result, we tested the HPs calculated both with and without the PAW contributions to the HXC potential. Item (i) also renders the represented radial NGWF projectors unnormalized. Finally, item (iii) does not influence the projectors as they are generated for the Fe $3d$ subspace for the neutral atom. Based on the way we performed the perturbations for the non-spin-polarized LS state, we were able to harvest the Hund's J for the Fe $3d$ subspace in addition to its Hubbard U via the simple '2x2' method,[22,30] adding yet another dimension to our analysis.

Interestingly, the Fe $3d$ NGWF projectors do double back on themselves as n_{3d} approximately reaches 6.849, as shown in Fig. 10.5. The NGWFs become slightly more delocalized, and their peaks shift slowly further and further from the nucleus, maximizing at a comparatively high value of n_{3d}. Recall that the neutral H atom NGWFs also became more delocalized with increasing n_{1s}, but their peaks shifted marginally leftwards and maximize at lower occupancy values. It's unclear whether these patterns have any influence on the expectation value of r; the projector variations here are so subtle anyway, it may not have made much of a difference. What is necessary in future, perhaps, is a type of projector with the capacity to dramatically engender changes in $\langle r \rangle$.

There is a conspicuous lack of extrema, however, in both the ground-state occupancies N_{3d} and the HPs that take into account PAW contributions for both molecules in any spin state. This indicates that the PAW contribution, seemingly dominant in the potential response and, for reasons that are not immediately apparent, monotonic, has the effect of extinguishing the effect of the projector extrema. The only exception to this is the LS J for the strong-field ligand molecule $[Fe(CNH)_6]^{2+}$, which (ignor-

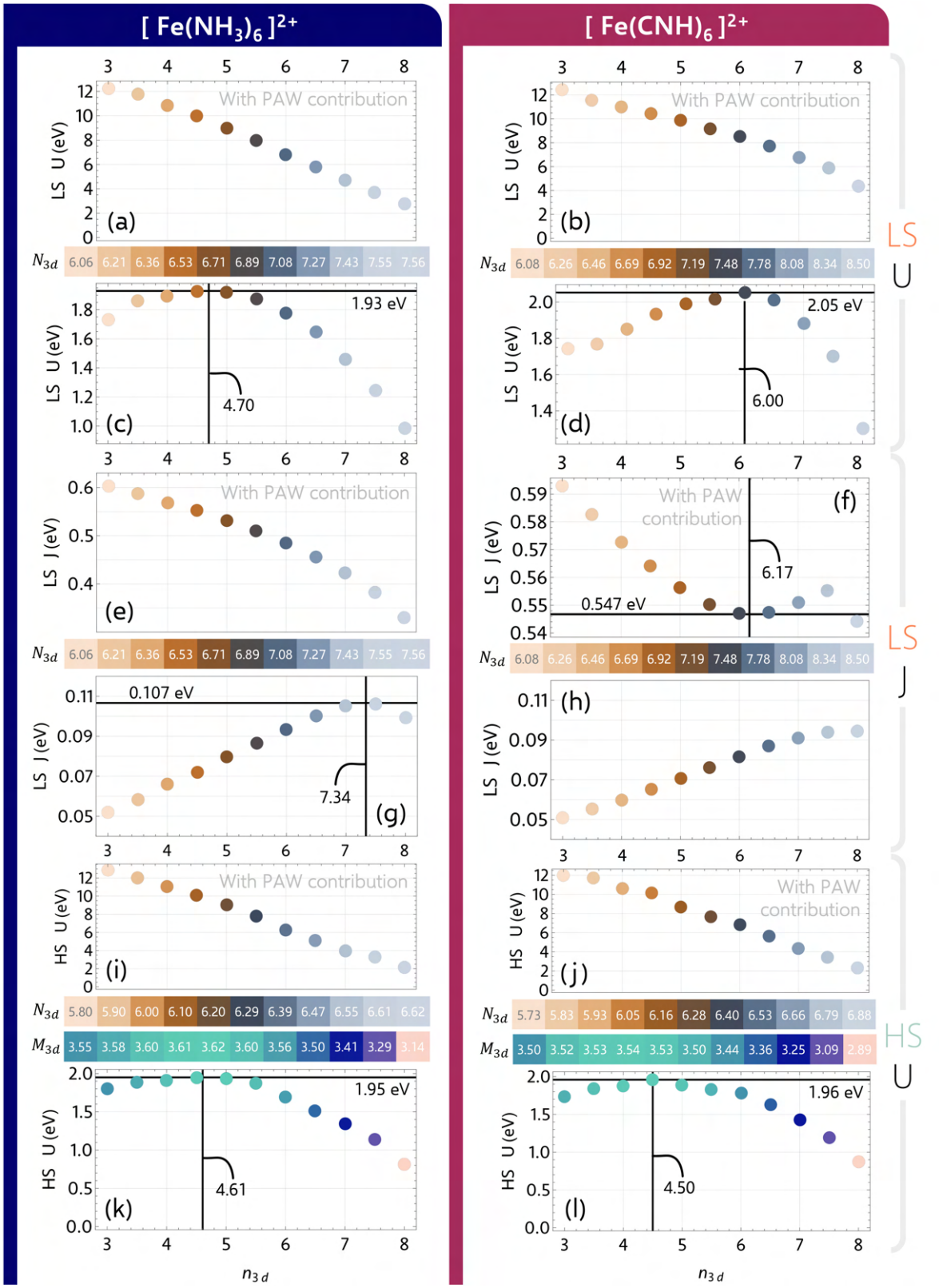

Figure 10.6: Plots (a)-(d) LS U, *(e)-(h) LS* J, *and (i)-(l) HS* U *versus projector metric n_{3d} for the [left column] $[Fe(NH_3)_6]^{2+}$ and [right column] $[Fe(CNH)_6]^{2+}$ molecules. Each shows the HPs calculated both with [(a, b, e, f, i, j); also labeled in gray] and without [(c, d, g, h, k, l); positioned below counterparts w/ PAW] the PAW contribution to $V^{\sigma}_{\mathrm{hxc}}$. Color of marker, corresponding to the swatch above or below it with the same color, indicates the converged occupancy N_{3d} or magnetization M_{3d} of the* Fe 3*d subspace. Extrema coordinates, where interpolated within range, are indicated with black lines and labels.*

ing, perhaps inappropriately, the tail at $n_{3d} = 8.0$) obtains a minimum of 0.547 eV when $n_{3d} = 6.17$ even with the PAW contribution. Even so, because N_{3d} does not extremize within the range of the values tested, this minimum does not correspond to any useful occupancy landmark.

The magnetization for the Fe $3d$ subspace $\boldsymbol{M}_{3d}$, for both molecules in their HS configurations, does present a noticeable landmark; it reaches a maximum value of 3.54 μ_B (3.62 μ_B) for $[Fe(CNH)_6]^{2+}$ ($[Fe(NH_3)_6]^{2+}$). Quite possibly, the local PAW contribution to each spin-resolved density cancels upon subtraction, whereas it compounds upon addition. The projector metrics $n_{3d} = 4.37$ ($n_{3d} = 4.78$) at which these magnetization maxima are obtained roughly correspond to the maxima in the HS U computed without its PAW contribution (numbers labeled in Figs. 10.6(k) and (l)).

Otherwise, maxima are (likely) always obtained when excluding the PAW contributions to the HPs (for Fig. 10.6(h), we extrapolate a maximum at $n_{3d} \approx 8.14$). Again, these do not necessarily correspond in an obvious manner to any occupancy landmarks, and even the maximum obtained by $n_{3d} = 6.85$ in the NGWF peaks in Fig. 10.5 lies slightly out of causal range. It's clear that the U $\Longleftrightarrow$ N mapping in Eq. (10.8) belies a more complex reality outside of the simple H_2^+ model.

Thinking these phenomenon could derive from shifting the response reference, a reference equal to unity in H_2^+ as there is no electron bath from which to draw charge, we looked at the potential response of all valence subspaces v in the bath (of which there are $A - 1$ if A is the total number of atoms in the molecule) with respect to perturbation. This body, which we call L for simplicity, was calculated as

$$\mathrm{L} = \frac{d\left(\sum_{v=1}^{A-1} V_{\mathrm{hxc},v}^{\uparrow} + V_{\mathrm{hxc},v}^{\downarrow}\right)}{d\left(\sum_{v=1}^{A-1} n_v^{\uparrow} + n_v^{\downarrow}\right)}, \tag{10.9}$$

and its magnetic analogue was calculated as

$$\mathrm{L_J} = \frac{d\left(\sum_{v=1}^{A-1} V_{\mathrm{hxc},v}^{\uparrow} - V_{\mathrm{hxc},v}^{\downarrow}\right)}{d\left(\sum_{v=1}^{A-1} n_v^{\uparrow} - n_v^{\downarrow}\right)}. \tag{10.10}$$

These objects, when not particularly noisy for unknown reasons (RMSE on L and $\mathrm{L_J}$ are the same order of magnitude as that on U and J for the noisiest data), sometimes exhibited interesting extrema in their own right, variations that were agnostic to the inclusion or exclusion of the PAW contribution to $V_{\mathrm{hxc}}^{\sigma}$. L was often negative for all systems, while $\mathrm{L_J}$ for the LS state of each molecule was positive. However, the variations were so subtle that categorically, the ratios U/L or J/$\mathrm{L_J}$ did not reveal any extrema outside of those already present in U or J. Other bath response metrics (e.g., the average response on only one species of atom) could warrant further investigation.

10.5 Summary and conclusions

This chapter recounts a methodical interrogation of controlled projector dynamics and their influence on the Hubbard parameters. By harnessing ONETEP's pseudoatomic solver, we were able to gradually manipulate the hydrogen-like radial atomic orbitals used to construct the atomic projectors that isolate the Hubbard manifold from the charge bath. In performing linear response with these

projectors on what were effectively six different systems—the H 1s subspaces of stretched and dissociated H_2^+ molecule, followed by the Fe 3d subspaces of LS- and HS-coordinated $[Fe(NH_3)_6]^{2+}$ and $[Fe(CNH)_6]^{2+}$—we confirmed that it is indeed possible to extremize the Hubbard U and/or Hund's J with respect to subtle changes in projector function. Furthermore, we identified theoretically a mapping of environments: the U landscape is tied to that of the total subspace occupancy. Should it scale to more relevant subspaces and systems, this finding would render the process of maximizing U significantly more practical. The fact that there exists at all a projector for which the Hubbard U may be maximized is crucial to understanding how to address SIE dynamically.

To avoid redundancy at this late stage of the thesis, we outline directions for future research in Section 2 of the forthcoming Final Remarks module.

Bibliography

[1] Y.-C. Wang, Z.-H. Chen, and H. Jiang, The Journal of Chemical Physics **144**, 144106 (2016).

[2] L. A. Mariano, B. Vlaisavljevich, and R. Poloni, Journal of Chemical Theory and Computation **16**, 6755 (2020).

[3] R. Mahajan, I. Timrov, N. Marzari, and A. Kashyap, Phys. Rev. Mater. **5**, 104402 (2021).

[4] I. Timrov, N. Marzari, and M. Cococcioni, Phys. Rev. B **103**, 045141 (2021).

[5] I. Timrov, N. Marzari, and M. Cococcioni, Computer Physics Communications **279**, 108455 (2022).

[6] L. MacEnulty and D. D. O'Regan, Phys. Rev. B **108**, 245137 (2023).

[7] E. Macke, I. Timrov, N. Marzari, and L. C. Ciacchi, Journal of Chemical Theory and Computation **20**, 4824 (2024), pMID: 38820347.

[8] D. D. O'Regan, N. D. M. Hine, M. C. Payne, and A. A. Mostofi, Phys. Rev. B **82**, 081102 (2010).

[9] T. Miyake and F. Aryasetiawan, Phys. Rev. B **77**, 085122 (2008).

[10] J. Avery, *Hyperspherical Harmonics and Generalized Sturmians* (Springer, Dordrecht, 2001) p. 205.

[11] I. N. Levine, "Quantum chemistry," in *Quantum Chemistry* (Pearson, Boston, 2014) Chap. 6, pp. 135–143, 7th ed.

[12] D. J. Griffiths, "Introduction to quantum mechanics," in *Introduction to Quantum Mechanics* (Pearson, Upper Saddle River, NJ, 2005) Chap. 4, pp. 134–140, 1st ed.

[13] H. J. Kulik and N. Marzari, The Journal of Chemical Physics **133**, 114103 (2010).

[14] R. Pnini, Y. Peleg, E. Hecht, and E. Zaarur, *Schaum's Outline of Quantum Mechanics, Second Edition* (McGraw-Hill, USA, 2010).

[15] L. I. Schiff, "Quantum mechanics," in *Quantum Mechanics* (McGraw-Hill, New York, 1968) Chap. 4, pp. 88–99, 3rd ed.

[16] R. Shankar, "Principles of quantum mechanics," in *Principles of Quantum Mechanics* (Springer, Boston, 1994) Chap. 13, 2nd ed.

[17] C.-K. Skylaris, P. D. Haynes, A. A. Mostofi, and M. C. Payne, The Journal of Chemical Physics **122**, 084119 (2005).

[18] N. D. Hine, "Using the pseudoatomic solver to generate NGWFs in ONETEP," (2011), updated February 2016.

[19] A. Ruzsinszky, J. P. Perdew, G. I. Csonka, O. A. Vydrov, and G. E. Scuseria, The Journal of Chemical Physics **126**, 104102 (2007).

[20] A. J. Cohen, P. Mori-Sánchez, and W. Yang, Science **321**, 792 (2008).

[21] G. Moynihan, G. Teobaldi, and D. D. O'Regan, arXiv preprint arXiv:1704.08076 (2017).

[22] E. B. Linscott, D. J. Cole, M. C. Payne, and D. D. O'Regan, Physical Review B **98**, 235157 (2018).

[23] J. Yang, "Opium - pseudopotential generation project," (2018).

[24] A. M. Rappe, K. M. Rabe, E. Kaxiras, and J. D. Joannopoulos, Phys. Rev. B **41**, 1227 (1990).

[25] I. Grinberg, N. J. Ramer, and A. M. Rappe, Phys. Rev. B **62**, 2311 (2000).

[26] G. Moynihan, *A self-contained ground-state approach for the correction of self-interaction error in approximate density-functional theory*, Physics, Trinity College Dublin, Trinity College Dublin, School of Physics (2018).

[27] J. P. Perdew, K. Burke, and M. Ernzerhof, Phys. Rev. Lett. **77**, 3865 (1996).

[28] G. J. Martyna and M. E. Tuckerman, The Journal of Chemical Physics **110**, 2810 (1999).

[29] N. D. M. Hine, J. Dziedzic, P. D. Haynes, and C.-K. Skylaris, The Journal of Chemical Physics **135**, 204103 (2011).

[30] D. S. Lambert and D. D. O'Regan, Phys. Rev. Res. **5**, 013160 (2023).

[31] P. E. Blochl, Physical Review B **50**, 17953 (1994).

[32] F. Jollet, M. Torrent, and N. Holzwarth, Computer Physics Communications **185**, 1246 (2014).

[33] X. Dong, A. R. Oganov, H. Cui, X.-F. Zhou, and H.-T. Wang, Proceedings of the National Academy of Sciences **119**, e2117416119 (2022).

[34] G. C. Moore, M. K. Horton, E. Linscott, A. M. Ganose, M. Siron, D. D. O'Regan, and K. A. Persson, Phys. Rev. Mater. **8**, 014409 (2024).

Final Remarks

Final Remarks

Harnessing the full potential of quantum materials necessitates both ingenuity and precision in addressing the limitations of contemporary theoretical methods. This dissertation underscores the pivotal role of DFT+U+J in refining our understanding of complex, open-shell systems by mitigating intrinsic errors and delivering more reliable predictions of material properties. By systematically investigating spin-based metrics and elucidating the interplay between corrective parameters and projector functions, this research advances the accuracy and applicability of Hubbard-corrected methods.

The contributions relayed herein—the precise conclusions and future work of which are transmitted part-by-part in Sections 10.1 and 10.2—not only expand the boundaries of first-principles modeling but also pave the way for the automation and scalability of high-throughput computational frameworks. A major extension of the hypotheses herein developed would take into account challenging magnetic systems with non-collinear spins or multiple magnetic sublattices and/or the incorporation of spin-orbit coupling. At the current level of sophistication regarding spin considerations, however, one of the loudest messages emerging from all projects combined is a general call for more considerate construction of DFT+U+J-type functionals to account for the unique static-correlation phenomena at play in strongly covalent and magnetic systems. This much becomes acutely evident in Chapters 7 and 9, where we observe a black-box cancellation of magnetic "error" terms scaled by identical, but not magnetic-environment-informed, Hubbard parameters, in addition to the general failure of the Hund's J term in rendering accurate total energy differences. Another global message stipulates that closer attention be paid to exactly *how* the projector functions isolate the Hubbard manifold; i.e., it's not simply through the charge they encapsulate, but what charge is encapsulated and at what weight. And let's not forget the prevalent role played by linear response, the importance of which was frequently underscored as we prodded the protocol's boundaries and stretched it to its limits. More assertive conclusions and precise extensions to follow.

It remains essential, and even more so as (semi-)local DFAs expand their realms of achievable accuracy to include coarse-grained spin-based properties, to work to establish the regime of reliability of first principles for DFT+U+J total-energy differences and to explore and delineate its remaining weaknesses and ambiguities. As the demand for innovative materials grows, so too must the tools we use to discover and design them. This work represents a meaningful step toward that future, offering a robust foundation for continued exploration in quantum materials and beyond.

1 Conclusions

All useful theses are accompanied by a sturdy and pertinent theoretical background. Part I, which the author ultimately wrote for their younger self, is a romanticized story about the development of the DFT field of electronic structure theory: the quantum mechanical foundations (Chapter 1) undergirding a mathematical understanding of many-body particle interactions; the utility and versatility of the collinear-spin DFT formalism (Chapter 2); and finally, the practicalities, approximations, and automations of the everyday material simulation (Chapter 3). The theory and background spill into Chapter 4, assigned to Part II for logistical purposes but no less foundational or generally applicable. There, we introduce and discuss the state-of-the-art for two linear response methods for the determination of the Hubbard U and Hund's J parameters.

Part II continues on to provide a detailed technical guide to `lrUJ`, the renovated SCF linear response post-processing utility programmed for the ABINIT software suite, and to a lesser extent the intricacies of ABINIT's DFT+U+J implementation. The `lrUJ` utility is designed to automate the first-principles determination of the Hubbard parameters to make the corrective technique more accessible to users of ABINIT and potentially other DFT codes. Unique features of this utility include (i) polynomial regression and error analysis for versatility across subspaces and evaluation of results, (ii) AbiPy Python plotting facilities to facilitate *in situ* data visualization, and (iii) comprehensive documentation, rendering the DFT+U+J methodology and its implementation more accessible and user-friendly. In parallel, we delve into the challenges posed by the PAW method and discuss strategies to address non-linear responses as well as ABINIT-specific pathologies. These insights are valuable for improving the precision and reliability of DFT+U+J simulations across platforms. Overall, this primarily programmatic work serves as both a practical guide and a resource for advancing the calculation of Hubbard parameters in electronic structure simulations.

In Part III, we interrogate the prototypical Mott-Hubbard insulator NiO, calculating its electronic structure in its three main stable, meta-stable or enforceable magnetic configurations: the AF_I, AF_{II}, and FM states. We establish accurate Heisenberg exchange-coupling parameters in terms of strict density-functional accessible total energy differences between magnetic configurations. We concisely compare these parameters against other available theoretical values—such as those from costly hybrid functionals—and available experimental parameters (i.e., derived from magnon frequencies). Furthermore, we reevaluate spin-parametrization conventions in the Heisenberg model as well as the aptness of their translation to untreated strongly correlated subspaces enveloping non-integer quantities of charge in the DFT context. Optimization of this parameter space corresponds to the particular combination of (i) a rudimentary-quantum, atomic-sphere-restricted intra-atomic spin moment ($|\mathbf{S}^{\mathrm{AS}}| = \sqrt{2}\,\mathrm{S}_z^{\mathrm{AS}}$), and (ii) a spin-parametrization scheme that assumes $|\mathrm{S}_{\mathrm{FM}}| = |\mathrm{S}_{\mathrm{AF_I}}| = |\mathrm{S}_{\mathrm{AF_{II}}}|$. The opposing effects of (i) and (ii) effectively cancel to yield $\{J_1, J_2\}$ exchange pairs with % RMS errors as low as 13%, an advance upon the state-of-the-art. Our investigation inspired a detailed examination of the sensitivity of the first-principles Hubbard U and Hund's J parameters to choices about PAW-based population analysis and reevaluation. We particularly recommend ABINIT's `dmatpuopt = 3` population analysis option, corresponding to the once-normalized projection of the PAW basis functions on bound AE atomic eigenfunctions and truncated at the PAW augmentation radius. We assessed several

DFT+U+J corrective functionals using *in situ*-calculated U and J parameters—comparing them to those where the {U, J} pairs were employed in the same magnitude to functionals for all MOs—and identified an effective, broadly implemented, minimally empirical, and straightforward workflow for rendering accurate spin-based total energy differences.

Part IV veers into quantum chemistry territory, underscoring an emerging class of technology based on SCO, a mechanism long observed and understood macroscopically that exhibits high potential for sustainable sensing and storage applications like carbon capture and spintronic devices. This study took as test cases a series of fictitious octahedrally coordinated Fe(II) molecules spanning the more covalent end of the ligand field spectrum, specifically querying whether the Hubbard-like corrective functionals, especially those incorporating the Hund's J, in spin DFT can achieve accurate adiabatic energy differences. Our recently established international collaboration addressed this query first by calculating and statistically analyzing trends of a dataset of 140 Hubbard U and Hund's J pairs, determined via linear response and with a variety of topical projector functions. Our results reveal that the projector significantly affects the magnitude of occupancy within the Hubbard manifold in a straightforward way. However, this clarity does not directly correlate with a specific pattern in response rigidity or the magnitude of screening. In essence, the projector functions impact not only the total charge calculated within the Hubbard manifold but also the nature of the charge being included—whether interstitial, off-axis, core, or otherwise. This selection exerts a notable influence on both the unscreened and screened response functions. The ONETEP Hubbard parameters are then applied via a range of common Hubbard functionals. We concluded that the simplest combination of techniques to yield reliable spin-state energetic properties with respect to those obtained by prodigious but costly wavefunction methods includes the Dudarev DFT+U_{eff} functional and, again, the employment of the same Hubbard parameter values regardless of the molecule's spin state. The results further illuminated the failure of the Hund's J in furthering DFT+U's already robust capacity to obtain accurate adiabatic energy differences. Perhaps most surprisingly, we unveil staggering differences between the U and J parameters calculated near-identically across three open-source DFT programs (ABINIT, ONETEP, and QUANTUM ESPRESSO) pointing to both (i) the potency of the basis-set projector functions and (ii) the breakdown of the equivalence between the minimum-tracking and SCF LR methods. This investigation maps previously uncharted limitations of first-principles DFT+U+J and precisely highlights the areas for improvement therein.

Lastly, Part V interrogates the projector functions directly and dynamically. Utilizing ONETEP's pseudoatomic solver, we incrementally modified the hydrogen-like radial atomic orbitals used to construct the NGWF projectors responsible for isolating the Hubbard manifold from the surrounding charge environment. Linear response calculations were performed using these projectors across six distinct systems: the H 1*s* subspaces of stretched and dissociated H_2^+ molecule and the Fe 3*d* subspaces of LS- and HS-coordinated $[Fe(NH_3)_6]^{2+}$ and $[Fe(CNH)_6]^{2+}$. This confirmed the feasibility of extremizing the Hubbard U and/or Hund's J by fine-tuning the projector functions. The study theoretically established a correlation between the U landscape and that of the total subspace occupancy. If scalable to larger subspaces and more complex systems, this insight could make the optimized isolation of SIE-ridden far more practical. The existence of projectors that maximize U is particularly significant for developing strategies to dynamically mitigate SIE.

2 Extensions and future work

When operationally synchronized, all cogs in a machine enable progress through the transfer of momentum. The following ideas for extensions and future work is intended to oil the gears, so to speak.

The only extension of Part I is the hope that one day, the author's work will feature in that romanticized story on the development of DFT electronic structure theory methods.

The work of Part II is what really gets the author's creative juices flowing. Intercalating electronic structure with more state-of-the-art statistical techniques for regression and error analysis are on the immediate horizon. In particular, a more solidified mathematical basis for the ζ-axis symmetry of linear response is crucial to validate some technical aspects of the `lrUJ` utility as currently implemented. What would be interesting to look at are more sophisticated unbiased regression-error quantifiers that incorporate ζ-axis or other types of symmetry considerations. With applications in electronic structure and beyond, this type of research would pave the way for concrete techniques to avoid overfitting. Moreover, the use of polynomial regressions for linear response has no physical basis. Turning a critical eye to the nature of the (non-)linearity of response in various systems would permit investigation of better, more fitting interpolating functions.

On the programmatic implementation of LR in `lrUJ`, specifically, immediately obvious expansions include the incorporation of minimum-tracking LR in ABINIT, with its simple and scaled 2×2 variations. This would facilitate the direct comparison between SCF and minimum-tracking LR called for in Part IV on SCO molecules. More technically, developing automated `lrUJ` workflows for parameter optimization would reduce user intervention and enhance reproducibility. Crucially, all developments here would require emphasis on comprehensive and user-friendly documentation in accordance with `lrUJ`'s founding ethos. Taking that one step further, it's good idea to expand educational resources and/or host workshops to train researchers in implementing these methods effectively.

In Part III (and, relatedly, Part IV), the prerogative is clear: figure out the black-box cancellation of errors between energetics of magnetic states, either through the methodical dissection of the current Hubbard functionals or through the development of more sophisticated, spin-state-attentive Hubbard functionals. Work on both fronts is currently underway at qToM (see Appendix A4 for a sample of this work). As mentioned earlier, moreover, the optimization techniques developed herein, specifically with regards to the spin-parameterization schema, are due for upgraded formalism built around complex magnetic systems with non-collinear spins or multiple magnetic sublattices. Incorporating spin-orbit coupling effects into exchange-coupling calculations to explore anisotropic interactions is also of particular relevance. As it relates to population analysis, addressing limitations in the PAW method as it is currently embedded in the ABINIT DFT+U+J ecosystem is on the to-do list, as well.

Avenues for expansion uncovered by Part IV include, first and foremost, a methodical revisitation of the determination of the unscreened response function in both the SCF and minimum-tracking linear response methodologies. Direct comparison will be necessary, involving the implementation of minimum-tracking LR into a plane-wave SCF program (why not ABINIT?) or SCF linear response into a linear-scaling algorithm (why not ONETEP?). Such an undertaking would enable the projector-based differences in HPs to be detached from the methodology-based differences in the population analysis of the Hubbard manifold. Next up, a continuation of the initiatives started in the French

Research Residency: application of these now well-thought-out methodologies and best practices to ferrous hexacyanometallate systems (Prussian Blue analogs) for which the Fe(II) molecules are localized and periodically repeating constituents. Getting DFT+U+J to work on such challenging systems would amount to considerable progress in computationally feasible materials simulation. The presence of two differently magnetized *d* subspaces on Fe centers in the same ground state could offer clarity on the surprisingly incomparable Hubbard functional energetics between magnetic orderings or spin states of the same material. In a different direction completely, we envision leveraging machine-learning models to either (a) predict U and J parameters from molecular properties or statistical analyses of Hubbard parameters, or (b) as our collaborators at UGA have at the ready, reinforce GGA potentials for strongly covalent SCO systems that span the ligand field spectrum, potentially expediting calculations for large material datasets.

Since the preliminary investigation conducted in Part V is only proof-of-concept, we restricted our assessment to the most convenient level of projector variation, which is quite subtle in terms of dysmorphia compared to what we hope to achieve. A more flexible and dramatic change would perhaps stretch the orbital in a spherically symmetric manner along the atomic radius, as this would alter the expectation radii of the electronic subspaces and, by extent, the charge localization. An obvious next step in this work, then, is to upgrade from projectors comprising pseudoatomic orbitals to those comprising a linear combination of atomic and molecular orbitals. The integrity of the mapping of the Hubbard U environment to the subspace total occupancy needs to be subjected to a variety of projector classes that manage to, in series, contract, dilate, transpose, or even completely transform the subspace with which the Hubbard parameters are to be derived and on which they are applied prescriptively. Moreover, a bigger challenge presents itself when we begin to apply this methodology to solid-state periodic systems, such as a TMO, Prussian Blue analogue, or an ion-intercalated battery cathode compounds like Li_xFePO_4. The idea is to obtain a better understanding of what projector properties, beyond the capacity to encompass charge, influence the emergence of HP extrema. In doing so, we would gain insight into the exact spatial manifestation of DFT self-interaction and static-correlation errors. Ambitiously, we envisage design and computational implementation of a diagnostic protocol of the extent of these errors and their manifestation in any DFT quantum material system, and prescribe maximally effective treatment of delocalization error *in situ*.

Appendices

Appendix A

Supplemental information for Part I

Density functional theory foundations- and implementation-related topics are expanded in the following appendix. In Section 1, we discuss the Hohenberg-Kohn theorems for DFT without spin considerations. Section A2 talks about the Kohn-Sham auxiliary system and Section A3 conventions regarding the writing and meaning of partial derivatives in physics as opposed to mathematics. Following this, Section A4 expands on the BLOR Hubbard functional. Finally, we develop considerations related to the compensation charge density in the PAW method in Section A5.

1 The Hohenberg-Kohn theorems

Density Functional Theory (DFT) emerged in the 1960s as the fruit of two theorems by Hohenberg and Kohn,[1] which proved not only that the total energy of a system of electrons immersed in an external potential is a unique functional of the electronic density $\rho(\mathbf{r})$, but that the same total energy functional $E_{\text{DFT}}[\rho]$ is minimized when $\rho = \rho_0(\mathbf{r})$, the ground-state electronic density. We transcribe these derivations and discuss the consequences of these two theorems presently, following the format as presented in Ref. [1].

1.1 The first Hohenberg-Kohn theorem

Theorem: In a system of N electrons moving under the influence of an external potential V, V is a unique functional of the system's ground-state charge density $\rho_0(\mathbf{r})$. That is, $\rho_0(\mathbf{r}) \Leftrightarrow V$.

Proof: In the system described, $\rho_0(\mathbf{r})$ is obtained directly from the ground-state electronic wavefunction ψ. Since ψ is the solution to the electronic eigenvalue problem in Eq. (1.5), ψ is considered a functional of V. Therefore, $V \Rightarrow \rho_0(\mathbf{r})$.

We must now prove that $\rho_0(\mathbf{r}) \Rightarrow V$, and we will do so by contradiction. Assume that there are two distinct external potentials V and V' that give rise to the same $\rho_0(\mathbf{r})$. As a condition of their distinctness, $V - V' \neq C$, because the wavefunction and charge density of either system is unchanged by addition of an arbitrary constant C. Furthermore, each potential corresponds to its own

wavefunction equation, giving rise, respectively, to electronic Hamiltonians $\hat{H}$ and $\hat{H}'$, ground-state eigenenergies E_0 and E_0', and ground-state wavefunctions ψ_0 and ψ_0', the latter of which are unequal.

By virtue of its status as the ground-state energy,

$$E_0' = \langle \psi' \mid \hat{H}' \mid \psi' \rangle < E_0' = \langle \psi \mid \hat{H}' \mid \psi \rangle = \langle \psi \mid (\hat{H} + V - V') \mid \psi \rangle, \tag{A.1}$$

and thus

$$E_0' < E_0 + \int [V(\mathbf{r}) - V'(\mathbf{r})]\, \rho_0(\mathbf{r})\, d\mathbf{r}. \tag{A.2}$$

The same conclusion can be drawn by swapping primed and unprimed variables, yielding

$$E_0 < E_0' + \int [V'(\mathbf{r}) - V(\mathbf{r})]\, \rho_0(\mathbf{r})\, d\mathbf{r}. \tag{A.3}$$

Addition of Eqs. (A.2) and (A.3) results in the absurd inequality,

$$E_0 + E_0' < E_0 + E_0' \,. \tag{A.4}$$

Thus, only one external potential corresponds to one ground-state density (i.e., $\rho_0(\mathbf{r}) \Rightarrow V$), which completes the bijective mapping $\rho_0(\mathbf{r}) \Leftrightarrow V$. □

1.2 The second Hohenberg-Kohn theorem

Theorem: The density functional that yields the ground-state energy of the system delivers the lowest energy if and only if the input density is the ground-state density $\rho_0(\mathbf{r})$. That is, $E_V[\rho_0(\mathbf{r})] = E_0 \leq E_V[\rho(\mathbf{r})]$.

Proof: As priorly mentioned, ψ is a functional of $\rho(\mathbf{r})$. So are, it follows, the electronic kinetic and interaction energies, defined as $\hat{H}_e$ in Eq. (1.4). We therefore define a universal functional $F[\rho(\mathbf{r})]$, which remains true for any electronic system subject to any external potential V:

$$F[\rho(\mathbf{r})] = \langle \psi \mid \hat{H}_e \mid \psi \rangle \,. \tag{A.5}$$

The total energy functional corresponding to a particular V is

$$E_V[\rho(\mathbf{r})] = F[\rho(\mathbf{r})] + \int V(\mathbf{r})\, \rho(\mathbf{r})\, d\mathbf{r}, \tag{A.6}$$

where, for some particular $\rho_0(\mathbf{r})$, $E_V[\rho_0(\mathbf{r})] = E_0$, its ground-state energy. We restrict $\rho_0(\mathbf{r})$ under the following condition:

$$N[\rho_0(\mathbf{r})] = \int \rho_0(\mathbf{r})\, d\mathbf{r} = N \,. \tag{A.7}$$

For such a system, which has N particles, the energy functional corresponding to any ψ is

$$E_V[\psi] = \langle \psi \mid V \mid \psi \rangle + \langle \psi \mid \hat{H}_e \mid \psi \rangle, \tag{A.8}$$

which is minimized for a particular ground-state wavefunction $\psi_0 \in \{\psi\}$, where $\{\psi\}$ is the set of all N-body antisymmetric wavefunctions. Let $\psi \in \{\psi\}$ be the ground state associated with a different external potential V', yielding a ground-state density $\rho(\mathbf{r})$. By Eq. (A.8) and the definition of the universal functional,

$$\overbrace{\underbrace{F[\rho(\mathbf{r})] + \int V(\mathbf{r})\,\rho(\mathbf{r})\,d\mathbf{r}}_{E_V[\rho(\mathbf{r})]}}^{E_V[\psi]} \geq \overbrace{\underbrace{F[\rho_0(\mathbf{r})] + \int V(\mathbf{r})\,\rho_0(\mathbf{r})\,d\mathbf{r}}_{E_V[\rho_0(\mathbf{r})]}}^{E_V[\psi_0]} \tag{A.9}$$

$$\therefore E_V[\rho(\mathbf{r})] \geq E_0. \tag{A.10}$$

Thus, the ground-state density will always yield the lowest, ground-state energy of the system. □

The second Hohenberg-Kohn theorem establishes the variational principle for a density-centered formulation of the many-body problem. Coupled with the first, one is in a position to make some very powerful and workable conclusions. For example, the (non-degenerate) ground-state electronic wavefunction as it is used in Eq. (1.5) is a unique functional of the ground-state density. That is,

$$\psi_0(\{\mathbf{r}_i\}) = \psi[\rho_0(\mathbf{r})]. \tag{A.11}$$

The ground-state expectation value of any observable $\hat{O}$ is thus a functional of $\rho_0(\mathbf{r})$:

$$O_0 = O[\rho_0(\mathbf{r})] = \langle \rho_0(\mathbf{r}) \,|\, \hat{O} |\, \psi[\rho_0(\mathbf{r})] \rangle \,. \tag{A.12}$$

By reformulating a multi-atomic system's observables—chief among them the energy, shown in Eq. (A.13)—in terms of the electronic density, one may find the ground state and its properties through variational minimization of

$$E_{\mathrm{DFT}}[\rho(\mathbf{r})] = T[\rho(\mathbf{r})] + E_{ee}[\rho(\mathbf{r})] + \int V(\mathbf{r})\,\rho(\mathbf{r})\,d\mathbf{r}, \tag{A.13}$$

where T is the electron kinetic energy of the system, E_{ee} is the electron-electron interaction energy, and $V(\mathbf{r})$ is the external potential term as a function of real-space coordinates, which includes the nucleus-electron interactions in addition to any other potential (e.g., electromagnetic field) in which the system is immersed.

What this means is we no longer have to keep track of the locations of individual electrons. Effectively, what DFT does is fractionalize the electron—breaking the electron into pieces of charge and attributing the property of charge to the space it most probabilistically occupies, yielding a continuous charge density. That continuity makes electrons easier to work with mathematically and simplifies significantly the computations required in solving the many-body problem. The only obstacle is that the precise kinetic and electron-electron interaction energy functionals remain unknown.

2 The Kohn-Sham auxiliary

To truly harness the power of DFT as a theory and approximatively circumvent the issue of the unknown universal functional, one must consider an auxiliary system identical in every way to that resulting from the BOA but with non-interacting electrons. In 1965, Kohn and Sham showed that the ground-state density of both the exact and auxiliary systems are identical.[2] The derivation of the Kohn-Sham (KS) equations in the spin-restricted case follows the same logic as that of the spin-independent case, which we transcribe below, mirroring the description in Ref. [3]. Both approaches map the system of N interacting electrons onto a system of N non-interacting electrons with the same density, expressed as

$$\rho(\mathbf{r}) = \sum_{i}^{N} |\psi_i(\mathbf{r})|^2 \,, \tag{A.14}$$

where $\{\psi_i(\mathbf{r})\}$ are called the KS orbitals or KS wavefunctions. To ensure the same number of electrons in this auxiliary system, we impose the normalization constraint

$$\int \rho(\mathbf{r})\, d\mathbf{r} = N \,. \tag{A.15}$$

Using the KS orbitals, we can express the kinetic energy functional of the interacting system in Eq. (A.13) as

$$T[\rho(\mathbf{r})] = \underbrace{\left(-\frac{1}{2} \sum_{i}^{N} \int \psi_i(\mathbf{r}) \nabla^2 \psi_i(\mathbf{r})\, d\mathbf{r} \right)}_{T_s[\rho(\mathbf{r})]} + \Delta T[\rho(\mathbf{r})] \,, \tag{A.16}$$

featuring the single-particle kinetic energy functional $T_s[\rho(\mathbf{r})]$ and a corrective term $\Delta T[\rho(\mathbf{r})]$. In other words, we approximate the total kinetic energy of the system of interacting electrons as the sum of kinetic energy terms pertaining to N non-interacting electrons, capturing non-descriptively in a separate term the effect of exchange and correlation on the electron movement.

Analogously, we may expand the electron-electron interaction energy E_{ee} as the sum of the Hartree energy E_{Ha}—the Coulomb repulsion of constituent one-electron densities—and a corrective term representing all other exchange and correlation effects not made explicit. That is,

$$E_{ee}[\rho(\mathbf{r})] = \underbrace{\frac{1}{2} \iint \frac{\rho(\mathbf{r})\, \rho(\mathbf{r}')}{|\mathbf{r} - \mathbf{r}'|} d\mathbf{r}\, d\mathbf{r}'}_{E_{\text{Ha}}[\rho(\mathbf{r})]} + \Delta E_{ee}[\rho(\mathbf{r})] \,. \tag{A.17}$$

Inserting Eqs. (A.16) and (A.17) in Eq. (A.13) yields

$$E_{\text{KS}}[\rho(\mathbf{r})] = T_s[\rho(\mathbf{r})] + E_{\text{Ha}}[\rho(\mathbf{r})] + E_{\text{xc}}[\rho(\mathbf{r})] + \int V(\mathbf{r}) \rho(\mathbf{r})\, d\mathbf{r}, \tag{A.18}$$

where $E_{\text{xc}}[\rho(\mathbf{r})] = \Delta T[\rho(\mathbf{r})] + \Delta E_{ee}[\rho(\mathbf{r})]$ is the infamously elusive exchange-correlation (XC) energy functional discussed in Section 2.3.1.

Section 2.2.2 establishes the existence of a minimal energy functional achieved with the ground-

state density. In the calculus of variations, we may therefore identify this energy functional as a stationary point subject to the constraint that the integrated density is equal to the total number of electrons N, i.e.,

$$\delta\left[E_{\mathrm{KS}}[\rho(\mathbf{r})]+\mu\left(N-\int\rho(\mathbf{r})\,d\mathbf{r}\right)\right]=0, \tag{A.19}$$

where μ is the chemical potential, found then via the Euler-Grange equation corresponding to Eq. (A.19) as

$$\mu=\frac{\delta E_{\mathrm{KS}}[\rho(\mathbf{r})]}{\delta\rho(\mathbf{r})}=\frac{\delta F_{\mathrm{KS}}[\rho(\mathbf{r})]}{\delta\rho(\mathbf{r})}+V(\mathbf{r}). \tag{A.20}$$

Eqs. (A.19) and (A.20) are precisely those obtained in applying DFT to a system of non-interacting electrons subject to a potential modeled by the derivative of Eq. (A.18) with respect to $\rho(\mathbf{r})$,

$$V_{\mathrm{KS}}[\rho(\mathbf{r})]=V(\mathbf{r})+\frac{\delta E_{\mathrm{xc}}[\rho(\mathbf{r})]}{\delta\rho(\mathbf{r})}+\int\frac{\rho(\mathbf{r}')}{|\mathbf{r}-\mathbf{r}'|}\,d\mathbf{r}'\,, \tag{A.21}$$

the last term of which is called the Hartree potential. Ground-state solutions may thus be sought variationally in the more restrained KS-energy eigenspace,

$$\left[-\frac{1}{2}\nabla^2+V_{\mathrm{KS}}(\mathbf{r})\right]\psi_i(\mathbf{r})=\epsilon_i\psi_i(\mathbf{r}), \tag{A.22}$$

wherein the set of wavefunctions $\{\psi_i(\mathbf{r})\}$ are the KS orbitals introduced earlier, and ϵ_i is the corresponding energy profile of the system. Under the KS scheme, therefore, solution to the electronic eigenvalue problem of N bodies is reduced to solution of N single-body wavefunction equations, one for each KS orbital $\psi_i(\mathbf{r})$. The only obstacle for practical implementation of the KS scheme remains the definition of E_{xc}.

3 Conventions concerning the writing of partial derivatives in physics

Due to the pervasiveness and complexity of functions that are both explicitly and implicitly functions of certain variables, physicists modified the tenets of calculus to allow for their compatible existence.

Canonically, physicists differentiate between the concepts of the 'total derivative,' in which the chain rule needs to be applied, and the 'explicit derivative,' in which the chain rule is not applied. The former is denoted by a regular 'd,' whereas the latter is indicated by a 'δ.' This deviates largely from standard mathematical conventions, however. Ref. [4] explains the intricacies between the mathematician's convention, denoted M, and the physicist's convention P, and furthermore provides a link between them called M+, which is identical to convention P but maintains the nomenclature of convention M. Here, we will summarize the convention P and how it differs from convention M.

In the convention P, there is no discrimination between the total and partial derivatives, between d or δ. Instead, all derivatives are considered total derivatives and may be represented by d. This liberates δ to be used for other purposes—notably, to identify a derivative with respect to an explicit variable only, not an implicit one.

The necessity for such a definition becomes obvious when looking at mixed functions, (i.e., functions that depend both explicitly and implicitly on a particular variable). An example of a mixed

function is the following:

$$g(f(h(x)), z(x, y), x, y)$$

Here, g is explicitly a function of f, z, x and y. By contrast, g is implicitly a function of x and y. Consider taking the derivative of this function with respect to x. In convention P,

$$\frac{dg(f(h(x)), z(x, y), x, y)}{dx} = \frac{\delta g}{\delta f}\frac{\delta f}{\delta h}\frac{dh}{dx} + \frac{\delta g}{\delta z}\frac{dz}{dx} + \frac{\delta g}{\delta x}$$

In convention M, the derivative of a mixed function like this would simply be disallowed because under its nomenclature, you would end up with a $\frac{dg}{dx}$ on both sides of the equation. This ambiguity is fixed in convention M+ with the introduction of a clarifying $|_e$ to indicate when a partial derivative is being taken explicitly. Convention P simply replaces $|_e$ with the δ, and so is identical to M+.

4 The BLOR Hubbard functional

Many failures of approximate DFT functionals can be traced back to their lack of adherence to the two physical constraints introduced in Section 2.4: (a) the piecewise linearity condition with respect to fractional electron count, and (b) the constancy condition with respect to fractional magnetization. The breaking of (a) leads to the many-electron SIE, and the breaking of (b) leads to SCE. The generalization of these two physical constraints is referred to as the flat-plane condition.

Consider, for example, a two-electron system, whose total energy $E_{\text{tot}}[N_{\text{tot}}, M_{\text{tot}}]$ may be visualized as two flat planes fused with derivative discontinuity at the $N_{\text{tot}} = 1$ line. This type of flat plane demonstrates adherence to the convexity condition:

$$2E_{\text{tot}}[N_{\text{tot}}] < E_{\text{tot}}[N_{\text{tot}} + 1] + E_{\text{tot}}[N_{\text{tot}} - 1] \tag{A.23}$$

For multi-atomic systems, there is a difference between what happens on a global scale (i.e., for the entire system comprising multiple, isolated atoms) and a local scale (i.e., fractional charge changes on each atomic site). When the system has fractional occupancies at more than one of its atomic sites, local SIE and local SCE—which arise from changes in orbital occupancy, keeping the total integer number of electrons in the whole system constant—are responsible for incorrect total energies globally. By contrast, global SIE is primarily quadratic in nature. If we assume the same for local SIE, then one should be able to add to an atomic site's energy a rectifying term of the form

$$E_{\text{U}} = \frac{\text{U}_{\text{eff}}}{2}[(N - N_0) - (N - N_0)^2] \,, \tag{A.24}$$

where N is the local occupancy, and N_0 is the floor-function of N (the closest integer that does not exceed the value of N). The Dudarev functional takes a similar form in that the correction is a combination of first- and second- order occupancy corrections. The only difference is that the occupancies in the Dudarev functional are subspace occupancy matrix elements, diagonalized in the appropriate basis. If the fractional occupancy at an atomic site is limited to only one spin channel of one orbital while all other spin channels are completely filled or empty, then the Dudarev functional will provide

an exact correction for local SIE for an appropriate parameter. This was a *post hoc* attribution upon derivation of the DFT+U functional from the Hubbard model, and it does not address SCE.

The BLOR functional, however, was derived by the authors of Ref. [5] to address the flat-plane condition explicitly, avoiding any derivation from the Hubbard model. The BLOR functional is at once shown to

1. be a continuous function of the subspace electron count N and subspace magnetization M.
2. yield no correction at integer values of N and M.
3. have constant curvature of $-U^\sigma$ with respect to n^σ (i.e., replicate the curvature of (semi)-local functionals with respect to the flat-plane condition).
4. have constant curvature J with respect to fractional M.

BLOR is similar to existing functionals like the judiciously modified (jmDFT),[6,7] a modification of Himmetoglu's DFT+U+J that addresses the global flat-plane condition but does not satisfy criterion (3) and (4). Particularly, BLOR was derived to have three terms and varies depending on if it is applied to orbitals that are more or less than half-filled. The three terms include

1. the symmetric SIE term (called MSIE). This guarantees no correction at integer values of N and maximal correction at $N = \frac{1}{2}, \frac{3}{2}$.
2. the SCE term, which yields zero correction when the subspace is maximally spin-polarized (i.e., either $n^\uparrow = 0$ and/or $n^\downarrow = 0$) and maximal correction when $n^\uparrow = n^\downarrow$, so $M = 0$.
3. the asymmetric SIE term. This accounts for the difference between $U^\uparrow$ and $U^\downarrow$ caused by the presence of an effective magnetic field.

It was noted that BLOR exceeds the accuracy of other Hubbard-like functionals in correcting total energies for a set of dissociated *s*-block dimers, but it cannot properly correct the KS potential.[5] BLOR's success at correcting total energies can be attributed to the fact that its SCE term is negative and therefore cancels the added effect of the asymmetric and symmetric SIE terms. Most other corrective functionals do not have this feature, as the corrective SCE term is positive in value. This framework leads to the assertion that if one were to make the value of J negative in employing the Himmetoglu DFT+U+J functional, thereby reversing the effect of the minority-spin and SCE terms, a similar cancellation of errors would occur and the exact corrective energy better recovered. In Part IV, we test this theory.

The non-self-consistent version of the BLOR functional has total energy defined by

$$E_{\mathrm{BLOR}} = E_{\mathrm{Dudarev}} + \begin{cases} \sum\limits_{\sigma mm'} -\frac{1}{2}(U+J) n^\sigma_{mm'} n^{\bar{\sigma}}_{m'm}, & N \leq 2\ell + 1 \\ \sum\limits_{\sigma mm'} \left[(U+J) n^\sigma_{mm'} \delta_{mm'} - \frac{1}{2}(U+J) n^\sigma_{mm'} n^{\bar{\sigma}}_{m'm} - \frac{U+J}{2(2\ell+1)} \right], & N > 2\ell + 1 \end{cases} \tag{A.25}$$

as in Section SI-III in Ref. [5].

5 On the compensation charge density

Shortly after Blöchl introduced the PAW method, the authors of Ref. [8] responded in 1998 by taking the Blöchl formalism and modifying it to make explicit PAW's relationship to the already well-established plane-wave and pseudopotential implementations in DFT codes. Some of the energy terms were rearranged and the treatment of the pseudized exchange-correlation contributions were modified. A term called the valence compensation charge density—a body similar to the pseudized augmentation function of Eq. (3.13), initially introduced to ensure correct calculation of the multipole moments of the Hartree energy—was added to the XC energy in order to ensure that the pseudo-density accurately represented the charge moments of atomic systems. The compensation charge has the capacity to introduce non-cancelling errors if it is not treated properly, as demonstrated by Holzwarth and colleagues in a series of investigations, which we describe briefly here.[9–11]

In the original formalism from Blöchl, which is explicitly implemented in ABINIT, the exchange-correlation energy term is a functional of the sum of two types of pseudo-densities: the valence pseudo-density and the core pseudo-density. The modified implementation tacks on another term to this sum—a term $\hat{n}$, the compensation charge density, defined as a sum of atom a-centered terms

$$\hat{n}(r) = \sum_a \hat{n}^a(\mathbf{r} - \mathbf{R}^t). \tag{A.26}$$

Initially, this compensation charge, which ensures correct and physical charge moment, was to be used only to correct the Coulomb energy. However, the term may also be included as a correction to the charge density, which, in turn, influences the XC functional, resulting in unphysical behavior of the XC potential as a function of distance from the nucleus r as it approaches the cutoff radius intrinsic to the PAW augmentation sphere. If ignored, the error can affect the binding energy by a tangible degree in addition to any derivatives of the total energy. It was discovered that this phenomenon derives from the sign of $\hat{n}$. For a spherical atom in the ground state, the compensation charge density is proportional to an integral inside the augmentation region of the AE density minus the pseudo-density,

$$\hat{n}^a(r) = \zeta(r) \int_{r<r_c} \left(n(\mathbf{r}) - \widetilde{n}(\mathbf{r}) \right) d\mathbf{r}. \tag{A.27}$$

In the case of sodium, for example, $\hat{n}$ doesn't present much of a problem because in the LDA, the pseudo-density is smaller than the AE density, corresponding to a positively valued compensation charge; however, in the case of cesium, the opposite is true. Furthermore, the compensation charge density term is sensitive to the choice of shape function $\zeta(r)$ used to mold it. If the shape function is appropriate, one can get good results, but in some extreme cases, the shape function imbues the system with the numerical instability close to the radial cutoff limit. Depending on the circumstance at hand, users may thus find valuable the option to exclude the compensation charge density from the XC potential.

Plane-wave SCF electronic structure theory codes such as VASP and Quantum ESPRESSO do not make such an option available to users, although they have since modified their PAW implementation somewhat in order to account for this error. ABINIT has an input variable called `usexcnhat`, which

stands for “USE Exchange-Correlation with N HAT," to toggle on or off its inclusion. The default setting is to determine the use of the compensation charge density through the incoming PAW dataset. The JTH PAW datasets, for example, exclude the compensation charge density from calculations impulsing the XC potential.

Appendix B

Supplemental information for Part III

Xenolithic appendices sometimes seem like an accumulation of rock fragments put at the edge a bigger, dissertative rock. Not so with this straightforward chapter, with a density-of-states plot for the DFT+U^d functional (Section B2), the expansion of the heat map in Table 7.4 (Section B3), and representative input files for Part III calculations (Section B1).

1 Representative input files

Linear response U on O 2*p* for all MOs of NiO supercell in ABINIT.

```
#################################################
##        NiO Oxygen Linear Response U         ##
##      for all magnetic configurations        ##
#################################################

ndtset 15
udtset 5 3

# 1 - FM configuration
# 2 - AFI configuration
# 3 - AFII configuration

#Run Parameters
nstep  80
toldfe 1.0d-8
ecut 900 eV
pawecutdg 1200 eV
chkprim 0
tolrde 1.0d-8

#Convergence Params
diemix 0.15
diemixmag 0.1
#nline 10

#General Structural
natom 64
ntypat 3
typat 1 31*2 32*3
znucl 8 8 28
rprim 2.0000000000   0.0000000000   0.0000000000
      0.0000000000   2.0000000000   0.0000000000
      0.0000000000   0.0000000000   2.0000000000
xred  0.2500000000   0.0000000000   0.0000000000
      0.2500000000   0.0000000000   0.5000000000
      0.2500000000   0.5000000000   0.0000000000
      0.2500000000   0.5000000000   0.5000000000
      0.7500000000   0.0000000000   0.0000000000
      0.7500000000   0.0000000000   0.5000000000
```

```
      0.7500000000   0.5000000000   0.0000000000
      0.7500000000   0.5000000000   0.5000000000
      0.2500000000   0.2500000000   0.2500000000
      0.2500000000   0.2500000000   0.7500000000
      0.2500000000   0.7500000000   0.2500000000
      0.2500000000   0.7500000000   0.7500000000
      0.7500000000   0.2500000000   0.2500000000
      0.7500000000   0.2500000000   0.7500000000
      0.7500000000   0.7500000000   0.2500000000
      0.7500000000   0.7500000000   0.7500000000
      0.0000000000   0.0000000000   0.2500000000
      0.0000000000   0.0000000000   0.7500000000
      0.0000000000   0.5000000000   0.2500000000
      0.0000000000   0.5000000000   0.7500000000
      0.5000000000   0.0000000000   0.2500000000
      0.5000000000   0.0000000000   0.7500000000
      0.5000000000   0.5000000000   0.2500000000
      0.5000000000   0.5000000000   0.7500000000
      0.0000000000   0.2500000000   0.0000000000
      0.0000000000   0.2500000000   0.5000000000
      0.0000000000   0.7500000000   0.0000000000
      0.0000000000   0.7500000000   0.5000000000
      0.5000000000   0.2500000000   0.0000000000
      0.5000000000   0.2500000000   0.5000000000
      0.5000000000   0.7500000000   0.0000000000
      0.5000000000   0.7500000000   0.5000000000
      0.0000000000   0.0000000000   0.0000000000
      0.0000000000   0.0000000000   0.5000000000
      0.0000000000   0.5000000000   0.0000000000
      0.0000000000   0.5000000000   0.5000000000
      0.5000000000   0.0000000000   0.0000000000
      0.5000000000   0.0000000000   0.5000000000
      0.5000000000   0.5000000000   0.0000000000
      0.5000000000   0.5000000000   0.5000000000
      0.0000000000   0.2500000000   0.2500000000
      0.0000000000   0.2500000000   0.7500000000
      0.0000000000   0.7500000000   0.2500000000
      0.0000000000   0.7500000000   0.7500000000
      0.5000000000   0.2500000000   0.2500000000
      0.5000000000   0.2500000000   0.7500000000
      0.5000000000   0.7500000000   0.2500000000
      0.5000000000   0.7500000000   0.7500000000
      0.2500000000   0.0000000000   0.2500000000
      0.2500000000   0.0000000000   0.7500000000
      0.2500000000   0.5000000000   0.2500000000
      0.2500000000   0.5000000000   0.7500000000
      0.7500000000   0.0000000000   0.2500000000
      0.7500000000   0.0000000000   0.7500000000
      0.7500000000   0.5000000000   0.2500000000
      0.7500000000   0.5000000000   0.7500000000
      0.2500000000   0.2500000000   0.0000000000
      0.2500000000   0.2500000000   0.5000000000
      0.2500000000   0.7500000000   0.0000000000
      0.2500000000   0.7500000000   0.5000000000
      0.7500000000   0.2500000000   0.0000000000
      0.7500000000   0.2500000000   0.5000000000
      0.7500000000   0.7500000000   0.0000000000
      0.7500000000   0.7500000000   0.5000000000

#General Spin
nsppol 2
nspden 2
nspinor 1

#Kpoint Grid
kptopt 1
chksymbreak 0

# DFT+U
usepawu 1
lpawu 1 1 2
upawu 0.0 0.0 0.0 eV
jpawu 0.0 0.0 0.0 eV
pawujat 1
macro_uj 1
pawujv:? -0.2 eV
pawujv+? 0.1 eV
dmatpuopt 3
```

```
#Printing Info
irdwfk 0
pawprtvol -3
prtvol 3
timopt 2
prteig 0
prtden 0
prtgsr 0
prtebands 0
prtwf 0

#Pseudos
pp_dirpath "./pseudos/JTH1.1_PAW_std"
pseudos "O.xml,␣O.xml,␣Ni.xml"
#============================================= FM
getwfk_filepath?1 "./2_0_initialize_DS1_WFK"
occopt?1 4
tsmear?1 0.005
acell?1 3*7.8820
ngkpt?1 3 3 3

#Spin
spinat?1 0 0 0
         0 0 0
         0 0 0
         0 0 0
         0 0 0
         0 0 0
         0 0 0
         0 0 0
         0 0 0
         0 0 0
         0 0 0
         0 0 0
         0 0 0
         0 0 0
         0 0 0
         0 0 0
         0 0 0
         0 0 0
         0 0 0
         0 0 0
         0 0 0
         0 0 0
         0 0 0
         0 0 0
         0 0 0
         0 0 0
         0 0 0
         0 0 0
         0 0 0
         0 0 0
         0 0 0
         0 0 0
         0 0 4
         0 0 4
         0 0 4
         0 0 4
         0 0 4
         0 0 4
         0 0 4
         0 0 4
         0 0 4
         0 0 4
         0 0 4
         0 0 4
         0 0 4
         0 0 4
         0 0 4
         0 0 4
         0 0 4
         0 0 4
         0 0 4
         0 0 4
         0 0 4
         0 0 4
         0 0 4
```

```
         0 0 4
         0 0 4
         0 0 4
         0 0 4
         0 0 4
         0 0 4
         0 0 4
         0 0 4
         0 0 4
#========================================== AF I
getwfk_filepath?2 "./2_O_initialize_DS2_WFK"
occopt?2 4
tsmear?2 0.005
ngkpt?2 3 3 3
acell?2 3*7.8764

#Spin
spinat?2 0 0 0
         0 0 0
         0 0 0
         0 0 0
         0 0 0
         0 0 0
         0 0 0
         0 0 0
         0 0 0
         0 0 0
         0 0 0
         0 0 0
         0 0 0
         0 0 0
         0 0 0
         0 0 0
         0 0 0
         0 0 0
         0 0 0
         0 0 0
         0 0 0
         0 0 0
         0 0 0
         0 0 0
         0 0 0
         0 0 0
         0 0 0
         0 0 0
         0 0 0
         0 0 0
         0 0 0
         0 0 4
         0 0 4
         0 0 4
         0 0 4
         0 0 4
         0 0 4
         0 0 4
         0 0 4
         0 0 -4
         0 0 -4
         0 0 -4
         0 0 -4
         0 0 -4
         0 0 -4
         0 0 -4
         0 0 -4
         0 0 -4
         0 0 -4
         0 0 -4
         0 0 -4
         0 0 -4
         0 0 -4
         0 0 -4
         0 0 4
         0 0 4
         0 0 4
         0 0 4
         0 0 4
```

```
         0 0 4
         0 0 4
         0 0 4

#========================================== AF II
getwfk_filepath?3 "./2_O_initialize_DS3_WFK"
occopt?3 0
nband?3 386
occ?3 384*1.0 2*0.0 384*1.0 2*0.0
acell?3 3*7.8800
ngkpt?3 5 5 5

#Spin
spinat?3 0 0 0
         0 0 0
         0 0 0
         0 0 0
         0 0 0
         0 0 0
         0 0 0
         0 0 0
         0 0 0
         0 0 0
         0 0 0
         0 0 0
         0 0 0
         0 0 0
         0 0 0
         0 0 0
         0 0 0
         0 0 0
         0 0 0
         0 0 0
         0 0 0
         0 0 0
         0 0 0
         0 0 0
         0 0 0
         0 0 0
         0 0 0
         0 0 0
         0 0 0
         0 0 4
         0 0 -4
         0 0 -4
         0 0 4
         0 0 -4
         0 0 4
         0 0 4
         0 0 -4
         0 0 -4
         0 0 4
         0 0 4
         0 0 -4
         0 0 4
         0 0 -4
         0 0 -4
         0 0 4
         0 0 -4
         0 0 4
         0 0 4
         0 0 -4
         0 0 4
         0 0 -4
         0 0 -4
         0 0 4
         0 0 -4
         0 0 4
         0 0 4
         0 0 -4
         0 0 4
         0 0 -4
         0 0 -4
         0 0 4
```

Liechtenstein functional applying AF_{II} parameters to all valence subspaces on all MOs of NiO PBE simulation in ABINIT.

```
#################################################
##       NiO Geometry Relax Calculation        ##
##      for all magnetic configurations        ##
#################################################

ndtset 3
# 1 - FM configuration
# 2 - AFI configuration
# 3 - AFII configuration

#Run Parameters
nstep 60
toldfe 1.0d-12
ecut 900 eV
pawecutdg 1200 eV
chkprim 0
tolrde 1.0d-12
paral_atom 0

#General Structural
natom 4
ntypat 2
typat 1 1 2 2
znucl 28 8

#General Spin
nsppol 2
nspden 2
nspinor 1

#Kpoint Grid
kptopt 1
chksymbreak 0

# DFT+U
usepawu 1
lpawu 2 1
upawu 5.78 11.27 eV
jpawu 0.50 1.83 eV
dmatpuopt 2

#Printing Info
outdata_prefix = "AF2_UdpJdp"
timopt 2
prteig 0
prtden 2
prtgsr 0
prtebands 0
prtwf 0
prtdos 3
prtdosm 2
pawprtdos 2

#Pseudos
pp_dirpath "./pseudos/JTH1.1_PAW_std"
pseudos "Ni.xml, O.xml"

#======================== FM
occopt1 4
tsmear1 0.005
ngkpt1 40 20 40
acell1 3*7.8820

#Spin
spinat1 0 0 4
        0 0 4
        0 0 0
        0 0 0

#Structural Parameters
xred1  0.0000000000 0.0000000000 0.0000000000
       0.5000000000 0.5000000000 0.5000000000
       0.5000000000 0.0000000000 0.5000000000
       0.0000000000 0.5000000000 0.0000000000
```

```
rprim1 0.5000000000  0.5000000000  0.0000000000
       0.0000000000  0.0000000000  1.0000000000
       0.5000000000 -0.5000000000  0.0000000000

#======================== AF I
occopt2 0
nband2 26
occ2  24*1.0 2*0.0 24*1.0 2*0.0
ngkpt2 40 20 40
acell2 3*7.8764

#Spin
spinat2 0 0 4
        0 0 -4
        0 0 0
        0 0 0

#Structural Parameters
xred2 0.0000000000 0.0000000000 0.0000000000
      0.5000000000 0.5000000000 0.5000000000
      0.5000000000 0.0000000000 0.5000000000
      0.0000000000 0.5000000000 0.0000000000

rprim2 0.5000000000  0.5000000000  0.0000000000
       0.0000000000  0.0000000000  1.0000000000
       0.5000000000 -0.5000000000  0.0000000000

#======================== AF II
occopt3 0
nband3 26
occ3  24*1.0 2*0.0 24*1.0 2*0.0
ngkpt3 30 30 30
acell3 3*7.8800

#Spin
spinat3 0 0 4
        0 0 -4
        0 0 0
        0 0 0

#Structural Parameters
xred3 0.0000000000 0.0000000000 0.0000000000
      0.5000000000 0.5000000000 0.5000000000
      0.2500000000 0.2500000000 0.2500000000
      0.7500000000 0.7500000000 0.7500000000

rprim3 0.5000000000 0.5000000000 1.0000000000
       1.0000000000 0.5000000000 0.5000000000
       0.5000000000 1.0000000000 0.5000000000
```

2 Density of states plot for DFT+U^d

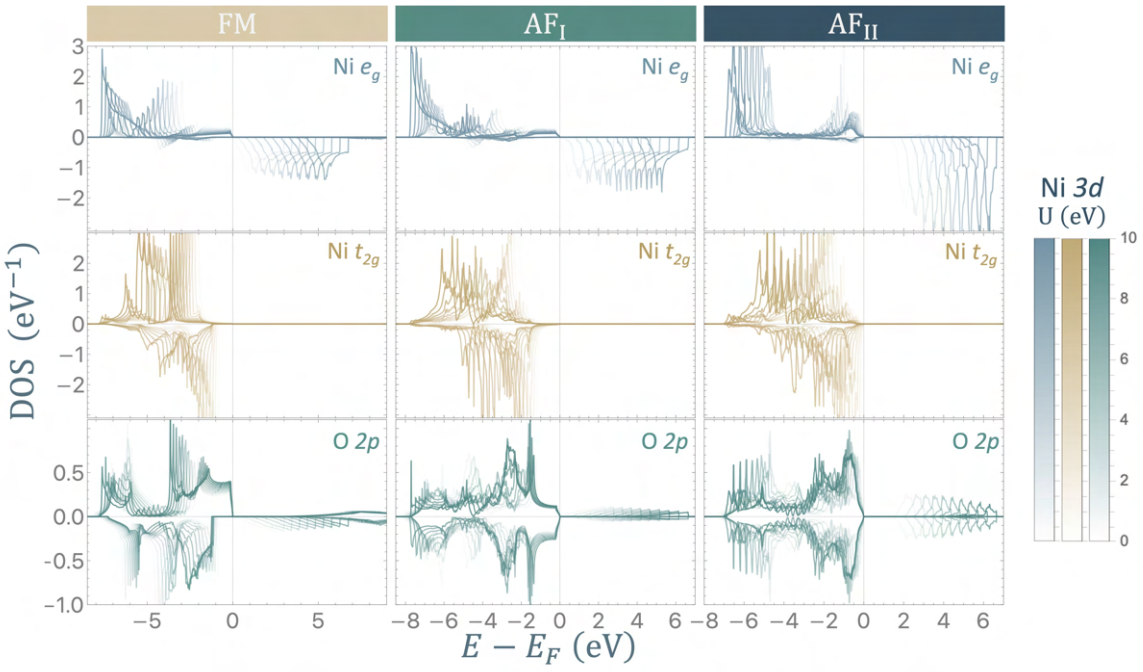

Figure B.1: Overlaid atomic (AE) orbital projected density of states (PDOS) on two particular atoms of the four-atom unit cell, resolved by crystal-field-splitting characterization on Ni *(e_g blue, top row; t_{2g} tan, middle row) and* O *(2p orbital green, bottom row) for each magnetic ordering (*FM *left column;* AF$_I$ *middle column;* AF$_{II}$ *right column) of* NiO. *Positive values indicate majority-spin PDOS, negative values indicate minority-spin. Opacity of plot is a function of* U^d (eV) *in the Dudarev* DFT+U^d *functional, where* U^d *is applied in the same magnitude to all MOs of* NiO. *Only the component within the PAW augmentation sphere cutoff r_c for each species is included, with no interstitial contributions, hence the relatively sharp (atomic-like) features of the PDOS. Moreover, only the conduction band edge position should be interpreted here, as the Kohn-Sham basis is not thought to be complete for the conduction band for all MOs in the energy range shown.*

3 Data concerning various spin-moment techniques

We report data pertaining to the S_z and |**S**| calculations across three population analysis methods for the spin-moment: the AS method of Eq. (6.7), the PAW method of Eq. (6.8), and the SD method of Eq. (6.9). Table 7.4 is a condensed version of this table. Table 7.4 numbers acquired by taking the cumulative % RMS error of the exchange parameter pairs with respect to the Hutchings *et al.*[12] experimental values, then averaging across all six Hubbard functionals.

	S_z						|**S**|					
	Method A		Method B		Method C		Method A		Method B		Method C	
Functional	J_1 (meV)	J_2 (meV)	J_1 (meV)	J_2 (meV)	J_1 (meV)	J_2 (meV)	J_1 (meV)	J_2 (meV)	J_1 (meV)	J_2 (meV)	J_1 (meV)	J_2 (meV)
DFT (PBE)	8.23	-29.32	19.46	-69.35	2.74	-60.96	8.23	-29.32	9.73	-34.68	1.37	-30.48
DFT+U^d	0.95	-10.20	1.34	-14.43	1.20	-13.91	0.95	-10.20	0.67	-7.22	0.60	-6.96
DFT+$U^{d,p}$	1.53	-7.11	2.15	-10.00	2.00	-9.76	1.53	-7.11	1.08	-5.00	1.00	-4.88
DFT+U^d_{eff}	1.03	-11.10	1.48	-16.00	1.32	-15.36	1.03	-11.10	0.74	-8.00	0.66	-7.68
DFT+$U^{d,p}_{\text{eff}}$	1.52	-8.41	2.19	-12.07	2.00	-11.72	1.52	-8.41	1.10	-6.04	1.00	-5.86
DFT+U^d + J^d_z	0.96	-10.24	1.37	-14.61	1.23	-14.08	0.96	-10.24	0.69	-7.31	0.62	-7.04
DFT+$U^{d,p}$ + $J^{d,p}_z$	1.00	-7.35	1.43	-10.44	1.32	-10.19	1.00	-7.35	0.72	-5.22	0.66	-5.10
DFT (PBE)	8.23	-29.32	19.00	-67.70	3.17	-60.58	8.23	-29.32	9.50	-33.85	1.59	-30.29
DFT+U^d	0.95	-10.20	1.28	-13.74	1.19	-13.40	0.95	-10.20	0.64	-6.87	0.60	-6.70
DFT+$U^{d,p}$	1.53	-7.11	2.05	-9.52	1.95	-9.35	1.53	-7.11	1.03	-4.76	0.98	-4.68
DFT+U^d_{eff}	1.03	-11.10	1.41	-15.26	1.31	-14.84	1.03	-11.10	0.71	-7.63	0.66	-7.42
DFT+$U^{d,p}_{\text{eff}}$	1.52	-8.41	2.09	-11.52	1.96	-11.27	1.52	-8.41	1.05	-5.76	0.98	-5.64
DFT+U^d + J^d_z	0.96	-10.24	1.31	-13.99	1.23	-13.64	0.96	-10.24	0.66	-7.00	0.62	-6.82
DFT+$U^{d,p}$ + $J^{d,p}_z$	1.00	-7.35	1.36	-10.00	1.29	-9.81	1.00	-7.35	0.68	-5.00	0.65	-4.91
DFT (PBE)	8.23	-29.32	15.89	-56.63	3.13	-46.94	8.23	-29.32	7.95	-28.32	1.57	-23.47
DFT+U^d	0.95	-10.20	1.15	-12.33	1.46	-11.66	0.95	-10.20	0.58	-6.17	0.73	-5.83
DFT+$U^{d,p}$	1.53	-7.11	1.84	-8.55	1.93	-8.02	1.53	-7.11	0.92	-4.28	0.97	-4.01
DFT+U^d_{eff}	1.03	-11.10	1.26	-13.62	1.61	-12.80	1.03	-11.10	0.63	-6.81	0.81	-6.40
DFT+$U^{d,p}_{\text{eff}}$	1.52	-8.41	1.83	-10.13	2.00	-9.52	1.52	-8.41	0.92	-5.07	1.00	-4.76
DFT+U^d + J^d_z	0.96	-10.24	1.17	-12.51	1.48	-11.80	0.96	-10.24	0.59	-6.26	0.74	-5.90
DFT+$U^{d,p}$ + $J^{d,p}_z$	1.00	-7.35	1.22	-8.95	1.44	-8.38	1.00	-7.35	0.61	-4.48	0.72	-4.19

Table B.1: Comparison of exchange-coupling parameters from various Hubbard functionals employing the AF_{II} *HPs listed in column 4 of Table 7.3. (A* ^{d} *superscript refers to parameter on* Ni *3d orbitals;* ^{p} *superscript refers to parameter on* O *2p orbitals;* $U_{\text{eff}} = U - J_H$*). Top block of functionals highlighted in blue refers to use of moments from* AS *method. Second block of functionals, highlighted in grey, refers to use of moments from* PAW *method. Moments from* SD *(bottom block of functionals, highlighted in green) harvested from* ABINIT *output using* C2x.[13]

Appendix C

Supplemental information for Part IV

Yielding further clarity into the methods and results of Part IV, Section C1 of this appendix illustrates the energetics for common Hubbard functionals with spin-state-specific HPs. Section C2 provides representative input files used for calculations across ABINIT, ONETEP, and QUANTUM ESPRESSO, serving as a practical reference for reproducing or extending the work.

1 Energetics for common Hubbard functionals with spin-state-specific HPs

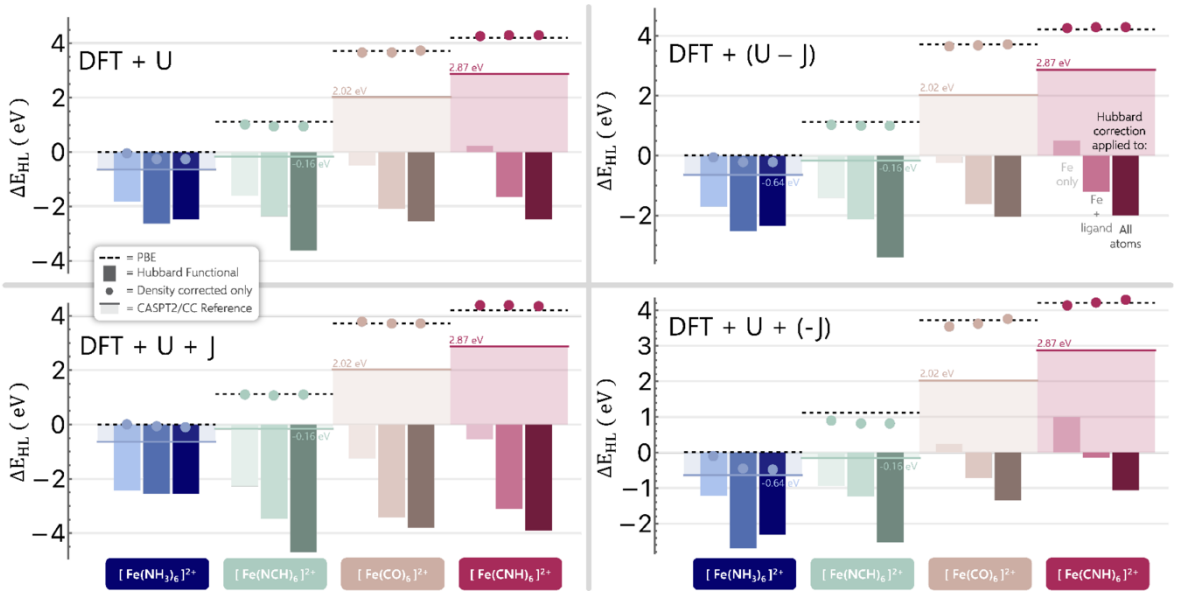

Figure C.1: Adiabatic energy differences ΔE_{HL} for all molecules obtained via the denoted Hubbard functional (Dudarev DFT+U *upper left;* DFT+U–J *upper right; Himmetoglu* DFT+U+J *lower left;* DFT+U+(-J) *lower right), where correction is applied to some combination of subspaces (*Fe = Fe 3*d only,* Fe+L = Fe 3*d and ligand* 2*p,* All = *all valence subspaces in molecule) with the {*U, J*} pairs are the spin-state-specific parameters (in situ), compared to uncorrected DFT (PBE XC functional; black dashed lines) and CASPT2/CC reference values (solid color line with shading). "*Density-corrected*" values (data points) are total energies converged with the denoted Hubbard functional, but Hubbard energy corrections are removed non-self-consistently.*

2 Representative input files

Linear response J on N $2p$ on LS $[Fe(NCH)_6]^{2+}$ in ABINIT.

```
#################################################
##       Fe(II) NCH Linear Response J          ##
##      perturbative runs for linear response  ##
#################################################

#Run Parameters
nstep 80
toldfe 1.0d-9
ecut 80 Ry
pawecutdg 320 Ry
chkprim 0
tolrde 1.0d-9

#Parallelize
#autoparal 1
np_spkpt 2
npband 1
npfft 1

#Convergence Params
diemix 0.25
diemixmag 0.50
diemac 2.0

#General Structural
natom 19
ntypat 5
typat 1 2 6*3 4 5 4 5 4 5 4 5 4 5 4
znucl 6 26 7 1 6
acell 3*37.7945     #37.7945 Bohr = 20 Angstroms
rprim   1.00000000000000   0.00000000000000   0.00000000000000
        0.00000000000000   1.00000000000000   0.00000000000000
        0.00000000000000   0.00000000000000   1.00000000000000
xcart   0.00000060670259  -3.07192132593068  -0.00000009615694 #C 8th
       -0.00000030983029   0.00000008482359   0.00000020320884 #Fe
        0.00000004071455   1.92780371414544   0.00000001613668 #N 2nd
       -1.92767133723787  -0.00000012622893  -0.00000004144136 #N
       -0.00000021243673   0.00000018496596  -1.92767091887810 #N
       -0.00000027627599   0.00000018971525   1.92767122220367 #N
        1.92767077962438  -0.00000025254418  -0.00000007371223 #N
        0.00000008897532  -1.92780353474477  -0.00000003355291 #N
        0.00000113825669  -4.14545336736201  -0.00000025896001 #H 9th
       -3.07179117508670  -0.00000044182076   0.00000003777538 #C
       -4.14532280401137  -0.00000082910929  -0.00000012220504 #H
       -0.00000024142450   0.00000034911248  -3.07179077092316 #C
       -0.00000016093900   0.00000059827987  -4.14532240854984 #H
        3.07179061731203  -0.00000064895676  -0.00000008864073 #C
        4.14532224090071  -0.00000095773243  -0.00000026818880 #H
       -0.00000035212410   0.00000036244945   3.07179107310456 #C
       -0.00000032811172   0.00000064303358   4.14532270123303 #H
        0.00000048688337   3.07192150555771  -0.00000006534057 #C
        0.00000089810861   4.14545355234648  -0.00000020711246 #H
        Angstrom

#General Spin
nsppol 2
nspden 2
occopt 0
nband 42
occ 37*1.0 5*0.0 37*1.0 5*0.0
cellcharge 2
#icutcoul 0
#rcut -1.0

#Kpoint Grid
kptopt 1
ngkpt 1 1 1
shiftk 0.0 0.0 0.0
chksymbreak 0

# DFT+U
usepawu 1
lpawu 1 2 1 -1 1
```

```
upawu 0.0 0.0 0.0 0.0 0.0 eV
jpawu 0.0 0.0 0.0 0.0 0.0 eV
pawovlp 10

#Linear Response
ndtset 6                            #Six perturbations => Seven LR data points
pawujat 1                           #Label of perturbed atom
pawujv1 -0.15 eV                    #List of perturbation strengths
pawujv2 -0.10 eV
pawujv3 -0.05 eV
pawujv4  0.05 eV
pawujv5  0.10 eV
pawujv6  0.15 eV
macro_uj 4
dmatpuopt 3                         #PAW projector for density matrix
irdwfk 0
getwfk_filepath "/ichec/work/tcphy222c/NCH/C/ls/ls_init_WFK"

#Printing Info
outdata_prefix = "J_ls_lr"
prtvol 3
timopt 2
prtxml 0
prtwf 0
prteig 0                            #Don't print eigenvalues
prtden 0                            #Don't print density
prtgsr 0                            #Don't print GSR
prtebands 0                         #Don't print ebands

#Pseudos
pp_dirpath "/ichec/work/tcphy222c/pseudos/PAW/"
pseudos "C.xml,Fe.xml,N.xml,H.xml,C.xml"

#Spin
spinat   0 0 0
         0 0 0
         0 0 0
         0 0 0
         0 0 0
         0 0 0
         0 0 0
         0 0 0
         0 0 0
         0 0 0
         0 0 0
         0 0 0
         0 0 0
         0 0 0
         0 0 0
         0 0 0
         0 0 0
         0 0 0
         0 0 0
```

Linear response J perturbation of strength $\beta = -0.05$ eV applied to N $2p$ on LS $[Fe(CNH)_6]^{2+}$ in ONETEP.

```
#-------------------------------------------------------------------------------#
#                            Fe(II)CNH Molecule                                 #
#                          Linear Response J on N                               #
#                               beta=-0.05                                      #
#-------------------------------------------------------------------------------#

# Parallelization parameters ======================
threads_max                         : 4  # = OMP_NUM_THREADS
threads_num_fftboxes                : 4  # = OMP_NUM_THREADS
threads_per_fftbox                  : 1  # = 1 (Recommended)
threads_per_cellfft                 : 4  # = threads_max (Recommended, speculated as 14 on Boyle)
threads_num_mkl                     : 1
comms_group_size                    : -1

# Run parameters ==================================
task                                : SINGLEPOINT
output_detail                       : VERBOSE
xc_functional                       : PBE
```

```
PAW                                 : T
check_atoms                         : F
do_properties                       : T
popn_calculate                      : T
turn_off_hartree                    : F
edft                                : T
edft_smearing_width                 : 0 K

# Cutoff Energy ======================================
cutoff_energy                       : 1088.4563181 eV

# Inner Loop Density Kernel Parameters ==============
maxit_lnv                           : 10
minit_lnv                           : 5

# Outer Loop: NGWFs =================================
ngwf_threshold_orig                 : 2.0e-6
maxit_ngwf_cg                       : 40
delta_e_conv                        : T
elec_energy_tol                     : 2.7211e-8 eV   #2.7211e-8 eV = 1.0d-9 Ha

# Electronic system-specific options ================
maxit_palser_mano                   : -1
charge                              : 2

# Spin ==============================================
spin_polarized                      : T
spin                                : 0

# Hubbard Parameters ================================
hubbard_unify_sites                 : F
hubbard_calculating_U               : T
hubbard_ngwf_spin_threshold         : 1.0e-20

# Writing/Reading Variables =========================
write_initial_radial_ngwfs          : F
write_denskern                      : F
write_tightbox_ngwfs                : F
write_density_plot                  : F
write_ngwf_plot                     : F
write_xyz                           : F
lumo_dens_plot                      : -1
homo_dens_plot                      : -1
lumo_plot                           : -1
homo_plot                           : -1
read_denskern                       : F
read_tightbox_ngwfs                 : F
print_qc                            : F
write_forces                        : T
cube_format                         : F
grd_format                          : F

# Blocks ============================================
%block species_ngwf_plot
NU
Fe
C
N
H
%endblock species_ngwf_plot

%block species
bohr
NU N  7  8  12.0
Fe Fe 28 26 14.0
C  C  6  8  12.0
N  N  7  8  12.0
H  H  1  2  10.0
%endblock species

%block species_atomic_set
NU "SOLVE conf=2s2:0.2 2p3:0.2"
Fe "SOLVE conf=3s2:0.2 3p6:0.2 3d6:0.2 4s2:0.2 4p0:0.2 INIT SPIN=0 CHARGE=+2"
C  "SOLVE conf=2s2:0.2 2p2:0.2"
N  "SOLVE conf=2s2:0.2 2p3:0.2"
H  "SOLVE conf=1s1:0.2"
%endblock species_atomic_set
```

```
%block species_pot
NU "N.PBE-paw.abinit"
Fe "Fe.PBE-paw.abinit"
C  "C.PBE-paw.abinit"
N  "N.PBE-paw.abinit"
H  "H.PBE-paw.abinit"
%endblock species_pot

%block lattice_cart
ang
20.0 0.00 0.00
0.00 20.0 0.00
0.00 0.00 20.0
%endblock lattice_cart

# Hubbard Parameters (species,L,U,J,projector,alpha,sigma)
%block hubbard
NU 1 0 0 -1.0 0.00 0.1000
Fe 2 0 0 -1.0 0.00 0.00
C  1 0 0 -1.0 0.00 0.00
N  1 0 0 -1.0 0.00 0.00
H  0 0 0 -1.0 0.00 0.00
%endblock hubbard

# Atomic Positions
%block positions_abs
ang
NU      9.999999283279960      6.942433250710800      10.00000032390771    #8th
Fe      10.00000016356901      10.00000001883341      10.00000004388317
C       9.999999879327980      11.90392164175866      10.00000018251570
C       8.096476812233410      9.999999468948550      9.999999735475170
C       10.00000038770608      10.00000054897913      8.096476720305730
C       10.00000035596704      10.00000052048448      11.90352333877423
C       11.90352346690779      9.999999374800180      9.999999734105970
C       9.999999746884190      8.096078329933050      10.00000018570493
H       9.999998807597550      5.936632602972260      10.00000033969773
N       6.942816779870070      9.999998827063230      9.999999752303930
H       5.937021325058640      9.999998082666460      9.999999512695780
N       10.00000044427049      10.00000109541506      6.942816688592810
H       10.00000065305725      10.00000172402335      5.937021237120600
N       13.05718350009071      9.999998814131110      9.999999684753950
H       14.06297894433273      9.999998340708830      9.999999417631850
N       10.00000038178598      10.00000113150434      13.05718336221952
H       10.00000054414653      10.00000184628422      14.06297878499432
N       9.999999380427680      13.05756671909915      10.00000035553131
H       9.999998843486900      14.06336736168372      10.00000049978560
%endblock positions_abs


#-------------------------------------------------------------------------------
#------------------------------ END INPUT FILE ---------------------------------
#-------------------------------------------------------------------------------
```

Linear response U perturbation of strength $\alpha = 0.1$ eV applied to Fe $3d$ on HS $[Fe(NH_3)_6]^{2+}$ in QUANTUM ESPRESSO.

```
&CONTROL
  calculation = 'scf',
  restart_mode = 'restart',
  outdir = './Fe-alpha0.1',
  prefix = 'Fe-0.0',
  pseudo_dir = '/projects/lmacenul/FrIr_Residency/pseudos/GBRV/',
  verbosity = 'high',
/

&SYSTEM
  tot_charge = 2,
  ibrav = 1,
  a = 20.0000000,
  nat = 25,
  ntyp = 3,
  ecutwfc = 80,
  ecutrho = 800,
  assume_isolated = 'mp',
  occupations = 'fixed',
  nspin = 2,
```

```
  tot_magnetization = 4,
  nosym = .true.,
  U_projection_type = "atomic",
  lda_plus_u = .true.,
  nbnd = 35,

  Hubbard_U(1) = 1.0d-40,
  Hubbard_J0(1) = 1.0d-40,
  Hubbard_alpha(1) = 0.1,
  Hubbard_beta(1) = 0.0d0,
  Hubbard_U(2) = 1.0d-40,
  Hubbard_J0(2) = 1.0d-40,
  Hubbard_alpha(2) = 0.0d0,
  Hubbard_beta(2) = 0.0d0,
  Hubbard_U(3) = 1.0d-40,
  Hubbard_J0(3) = 1.0d-40,
  Hubbard_alpha(3) = 0.0d0,
  Hubbard_beta(3) = 0.0d0,

/

&ELECTRONS
  startingpot = file,
  startingwfc = file,
  electron_maxstep = 500,
  conv_thr = 1.0d-9,
  diago_thr_init = 1.0d-12,
/

&IONS
 /

&CELL
 /

ATOMIC_SPECIES
Fe  55.845  Fe.upf
N   14.007  N.upf
H   1.008   H.upf

ATOMIC_POSITIONS {angstrom}
Fe  -1.69167879061757  -0.55799116186911  -0.00395107614296
N   -1.76463324179801   1.71192626593140   0.02393290574124
H   -2.40094373257026   2.09673665376199   0.72194369305460
H   -0.86129341142145   2.13243772528745   0.23990261442027
H   -2.05089936419107   2.14911192801191  -0.85174320179156
N    0.58591195782583  -0.52120995781133  -0.01257075018538
H    1.01171695012455  -0.33498419446258   0.89486175511240
H    1.03058903284816  -1.38058986520593  -0.33487807210837
H    0.95671941009113   0.20264275557852  -0.62767427625672
N   -3.95661991494071  -0.50760692545802  -0.07114873136740
H   -4.37157085098101  -1.41934135830422  -0.26129871322702
H   -4.40854443351751  -0.19066779133882   0.78630645146501
H   -4.32973267782406   0.10109213086505  -0.79945578795939
N   -1.63840258120082  -2.82951523073656   0.04344700944026
H   -2.47990487168354  -3.22738003220791   0.45973559864249
H   -1.56266669890145  -3.27983382744749  -0.86793109731958
H   -0.87476211055708  -3.22397782963094   0.59258594800002
N   -1.70284433143333  -0.59506023578925   2.28598334692030
H   -0.96463093641680  -1.17985497870139   2.67735244619778
H   -1.56684602752220   0.31365724458847   2.72769695175257
H   -2.55905718210244  -0.95993072604048   2.70252882154726
N   -1.63069457789330  -0.60351988990336  -2.29340329036715
H   -0.86347055831701  -1.16877988952671  -2.65681531396245
H   -2.46462590568614  -0.99337316069821  -2.73186140253035
H   -1.50529515231387   0.30471265110754  -2.73930573007585

K_POINTS (automatic)
1 1 1 0 0 0
```

Appendix D

Supplemental information for Part V

$\mathbb{Z}_{\text{eff}}$, the effective nuclear charge, is the variable with which we take the derivative of the hydrogenic radial atomic orbitals in Section D1. These equations are the basis for the implementation in ONETEP of the same name. Section D2 provides representative input files used for calculations in ONETEP, again, serving as a practical reference for reproducing or extending the work.

1 Hydrogen-like radial atomic orbital derivatives in ONETEP

The convenience of the hydrogen-like atomic orbitals [14] as functions of Z_{eff} (see Section 10.1 for further description and citations) stems from their q-space implementation in a rarely used but functional ONETEP subroutine called `hubbard_internal_radial_proj` in `hubbard_build_mod.F90`. We have expanded this functionality by coding up a similar subroutine, `hubbard_deriv_radial_proj`, featuring the derivative of these projectors with respect to Z_{eff}.

If we take the projectors $\hat{P}$ to be the hydrogen-like radial function, then

$$R_{n\ell}^{(Z_{\text{eff}})}(r) = \sqrt{\frac{1}{4\pi}\left(\frac{2Z_{\text{eff}}}{n}\right)^3 \frac{(n-\ell-1)!}{2n\,[(n+\ell)!]}}\, e^{\frac{-rZ_{\text{eff}}}{n}} \left(\frac{2rZ_{\text{eff}}}{n}\right)^{\ell} \mathcal{L}_{n-\ell-1}^{2\ell+1}\left(\frac{2rZ_{\text{eff}}}{n}\right), \tag{D.1}$$

Assuming $\ell = n-1$, Eq. (10.1) simplifies to

$$R_{n,n-1}^{(Z_{\text{eff}})}(r) = \sqrt{\frac{Z_{\text{eff}}^3}{\pi n^4\,[(2n-1)!]}}\, e^{\frac{-rZ_{\text{eff}}}{n}} \left(\frac{2rZ_{\text{eff}}}{n}\right)^{n-1}. \tag{D.2}$$

Then the derivative of the projectors $\hat{P} = R_{n,n-1}^{(Z_{\text{eff}})}$ in Eq. (D.2) with respect to Z_{eff} are found to be

$$\frac{dR_{n,n-1}^{(Z_{\text{eff}})}(r)}{dZ_{\text{eff}}} = \sqrt{\frac{1}{16\pi r^2 Z_{\text{eff}} n^4\,[(2n-1)!]}} e^{\frac{-rZ_{\text{eff}}}{n}} \left(\frac{2rZ_{\text{eff}}}{n}\right)^{n} \left(2n^2+n-2rZ_{\text{eff}}\right) \tag{D.3}$$

Eqs. (D.1) and (D.3) for $n = 3$, $\ell = 2$ as functions of a varying Z_{eff} are shown in Fig. 10.4 of Section 10.1 in the main manuscript, where it becomes obvious that an increasing Z_{eff} serves to localize these functions about their simulated nucleus.

The Fourier-Bessel transform,

$$\frac{d\widetilde{R}_{n\ell}^{(Z_{\text{eff}})}(r)}{dZ_{\text{eff}}} = \int_0^\infty r^2 \frac{dR_{n\ell}^{(Z_{\text{eff}})}(r)}{dZ_{\text{eff}}} j_\ell(qr)\, dr\,, \tag{D.4}$$

where $j_\ell(qr)$ is a spherical Bessel function of order ℓ, grafts the orbital into reciprocal space. To our knowledge, this form of the Fourier-Bessel function only appears in the work of King-Smith *et al.*[15] This Fourier-Bessel transform is not to be confused with the Hankel Transform, which is sometimes referred to as the Fourier-Bessel transform. The Hankel Transform uses an integral of the same bounds, but the integrand is not multiplied by a factor of r^2, and instead of a spherical Bessel function of order ℓ, the function undergoing transform is multiplied by any Bessel function of the first kind (be it spherical, Hankel, or modified).

Using Eqs. (D.3) and (D.4), we explicitly program the following four projector derivative functions, corresponding to the $n\ell$ orbitals, where $n = 0, 1, 2, 3$ and $\ell = n-1$, as implemented in ONETEP.

$$\frac{d\widetilde{R}_{1s}^{(Z_{\text{eff}})}(r)}{dZ_{\text{eff}}} = \sqrt{\frac{Z_{\text{eff}}^3}{\pi}} \frac{\left(5q^2 - 3Z_{\text{eff}}^2\right)}{\left(q^2 + Z_{\text{eff}}^2\right)^3} \tag{D.5}$$

$$\frac{d\widetilde{R}_{2p}^{(Z_{\text{eff}})}(r)}{dZ_{\text{eff}}} = 16\sqrt{\frac{2Z_{\text{eff}}^5}{3\pi}} \frac{q\left(28q^2 - 5Z_{\text{eff}}^2\right)}{\left(4q^2 + Z_{\text{eff}}^2\right)^4} \tag{D.6}$$

$$\frac{d\widetilde{R}_{3d}^{(Z_{\text{eff}})}(r)}{dZ_{\text{eff}}} = 216\sqrt{\frac{6Z_{\text{eff}}^7}{5\pi}} \frac{q^2\left(81q^2 - 7Z_{\text{eff}}^2\right)}{\left(9q^2 + Z_{\text{eff}}^2\right)^5} \tag{D.7}$$

$$\frac{d\widetilde{R}_{4f}^{(Z_{\text{eff}})}(r)}{dZ_{\text{eff}}} = 32768\sqrt{\frac{Z_{\text{eff}}^9}{35\pi}} \frac{q^3\left(176q^2 - 9Z_{\text{eff}}^2\right)}{\left(16q^2 + Z_{\text{eff}}^2\right)^6} \tag{D.8}$$

2 Representative input files

Linear response U perturbation of strength $\alpha = 0.05$ eV applied to spin-up channel of H $1s$ of the dissociated ionized hydrogen diatomic molecule in ONETEP. Z_{eff} is set to 0.045.

```
#-------------------------------------------------------------------------------#
#                            H2+ Equation of Motion                             #
#                              ONETEP Input File                                #
#                             Z=0.045 alpha^=0.05                               #
#-------------------------------------------------------------------------------#

# Parallelization parameters ==========================
#threads_max                     : 4     #This must match "OMP_NUM_THREADS" and "-d" options in submission script
#threads_num_fftboxes            : 4     #This must match "OMP_NUM_THREADS" and "-d" options in submission script
#threads_per_fftbox              : 1     # Reccomended value is 1
#threads_per_cellfft             : 4     # =threads_max is reasonable #On Boyle, this is speculated to be 14
#threads_num_mkl                 : 1
#comms_group_size                : -1


# Run parameters ====================================
task                             : SINGLEPOINT
output_detail                    : VERBOSE
xc_functional                    : PBE
check_atoms                      : F #T !
do_properties                    : T
popn_calculate                   : T
turn_off_hartree                 : F

# Cutoff Energy =====================================
psinc_spacing                    : 0.278951817413 0.278951817413 0.278951817413

# Inner Loop Density Kernel Parameters ==============
lnv_threshold_orig               : 1.0e-6
lnv_cg_max_step                  : 10.0
maxit_lnv                        : 10
minit_lnv                        : 3 #1
lnv_check_trial_steps            : T
kernel_update                    : T

# Outer Loop: NGWFs =================================
ngwf_threshold_orig              : 1.0e-7
ngwf_cg_max_step                 : 100.0
maxit_ngwf_cg                    : 100
elec_cg_max                      : 100
delta_e_conv                     : T
ELEC_ENERGY_TOL                  : 1.0e-6 eV
ngwf_analysis                    : F

# Electronic system-specific options ================
maxit_pen                        : 0
maxit_palser_mano                : -1
maxit_kernel_fix                 : 0
kerfix                           : 1
maxit_hotelling                  : 0
charge                           : 1
dos_smear                        : 0.10 eV
occ_mix                          : 0.0 #speeds up convergence; default 0.25
pbc_correction_cutoff            : 7.0
timings_level                    : 1

# Spin ==============================================
spin_polarized                   : T
spin                             : 1.0
polarisation_calculate           : F

# Hubbard Parameters ================================
hubbard_unify_sites              : F
hubbard_calculating_U            : T
hubbard_ngwf_spin_threshold      : 1.0e-20

# Writing/Reading Variables =========================
write_converged_dk_ngwfs         : T
write_initial_radial_ngwfs       : T #Printed to plot, make sure set to something reasonable
write_denskern                   : F #T
write_tightbox_ngwfs             : F #T
```

```
write_density_plot                  : F
write_ngwf_plot                     : F
lumo_dens_plot                      : -1
homo_dens_plot                      : -1
lumo_plot                           : -1
homo_plot                           : -1
read_denskern                       : F
read_tightbox_ngwfs                 : F
print_qc                            : F
write_forces                        : T
cube_format                         : F
grd_format                          : F

# Blocks ======================================
%block species_ngwf_plot
H1
H2
%endblock species_ngwf_plot

%block species
bohr
H1 H 1 1 10.0
H2 H 1 1 10.0
%endblock species

%block species_atomic_set
H1 "SOLVE conf=1s0.045"
H2 "SOLVE conf=1s0.045"
%endblock species_atomic_set


%block species_pot
H1 H_OPIUM_PBE_0.65_1500eV.recpot
H2 H_OPIUM_PBE_0.65_1500eV.recpot
%endblock species_pot


%block species_ldos_groups
H1
H2
%endblock species_ldos_groups


%block lattice_cart
bohr
60.0 0.00 0.00
0.00 42.0 0.00
0.00 0.00 42.0
%endblock lattice_cart

# Hubbard Parameters (species,L,U,J,projector,alpha,sigma)
%block hubbard
H1 0 0 0 -1.0 0.0250 -0.0500
H2 0 0 0 -1.0 0.00 0.00 #leave as 0.0; perturbations only to first atom
%endblock hubbard

# Atomic Positions
%block positions_abs
bohr
H1      44.25   30.0    30.0
H2      35.75   30.0    30.0
%endblock positions_abs

#------------------------------------------------------------------------------
#------------------------------ END INPUT FILE --------------------------------
#------------------------------------------------------------------------------
```

Opium input file used to generate a norm-conserving PBE pseudopotential in `.recpot` format.

```
############################################################
#     Opium Parameter File                                 #
############################################################

[Atom]
H
1
100   1.00   -

[Pseudo]
1  0.65
opt

[Optinfo]
10.5  10

[Configs]
4
#
100  0.80  -
#
100  0.60  -
#
100  0.40  -
#
100  0.20  -

[XC]
pbe

[Relativity]
nrl
END COMMENT

############################################################
#     End File                                             #
############################################################
```

Bibliography

[1] P. Hohenberg and W. Kohn, Phys. Rev. **136**, B864 (1964).

[2] W. Kohn and L. J. Sham, Phys. Rev. **140**, A1133 (1965).

[3] O. K. Orhan, *Corrective First-Principles Approaches for the Theoretical Spectroscopy of Transition-Metal Systems*, Physics, School of Physics, Trinity College Dublin, The University of Dublin, College Green, Dublin 2, Ireland (2018).

[4] Unknown, Astrophysical Institute Neunhof **77211**, 1 (2010).

[5] A. C. Burgess, E. Linscott, and D. D. O'Regan, Phys. Rev. B **107**, L121115 (2023).

[6] A. Bajaj, J. P. Janet, and H. J. Kulik, The Journal of Chemical Physics **147**, 191101 (2017).

[7] A. Bajaj, F. Liu, and H. J. Kulik, The Journal of Chemical Physics **150**, 154115 (2019).

[8] G. Kresse and D. Joubert, Physical Review B **59**, 1758 (1999).

[9] M. Torrent, N. Holzwarth, F. Jollet, D. Harris, N. Lepley, and X. Xu, Computer Physics Communications **181**, 1862 (2010).

[10] N. Holzwarth, Computer Physics Communications **243**, 25 (2019).

[11] N. Holzwarth, A. Tackett, and G. Matthews, Computer Physics Communications **135**, 329 (2001).

[12] M. T. Hutchings and E. J. Samuelsen, Phys. Rev. B **6**, 3447 (1972).

[13] M. Rutter, Computer Physics Communications **225**, 174 (2018).

[14] J. Avery, *Hyperspherical Harmonics and Generalized Sturmians* (Springer, Dordrecht, 2001) p. 205.

[15] R. D. King-Smith, M. C. Payne, and J. S. Lin, Physical Review B **44**, 13063 (1991).